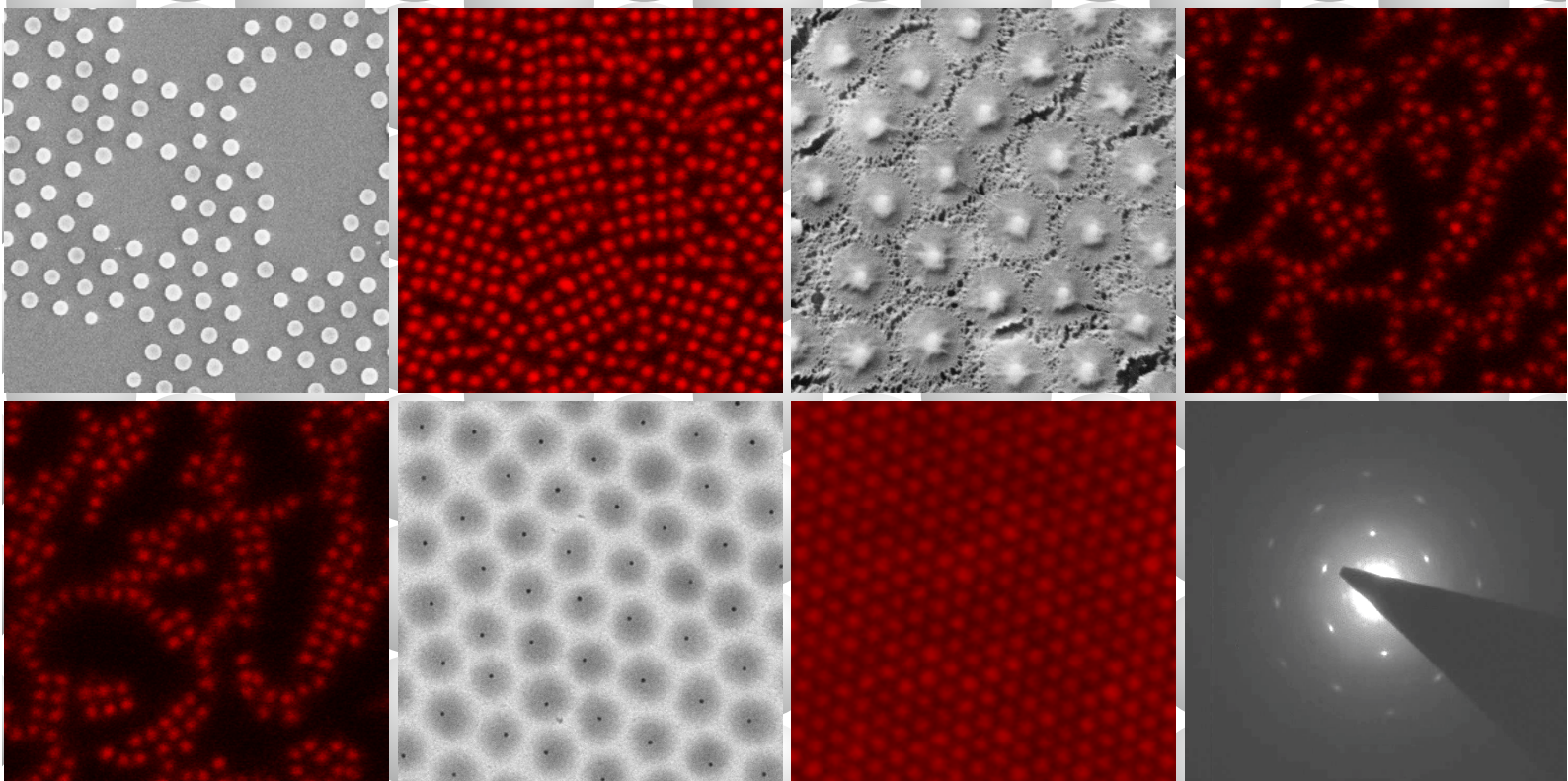


Self-Assembly of Hard-Core/Soft-Shell Colloids in Bulk and at the Interface

Astrid Rauh
Dissertation
Universität Bayreuth, 2018



SELF-ASSEMBLY OF HARD-CORE/SOFT-SHELL
COLLOIDS
IN BULK AND AT THE INTERFACE

DISSERTATION

zur Erlangung des akademischen Grades eines
Doktors der Naturwissenschaften
Dr. rer. nat.

an der
Universität Bayreuth,
Fakultät für Biologie, Chemie und Geowissenschaften

vorgelegt von

Astrid Rauh

geboren in Nürnberg

Bayreuth, Februar 2018

Die vorliegende Arbeit wurde in der Zeit von März 2014 bis Februar 2018 in Bayreuth am Lehrstuhl Physikalische Chemie I unter der Betreuung von Herrn Prof. Dr. Matthias Karg angefertigt.

Vollständiger Abdruck der von der Fakultät für Biologie, Chemie und Geowissenschaften der Universität Bayreuth genehmigten Dissertation zur Erlangung des akademischen Grades einer Doktorin der Naturwissenschaften (Dr. rer. nat.).

Dissertation eingereicht am:	06.02.2018
Zulassung durch die Promotionskommission:	14.02.2018
Wissenschaftliches Kolloquium:	25.05.2018

Amtierender Dekan:

Prof. Dr. Stefan Pfeiffer

Prüfungsausschluss:

Prof. Dr. Matthias Karg (Erstgutachter)

Prof. Dr. Anna Schenk (Zweitgutachter)

Prof. Dr. Josef Breu (Vorsitz)

Prof. Dr. Andreas Greiner

FÜR MEINE FAMILIE
FÜR BASTI

Contents

List of Publications	V
List of Abbreviations and Symbols	VII
Abstract	1
Zusammenfassung	3
1 Introduction	5
2 Theoretical Background	17
2.1 Colloidal Self-Assembly in Bulk	17
2.1.1 Hard Colloids	17
2.1.2 Microgels	20
2.1.3 Introduction of Anisotropic Forces	23
2.2 Colloidal Self-Assembly at Liquid-Liquid Interfaces	25
2.2.1 Hard Colloids	25
2.2.2 Microgels	28
2.3 Predictions for Core-Shell Particles	31
2.4 Investigation of Structure and Dynamics	32
2.4.1 Image Analysis	32
2.4.1.1 Radial Distribution Function	32
2.4.1.2 Bond-Order Parameter	35
2.4.2 Scattering Techniques	35
2.4.2.1 Light Scattering	37
2.4.2.2 Small Angle Neutron and X-ray Scattering	40
3 Experimental Section	49
3.1 Materials	49
3.2 Synthesis	50
3.2.1 Synthesis of Au-PNIPAM Particles	50
3.2.2 Synthesis of SiO ₂ -PNIPAM Particles	55

3.3	Sample Preparation	60
3.3.1	Samples for LS	60
3.3.2	Samples for SANS	60
3.3.3	Crystalline Samples for UV-Vis Spectroscopy and SANS	60
3.3.4	Samples for CLSM	61
3.3.5	Samples for EM and AFM	63
3.3.6	Samples for Cryogenic SEM	65
3.4	Methods	65
3.4.1	LS	65
3.4.2	SANS	66
3.4.3	SAXS	67
3.4.4	UV-Vis Spectroscopy	68
3.4.5	CLSM	68
3.4.6	TEM	69
3.4.7	SEM	69
3.4.8	AFM	70
3.4.9	ζ -Potential Measurements	70
3.4.10	TGA	70
3.4.11	Refractive Index Measurements	70
4	Hard-Core/Soft-Shell Particles via Seeded Precipitation Polymerization	71
4.1	Influence of the Seed Surface Functionalization	71
4.2	Influence of the Seed Concentration	75
4.3	<i>In Situ</i> Monitoring of the Seeded Precipitation Polymerization	81
4.4	Post-Modification of the Gold Cores	84
5	Self-Assembly of Hard-Core/Soft-Shell Particles in Bulk	89
5.1	Influence of Cross-Linker Content and Particle Size	90
5.1.1	Particle Structure and Softness	90
5.1.2	Optical Properties in the Dilute Regime	94
5.1.3	Optical Properties in the Crystalline State	96
5.2	Influence of the Gold Core	106
5.2.1	Structural Prerequisites of Core-Shell and Pitted Particles	107
5.2.2	Optical Properties in the Dilute State	115
5.2.3	Photonic Properties of the Superstructures	117
5.2.4	Crystal Structure	122
5.3	Core-Shell Particles with a Small Shell-to-Core Ratio	129
5.3.1	Crystal Structure	129
5.3.2	Optical Properties	136

6	Influence of an Electric Field on Hard-Core/Soft-Shell Particles in Bulk	139
6.1	Characterization of SiO ₂ -PNIPAM Particles in the Dilute Regime	140
6.2	Overview of the Electric Field-Induced Phase Transitions	142
6.3	Analysis of the Electric Field-Driven Transitions	146
6.4	Comparison with Hard Colloids and Microgel Systems	152
7	Self-Assembly of Hard-Core/Soft-Shell Particles at Oil-Water Interfaces	155
7.1	Particle Morphology in Bulk	156
7.2	Particle Morphology at the Interface	159
7.3	Influence of Compression	164
7.4	Microstructure Characteristics	171
7.5	Core-Shell Particles with a Small Shell-to-Core Ratio	175
7.6	Stability in Bulk and at Liquid Interfaces	177
7.6.1	Structural and Dynamic Properties in Bulk	177
7.6.2	Comparison of the Structural Behavior	181
8	Conclusions and Future Perspectives	183
8.1	Conclusions	183
8.2	Future Perspectives	190
A	Appendix	193
	References	219
	Danksagung	235

List of Publications

Parts of this thesis are based on contents published in the following peer-reviewed journals:

1. **Rauh, A.**; Honold, T.; Karg, M. Seeded Precipitation Polymerization for the Synthesis of Gold-Hydrogel Core-Shell Particles: The Role of Surface Functionalization and Seed Concentration. *Colloid Polym. Sci.* **2016**, *294*, 37-47.

Contents of this publication are mainly adapted in Chapter 3, 4, 8 and in the Appendix.

2. **Rauh, A.**; Rey, M.; Barbera, L.; Zanini, M.; Karg, M.; Isa, L. Compression of Hard Core-Soft Shell Nanoparticles at Liquid-Liquid Interfaces: Influence of the Shell Thickness. *Soft Matter* **2017**, *13*, 158-169.

Chapter 1, 3, 7, 8 and the Appendix are partially based on this paper.

3. **Rauh, A.**; Carl, N.; Schweins, R.; Karg, M. Role of Absorbing Nanocrystal Cores in Soft Photonic Crystals: A Spectroscopy and SANS Study. *Langmuir* **2017**, DOI: 10.1021/acs.langmuir.7b01595.

Adapted contents of this publication can be found in Chapter 1, 2, 3, 5, 8 and in the Appendix.

4. Vasudevan, S.A.; **Rauh, A.**; Barbera, L.; Karg, M.; Isa, L. Stable in Bulk and Aggregating at the Interface: Comparing Core-Shell Nanoparticles in Suspension and at Fluid Interfaces. *Langmuir* **2017**, DOI: 10.1021/acs.langmuir.7b02015.

Contents reported in this paper are adapted in Chapter 1, 3, 7, 8 and in the Appendix.

Results from the following publication are not adapted in this thesis:

1. Honold, T.; Volk, K.; **Rauh, A.**; Fitzgerald, J. P. S.; Karg, M. Tunable Plasmonic Surfaces via Colloid Assembly. *J. Mater. Chem. C* **2015**, *3*, 11449–11457.

List of Abbreviations and Symbols

a	Lattice constant
A	Area
Abs	Absorbance
AFM	Atomic force microscopy
A_p	Area per particle
aq.	Aqueous
a.u.	Arbitrary units
Au	Gold
α	De-swelling ratio
BA	Butylamine
BCC	Body-centered cubic
BCT	Body-centered tetragonal
B- <i>en</i> -A	Butenylamine hydrochloride
BIS	<i>N,N'</i> -methylenebisacrylamide
β	Swelling ratio
β_s	Stretching exponent
c	Concentration
C	Core
C-D	Compression-deposition
CDDM	Confocal differential dynamic microscopy
CLSM	Confocal laser scanning microscopy
CS	Core-shell
C_dS	Pitted microgel particles; Core _{<i>dissolved</i>} Shell
CTAC	Cetyltrimethylammonium chloride
γ	Optical ratio describing the balance of plasmonic and scattering contribution
Γ	Relaxation rate
d	Pathlength of the sample
D	Expression to describe the intensity fluctuations
d_{cc}	Center-to-center distance
DDM	Differential dynamic microscopy

DISF	Dynamic image structure function
d_{hkl}	Lattice plane distance
D_l	Longitudinal domain size
DLS	Dynamic light scattering
d_{NN}	Nearest neighbor distance
D_Ψ	Azimuthal domain size
D_T	Translational diffusion coefficient
E	Electric field strength
E_{ext}	External electric field
E_{dip}	Electric field originating from other dipoles
E_{loc}	Local electric field
FCC	Face-centered cubic
FreSCa	Freeze-fracture shadow-casting
FWHM	Full width at half maximum
$F(\Gamma)$	Distribution function of relaxation rates
$g^1(q, \Delta t)$	Field-time autocorrelation function
$g^2(q, \Delta t)$	Intensity-time autocorrelation function
g_{max}	Intensity of the position of the first maximum in the radial distribution function
$g(r)$	Radial distribution function
$G(q)$	Debye-Waller factor
H	Scattering amplitude
HAuCl ₄	Gold(III)chloride trihydrate
HCP	Hexagonal close-packed
h, k, l	Miller indices
η	Viscosity
η_x	Scattering length density whereas x is given and explained in the respective model
$\Delta\eta_S$	Scattering length density contrast
θ	Scattering angle
θ_c	Contact angle
θ_e	Angle between the field direction and the direction fixed by two colloids
θ_i	Bond angle between the particle and its nearest neighbor pair
I	Intensity
$I_L(0)$	Amplitude of the Ornstein-Zernike contribution
ITO	Indium tin oxide
\vec{k}	Wave vector
k_B	Boltzmann constant

LB	Langmuir-Blodgett
LCST	Lower critical solution temperature
LS	Light scattering
LSPR	Localized surface plasmon resonance
λ	Wavelength
λ_b	Shell-to-core ratio in bulk
$\lambda_b\sigma$	Hydrodynamic diameter in the bulk phase
λ_i	Shell-to-core ratio at the interface
$\lambda_i\sigma$	Diameter at the interface
m	Mass
M	Molar mass
m_{diff}	Diffraction order
MUA	11-mercaptoundecanoic acid
μ_e	Electrophoretic mobility
n	Refractive index
N	Number
NIPAM	<i>N</i> -isopropylacrylamide
ξ	Correlation length
OZ	Ornstein-Zernike
PNIPAM	Poly- <i>N</i> -isopropylacrylamide
PPS	Potassium peroxodisulfate
$P(q)$	Form factor
PY	Percus Yevick
Π	Surface pressure
q	Momentum transfer
r	Distance
R	Radius
ΔR	Thickness of the outer volume element with an exponentially decaying density
rcf	Relative centrifugal force
RDG	Rayleigh-Debye-Gans
R_g	Radius of gyration
R_h	Hydrodynamic radius
RHCP	Random hexagonal close-packed
R_{hom}	Radius of the inner homogeneous volume segment
r_{max}	Average inter-particle distance determined using $g(r)$
rms	Root mean square
R_{total}	Overall radius
ρ	Density

ρ_N	Number density
SANS	Small angle neutron scattering
SAXS	Small angle X-ray scattering
SD	Sample-to-detector
SEM	Scanning electron microscopy
SiO ₂	Silica
SLR	Surface lattice plasmon
SLS	Static light scattering
$S(q)$	Structure factor
σ	Diameter of a hard colloid; here: often hard nanoparticle cores
TEM	Transmission electron microscopy
TGA	Thermogravimetric analysis
t	Time
Δt	Lag time
T	Temperature
τ	Relaxation time
$U(r)$	Potential energy
ϕ	Volume fraction
Ψ_6	Hexagonal order parameter
V	Volume
VPTT	Volume phase transition temperature
ω	Rotational angle

Abstract

One of the most fascinating phenomena of colloids is the spontaneous self-assembly from a disordered system to a colloidal crystal. A well-known example from nature are opals built up from silica colloids. Light is diffracted on these periodic superstructures resulting in extraordinary iridescence. In the past decades, self-organized structures from nature have served as models for scientists dealing with the phase behavior of artificial colloids. Their main focus has been the preparation of functional devices such as lightguiding, nanolasing and sensing devices. In particular, hard spheres have been intensely investigated. However, they offer only a limited parameter space as they consist solely of one material component.

The scope of this thesis is the self-assembly of hard-core/soft-shell particles. As they combine two material components, these particles offer a broad spectrum of single particle properties as well as inter-particle interactions. The hard cores can exhibit functionality as for example unique electronic, optical or magnetic properties. The soft microgel shells can interpenetrate and/or deform upon increasing volume fraction. Their softness significantly extends the range of accessible inter-particle distances in the superstructures resulting in a rich phase behavior.

The core-shell colloids are synthesized via seeded precipitation polymerization. Silica or gold nanoparticle cores are encapsulated in cross-linked poly-*N*-isopropylacrylamide shells. For the self-assembly studies large quantities of highly monodisperse single-core core-shell particles are required. Additionally, structural aspects such as overall and core size, cross-linker content of the shell as well as shell-to-core ratio have to be controlled reliably. In order to ensure these prerequisites, this precipitation reaction is investigated thoroughly. The seed encapsulation is monitored *in situ* which allows conclusions on the reaction kinetics. Moreover, the influence of functionalization and concentration of the cores is investigated. The gained knowledge allows to adjust the synthesis in order to prepare specific particle types.

The self-assembly of these particles in bulk and at the oil-water interface is analyzed. In bulk, crystalline superstructures are obtained for all particle types in a certain range of volume fractions. Crystalline structures in the centimeter-range are prepared without applying shear forces. The accessible range of inter-particle distances in the superstructures can be influenced by the particle structure. Particularly, the influence of overall dimen-

sion, softness, shell-to-core ratio and the presence of the gold core is analyzed. The soft character of the particles enables to exceed the maximum volume fraction of hard spheres in a face-centered cubic lattice of 0.74. Sharp diffraction peaks with widths on the order of 10 nm can be shifted from the ultraviolet to the near-infrared region by adjusting particle structure and volume fraction. Scattering methods reveal diffraction patterns with several orders of Bragg peaks belonging to face-centered cubic lattices. Furthermore, electric fields are applied to the particle dispersions to study them in non-equilibrium conditions. Depending on the field strength the particles align to strings, to sheets or to square lattices.

At the interface, inter-particle interactions are altered as compared to the bulk phase. Hence, a different phase behavior of the core-shell particles at oil-water interfaces is expected. In order to understand the phase behavior of the particles, their morphology at the interface in dependence on the core size and the dimension of the polymer shell is analyzed using freeze-fracture shadow-casting cryogenic scanning microscopy. All particles show larger dimensions at the interface as compared to the bulk phase. The soft, surface-active shells aim for hydration to a high extent leading to a maximal deformation at the interface. The interfacial microstructures upon compression are investigated using Langmuir-Blodgett experiments. Quantitative image analysis allows to draw conclusions on the area per particle, the inter-particle distance and the degree of order of the interfacial microstructures. At low surface coverage, the particles are driven together into clusters at a defined inter-particle distance due to attractive capillary forces. For the first time, it is revealed that these attractions originate from interface deformation caused by the hydrogel shells. Upon further compression a highly non-linear reaction of the shells is found. First, a non-close-packed lattice in which the particles are just in contact is observed. Then, a rapid transition to two-dimensional particle clusters in which the particles are compressed takes place. Both observations are in strong contrast to the structural behavior in bulk. In bulk, the hydrogel shells of the particles preserve stability in the whole range of investigated volume fractions as deduced from confocal differential dynamic microscopy.

Summarizing, correlations between the particle structure and the corresponding phase behavior are revealed. These results are the essential foundation for future works that deal with the preparation of two- and three-dimensional colloidal functional devices e.g. in the field of photovoltaics, photonics and sensing.

Zusammenfassung

Einer der faszinierendsten Prozesse der Kolloidik ist die spontane Selbst-Assemblierung eines ungeordneten Systems zu einem kolloidalen Kristall. Ein bekanntes Beispiel dafür sind Opale, welche sich aus Silica-Kolloiden zusammensetzen. Ihr charakteristisches Schillern entsteht durch die Lichtbeugung an ihrer periodischen Überstruktur. In den letzten Jahrzehnten dienten selbst-organisierte Strukturen aus der Natur als Vorbilder für Wissenschaftler, welche sich mit dem Phasenverhalten künstlicher Kolloide beschäftigten. Ihr Fokus hierbei lag auf der Entwicklung funktionaler Bauteile wie Lichtleiter-, Nanolaser- und Sensorik-Bauteile. Insbesondere harte, kolloidale Kugelsysteme wurden intensiv untersucht. Diese bieten allerdings nur einen begrenzten Parameterraum, da sie nur aus einer Materialkomponente bestehen. Die vorliegende Arbeit beschäftigt sich mit der Selbst-Assemblierung von Kern-Schale-Kolloiden, die aus einem harten Kern, welcher in eine weiche Mikrogelhülle eingekapselt ist, bestehen. Der Aufbau aus den unterschiedlichen Komponenten sorgt für ein breites Spektrum an Eigenschaften der einzelnen Partikel als auch an Wechselwirkungen zwischen den Kolloiden. Indem harte Kerne mit besonderen elektronischen, magnetischen oder optischen Eigenschaften eingekapselt werden, kann Funktionalität in die Partikelstruktur eingebracht werden. Die weiche Schale ermöglicht ein Durchdringen und/oder eine Deformation der Partikel mit zunehmenden Volumenbruch. Dadurch wird der Bereich der zugänglichen Interpartikelabstände massiv erweitert, was zu einem vielseitigen Phasenverhalten dieser Kolloide führt.

Die Herstellung der Kolloide erfolgt mit Hilfe der Fällungspolymerisation. Silica- oder Gold-Nanopartikel Kerne werden in quervernetzte Poly-*N*-isopropylacrylamid Mikrogelschalen eingekapselt. Für die Selbst-Assemblierungsstudien werden große Mengen an monodispersen Kern-Schale-Partikeln mit nur einem Kern benötigt. Zudem müssen strukturelle Aspekte wie die Gesamt- und Kerngröße, der Quervernetzergehalt der Schale sowie das Schale-zu-Kern Verhältnis gezielt in der Synthese einstellbar sein. Damit diese Anforderungen erfüllt werden können, wird die Reaktion genau untersucht. Um die Reaktionskinetik besser zu verstehen, wird die Einkapselung *in situ* verfolgt. Außerdem wird der Einfluss der Funktionalisierung und Konzentration der Kerne analysiert. Dieses Wissen ermöglicht die gezielte Synthese von verschiedenen Partikeltypen.

Die Selbst-Assemblierung dieser Partikel wird in der Bulkphase und an der Öl-Wasser Grenzfläche untersucht. In der Bulkphase werden für alle hergestellten Partikeltypen

kristalline Überstrukturen in einem bestimmten Volumenbruchbereich erhalten. Strukturen im Zentimeter Bereich können sogar ohne Anwendung von Scherkräften hergestellt werden. Der zugängliche Bereich der Interpartikelabstände in den Überstrukturen wird durch die Partikelstruktur beeinflusst. Der Fokus liegt hier auf dem Einfluss von Kern, Gesamtdimension, Schalendeformierbarkeit und Schale-zu-Kern Verhältnis. Durch den weichen Charakter der Partikel wird der maximale Volumenbruch von 0.74 für harte Kugeln in einem kubisch flächenzentrierten Gitter überstiegen. Schmalbandige Bragg Peaks mit Breiten von 10 nm werden vom ultravioletten bis zum nah-infraroten Spektralbereich verschoben, indem Partikelstruktur und Volumenbruch angepasst werden. Streumethoden liefern Beugungsmuster mit höheren Ordnungen an Bragg Peaks, welche einem kubisch flächenzentrierten Kristallgitter zugeordnet werden. Um die beobachteten Phasen des Gleichgewichtszustands zu verlassen, wird auch der Einfluss eines elektrischen Feldes auf die Partikeldispersionen getestet. Je nach Feldstärke ordnen sich die Partikel zu Perlenketten, zu *Sheets* oder zu quadratisch geordneten Gitterstrukturen an.

An der Grenzfläche sind die Wechselwirkungen zwischen den Kolloiden anders als in der Bulkphase. Folglich kann mit einem anderen Phasenverhalten der Kern-Schale-Partikel an der Öl-Wasser Grenzfläche gerechnet werden. Um das Phasenverhalten der Partikel verstehen zu können, wird zunächst deren Morphologie an der Grenzfläche in Abhängigkeit von Kerngröße und Schalendicke mittels *freeze-fracture shadow-casting cryogenic scanning microscopy* analysiert. An der Grenzfläche zeigen alle Partikel größere Dimensionen als in der Bulkphase. Die weichen, oberflächenaktiven Schalen streben nach maximaler Hydrierung, was zu einer starken Deformation an der Grenzfläche führt. Mittels Langmuir-Blodgett Experimenten werden Mikrostrukturen an der Grenzfläche bei verschiedenen Oberflächenbelegungen hergestellt. Durch die quantitative Bildanalyse dieser Strukturen ist es möglich Rückschlüsse auf die Fläche pro Partikel, den Interpartikelabstand und den Ordnungsgrad zu ziehen. Schon bei kleiner Oberflächenbelegung bilden sich Cluster, in denen die Partikel, bedingt durch attraktive Kapillarkräfte, in Kontakt sind. Erstmals wird gezeigt, dass diese Kräfte auf der Deformation der Grenzfläche beruhen, welche auf der Verformung der Mikrogelschale basiert. Desweiteren wird bei zunehmender Oberflächenbelegung anstatt eines kontinuierlichen ein abrupter Übergang von einem nicht-dichtgepackten zu einem dichtgepackten Gitter beobachtet. Diese Beobachtungen stehen im Gegensatz zum Phasenverhalten in der Bulkphase. Hier sind die Partikel über den gesamten Volumenbruchbereich durch die Mikrogelhüllen stabilisiert, was mit konfokaler, differentieller, dynamischer Mikroskopie ermittelt werden kann. Zusammenfassend zeigt diese Arbeit die Zusammenhänge zwischen der Struktur der Partikel und dem dazugehörigen Phasenverhalten auf. Die Ergebnisse sind die essentielle Grundlage für zukünftige Arbeiten, welche sich mit der Herstellung von zwei- und drei-dimensionalen kolloidalen, funktionalen Bauteilen im Bereich Photovoltaik, Photonik und Sensorik beschäftigen.

Chapter 1

Introduction

Colloids exhibit exceptional properties that allow to address fundamental condensed matter questions. In addition, they represent essential building blocks for a broad range of applications.^[1,2] They are defined as particles with at least one spatial dimension on a length scale between 1 nm to 1 μm .^[3] Several decades ago, colloidal particles have been found to be ideal model systems for atoms. An often-cited example that indicates parallels between atoms and colloids are J. Perrin's experiments. It has been revealed that the sedimentation of colloids follows the barometric density distribution in an ideal gas. Both phenomena are based on the balance between thermal (Brownian) motion and gravitational force. These results confirm the theory predicted by Einstein and provided evidence of the granularity of matter, i.e., the existence of atoms.^[1,4,5] Despite the size difference of atoms and colloids, the fundamental physics are very similar. This has been shown by numerous examples, such as the gas-liquid condensation or crystal nucleation and growth. There are several advantages that colloids offer: As they exhibit slower dynamics as atoms, investigations are easier to realize. Due to their larger size they can be studied by light scattering and microscopy methods.^[1,6] However, their major advantage is that interaction forces in colloidal systems can be adjusted. This can be realized in numerous ways such as the addition of electrolytes, surface modification and colloid shape as well as dimensions.^[2,7] This is of significant importance for the study of the probably most fascinating phenomenon related to colloids - the spontaneous transition from a disordered, fluid state to a perfectly ordered colloidal crystal. The presumably best known representative for colloidal superstructures are opals that can be found in nature.^[7] Despite ongoing progress in the field of colloidal self-organization, there are still many challenges to face in order to fully understand and control spontaneous self-assembly.^[8] The self-assembly of hard spheres is well studied. This is owed to their easy fabrication as well as their relatively simple interaction potential.^[1] In the ideal case, the repulsive potential is zero as long as the particles are separated. It abruptly reaches infinity when they are in contact. There are no attractive forces between ideal hard spheres. Thus, for a long time it has not been clear why hard spheres are able to form crystals. Counterintuitively,

it has been discovered that hard spheres have a higher degree of freedom in a crystal than in a metastable fluid of the same particle density.^[1] In order to extend the range of accessible inter-particle distances in the interaction potential of hard spheres, charges can be introduced. Charges lead to a softer potential that is influenced by Coulomb repulsion.^[9] A versatile alternative to hard colloids are soft particles. Prominent representatives are microgels. Microgels are polymeric particles which swell in a good solvent. The most studied microgel particles are poly-*N*-isopropylacrylamide (PNIPAM) microgels introduced by Chibante and Pelton in 1986.^[10] Due to their softness, microgel particles are often used as model system as they exhibit an easily tunable interaction potential. The interaction between these particles is described by a softer potential as compared to the charged hard sphere potential. The interaction potential approaches finite repulsion that is defined by the elasticity of the particle.^[11,12] In contrast to hard spheres, these particles can interpenetrate and deform due to their soft, cross-linked polymer network as schematically shown in Figure 1.1.^[13] In Figure 1.1 A two hard spheres in contact are depicted. As soon as they are in contact, their smallest inter-particle distance is achieved. In Figure 1.1 B microgel particles are shown as representatives for soft particles. They exhibit a gradually decreasing density of the cross-linker content resulting in a denser inner part ("core") and a more loosely cross-linked outer corona.^[14] The core-corona structure results in two characteristic inter-particle distances given by the microgel structure. When the particles are just in contact they are in the so-called shell-shell contact. At higher volume fractions they can interpenetrate and deform due to their soft character.^[13] The smallest inter-particle distance they can achieve is their distance in the so-called core-core contact. In this state the inner denser volume elements of the particles are in contact.

A clever strategy to combine the advantages of hard and soft colloids are hard-core/soft-shell particles. In similarity to purely organic microgel particles, their soft shells allow a flexible manipulation of the interaction potential. The adjustment of inter-particle distances is even facilitated due to the presence of a hard core acting as impenetrable place holder. At very high volume fractions the soft shells can interpenetrate and/or deform. Therefore, inter-particle distances smaller than the diameter of the core-shell (CS) particle are possible. If the particles are in their maximally compressed state, they are in core-core contact (see Figure 1.1 C). Note that the core-core contact is not corresponding to the contact of the hard inorganic cores. Instead, core-core contact implies that the soft shells are maximally compressed. In other words, the "core" indicates the inorganic hard nanoparticle plus the dense, highly cross-linked part of the microgel particle that is not penetrable and/or deformable. In similarity to microgels, CS particles are in shell-shell contact as soon as their shells are in contact. Several theoretical works suggest a rich phase behavior of such objects upon increasing particle density as they include two length scales in their particle structure (defined by "core" and "shell"). Even quasicrystalline

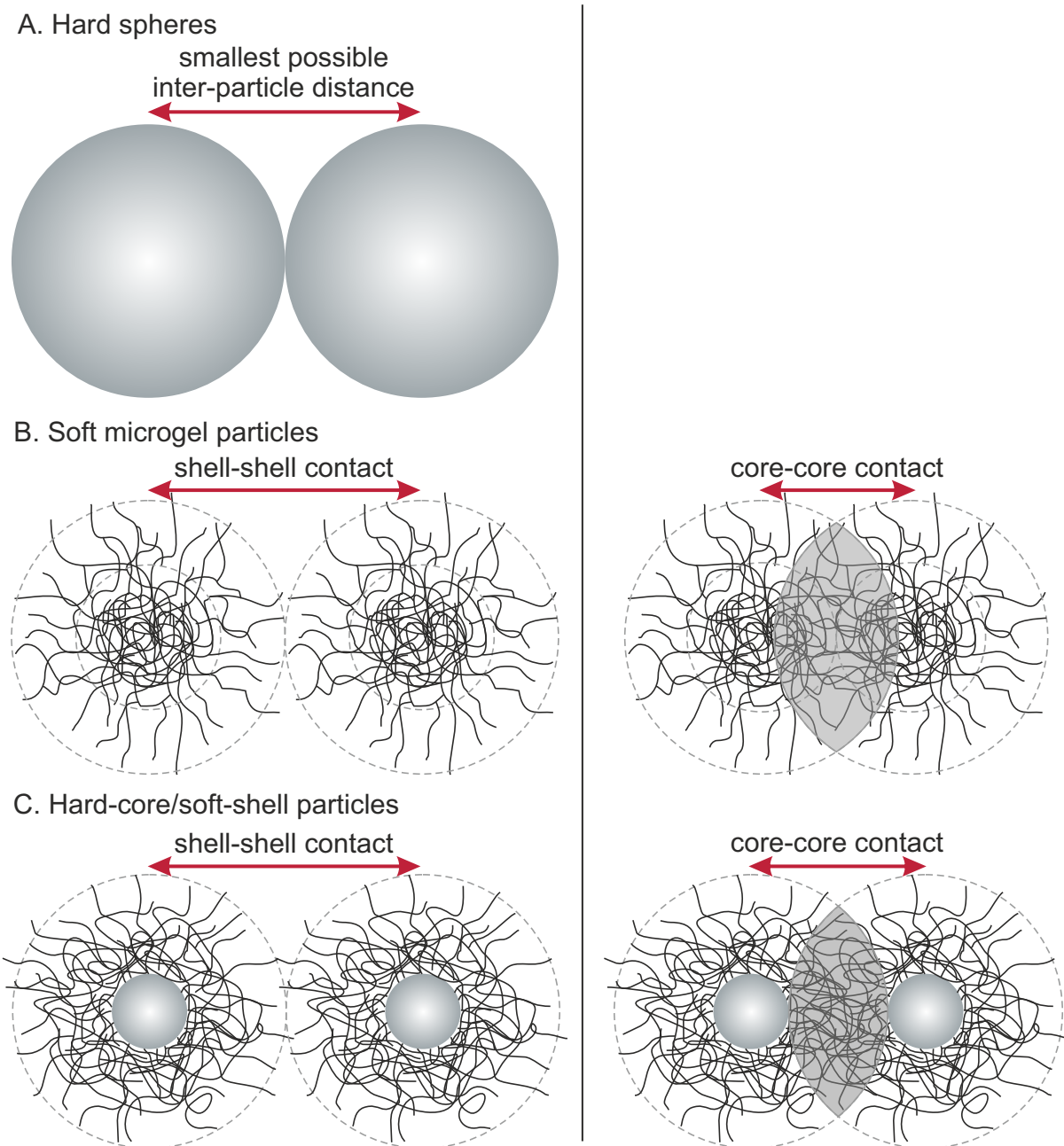


Figure 1.1: Schematic depiction of the accessible inter-particle distances (red arrows) that are determined by the particle structure. The gray-shaded area gives the overlap volume of the particles. A. Hard spheres in contact. B. Microgel particles in shell-shell contact (left). At high volume fractions the particles can deform and/or interpenetrate enabling the particles to arrange in core-core contact (right). In this state, the highly cross-linked volume elements are in contact. C. Hard-core/soft-shell particles in shell-shell contact (left) and core-core contact (right). Note that core-core contact implies not that the hard inorganic cores are in contact. Instead, it describes the maximally compressed state of the particles. In this state, the denser inner volume elements of the microgel shells, that are not penetrable and/or deformable, are in contact.

phases have been predicted.^[15,16] Simultaneously, the hard nanoparticle cores offer the possibility to add functionality. Functional hard cores with unique optical, electronic or magnetic properties can be encapsulated which allow the fabrication of functional devices like solar cells^[17,18], nanolasing^[19,20] and sensing devices.^[21–23]

The scope of this thesis is to investigate the self-assembly of hard-core/soft-shell particles in bulk and at oil-water interfaces. More specifically, the influence of the volume fraction (bulk) or interface coverage (interface) and of different structural aspects of the CS particles on the self-assembly is analyzed. The particles may behave differently in bulk and at the interface.^[24–26] At the interface additional forces that are not present in bulk can influence the self-assembly process, e.g., attractive capillary forces.^[27] Further, the involved interaction forces may have a different magnitude and effect as in the bulk phase.^[28,29]

Self-Assembly in the Bulk Phase. Numerous studies deal with colloidal self-assembly in bulk which is owed to the fascinating properties of colloidal crystals. These superstructures find applications in photonic bandgap materials^[7,30], lasing devices^[31–33], photonic/plasmonic devices^[7,34–36] or biosensors^[37]. Hard spheres crystallize typically in a face-centered cubic (FCC) lattice which is their thermodynamically stable phase. Yet, mixtures between the hexagonal close-packed (HCP) and the FCC phase exist as the Gibbs free energy difference between them is very small.^[38,39] In highly charged spherical systems also body-centered cubic (BCC) structures are observed. Due to their softer interaction potential, crystallization of charged particles occurs at lower volume fractions as compared to the respective non-charged particles.^[40,41] The interaction potential of soft particles is even more complex and can be manipulated by adjusting the structure of the microgel, e.g., by changing the cross-linker density, or by external stimuli such as temperature or pH.^[42,43] Several theoretical works predict a diverse phase behavior of soft particles in dependence on their interaction potential and the volume fraction.^[44,45] This is partly caused by their soft interaction potential that allows them to crystallize at volume fractions that exceed the maximum volume fraction of 0.74 for hard spheres in a FCC packing.^[13,46] In the majority of cases either a FCC^[47,48] or a random mixture of a FCC and a HCP lattice is obtained for different microgel particles.^[49–51] However, Gasser *et al.* reported BCC phases.^[52] Further, Mohanty *et al.* found a coexistence of FCC and BCC crystal structures for concentrated microgel dispersions, which agrees with theoretical predictions.^[53,54] Encapsulating hard nanoparticles in soft microgel shells allows to harness the advantages of both particle types. The hard nanoparticle cores offer the possibility to add functionality if, e.g., metallic or semiconducting cores are encapsulated. The soft hydrogel shells lead to a soft interaction potential. In similarity to microgels, the softness of the shells extends the range of accessible inter-particle distances. In ad-

dition, their structural composition including a soft (shell) and a hard (core) component can be advantageous for the formation of diverse crystal structures. Objects that include two length scales directly in their particle structure are predicted to exhibit a rich phase behavior. Dotera *et al.* and Schoberth *et al.* presented phase diagrams in dependence on the shell-to-core ratio and the volume fraction, which even state the existence of quasicrystalline phases.^[15,16]

However, the formation of superstructures consisting of CS particles is challenging, so that only a few studies exist. As a considerable quantity of structurally well-defined CS particles is required, a large-batch synthesis protocol resulting in highly monodisperse, single-core CS particles has to be chosen. A promising synthetic strategy for this purpose is the seeded precipitation polymerization of gold-PNIPAM particles that allows to easily tailor structural aspects of the particles.^[55] *In order to determine the utility of the synthesis for large quantities and to achieve maximal control on the reaction products, this reaction protocol is investigated thoroughly. Therefore, the influence of the functionalization and the gold (Au) seed concentration on the final reaction products are analyzed. In addition, an in situ study during the precipitation polymerization allows to gain further knowledge about the reaction mechanism.* Such Au-PNIPAM particles have already been shown to form FCC superstructures by Karg *et al.*^[56] The photonic band gap has been tuned over a remarkable range of wavelengths from 560 to 440 nm with increasing volume fraction. Volume fractions above the hard sphere limit of 0.74 have been realized, since the soft shells can interpenetrate and/or deform. In addition, the microgel shells are thermoresponsive: They undergo a volume phase transition with temperature. At room temperature, below their volume phase transition temperature (VPTT), water is a good solvent for the microgel shells, so that they are highly swollen with water. Above the VPPT, polymer-polymer interactions are favored. Water is expelled leading to the collapse of the polymer network. The thermoresponsiveness of these particles has been used to crystallize and recrystallize the superstructures, indicating the reversibility of the crystallization process. This study highlights the benefits that the soft polymer shells offer. *However, a detailed study analyzing the role of structural aspects of the particles such as cross-linker content, shell thickness, core presence and size is missing. Therefore, the self-assembly in bulk of different CS particle types covering these issues is studied revealing correlations between particle structure, optical properties as well as the crystal structure.*

Although the Au core might significantly affect the optical properties as well as the crystal structure, its actual role in these superstructures consisting of Au-PNIPAM particles remains still unclear. In particular, the optical response of the superlattice is important which is significantly influenced by the localized surface plasmon resonance (LSPR) of the Au core. The LSPR is based on the collective electron oscillations caused by the incident light.^[57,58] In such superstructures coupling between the single-particle LSPRs

of the Au nanoparticles and the diffractive lattice mode can occur.^[59] This type of coupling requires inter-particle distances that are in the same range as the position of the plasmon resonance. The resulting surface lattice resonances (SLRs) have remarkable lifetimes that make them very interesting for nanophotonic devices e.g. in the field of lasing.^[20,60] The fabrication of defined superstructures with suitable and highly regular inter-particle distances is challenging. Therefore, research has mainly focused on SLRs in two-dimensional arrays or on other types of coupling such as near-field coupling phenomena in dimers, trimers and small clusters.^[34,35,61,62] Since the superstructures consisting of Au-PNIPAM particles show diffraction modes in the visible wavelength range and thus in close proximity to the position of the LSPR, they are very promising for the fabrication of SLR devices.^[56] Additionally, similar particles (Au-Ag-PNIPAM) have already shown such SLRs in two-dimensional hexagonally ordered monolayers.^[61] *Herein, the role of the Au core in superstructures of Au-PNIPAM particles is characterized. The optical properties of the superstructures from Au-PNIPAM particles and their pitted references are compared thoroughly. In the course of these investigations, the influence of the Au core on the lattice type is characterized.* The hard core plays an important role in the particle structure as it contributes distinctly to the achievable core-core contact present in the CS particle type (see Figure 1.1). Consequently, it could have an influence on the accessible inter-particle distances in the crystal structures.

So far, the influence of the structural aspects of the CS particles on the self-assembled superstructures were discussed. An elegant alternative to alter the phase behavior is the influence of external triggers. This way non-equilibrium phases can be induced. External electric fields can be applied to induce phase transitions, as shown for hard nanoparticles^[63,64] as well as for soft microgel particles.^[65–67] Applying electric fields, the interaction potential is extended by a dipolar interaction leading to a more complex, anisotropic interaction.^[66] *This thesis reveals if and to what extent the influence of an electric field affects the phase behavior of hard-core/soft-shell particles. The effect of different field strengths on dispersions of different volume fractions is studied.*

An overview of the experiments that address the mentioned tasks is given in Figure 1.2. Different CS particle types such as particles with different cross-linker content, shell thickness, core sizes as well as pitted particles are prepared. Initially, the seeded precipitation polymerization is investigated thoroughly. Details regarding the encapsulation mechanism are gathered from *in situ* monitoring of the synthesis by UV-vis absorbance spectroscopy and light scattering (LS). Additionally, the influence of seed functionalization and concentration is revealed. The results are the foundation for the synthesis of large quantities of monodisperse particles with a tailored structure that are required for the self-assembly studies. In the next step, different concentrated dispersions of these particles self-assemble after annealing at temperatures above the VPTT. Moreover, different structural phases

of dye-labeled silica-PNIPAM particles are prepared by applying an electric field. Field-induced transitions at different volume fractions and field strengths are studied. The crystal lattices of the organized structures are analyzed using either small-angle scattering methods or confocal laser scanning microscopy (CLSM). The optical properties of the superstructures are investigated by UV-vis absorbance spectroscopy. Correlations between crystal lattice, optical properties and the particle structure are investigated.

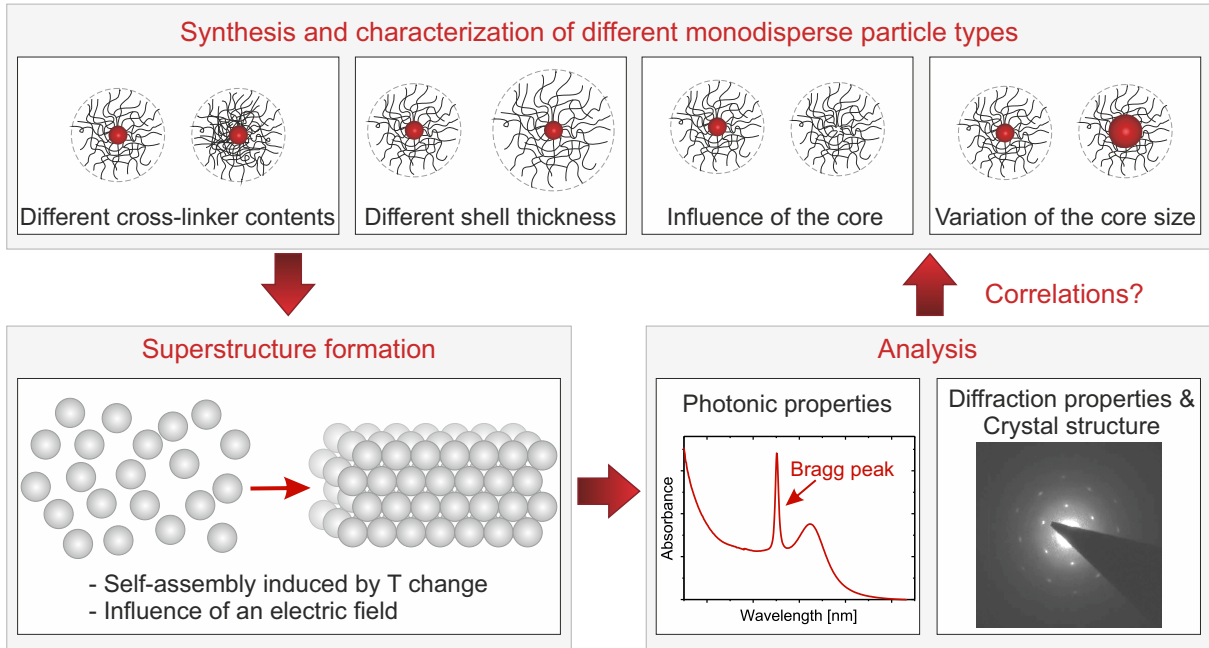


Figure 1.2: Strategy for the self-assembly studies in bulk.

Self-Assembly at Interfaces. Controlling the self-assembly of colloids at liquid-liquid interfaces (oil-water) is of major interest for stabilization of emulsions^[68–70], surface patterning^[71] and biological membranes.^[72] The adsorption of hard spheres at liquid-liquid interfaces has been thoroughly studied.^[73] A well-known example are Pickering emulsions in which hard particles are used as emulsifiers.^[68] Often silica, poly(methylmethacrylate) or polystyrene particles are applied to stabilize oil-water emulsions. In contrast to amphiphilic molecules like surfactants, hard particles can adsorb irreversibly to the interface resulting in very stable emulsions. To guarantee successful stabilization, numerous parameters such as contact angle, colloid size and stability have to be considered.^[74–77] In the case of hard particles the tunability of these parameters is limited. Hence, numerous studies have focused on the self-assembly of soft spheres like microgels at liquid-liquid interfaces, since they allow to add further functionality.^[25] This is firstly related to their softness which allows spontaneous adsorption. Secondly, their sensitivity towards external stimuli like temperature and pH enhances their functionality.^[69,70,74,78–80] Both enables

these particles to change their structure and interaction potential. Their stimuli responsiveness allows the development of so-called "smart" emulsions. Van der Waals forces and electrostatic repulsion, that dominate the interfacial microstructures of hard particles, play a minor role in the self-assembled microstructures of microgels. Instead, deformation and steric interactions are the driving forces.^[74,81] PNIPAM microgels have been found to possess a significantly different interfacial footprint as compared to hard particles. Due to the surface activity of the polymer chains, wetting at the interface is ruled by the balance between internal elasticity and maximal deformation of the hydrogel network at the interface.^[82] Since the particles prefer to remain hydrated, only a small fraction protrudes into the oil phase. They appear flattened in a so-called core-corona morphology as a result of the internal inhomogeneous distribution of cross-linker.^[83,84] Hence, they typically achieve larger dimensions at the interface than in bulk. The degree of deformation can be adjusted by variation of the cross-linker content.^[84–86] The correlation between structural and mechanical properties of particle monolayers has been studied using Langmuir-Blodgett (LB) trough experiments or by pendent-drop measurements. Upon compression, highly ordered microstructures with defined inter-particle distances have been realized.^[87–89] Due to the soft character of the microgel particles, area fractions above the close-packing value of 0.91 can be achieved. The particles can deform and/or interpenetrate. The ability to control inter-particle distances in the microgel monolayers makes them suitable for applications as lithography masks for nanopatterning,^[71] structural colors^[90] or microlens arrays.^[91] A promising approach to harness advantages of both - hard and soft material components - are hard-core/soft-shell particles. They offer benefits, e.g., for the preparation of (smart) emulsions^[92] or functional materials as functional cores can be introduced into the particle structure.^[9,23] Recently, Buchcic *et al.* have found that the combination of hard and soft components in a polystyrene-PNIPAM core-shell system presents a convenient system for the stabilization of emulsions.^[92] These particles spontaneously adsorb onto fluid interfaces due to their soft shells. At the same time, CS particles reveal good stability against coalescence due to synergistic effects of soft and hard components. Additionally, the encapsulation of metal, metal oxide or semiconducting nanoparticle cores in soft hydrogel shells is essential for the formation of interfacial microstructures with extraordinary optical, electronic and/or magnetic properties.^[61,93–95]

Due to their unique benefits, CS particles attracted interest for several studies at the interface: Honold *et al.* prepared homogeneous, highly ordered plasmonic monolayers on large scale at the air-water interface.^[96] Their CS particles consisted of a plasmonic particle encapsulated in hydrogel shells. They investigated the influence of the core size in the microstructures by keeping the overall diameter constant. Interestingly, similar inter-particle distances have been obtained for the different particle types resulting in monolayers of similar particle densities. The self-assembly of silica-PNIPAM particles

and their pitted counterparts at the oil-water interface was investigated by Geisel *et al.*^[97] They found that the hard core reduces the interfacial deformation upon comparing CS and pitted particles. This suggests a complex interplay between deformation of the particle shells and the microstructure. Nazli *et al.* have proposed that thicker shells and a lower cross-linker density in the microgel shells supports the stability of silica-PNIPAM particles at the oil-water interface.^[98] These assumptions were based on the observation of more dense and regular packings of particles. The self-assembly of Au-PNIPAM particles at air-water interfaces were analyzed by Vogel *et al.*^[99] They observed that the monolayer morphology can be used to adjust the inter-particle distances over several hundreds of nanometers. Buchcic *et al.* found that polystyrene-PNIPAM particles with thin shells adsorb with very low adsorption rates at air-water interfaces.^[92] *All the mentioned studies present the unique potential of soft microgel shells assembled at the interface. However, a fundamental knowledge about the effects of the core size or presence as well as the shell thickness and the respective ratio of shell to core on the self-assembled microstructures is still missing. This thesis presents a systematic study that focuses on the role of shell thickness relative to the dimension of the hard, non-deformable nanoparticle core.*

Other self-assembly studies on hard-core/soft-shell particles have suggested the existence of attractive inter-particle forces that are not present in bulk: Volk *et al.* investigated the expansion of a freely floating monolayer of Au-Ag-PNIPAM particles with time.^[100] The monolayers formed a highly ordered hexagonal arrangement, independent of the inter-particle distance. Their observation might be related to attractive inter-particle interactions at the interface. Further work that proposes the existence of attractive inter-particle interactions between Au-PNIPAM particles at low surface coverage was published by Vogel *et al.*^[99] *The origin of these attractive interactions is still unclear. However, understanding the nature of these interactions and how to manipulate them is crucial in order to gain further control over self-assembled structures at the interface. Therefore, the basis of these interactions is investigated in this thesis. For this purpose, the particle morphology at the interface is revealed using freeze-fracture shadow-casting cryogenic scanning electron microscopy (FreSCa cryo-SEM).*

Inter-particle interactions as well as stability in bulk and at liquid-liquid interfaces can be different as suggested by the mentioned attractive forces in the previous paragraph.^[24–26] This implies that the magnitude and effect of interactions that are acting in bulk may be altered at the interface.^[28,29] Additionally, other interactions such as attractive capillary interactions that are not present in bulk may exist at the interface.^[27] Consequently, colloids that are optimized for bulk stability and assembly can show a different phase behavior upon adsorption and confinement at the interface. *So far, a direct comparison of the self-assembly of hard-core/soft-shell particles in bulk and at the interface has been missing. However, for applications it is of significant importance to consider the prereq-*

uisites for particle stability in both regimes. Thus, the structural behavior of a specific CS model system in bulk and at the oil-water interface is investigated in dependence on different volume fractions (bulk) or surface coverages (interface), respectively.

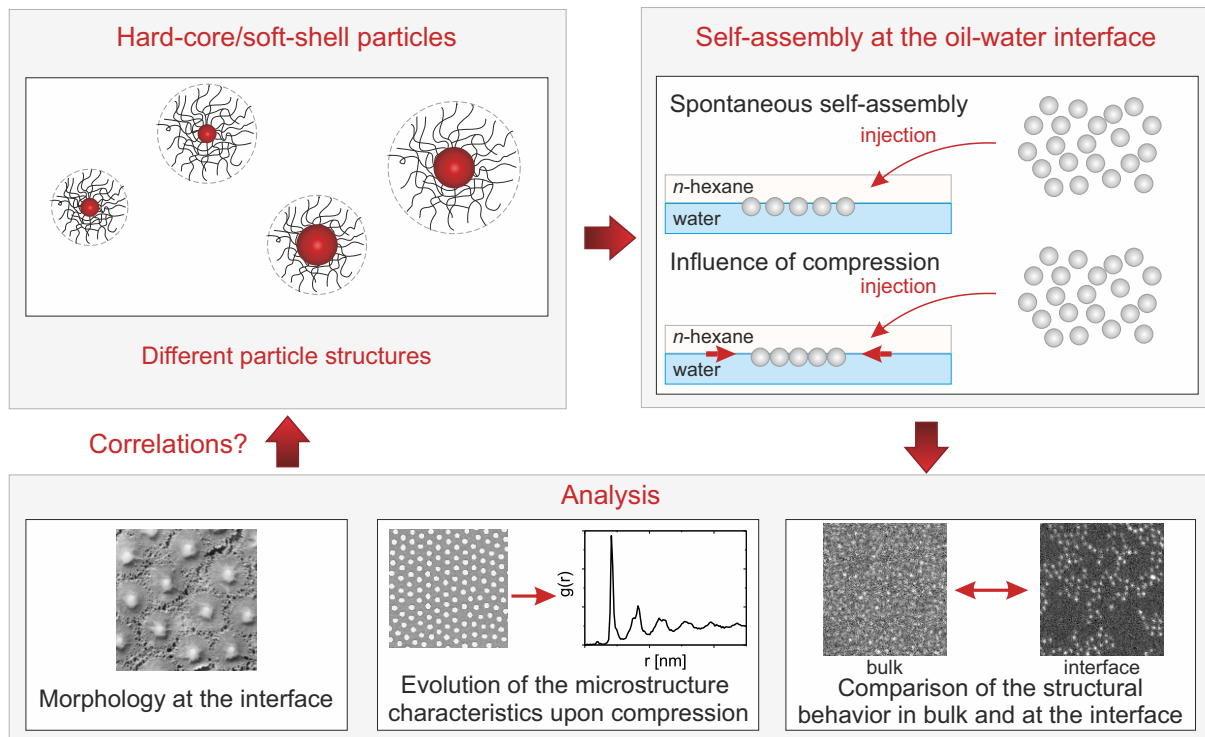


Figure 1.3: Strategy for the self-assembly studies at the oil-water interface.

The strategy to address all the described tasks is shown in Figure 1.3. Similar to the experiments in bulk, CS particles with different structures are synthesized. Here, dye-labeled silica-PNIPAM CS particles are used. Next, their morphology at the oil-water interface after spontaneous adsorption is revealed using FreSCa cryo-SEM analysis. In addition, the self-assembly of different particles upon compression is investigated using a modified LB trough protocol. The atomic force microscopy (AFM) and scanning electron microscopy (SEM) images of the resulting microstructures are analyzed in detail using different image analysis methods. The phase behavior is related to the particle structure and compared to the behavior of purely organic microgels at oil-water interfaces. Finally, the results of the self-assembly at the interface of a specific CS model system are compared to the phase behavior in bulk of this system that is studied using confocal differential dynamic microscopy (CDDM).

Organization of this Thesis. This thesis is organized as follows: **Chapter 2** includes theoretical background information about interaction potentials and fundamental studies regarding the self-assembly of hard, inorganic colloids and soft microgel particles in the bulk phase and at the interface. Further, the basics of image analysis and scattering methods used in this thesis are outlined. The synthesis protocols, sample preparation and methods are presented in **Chapter 3**. In Chapter 4 to 7 the results of the studies in bulk and at the interface are discussed. **Chapter 4** deals with a detailed study on the synthesis of the hard-core/soft-shell particles *via* free radical seeded precipitation polymerization. In **Chapter 5** the self-assembly of different Au-PNIPAM particles in the bulk phase is studied. The influence of an external electric field on particle dispersions of SiO₂-PNIPAM particles is addressed in **Chapter 6** of this thesis. **Chapter 7** focuses on the self-assembly of SiO₂-PNIPAM particles at oil-water interfaces. Finally, the structural behavior of a specific CS system at the oil-water interface is compared to its behavior in bulk. In **Chapter 8** the key results of this thesis are summarized.

Chapter 2

Theoretical Background

This chapter gives a theoretical overview on the self-assembly of hard spheres and microgels in bulk and at the oil-water interface. Further, a brief summary of the theoretical predictions regarding the phase behavior of hard-core/soft-shell particles is represented. Finally, fundamentals on image analysis and scattering methods are addressed.

2.1 Colloidal Self-Assembly in Bulk

In this section important research dealing with the self-assembly in bulk is presented. It is outlined how the particle morphology influences the interaction potential. Further, a state of the art regarding the phase diagram of hard colloids and soft microgels is given.

2.1.1 Hard Colloids

The self-assembly of hard colloids has been thoroughly studied over the last decades. Ideal hard spheres are monodisperse, spherical particles that exclusively interact when they are in contact. Due to their rigidity, no overlap or elastic deformation of these particles is possible. Equation 2.1 gives their interaction potential. Here, $U(r)$ denotes the potential energy, r describes the distance between the particles and σ is the diameter of the hard sphere.

$$U(r) = \begin{cases} \infty, & r \leq \sigma \\ 0, & r > \sigma \end{cases} \quad (2.1)$$

Figure 2.1 A displays the interaction potential. The potential approaches infinity as soon as the particles are in contact. There are not many parameters affecting the phase behavior of hard spheres. Entropy, which is determined by the volume fraction, has the major influence on the system. Hard spheres can achieve a maximum volume fraction ϕ of 0.74 assuming FCC packing. In this state, all hard spheres are in contact. In experiments hard colloids are stabilized electrostatically by charge or sterically by surface grafted

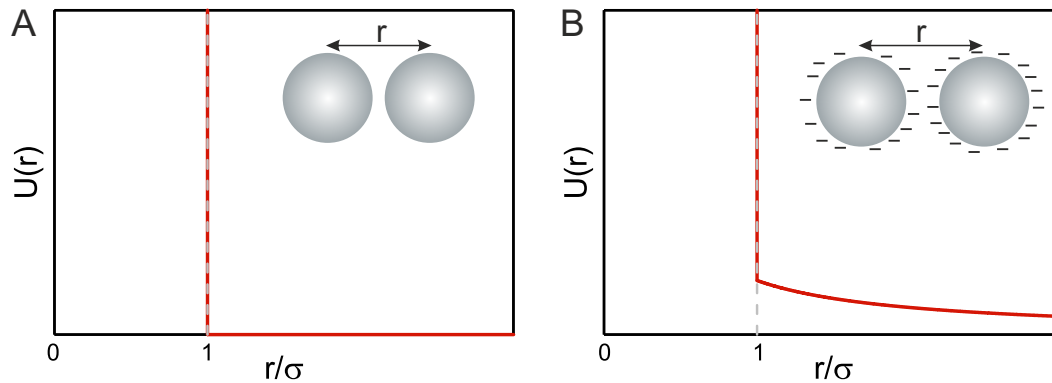


Figure 2.1: Interaction potential of hard spheres (A) and charged, hard colloids (B) with a diameter σ . The potential energy $U(r)$ is shown as a function of the inter-particle distance r normalized by σ . A Coulomb interaction potential is used to describe the interaction between the charged, hard colloids. For both particle types $U(r)$ approaches infinity as soon as the particles are in contact, since they cannot interpenetrate. In contrast to ideal hard spheres, their charged equivalents interact already at inter-particle distances larger than their diameter. Thus, if two oppositely charged colloids at $r > \sigma$ approach contact, energy is required to overcome electrostatic repulsion between the particles.

polymer chains (polymer ligands). Figure 2.1 B exemplarily depicts the effect of charges on the interaction potential. The potential is approximated using a Coulomb potential, that scales with $1/r$ at $r > \sigma$.^[101] Oppositely charged, hard colloids need to expend energy in order to approach. Polymer ligands would have a similar but less pronounced effect on the interaction potential. As polymer chains usually form a thin polymer layer their interaction potential is very similar to the ideal hard sphere potential. In Figure 2.2 a schematic phase diagram of hard sphere dispersions for $0 < \phi \leq 0.74$ is illustrated.

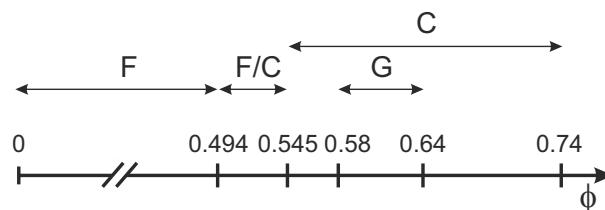


Figure 2.2: Schematic illustration of the hard-sphere phase diagram with its different regions: F (fluid), C (crystal), F/C (coexistence of fluid and crystal), G (glass).

Below $\phi = 0.494$ a fluid phase exists, i.e., a random particle distribution without any long-range order is present. Between $\phi = 0.494$ and 0.545 a coexistence of a fluid and a crystalline phase is found. The crystalline phase grows with increasing ϕ . Above $\phi = 0.545$ different phases have been predicted and experimentally confirmed.^[102,103] Under thermodynamic equilibrium conditions a crystal phase should (always) be present between $\phi = 0.545$ and 0.74 .^[102] However, this was disapproved by experiments of Pusey and van Megen.^[103] They approximated ideal hard spheres using sterically stabilized hard colloids.

These colloids resemble a good approximation as ideal hard spheres are experimentally not realizable.^[103,104] Their experiments showed that crystalline phases are present between $\phi = 0.545$ and 0.58 . Above $\phi = 0.58$ they revealed the existence of a glass phase.^[48,103] Bernal *et al.* confirmed the existence of a glass phase. They state a maximum upper volume fraction of 0.64 for this glass phase. At this volume fraction the system is termed random close-packed phase. The formation of this glass phase is attributed to crowding effects upon increasing volume fractions.^[105,106] In the first place, it is uncertain why the particles should prefer a crystalline phase as compared to a disordered phase. Counter-intuitively, the entropy is increased in the crystalline phase compared to a disordered phase. This is related to entropic contributions of configurational and free volume effects. In the fluid state, the configurational term dominates over the small free volume term that is based on the limited motion of each particle as it is constricted by its neighbors. In the crystalline state, the configurational term is reduced while the free volume term has a strong contribution. $\phi = 0.64$ is the maximum volume fraction of randomly packed spheres in a glassy phase. At this volume fraction, the free volume contribution approaches zero leading to a frozen phase.^[107-109]

Crystalline phases formed by spherical, hard colloids typically consist of hexagonal layers that can be arranged in different stacking orders. The two most prominent crystal structures are FCC and HCP lattices. Figure 2.3 A illustrates a FCC lattice (ABC stacking) and Figure 2.3 B a HCP lattice (AB stacking). Since the Gibbs free-energy difference between these two stacking types is quite low, random mixtures of the two types are often obtained. These are termed as random hexagonal close-packed (RHCP) phases.^[38,39]

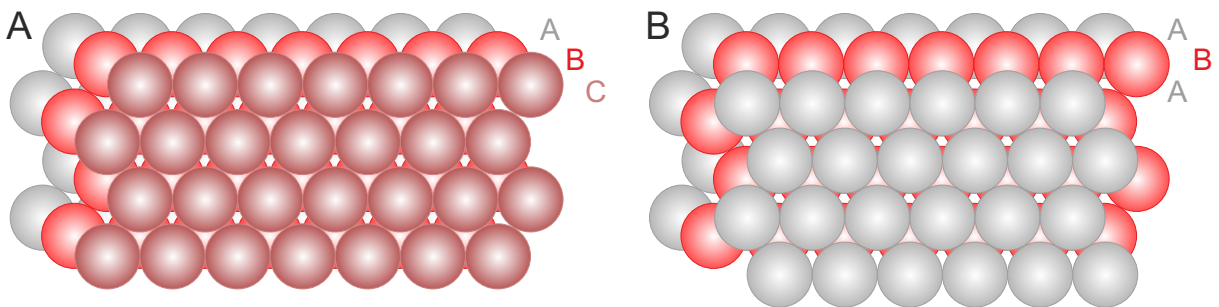


Figure 2.3: Top view of crystal lattices consisting of colloids: A. FCC lattice (ABC stacking), B. HCP lattice (AB stacking). For the sake of clarity the A, B and C layers are labeled with different colors.

In the case of highly charged, hard colloids also BCC crystal phases were found. As charged particles start to interact already at large distances (Figure 2.1 B), long-range ordered phases are formed at lower volume fraction than with their of non-charged equivalents.^[40,41]

2.1.2 Microgels

In contrast to hard spheres, microgels are soft and very flexible. Tailoring the network structure of microgels allows to influence their interaction potential to a great extent and to adjust the particle properties for the needs of specific applications. The most prominent microgel particles are poly-*N*-isopropylacrylamide particles. The interaction potential is strongly governed by the polymer network of the microgel particle. Their internal network structure can be controlled by adjusting their cross-linker content that directly influences their softness. Small angle neutron scattering (SANS) investigations by Stieger *et al.* revealed an inhomogeneous density profile in microgel particles. This profile comprises a high degree of cross-linking in the center (often termed as core) and a decreasing cross-linker density from the center to the periphery of the particles (often termed as corona or shell).^[14] The structure is the result of a higher reactivity and, therefore, faster consumption of the cross-linker *N,N'*-methylenebisacrylamide as compared to the monomer *N*-isopropylacrylamide.^[110,111] Further, very recently, Boon *et al.* discovered that a considerable amount of dangling chains extends from the cross-linked core.^[112] Figure 2.4 A illustrates the network structure of a microgel particle schematically. Varga *et al.* investigated the structure of microgel particles using dynamic light scattering (DLS) and static light scattering (SLS). For low cross-linker contents, they found that the internal network structure can be well described by a core-shell morphology. In contrast to this, a more homogeneous structure was reported for particles with increasing cross-linker content.^[113] If microgel particles with a homogeneous network structure are required, the synthesis can be performed in a semi-batch fashion.^[114] Summarizing, the softness and the interaction potential can be easily tuned by adjusting the internal network structure.

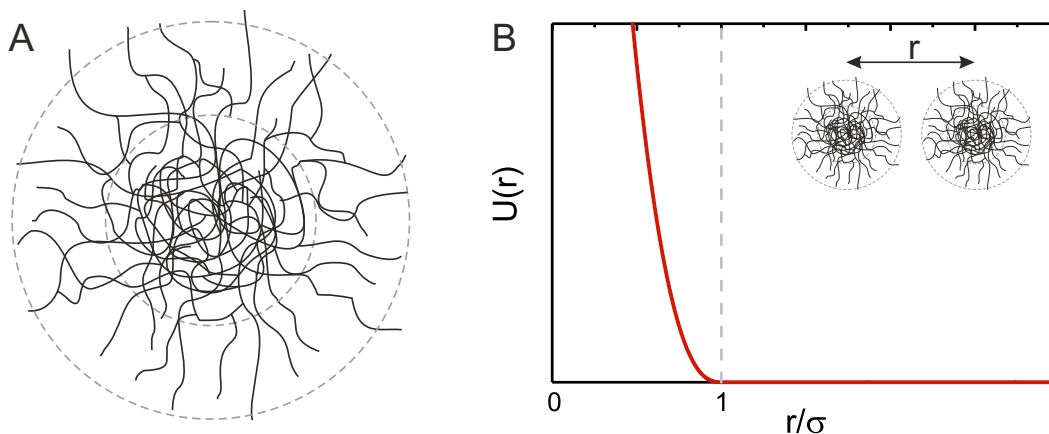


Figure 2.4: A. Schematic depiction of the network structure of a microgel particle illustrating the typical gradient in cross-linking density that decreases from the center to the periphery. B. Hertzian potential describing the interaction between microgel particles with a diameter σ . The potential energy $U(r)$ is plotted as a function of the distance r .

As an additional feature, PNIPAM particles are thermoresponsive, i.e., their size can be controlled *in situ* via temperature changes. In this thesis the thermoresponsive swelling behavior was used to evaluate the softness of the particles. At room temperature PNIPAM particles are highly swollen with water achieving water contents around 82%.^[115] At these temperatures water-polymer interactions via hydrogen bonding to the amide groups are favored. Increasing the temperature above the VPTT these hydrogen bonds are disrupted. Hydrophobic attractions between the isopropyl groups of the polymer support partial dehydration while the microgel particle collapses. The VPTT of PNIPAM microgels is typically around 32-33°C.^[6,115,116] Increasing the temperature well above the VPTT induces a collapse of the particle volume and results in a strongly attractive interaction potential.^[117,118] Apart from their responsiveness to temperature, there are additional external triggers like pH and ionic strength that allow to change the internal network structure of microgels and thus their interaction potential.^[116]

Several theoretical studies predict a versatile phase behavior of microgels.^[44,45] Their phase behavior depends on several factors like the described external triggers, e.g., temperature, their softness and the volume fraction. In addition, the charge density has an influence in the case of charged microgels. A detailed experimental study on the phase behavior of charge "neutral" PNIPAM microgels, i.e., microgels without ionic groups except for those stemming from the initiator, was performed by Paloli *et al.*^[12] The study was conducted at constant temperature to ensure that the softness of the particles is unaffected by temperature. The phase behavior has been investigated at different volume fractions. In the course of the sample preparation, the samples were annealed at temperatures slightly above the VPTT. Afterwards, they were allowed to cool to room temperature. At low volume fractions up to 0.52 a disordered, fluid state has been found. At a volume fraction of 0.56 a fluid and a crystal phase coexisted. In the crystal phase, a mixture of a FCC and a HCP phase were present. Increasing the volume fraction further, a purely crystalline phase has been observed if the equilibration or the annealing time during the sample preparation were long enough. Glassy phases have been obtained, if the samples were quenched quickly after the annealing phase. In agreement with several theoretical studies, a repulsive Hertzian potential has been suitable to describe the phase behavior of the samples at low volume fractions, i.e., below the fluid state. This has been verified by simulation of the radial distribution functions $g(r)$ calculated from experimental data. Equation 2.2 describes the Hertzian interaction potential.^[12,44]

$$U(r) = \begin{cases} \epsilon_H \left(1 - \frac{r}{\sigma}\right)^{\frac{5}{2}}, & r \leq \sigma \\ 0, & r > \sigma \end{cases} \quad (2.2)$$

Here, σ is the diameter of the microgel particle, ϵ_H describes the strength of the potential, $U(r)$ represents the potential energy and r the distance.

The interaction potential is shown in Figure 2.4 B. Depending on their softness, microgel particles achieve inter-particle distances smaller than their diameter as visible in the evolution of their interaction potential. Therefore, they can exceed the maximum hard-sphere volume fraction for FCC packing of 0.74 in self-assembled structures. However, the Hertzian potential is not ideally suited to describe the phase behavior at high volume fractions. In opposite to theoretical predictions, a re-entry into the fluid phase has not been observed at these volume fractions. At such high particle concentrations, it has to be considered that the particles may deform, interpenetrate or shrink.^[13] A major challenge regarding the studies on the phase behavior of microgels is that the particle size, volume fraction and interaction potential are dependent on the concentration of the samples.

As compared to their non-charged equivalents, ionic microgels are believed to be a more versatile system. They offer the possibility to tune the range and strength of their inter-particle interaction energy by changing the Debye screening length by adjusting, e.g., particle and salt concentration or charges.^[53] Their interaction potential is a combination of the Hertzian potential at distances smaller than their particle diameter and a screened Coulomb potential at increased inter-particle distances.^[119] Although simulations predict a versatile phase behavior for ionic microgels^[45], so far, similar phases as for hard colloids, e.g., FCC, RHCP or polycrystalline phases, have been obtained in most cases.^[49,50,120] Apart from these phases, the following exceptions were found: Gasser *et al.* investigated the phase behavior of PNIPAM particles copolymerized with acrylic acid. They found BCC crystallites that formed at the walls of their sample cell in addition to FCC and RHCP crystal phases.^[52] Mohanty *et al.* observed a coexistence of FCC and BCC crystalline structures for similar particles.^[53] Furthermore, an interesting observation regarding the correlation of particle softness and phase behavior has been made.^[121] Here, microgels consisting of 2-vinylpyridine cross-linked with divinylbenzene have been used. These ionic microgels with increased stiffness have shown a transition from a fluid to a crystal phase and finally to a glass phase. This is in accordance with the observations of hard spheres, although the positions of the boundaries were different. Instead, softer particles have displayed a direct transition from a fluid to a glass and even softer microgels have been found to exist in a continuous fluid phase.

2.1.3 Introduction of Anisotropic Forces

The introduction of anisotropic forces for instance by applying alternating electric fields, is an elegant way to explore non-equilibrium phases. Several experimental and theoretical studies on electric field-induced rearrangement in the course of phase transitions of dispersions comprising hard^[63,64,122–127] and soft colloids^[65–67,123] exist. Due to the change of viscosity upon structure formation or transitions in the presence of an electric field, these dispersions are also termed electrorheological fluids.^[63,128] The application of an electric field to a colloidal dispersion can induce electric dipoles that are oriented along the field lines. Considering the interaction potential of the respective colloids, the isotropic interaction potential is extended by a directed, dipolar term in the presence of an electric field.^[66]

In the case of hard colloids a dipolar interaction arises if the dielectric permittivity difference between particles and solvent is sufficiently large. The interaction between two dielectric hard particles is expressed using the dipole approximation given in equation 2.3. Here, k_B is the Boltzmann constant and T is the temperature. The strength of the potential is defined by γ_e according to equation 2.4. E_{loc} is the sum of the external electric field E_{ext} and the field originating from other dipoles E_{dip} . α_p is the polarizability that is given by $(\epsilon_p - \epsilon_s)/(\epsilon_p + \epsilon_s)$. ϵ_p and ϵ_s denote the dielectric constants of the particles and the solvent, respectively.^[129]

$$\frac{U(r)}{k_B T} = \frac{\gamma_e}{2} \left(\frac{\sigma}{r} \right)^3 (1 - 3 \cos^2 \theta_e) \quad (2.3)$$

$$\gamma_e = \frac{\pi \sigma^3 \alpha_p^2 \epsilon_s |E_{loc}|^2}{8 k_B T} \quad (2.4)$$

All other variables are explained using Figure 2.5 A which depicts two particles with a diameter σ in an electric field. The displacement of the particles from each other can be described using the vector \vec{r} which forms an angle θ_e with the direction of the electric field \vec{E} . Applying an electric field can induce an electric dipole moment on the particles that is parallel to the field direction as indicated by the arrows in Figure 2.5 B.^[129] If θ_e is small, the potential becomes attractive according to eq. 2.3. This results in an arrangement of the dipoles/particles into chains, sometimes also termed as strings, that are oriented parallel to the field direction. Due to thermal fluctuations in the solvent the strings begin to undulate. Two chains of particles start to attract each other due to dipolar interaction when they are displaced by half of an inter-particle distance along their long axis.^[128] This can lead to the formation of sheets. Sheets are planes of self-assembled chains oriented in the field direction (z -direction). Hence, they appear as chain-like structures in the xy -plane. If the strength of the potential increases further, e.g., by an increasing field strength, these sheets can assemble into crystal lattices.^[63]

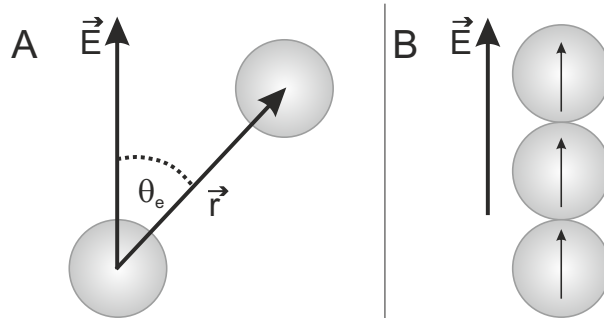


Figure 2.5: A. Schematic depiction of two colloids displaced by a vector \vec{r} in an electric field. θ_e is the angle between the field direction \vec{E} and \vec{r} . B. Head-to-toe arrangement, so-called string or chain, of the electric field-induced dipoles which are indicated by arrows.

One should note that the interaction potential of charged, hard colloids in the electric field depends on the applied frequency of the electric field. At low frequencies in the kHz regime, the ionic polarization of the free ions in the double layer has an additional impact on the interaction potential.^[65,130,131] This has to be considered in addition to the previously described dielectric polarization. At high frequencies close to the MHz regime, the ionic polarization is decreased and the dielectric polarization becomes more important.^[63,65,124,132]

So far, the interaction potential of hard colloids in an electric field was discussed. For soft microgel colloids, the directed contribution to the interaction potential is believed to be different.^[65] Ionic microgels incorporate more than 80% of water in the swollen state. Hence, the difference in electric permittivity between the microgel particle and water is small. This implies that the dielectric polarization is decreased as well. Nöjd *et al.* presented a different mechanism for the polarization of these particles.^[65] As ionic microgels include more counter ions as compared to surface charges, the authors suggest that the polarization is based on these counter ions. In contrast to the structures found for hard colloids, which include a fluid, string, sheet and crystal phase, no sheet phase was found for ionic microgels. A direct transition from strings to crystalline areas with square symmetry has been reported.

2.2 Colloidal Self-Assembly at Liquid-Liquid Interfaces

Two-dimensional layers of colloids, i.e., monolayers, can be formed at liquid-liquid interfaces. At the interface, the magnitude of the inter-particle interaction forces may be different and additional forces that are not present in the bulk phase have to be considered.^[27-29] Similar to particles in bulk, hard and soft colloids will interact differently at oil-water interfaces which can influence the self-assembled structures. In the following, research representing the state of the art regarding the morphology and the self-assembly of hard and soft microgel colloids at oil-water interfaces is summarized.

2.2.1 Hard Colloids

If colloids adsorb at an oil-water interface, the interfacial energy is altered. The interfacial area between the two liquid phases, oil and water, decreases during the adsorption of colloids. Simultaneously, two new interfaces arise which are defined by the colloid and the oil phase or the water phase, respectively. In order to prevent that the colloids submerge in one of the two liquid phases, the interfacial energy barrier has to be larger than the thermal energy of the colloids. In other words, a minimum in the total interfacial energy has to be achieved. The total interfacial energy is dependent on the following parameters: the interfacial tensions between the involved materials (oil, water, material of the particles), the radius of the colloids and the vertical distance between the particle center and the interface level.^[133] The vertical distance is defined by the position of the colloid at the interface which is related to the contact angle θ_c . The definition of the total interfacial energy indicates that the surface chemistry of the colloids and the composition of the interface are particularly crucial regarding the adsorption. Considering hard colloids at an oil-water interface, there are three scenarios of the interfacial position that depend on the surface chemistry of the particles. The three cases are schematically shown in Figure 2.6.

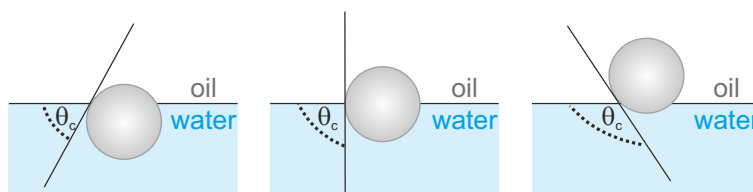


Figure 2.6: Schematic illustration of a hard colloid located at an oil-water interface with a contact angle θ_c below (left), equal to (middle) or above 90° (right) with respect to the water phase.

Particles with a hydrophilic surface form a contact angle θ_c below 90° with respect to the water phase. In the case of hydrophobic colloids θ_c is above 90° . The intermediate case

is described by a particle that is located at $\theta_c=90^\circ$ with respect to the water phase.^[75] Additionally, the radius influences the interfacial energy. Colloids that exhibit dimensions larger than a few tens of nanometers typically adsorb irreversibly at the oil-water interface.^[9]

If the adsorption of the colloids at the oil-water interface is energetically favorable, stable assemblies can be formed. The self-assembly of hard colloids at interfaces is governed by the interplay of attractive forces like capillary forces (long-range flotation forces) and van der Waals forces (short-ranged) as well as repulsive forces like electrostatic forces and dipole-dipole interactions. The structure of the self-assembled monolayer is dependent on the balance between attractive and repulsive forces. In particular, the absence of sufficiently repulsive forces results in disordered monolayers as capillary forces cause the particles to attract each other and to form aggregates stabilized by van der Waals forces.^[134] In a fluid phase the electrostatic interaction between charged colloids can be described by a screened Coulomb potential. At the interface, the situation becomes different since the colloid is surrounded by materials that differ in their dielectric properties.^[9] Pieranski *et al.* revealed in experiments that dipole-dipole interactions are dominant at the interface.^[133] These repulsive forces are based on the charge imbalance at the oil-water interface and represent the driving force during the self-assembly process.^[9,133,135] The charge imbalance arises due to an asymmetric distribution of the particles surface charges that is a result of the strong difference in dielectric constants between water and oil.^[133,134] Water exhibits a high dielectric constant ($\epsilon(\text{H}_2\text{O})=78.5$ at 20°C).^[136] Therefore, it supports the dissociation of functional groups and stabilizes charged surfaces.^[134] In contrast, the particles are uncharged in oil ($\epsilon(n\text{-hexane})=1.89$ at 20°C)^[136] or other media with low dielectric constants.^[134] Hence, dipole moments that are vertically aligned to the interface arise. Although these dipole moments would preferably align, they cannot as the particles are trapped at the interface. Therefore, repulsions between the colloids are induced. In Figure 2.7 particles stabilized by dipole-dipole interactions are depicted.

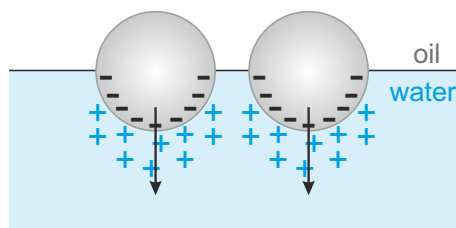


Figure 2.7: Schematic depiction of dipole-dipole interactions between two hard colloids at an oil-water interface. The asymmetric distribution of counter-ions results in dipole moments that are aligned perpendicular to the interface.

Sufficiently strong, electrostatic repulsion increases the energy barrier between the particles, so that they exhibit a higher lateral mobility. This allows the particles to occupy a

minimum free energy configuration. In the case of monodisperse spherical particles at an oil-water interface, hexagonally ordered monolayers are typically obtained at sufficiently high surface coverages^[134] The long-range dipole-dipole interactions present at oil-water interfaces cause the formation of crystalline and glassy monolayers with lattice spacings in the order of several particle radii already at low surface coverage. Consequently, the pair potential is only weakly influenced by the inter-particle distance. These properties lead to structures which are very robust against local impurities and polydispersity.^[9] Based on the increased repulsion and decreased attraction during the self-assembly of hard charged colloids at oil-water interfaces, these colloids are ideally suited to prepare non-close-packed monolayers. For the first time, Aveyard *et al.* reported the formation of non-close-packed monolayers upon compression at octane-water interfaces in a LB trough. Different sizes of polystyrene particles with sulfate groups have been investigated. Monolayers with a hexagonal structure were obtained upon compression. At very high compression, close to monolayer collapse, a rhombohedral structure was observed which is related to the anisotropic compression of the initially hexagonal monolayer. The authors introduced a model for the increased repulsion. They found that in the course of monolayer collapse, the monolayer folds rather than ejecting particles into one of the bulk phases. In the beginning of the measured compression curves, i.e., at low surface coverage, the surface pressure rises slowly. This initial, shallow rise indicates the long-range repulsion between the particles. As the surface coverage is increased during further compression, a steep rise in surface pressure due to repulsion is found. Finally, at maximal compression, as the monolayer begins to fail, the rate of surface pressure increase starts to reduce.^[73] Horozov *et al.* studied the self-assembly of surface-modified silica (SiO₂) particles at octane-water interfaces. Changing the surface functionality of the particles alters the contact angle at the interface. Colloids that exhibit a hydrophobic surface result in strong Coulomb repulsion acting through the oil phase between the particles as compared to particles with a hydrophilic surface. Hence, the degree of order in the monolayer is increased.^[137,138] Eventually, Isa *et al.* managed to transfer non-close-packed, ordered monolayers formed at the oil-water interface onto solid substrates. Positively charged, amide functionalized polystyrene particles of different sizes were assembled at a hexane-water interface and collected onto negatively charged supports by vertical lifting deposition. Hexane was found to be a suitable solvent as its low viscosity and high volatility favor the transfer of the monolayer by preventing viscous drag and supporting fast drying. With decreasing size of the particles the degree of order in the monolayers reduces. They attribute this to the increased polydispersity of the small particles and to the enhanced influence of Brownian motion that displaces the particles from the minimum of their potential well.^[135]

2.2.2 Microgels

The inter-particle interactions of microgels at oil-water interfaces differentiate from those of hard colloids giving rise to a different phase behavior. As microgel particles are strongly swollen, van der Waals attractions are rather weak. Consequently, significantly less electrostatic repulsion is required to prevent aggregation. This implies that the interactions, which are crucial for hard spherical particles are almost negligible for microgels. The self-assembly of microgels is governed by soft steric interactions and their deformation at the interface. Further, it is known that capillary forces are stronger as compared to hard colloids.^[74] Their polymeric, soft character facilitates spontaneous adsorption from bulk phase to the fluid interface.^[74,92]

Furthermore, their soft shells result in a distinctly different particle morphology at the interface as compared to hard colloids. Geisel *et al.* provide a qualitative description of the interfacial morphology of microgels using FreSCa cryo-SEM.^[83] They reveal 3D information on the deformation and protrusion of the microgels at the oil-water interface. In order to determine the particle position relative to the interface, i.e., their contact angle, a cryo-fracture along the interface is performed. This results in an oil phase with imprints and a water phase containing the colloids at its surface. The frozen water phase is coated with a thin tungsten layer at an angle of 30° relative to the surface. If the colloids protrude from the interface, they cast a shadow behind them. By measuring the length of this shadow and knowing the colloid size at the interface, the vertical position of the colloids at the interface can be calculated.^[139] Analyzing the results of their FreSCa cryo-SEM experiments, Geisel *et al.* reported the absence of a clear shadow for pure microgel particles. This implies that the contact angle of the objects to the interface must be smaller than the shadowing angle of 30° . Depending on the thickness of the tungsten coating, small halos could sometimes be identified behind the microgel. This indicates that the contact angle approaches 30° . Hence, the particles are strongly hydrophilic. Further, it has been found that the microgels deform at the interface, leading to a footprint/cross-section twice as large as in bulk. The equilibrium deformation at the interface is a balance between the maximum solvation of the hydrogel in both phases, the surface activity as well as the internal elasticity of the microgel particles, determined by the cross-linker content. Figure 2.8 shows a qualitative sketch of a cross-section of a microgel particle located at an oil-water interface. Due to the gradient in cross-linking in the polymer network of microgel particles these colloids possess a core-corona structure, also termed "fried-egg" morphology, in their top view at the interface. This is well visible in the SEM image in Figure 2.8.^[83,84]

The particles are strongly flattened which is confirmed by investigation of the imprints within the frozen oil phase as only shallow prints are visible. The surface-active microgel shells of the particles aim for maximization of their interfacial area. The resulting de-

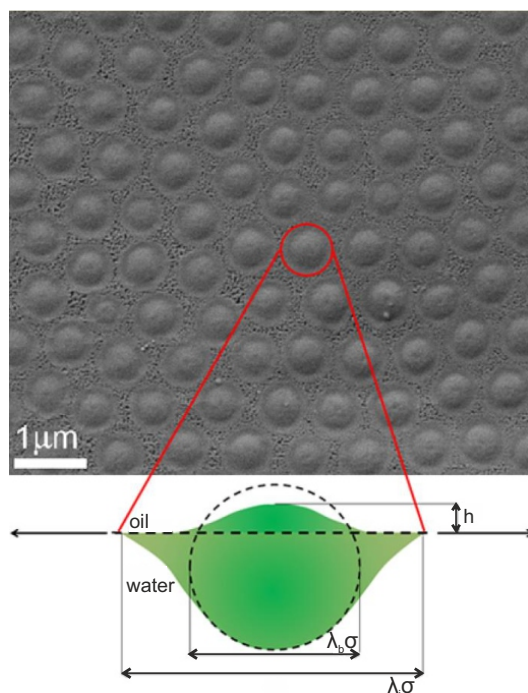


Figure 2.8: SEM image showing the top-view of a microgel monolayer at the oil-water interface. The morphology of the particles resembles a "fried-egg" morphology arising from the gradient in cross-linker content. Below a schematic cross-section of a microgel particle located at the oil-water interface is shown. $\lambda_b \sigma$ is the diameter of the hydrated particle in bulk and $\lambda_i \sigma$ gives its diameter at the interface. h denotes the protrusion height of the particle into the oil phase. Adapted with permission from "Unraveling the 3D Localization and Deformation of Responsive Microgels at Oil/Water Interfaces: A Step Forward in Understanding Soft Emulsion Stabilizers", by Geisel, K.; Isa, L.; Richtering, W. *Langmuir* **2012**, *28*, 15770-15776. Copyright 2012 by American Chemical Society.

formation at the interface proceeds until the corresponding energy gain is compensated by the internal elastic deformation of the hydrogel. This is confirmed by the observation that more rigid particles with higher cross-linker content are less deformed as softer particles.^[83-86]

The unique structural properties of microgels influence their 2D phase behavior at the oil-water interface. To analyze the respective microstructures upon compression, experiments in a LB trough have been performed by several groups.^[81,87,89,140] In a recent approach, the wafer was continuously withdrawn through the interface while the compression was continuously increased.^[89] Simultaneously, the surface pressure at the interface was measured. The deposited microstructures at the substrate correspond to a certain surface pressure or area coverage. Figure 2.9 shows the compression curve, i.e., the surface pressure plotted as a function of the area per particle A_p , of poly-*N*-isopropylacrylamide-*co*-methacrylic acid microgels at the interface. The microstructures along the compression curve are illustrated by the respective AFM images.

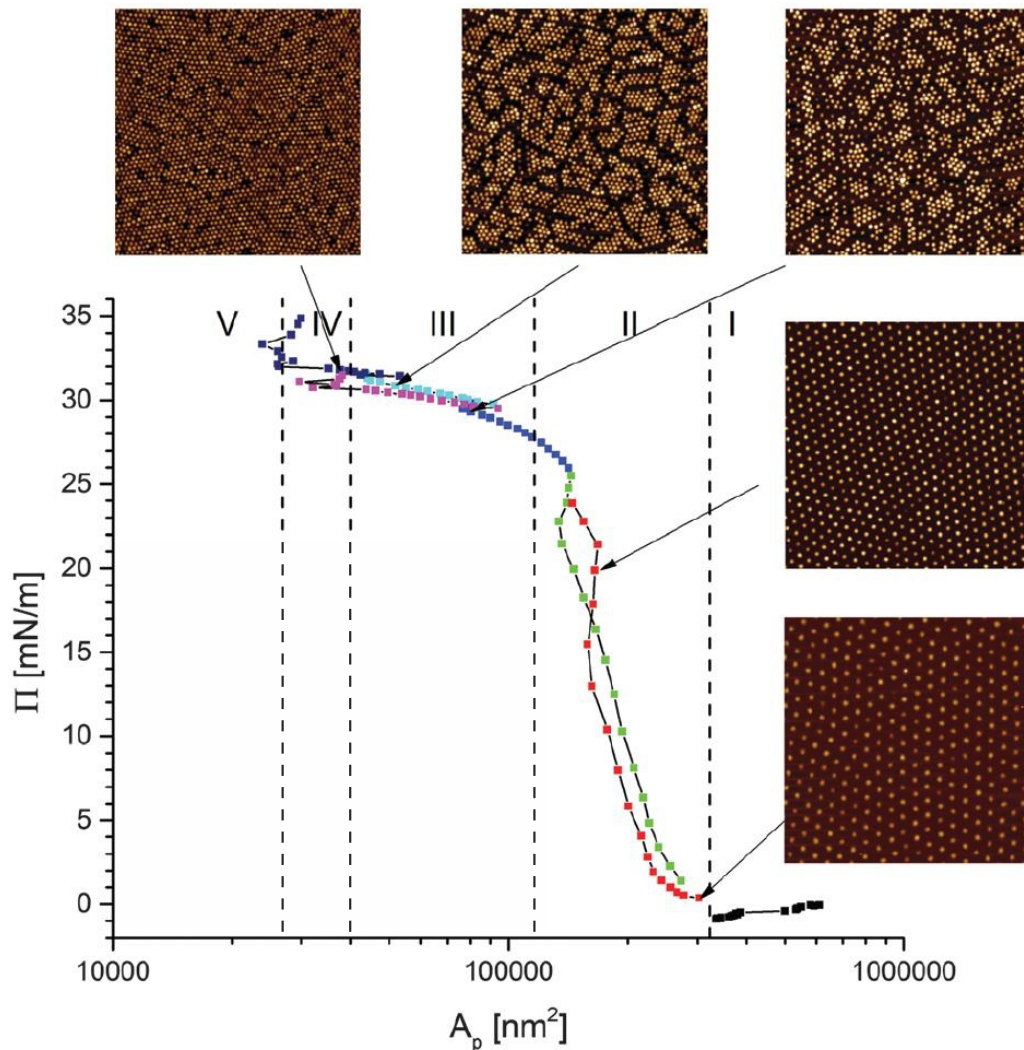


Figure 2.9: Compression curve of microgel particles at a *n*-hexane-water interface: Surface pressure Π plotted versus the area per particle A_p . The AFM height images correspond to the specific data points indicated by the arrows. The size of the scan region is $10 \mu\text{m} \times 10 \mu\text{m}$. Adapted with permission from "Isostructural Solid-Solid Phase Transition in Monolayers of Soft Core-Shell Particles at Fluid Interfaces: Structure and Mechanics", by Rey, M.; Fernández-Rodríguez, M. Á.; Steinacher, M.; Scheidegger, L.; Geisel, K.; Richtering, W.; Squires, T. M.; Isa, L. *Soft Matter* **2016**, *12*, 3545-3557. Copyright 2016 by The Royal Society of Chemistry.

Analyzing the compression curve and the corresponding microstructures, Rey *et al.* identified five regions that are labeled in Figure 2.9.^[89] They termed the inner, highly cross-linked volume element of the microgel particle as "core". The outer, more loosely cross-linked part was defined as "shell". In the first region, at low surface pressure, the particles are statistically distributed (gas phase). The average inter-particle distance between the microgels is larger than their diameter at the interface. At the beginning of the second region, A_p equals the footprint of the microgels at the interface. The particles are in shell-shell contact and form a hexagonal lattice of non-close-packed "cores". Upon further

compression, a steep increase of the surface pressure is observed. The lattice constant of this lattice is continuously decreased due to compression of the particle shells. In the third region, shell-shell contacts mechanically fail and clusters with particles in core-core contact are formed. Here, the surface pressure approaches a plateau value. A complete phase transition is observed from a lattice with particles in shell-shell contact to a lattice consisting of particles in core-core contact. Upon further compression in the fourth region, the inter-particle distances in the close-packed phase are slightly reduced. At maximal compression monolayer buckling and failure is found (fifth region).

In order to analyze the effect of charge in the microgels, Geisel *et al.* recorded compression curves of charged and uncharged microgels in a LB trough.^[81] The respective microstructures were thoroughly analyzed. Interestingly, they found that charged microgels can be compressed further than their uncharged equivalents. This suggests that Coulomb interaction between the different microgel particles plays a minor role. Instead, the charges have a major impact on the swelling behavior of the microgels. This has a significant influence on the deformation of the particles at the interface and thus on their interfacial morphology. In contrast to this, Aveyard *et al.* showed that Coulomb interactions have a strong impact on hard colloids at oil-water interfaces.^[73] These examples highlight that the interactions between soft microgel particles and hard colloids at liquid-liquid interfaces are significantly different.

2.3 Predictions for Core-Shell Particles

Experimental studies on the self-assembly of core-shell particles in the bulk phase and at liquid-liquid interfaces are barely available. However, theoretical work on two-dimensional core-shell systems has predicted a rich phase behavior.^[15,16] It has been suggested that this is related to the two length scales present in core-shell systems. These length scales are defined by core-core and shell-shell contacts. Dotera *et al.* used a minimalistic step potential to describe the interaction forces of core-shell disks and discovered a variety of crystalline phases including quasicrystalline phases.^[15] This was further confirmed by Schoberth *et al.* who extended the step potential by consideration of repulsive forces.^[16]

2.4 Investigation of Structure and Dynamics

In this section the most important methods used in this thesis for the characterization of CS particles and their self-assembled structures are presented. First, the basics of the image analysis that were used for images obtained by microscopy methods, such as CLSM, electron microscopy and AFM, are outlined. In the second part, the used scattering methods and the analysis of the scattering data are briefly explained.

2.4.1 Image Analysis

2.4.1.1 Radial Distribution Function

Radial distribution functions ($g(r)$), describe the normalized average point density around a reference point as a function of the radial distance. In the case of colloids, the probability to find a particle at a given distance r from a reference particle, which is located at $r = 0$, is described. Hence, in similarity to the structure factor, $g(r)$ functions provide information on the spatial distribution of the colloids. The Fast Fourier transformation of the structure factor yields the radial distribution function.^[141] In order to calculate $g(r)$ in a given plane or volume element of a sample, an algorithm is used. The procedure is described in the following. Differences between 2D (plane) and 3D (volume element) data are highlighted.

- The basis for the calculation of $g(r)$ is a microscopic real space image (2D) or a stack of microscopic real space images describing a volume element (3D) of a given sample. To locate the particles in the recorded data, a particle tracking algorithm searches local brightness maxima. This implies that the position of the brightest pixel gives the possible xy -coordinates if no other pixel within a threshold distance v is brighter. The value for v has to be chosen, e.g., for hard spheres v cannot be smaller than their diameter in order to get reasonable results. Regarding 3D data, the algorithm correlates the maxima of the different xy -planes with similar xy -coordinates with each other and identifies the brightest pixel in z -direction. This provides the xyz -coordinates of the particles.^[142]
- Knowing the particle coordinates in the plane/volume element, the number of particles $N(r)$ in thin shells with a thickness dr , i.e., at a distance r and $r + dr$, around a reference particle is counted. This procedure is repeated for each particle in the plane/volume element.
- Subsequently, this number is divided by the total number of particles. This provides the fraction of particles being in the shell area/volume.

- As expected, more particles are found in thin shells that are at larger distances from the reference point. To consider this, the number of particles in a shell is divided by the area/volume of the spherical shell.
- This value is then normalized by the particle number density ρ_N in the whole area or volume element. This ensures that $g(r) = 1$ if there are no structural correlations in the data.^[143]

All imaging techniques result in finite particle coordinates per area/volume element. Hence, artificial boundaries are created. If the reference particle is located at the border of the sample area/volume element, the results are strongly defective as the algorithm will find no particles outside of the area/volume element. Therefore, such boundaries have to be considered in the used algorithm.^[143] Eq. 2.5 and 2.6 give the radial distribution functions for the two-dimensional or three-dimensional case, respectively:^[144,145]

$$g(r) = \frac{N(r)}{2\pi r \Delta r \rho_N} \quad (2.5)$$

$$g(r) = \frac{N(r)}{4\pi r^2 \Delta r \rho_N} \quad (2.6)$$

Figure 2.10 B shows the radial distribution function for a disordered system of hard disks depicted in Figure 2.10 A.

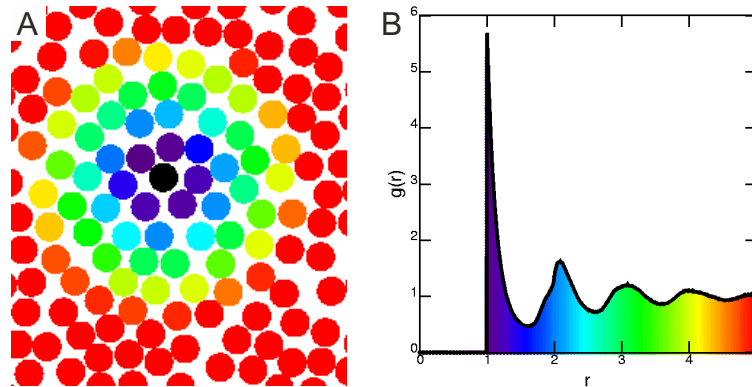


Figure 2.10: A. Disordered system of two-dimensional disks. B. Respective radial distribution function, $g(r)$, that was calculated for all possible pairs of particles. For the sake of clarity, one reference particle is highlighted in black. All other particles around the reference particle are colored corresponding to the distance from the reference particle. Reprinted from reference^[143].

As the particles cannot interpenetrate, the probability to find a particle at distances r smaller than the diameter is zero. At a distance resembling the diameter of the disks a maximum in the $g(r)$ is visible since the first shell (purple) filled with particles is found at this distance. All following maxima correspond to further shells of particles which were

highlighted using different colors. As long-range order is not present, the probability to find particles at specific distances decreases, until, finally, the radial distribution function approaches unity. In the case of charged spheres, the first peak will be at a distance larger than their diameter due to repulsive interactions in the system. If the spatial distribution of soft spheres is analyzed, distances smaller than their diameter are achievable due to interpenetration and/or deformation of these colloids. Hence, apart from the spatial distribution, also conclusions on the inter-particle interactions are possible. Further, radial distribution functions allow to derive the degree of order and the type of crystal lattice. Figure 2.11 shows a CLSM image (A) and the respective $g(r)$ function (B) for a crystalline sample of Au-PNIPAM particles.

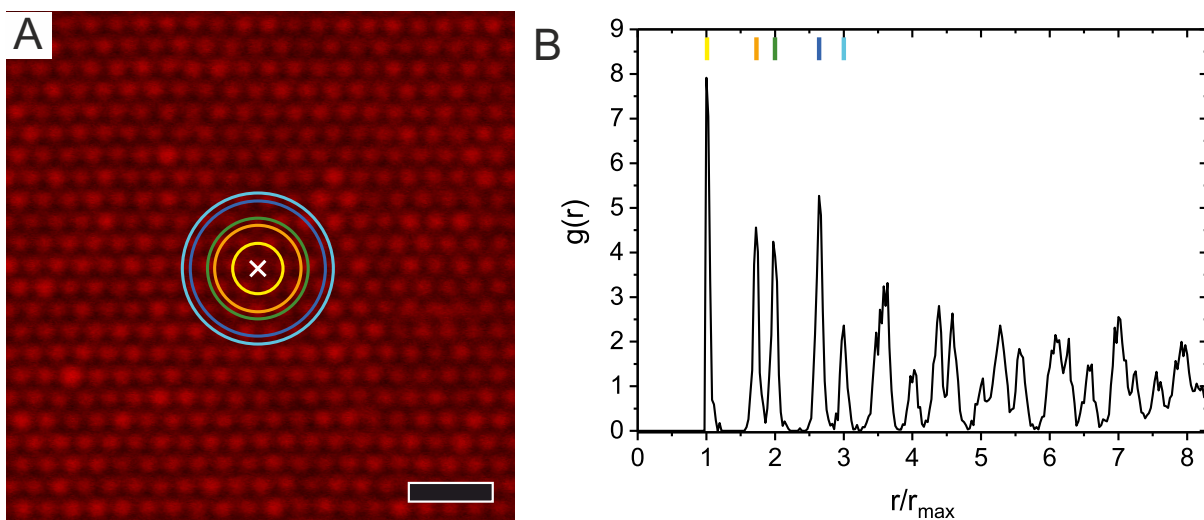


Figure 2.11: A. CLSM image of a hexagonally arranged sample of Au-PNIPAM particles. The colored circles show five different average inter-particle distances referred to a reference particle indicated by a white cross. The scale bar is $2 \mu\text{m}$. B. Respective two-dimensional $g(r)$ function normalized using the average inter-particle distance r_{max} . The respective peaks in the $g(r)$, that correspond to the colored circles in A, are highlighted using the same color code.

The radial shells that correspond to the first five maxima are labeled using colored circles with the same color code for a selected reference particle indicated by a white cross. Due to the present long-range order in crystals, sharp maxima at much larger distances than the particle diameter are found. Calculating the linear combinations of the real space lattice vectors gives the position of the peaks in $g(r)$ for a specific lattice type. Here, the positions coincide well with the ones of a hexagonal lattice (e.g.: $(1, \sqrt{3}, 2, \sqrt{7}, 3) \cdot r_{max}$). r_{max} denotes the position of the first peak in the $g(r)$ and gives the average inter-particle distance.

2.4.1.2 Bond-Order Parameter

The two-dimensional hexagonal local bond orientational order parameter Ψ_6 is used as a measure of the order in interfacial monolayers. In this case "bond" is not a chemical bond. Instead, a "bond" characterizes the lines that result from the assignment of nearest neighbors. The nearest neighbors are found using Voronoi tassellations and Delaunay triangulations. The average hexagonal bond orientation order parameter Ψ_6 is determined from the sum of all bonds in the sample:^[146-148]

$$\Psi_6 = \left\langle \frac{1}{N_b} \sum_{j=1}^{N_b} \exp(in\theta_j) \right\rangle \quad (2.7)$$

Here, N_b gives the number of nearest neighbors of the reference particle. θ_j denotes the bond angle between the particle and its nearest neighbor pair j and n is set to 6. If $\Psi_6 = 1$, the system is perfectly ordered. If $\Psi_6 \ll 1$, hexagonal order is not present.

2.4.2 Scattering Techniques

Different scattering methods, such as dynamic and static light scattering (DLS/SLS), small-angle neutron scattering (SANS) and small-angle X-ray scattering (SAXS), were used in this thesis to study the size, shape, internal microgel network structure and/or crystal lattice of the hard-core/soft-shell systems. The choice of technique is related to the length scale which is probed.^[149] Figure 2.12 depicts a typical scattering event at a scattering center. \vec{k}_i describes the wave vector of the incident beam, \vec{k}_s is the wave vector of the scattered beam and θ is the scattering angle. In a typical static scattering experiment, the time-averaged intensity of elastically scattered radiation is studied as function of the scattering angle θ . θ is the angle between the incident and the scattered radiation. In the dilute regime, it can be assumed that the evolution of the average scattered intensity gives the qualitative profile of a single particle. Depending on its size, a single colloid includes several scattering centers. The scattered radiation waves can add up by constructive interference or they extinguish each other by destructive interference. A maximum of constructive interference results in a maximum of the detected time-averaged intensity at a certain scattering angle. In contrast to this, a maximum of destructive interference leads to a minimum of the time-averaged intensity.^[150] In the dilute state, the scattered radiation waves of the different particles are not interfering. Hence, the scattering profile contains information about the size and shape of a single particle. In the concentrated regime, inter-particle distances are decreased. Thus, the scattered radiation waves of adjacent particles interfere additionally. In this case, it is more difficult to extract information about the single particle. However, the spatial arrangement of the particles, e.g., the type of crystal lattice, can be analyzed.

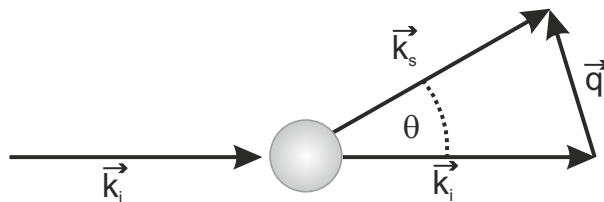


Figure 2.12: Schematic illustration of a single scattering event. The incident beam \vec{k}_i is scattered at a scattering center. This results in the scattered beam \vec{k}_s that is shifted by the angle θ with respect to \vec{k}_i . The scattering vector \vec{q} is given by the difference $\vec{k}_i - \vec{k}_s$.

A suitable measure is required to compare the data that is recorded in different scattering techniques which is independent of the wavelength of the radiation. Therefore, the scattering vector \vec{q} is introduced. In Figure 2.12 \vec{q} is the difference of \vec{k}_i and \vec{k}_s . The magnitude of \vec{q} , $|\vec{q}|$, is given by:^[149]

$$|\vec{q}| = q = \frac{4\pi n}{\lambda_v} \sin \frac{\theta}{2} \quad (2.8)$$

Here, n is the refractive index of the solvent and λ_v is the vacuum wavelength of the incident radiation. λ is defined by λ_v/n . q gives the spatial resolution in a scattering experiment in reciprocal units. In a scattering experiment, the q -range is determined by the investigated range of angles and by the wavelength of the used radiation. In this thesis, either light, neutrons or X-rays were used. The wavelength range, the corresponding q -ranges and resolved length scales of the used scattering methods are summarized in Table 2.1. Different radiation interacts differently with matter. In LS experiments the interaction between light, i.e., photons, and matter is studied. A difference in refractive index within the investigated sample is required to obtain a signal. In a light scattering experiment, the incident radiation is produced by a laser. As compared to SANS or SAXS experiments, the wavelength in a LS experiment is rather large, i.e., the recorded q -values are rather small. In LS experiments, the refractive index has to be considered for the calculation of q . In SANS experiments, the incident neutrons are scattered at the atom nuclei of the sample. Thus, different atom nuclei within the sample are needed to obtain contrast. In contrast to this, a sufficient difference in electron density within the sample is required to achieve enough contrast in SAXS experiments. Here, the radiation (X-rays) interacts with electrons. Therefore, a combination of different scattering methods offers the opportunity to collect data for a large q -range.^[149]

In the case of the investigated colloids, conclusions on the overall size and shape (low q -range, measured by LS) as well as on the internal microgel network structure on nm scale (high q -range, measured by SANS) could be drawn in the dilute state. Structural correlations between CS particles in concentrated dispersions could be revealed using SAXS and SANS.

Table 2.1: Wavelength λ , q -range and range of resolved length scales for the scattering techniques used in this thesis.

Scattering method	λ [nm]	q -range [nm ⁻¹]	Resolved length scale ^b [nm]
SANS	0.6 – 1	0.009 – 4.340	1 – 698
SAXS	0.095	0.004 – 0.080	79 – 1571
Light scattering	632.8	0.005 – 0.026 ^a	242 – 1257

^a The respective values were calculated using the refractive index of water at 25°C.

^b The values were estimated using the assumption that the given q -range refers to the position of the first maximum in the scattering profile. Hence, $2\pi/q_{max}$ was used for the calculation of the range of resolved length scales.

2.4.2.1 Light Scattering

Angular-dependent dynamic and static light scattering was frequently used in this thesis to determine the size of the CS colloids. Further, temperature-dependent DLS measurements were employed to study the swelling behavior, which provided information about the softness of the colloids. In the following, the principles of DLS and SLS are depicted.

Dynamic Light Scattering. In dynamic light scattering experiments intensity fluctuations of the light scattered by a colloidal dispersion are analyzed. The diffusion of the colloids in their dispersing medium due to Brownian motion results in intensity fluctuations of the scattered light. These fluctuations are caused by differences in the phase relation of the scattered light as the particles are moving. Exemplarily, the time-dependent evolution of the scattering intensity is illustrated in Figure 2.13 A. The velocity of the diffusion is influenced by the size of the colloids, since larger particles diffuse slower than smaller particles of the same density. These measured intensity fluctuations are automatically transformed into a normalized intensity-time autocorrelation function $g^2(q, \Delta t)$ using a hardware correlator:

$$g^2(q, \Delta t) = \frac{\langle I(q, t)I(q, t + \Delta t) \rangle}{\langle I(q, t)^2 \rangle} \quad (2.9)$$

Here, $I(q, t)$ is the scattered intensity at a time t and $I(q, t + \Delta t)$ is the scattered intensity after a certain delay time Δt .^[151] The autocorrelation function describes the similarity of the two intensities. Figure 2.13 B depicts the intensity-time autocorrelation function $g^2(q, \Delta t)$ (red trace) that corresponds to the intensity fluctuations in A.

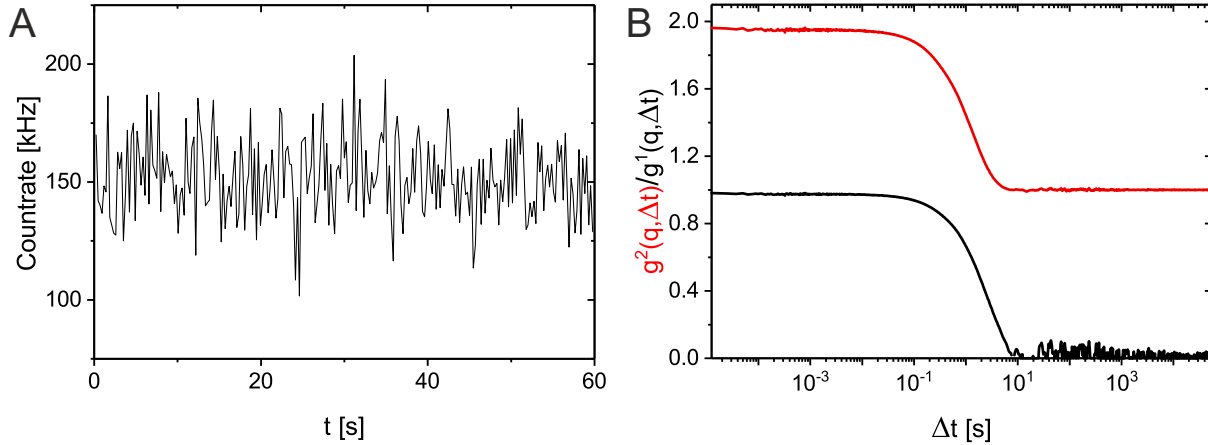


Figure 2.13: Light scattering data of a dilute Au-PNIPAM dispersion acquired at 25°C and at a scattering angle θ of 60°. A. Evolution of the count rate as a function of time. B. Corresponding intensity-time autocorrelation function $g^2(q, \Delta t)$ and field-time autocorrelation function $g^1(q, \Delta t)$ versus the delay time Δt .

To analyze the DLS data, the field-time autocorrelation function $g^1(q, \Delta t)$ is needed:

$$g^1(q, \Delta t) = \frac{\langle E(q, t)E(q, t + \Delta t) \rangle}{\langle E(q, t)^2 \rangle} \quad (2.10)$$

$E(q, t)$ and $E(q, t + \Delta t)$ describe the scattered electric field at the time t and $t + \Delta t$, respectively. As $g^1(q, \Delta t)$ is not experimentally accessible, the Siegert relation is used to transform $g^2(q, \Delta t)$ into $g^1(q, \Delta t)$:^[151]

$$g^2(q, \Delta t) = 1 + \beta_{Siegert}[g^1(q, \Delta t)]^2 \quad (2.11)$$

Here, $\beta_{Siegert}$ is a factor that depends on the experimental geometry. If $\beta_{Siegert} = 1$, the field-time autocorrelation function $g^1(q, \Delta t)$ (black trace) illustrated in Figure 2.13 B is obtained. In the case of monodisperse, spherical and non-interacting scattering objects, the normalized field autocorrelation function resembles a single exponential decay that is given by:^[151]

$$g^1(q, \Delta t) = \exp(-\Gamma \Delta t) \quad (2.12)$$

Here, Γ is the relaxation rate.

However, real samples exhibit a certain polydispersity. Therefore, $g^1(q, \Delta t)$ cannot be described by a single exponential function. It has to be described by a sum or an integral over a distribution of relaxation rates $F(\Gamma)$.

$$g^1(q, \Delta t) = \int_0^{\infty} F(\Gamma) \exp(-\Gamma \Delta t) d\Gamma \quad (2.13)$$

Here, $F(\Gamma)$ has to be normalized:

$$\int_0^{\infty} F(\Gamma) d\Gamma = 1 \quad (2.14)$$

In this case, an average relaxation rate $\langle\Gamma\rangle$ is determined.^[151] The derivation of $\langle\Gamma\rangle$ is typically carried out using the Cumulant method^[151] or the CONTIN algorithm.^[152,153] In the Cumulant method a Taylor series expansion of the field-time autocorrelation function is applied:

$$\ln(g^1(q, \Delta t)) = -\langle\Gamma\rangle\Delta t + \frac{\mu_2\Delta t^2}{2!} - \frac{\mu_3\Delta t^3}{3!} + \dots \quad (2.15)$$

The first cumulant gives the mean value of the relaxation rate $\langle\Gamma\rangle$ and the second cumulant μ_2 defines the variance of the relaxation rate distribution. The ratio of the second cumulant and the square of the first cumulant gives the polydispersity index.^[151]

The CONTIN algorithm uses inverse Laplace transformations in order to derive a distribution of relaxation rates.^[152,153]

The relaxation rate Γ can be used to determine the translational diffusion coefficient D_T :

$$\langle\Gamma\rangle = q^2 D_T \quad (2.16)$$

To ensure that purely translational diffusion is probed, i.e., to verify the absence of other dynamic processes, angular-dependent measurements are often used. The resulting average relaxation rate $\langle\Gamma\rangle$ can then be plotted as function of q^2 . A linear relationship between $\langle\Gamma\rangle$ and q^2 described by a regression curve with an intercept close to zero indicates that only translational diffusion is probed. Further, angular-dependent measurements allow a very precise determination of D_T .

Assuming translational diffusion, the Stokes-Einstein equation can be used to calculate the hydrodynamic radius R_h :

$$R_h = \frac{k_B T}{6\pi\eta D_T} \quad (2.17)$$

Here, k_B gives the Boltzmann constant, T is the temperature and η is the viscosity of the dispersion medium.^[151]

To determine the swelling behavior of the microgel systems, temperature-dependent DLS measurements were conducted. The swelling ratio β (eq. 2.18) and de-swelling ratio α (eq. 2.19) were used as measures for their swelling capacity, i.e., their relative water uptake.^[154]

$$\beta = \frac{V_h(T)}{V_h(60^\circ\text{C})} = \frac{R_h(T)^3}{R_h(60^\circ\text{C})^3} \quad (2.18)$$

$$\alpha = \frac{V_h(T)}{V_h(20^\circ\text{C})} = \frac{R_h(T)^3}{R_h(20^\circ\text{C})^3} \quad (2.19)$$

Static Light Scattering. In a typical SLS experiment, the time-averaged scattering intensity $I(q)$ is recorded in dependence on the angle θ . In contrast to DLS, structural information is accessible in SLS. For instance, the form factor $P(q)$ that provides information about the size and shape of the colloids, can be determined in very dilute dispersions. More concentrated dispersions allow to access information on the spatial distribution of the colloids. For small enough radii and/or for small enough q ($qR_g \ll 1$), the Guinier plateau of the scattering profile is probed. If $qR_g \ll 1$ is valid, the Guinier approximation can be used to estimate the radius of gyration or Guinier radius R_g .^[154]

$$\ln I(q) = \ln I_0 - \frac{q^2 R_g^2}{3} \quad (2.20)$$

Here, I_0 denotes the scattering intensity at $q = 0 \text{ nm}^{-1}$. The values for $\ln I(q)$ are plotted versus q^2 . The slope of this evolution can be used to determine R_g .

In the case of a monodisperse, hard sphere with radius R , R_g and R are related by the following equation:^[113,149]

$$R_g = \sqrt{\frac{3}{5}} R \quad (2.21)$$

The position of the first minimum q_{min} in the $I(q)$ versus q plot, can be used to estimate the radius of the scattering objects:^[155]

$$q_{min} = \frac{4.493}{R} \quad (2.22)$$

Eq. 2.22 is only valid for monodisperse, spherical, hard colloids.

2.4.2.2 Small Angle Neutron and X-ray Scattering

In this work SANS was used to characterize dilute dispersions. Both, SANS and SAXS data, were available to characterize concentrated, crystalline samples of the microgel systems. The scattered intensity consists of a coherent ($I_{coh}(q)$) and an incoherent ($I_{incoh}(q)$) part. Within this work, $I_{coh}(q)$ is used for the analysis. It is influenced by the number density ρ_N , the scattering length density contrast $\Delta\eta_s$ between the scattering objects and the solvent, the particle volume V_p , the form factor $P(q)$ of a single particle, the structure factor $S(q)$ and a dynamic component $I_{dyn}(q)$ that arises due to network fluctuations in the microgel particles.^[156] $I_{incoh}(q)$ and other background contributions can be considered as simple offset I_{offset} as they are not dependent on q in the investigated q -range. Hence, $I(q)$ is given by:

$$I(q) = I_{coh}(q) + I_{incoh}(q) = \rho_N \Delta\eta_s^2 V_p^2 P(q) S(q) + I_{dyn}(q) + I_{offset} \quad (2.23)$$

First, the analysis of the recorded isotropic 2D scattering patterns of dilute dispersions

is outlined. Afterwards, the analysis of the 2D scattering patterns of concentrated, crystalline samples is described.

Scattering in the Dilute Regime. Samples of randomly oriented particles in the dilute regime usually result in isotropic 2D scattering patterns, i.e., the intensity along the concentric circles is constant. Figure 2.14 A exemplarily gives the isotropic 2D scattering pattern of a dilute dispersion of Au-PNIPAM particles.

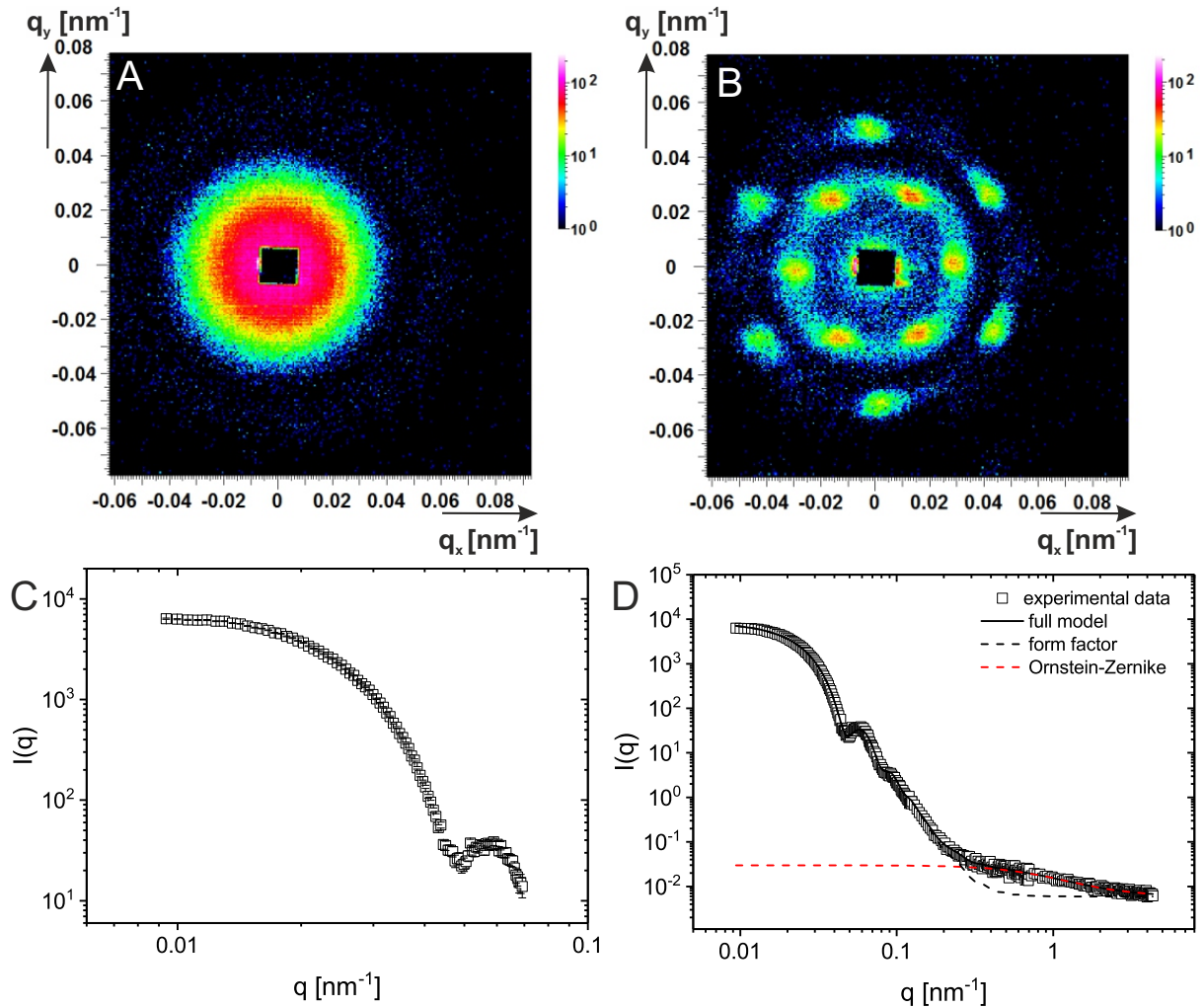


Figure 2.14: A. Isotropic 2D scattering pattern of a dilute dispersion of Au-PNIPAM particles measured at a sample-to-detector (SD) distance of 39 m. B. 2D scattering pattern of a concentrated, crystalline sample of a microgel system showing several orders of diffraction peaks recorded at a SD distance of 39 m. C. Respective radially averaged intensity profile of the depicted isotropic 2D pattern in A. D. Radially averaged scattering data of a dilute dispersion of Au-PNIPAM particles recorded at different SD distances (1.2 m, 8 m, 28 m and 39 m). The depicted data was merged resulting in a scattering profile that covers a large q -range. The scattering profile that was shown in C is also included.

For the sake of clarity, a 2D SANS pattern of a concentrated, crystalline sample is shown for comparison in Figure 2.14 B. Here, distinct diffraction peaks are visible indicating a specific orientation and periodicity. Isotropic scattering patterns are usually radially averaged for analysis resulting in a 1D scattering profile. The radially averaged profile of the scattering pattern in Figure 2.14 A is depicted in Figure 2.14 C. In order to extend the measured q -range, measurements at different angles are performed. This is achieved by adjusting the sample-to-detector (SD) distances. In Figure 2.14 D the merged data measured at four different SD distances is shown, including the data shown in Figure 2.14 C. The scattering profile in Figure 2.14 D can be described by two main contributions: (1) The form factor contribution that influences the scattering profile mainly at low q -values (dashed black line in D); (2) The Ornstein-Zernike contribution that contributes particularly in the high q -range (dashed red line in D). Both contributions add up to a full model (black solid line in D) that describes the whole profile. The structure factor is negligible in the dilute regime of non-interacting particles, therefore $S(q) = 1$ can be assumed.

The form factor $P(q)$ for a single, hard sphere with a radius R is described by eq. 2.24. In order to consider the polydispersity of the particles, it is usually convoluted with a size distribution function.

$$P(q) = \left[3 \frac{\sin(qR) - qR \cos(qR)}{(qR)^3} \right]^2 \quad (2.24)$$

However, in the case of microgel systems, it has been demonstrated that this form factor model is not accurate. In particular, the low q -range is not properly described.^[14,118] As previously discussed, the microgel shell exhibits a gradually decreasing degree of cross-linking from the inner to the outer region. Hence, the density distribution deviates from the simple box profile which is used for hard spheres. Stieger *et al.* successfully developed a model which considers the decaying density distribution of microgels. This model is based on a radial density profile with a gradually reducing segment density in the outer volume element.^[14] In this thesis, a core-shell model developed by Kohlbrecher was used to fit the data of dilute microgel samples.^[157] This model comprises an inner "core" volume element with a homogeneous density distribution and an outer "shell" volume element that accounts for the exponentially decaying density in the PNIPAM shell. One should note that core describes the inner, homogeneous part of the microgel shell without the hard inorganic core. The hard nanoparticle core was found to have a negligible scattering contribution due to its small size. The analyzed particles included a gold core that was 15 nm in diameter. This model has already been successfully applied by Dulle *et al.*^[154] They fitted the profiles of microgel systems synthesized with a semi-batch polymerization method using this approach. Figure 2.15 shows this model with its different contributions for a representative microgel system ($C_{15}S_{16.2}(10\%)$).

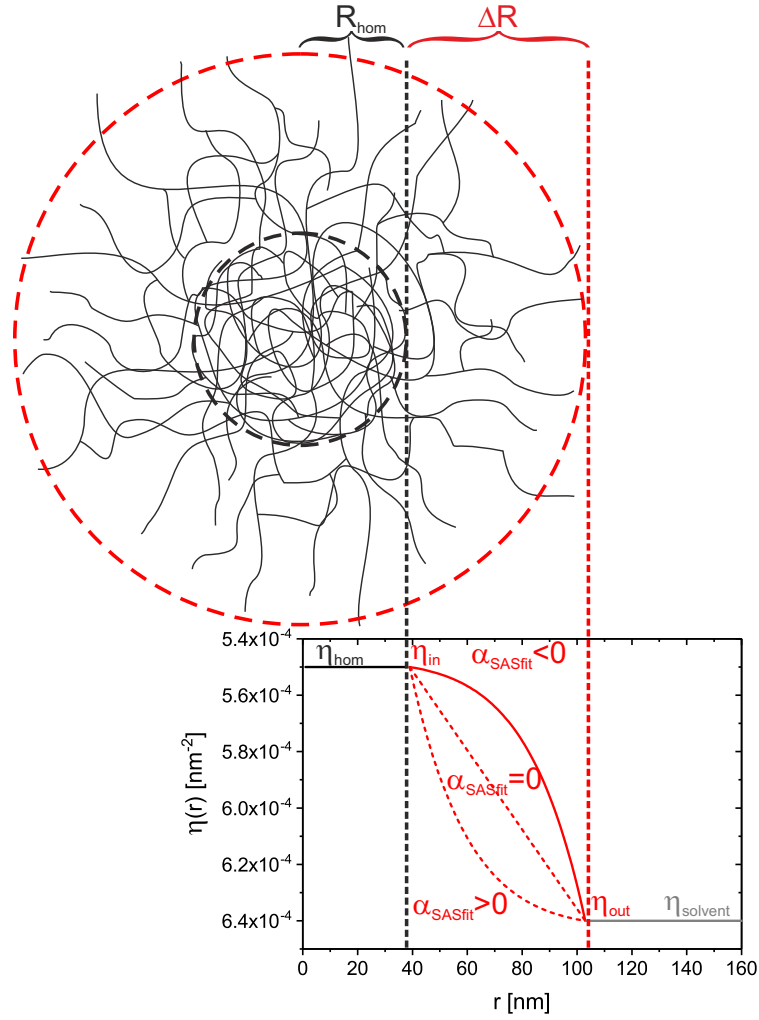


Figure 2.15: Radial scattering length density profile that was used to calculate the form factor of a representative system of microgel particles ($C_{15}S_{16.2}(10\%)$). The used model was developed by Kohlbrecher.^[157] Up to R_{hom} the scattering length density profile is constant and given by η_{hom} . The outer volume element between R_{hom} and $R_{hom} + \Delta R$ is described by an exponentially decreasing scattering length density profile $\eta_{exp}(x)$ defined by the parameter α_{SASfit} . The profiles of the $C_{15}S_{16.2}(10\%)$ particles could be fitted using $\alpha_{SASfit}=-2.2$ (red solid line). Exemplarily, the exponentially decaying profile using $\alpha_{SASfit}=0$ and $\alpha_{SASfit}=+2.2$ are shown using red dashed lines. The scattering length density at R_{hom} is given by η_{in} . η_{out} describes the scattering length density at $R_{hom} + \Delta R$. $\eta_{solvent}$ is the scattering length density of the solvent. As the scattering contribution of the gold core could be neglected, the core is not shown in the particle sketch.

The model includes different scattering lengths density profiles that are assigned to the respective volume segments at different distances r from the particle center.^[157]

$$\eta(r, R_{hom}, \Delta R, \alpha_{SASfit}, \phi_{in}, \phi_{out}) = \begin{cases} \eta_{hom}, & r \leq R_{hom} \\ \eta_{exp}(x), & R_{hom} < r < R_{hom} + \Delta R \\ \eta_{solvent}, & r > R_{hom} + \Delta R \end{cases} \quad (2.25)$$

In the inner volume element up to a distance $r = R_{hom}$ from the particle center, η_{hom} gives the constant scattering length density.

$\eta_{exp}(x)$ describes the scattering length density profile in the outer volume segment between R_{hom} and $R_{hom} + \Delta R$. Within this volume segment the scattering length density is exponentially decreasing leading to the following profile:

$$\eta_{exp}(x) = \begin{cases} \eta_{in} + (\eta_{out} - \eta_{in})x \exp[(1-x)\alpha_{SASfit}], & \alpha_{SASfit} < 0 \\ (\eta_{in} - \eta_{out})(1-x) \exp(-x\alpha_{SASfit}) + \eta_{out}, & \alpha_{SASfit} \geq 0 \end{cases} \quad (2.26)$$

Changing the magnitude and sign of the parameter α_{SASfit} the curvature of this profile can be adjusted. Further, x gives the relative distance of a volume segment belonging to the exponentially decaying shell to R_{hom} . The thickness of this volume element is described by ΔR .

$$x = \frac{r - R_{hom}}{\Delta R} \quad (2.27)$$

η_{in} gives the scattering length density at R_{hom} :

$$\eta_{in} = \phi_{in}\eta_{solvent} + (1 - \phi_{in})\eta_{shell} \quad (2.28)$$

Here, ϕ_{in} denotes the volume fraction of the solvent at $r = R_{hom}$ and $\eta_{solvent}$ is the scattering length density of the solvent. η_{shell} is the scattering length density of the pure shell material (cross-linked PNIPAM).

The scattering length density η_{out} at $R_{hom} + \Delta R$ is given by:

$$\eta_{out} = \phi_{out}\eta_{solvent} + (1 - \phi_{out})\eta_{shell} \quad (2.29)$$

Here, ϕ_{out} denotes the volume fraction of the solvent at $r = R_{hom} + \Delta R$.

Beyond the distance $r = R_{hom} + \Delta R$ from the particle center, the profile in equation 2.25 is described by the scattering length density of the solvent $\eta_{solvent}$.

If the radially symmetric density profile in eq. 2.25 is integrated over r , the scattering amplitude $H_{exp}(q)$ is obtained:

$$H_{exp}(q) = \int_0^{\infty} 4\pi r^2 \frac{\sin qr}{qr} \eta(r, R_{hom}, \Delta R, \alpha_{SASfit}, \phi_{in}, \phi_{out}) dr \quad (2.30)$$

The high q -range of the scattering profile is dominated by the dynamic component, $I_{dyn}(q)$, also termed as Ornstein-Zernike contribution, which is described by a Lorentzian function:^[158]

$$I_{dyn} = \frac{I_L(0)}{1 + q^2\xi^2} \quad (2.31)$$

Here, $I_L(0)$ is the amplitude and ξ the correlation length that is influenced by the cross-

linker density of the PNIPAM network and the volume fraction of the polymer.^[118,156] This dynamic component describes the network fluctuations of the microgel network. In particular, it influences the scattering profiles in the high q -range which is related to the small size (nm range) of the network fluctuations. Among the described scattering methods, neutron scattering is the only one that allows to explore these small dimensions. Summarizing the two main contributions, the overall scattering intensity of a dilute system is given by:

$$I(q) = \rho_N H_{exp}^2(q) + \frac{I_L(0)}{1 + q^2 \xi^2} + I_{offset} \quad (2.32)$$

Scattering in the Concentrated, Crystalline Regime. Analyzing scattering data of highly concentrated dispersions, the significantly smaller inter-particle distances have to be considered. In this case, the interference pattern obtained in the SANS or SAXS experiment will not only include information of single particles but also contributions from adjacent particles due to a superposition of their scattered radiation. Hence, the spatial distribution of particles and thus $S(q)$ has to be considered in contrast to the dilute state. As shown in the 2D SANS pattern in Figure 2.14 B, crystalline samples exhibit Bragg diffraction peaks in their scattering pattern which is related to coherent diffraction at their lattice planes. The lattice planes are defined by the Miller indices h , k and l . The q -position of the first order Bragg peaks can be used to derive the average lattice plane distance d_{hkl} :^[47]

$$d_{hkl} = \frac{2\pi}{q_{max}} \quad (2.33)$$

For cubic crystals the average lattice plane distance allows to calculate the lattice constant a as follows:^[47]

$$a = d_{hkl} \sqrt{h^2 + k^2 + l^2} \quad (2.34)$$

Assuming a FCC crystal lattice with its (111) plane perpendicular to the incoming radiation, i.e., parallel to the glass wall of the sample cell, eq. 2.34 can be simplified to:

$$a = d_{hkl} \sqrt{3} \quad (2.35)$$

In order to determine the lattice type of the crystalline samples, the positions and relative arrangements of the diffraction peaks in the 2D scattering pattern are analyzed. Further conclusions on the domain sizes and coherence lengths can be drawn using the intensities as well as the azimuthal and longitudinal peak widths.^[159]

The SANS patterns of concentrated, crystalline samples were analyzed using the software *Scatter* by Förster and Apostol.^[160] The software provides different models to simulate the scattering patterns. These simulations allow to obtain information on the type of crystal lattice, the crystalline domain sizes and the particle structure. Depending on the

cross-linker density of the colloids in the crystal, either a homogeneous sphere model or an inhomogeneous core-shell model was used to describe the form factor of the investigated microgel systems in the crystalline state. In the case of an inhomogeneous core-shell model, a model with an algebraic density profile $\phi(r) = r^{-\alpha_{Scatter}}$ was applied. Eq. 2.36 gives a detailed description of this density profile:

$$\phi(r) = \begin{cases} \phi_c, & 0 \leq r < R_{hom} \\ \phi_s = \phi_{cs} \left(\frac{r}{R_{hom}} \right)^{-\alpha_{Scatter}}, & R_{hom} \leq r < R_{total} \\ 0, & R_{total} \leq r \end{cases} \quad (2.36)$$

R_{hom} denotes the radius of the core, R_{total} is the overall core-shell particle radius and $\alpha_{Scatter}$ describes the algebraic density decay. ϕ_c gives the volume fraction of the inner volume element with a homogeneous density (core) and ϕ_s characterizes the volume fraction of the shell with a decaying density profile between R_{hom} and R_{total} . ϕ_{cs} is the volume fraction of the shell at the core-shell interface.^[161,162] ϕ_c and ϕ_s are related to the scattering length of the core, b_c , and shell, b_s , by eq. 2.37 and 2.38:

$$b_c = (b_c^0 - b_{solvent})\phi_c \quad (2.37)$$

$$b_s = (b_s^0 - b_{solvent})\phi_s \quad (2.38)$$

Here, b_c^0 is the scattering length of the pure core material and b_s^0 is the scattering length of the pure shell material. $b_{solvent}$ is the scattering length of the solvent. Assuming $\alpha_{Scatter} = 0$ this model reduces to a core-shell model with a homogeneous shell of constant density. In order to further simplify the model, two other parameters have to be considered: p which is the ratio R_{hom}/R_{total} and $\eta_{core-corona}$ that indicates the contrast ratio of the core and corona at the core-corona interface. If additionally both, $p=1$ and $\eta_{core-corona}=1$, a further reduction to a homogeneous sphere model, that describes a spherical particle with a homogeneous density profile, takes place.^[161]

For the analysis of the Bragg peaks, a normalized Gaussian peak shape function was used. This function is suitable if the peak width are specified by limited domain sizes or coherence lengths. Finite peak widths result from limited coherence. The latter one is typically related to limitations in the instrumental resolution (variance of angle and wavelength, finite detector resolution, sample aperture) and lattice imperfections (finite domain sizes, defects). For the description of these coherence limitations, the longitudinal coherence length l_l and transversal coherence length l_t are introduced. Analyzing the longitudinal (δ_{G_q}) and azimuthal (δ_{G_ψ}) peak widths allows to determine the corresponding

domain size D_l or D_Ψ and coherence lengths l_l or l_t , respectively.^[159]

$$D_l = \frac{4}{\delta_{G_q}} = l_l \quad (2.39)$$

$$D_\Psi = \frac{4}{\delta_{G_\Psi}} = l_t \quad (2.40)$$

Furthermore, the Debye-Waller factor $G(q)$ is considered in the simulations of the 2D scattering patterns. It indicates the deviation from the ideal lattice points. A Gaussian lattice point distribution function with a mean square displacement is used to describe $G(q)$.^[159]

Chapter 3

Experimental Section

3.1 Materials

Gold(III)chloride trihydrate (HAuCl_4 , Sigma-Aldrich, $\geq 99.9\%$), sodium citrate dihydrate (Sigma-Aldrich, $\geq 99\%$), sodium dodecyl sulfate (SDS, Merck, Ph. Eur.) and the functionalizing agents butenylamine hydrochloride (*B-en-A*, Sigma-Aldrich, 97%), butylamine (BA, Sigma-Aldrich, $\geq 99\%$) and 11-mercaptoundecanoic acid (MUA, Sigma-Aldrich, 95%) were used as received. Tetraethylorthosilicate (TEOS, Sigma-Aldrich, 98%), ammonium hydroxide solution (NH_3 (aqueous (aq.)), Sigma-Aldrich, 30-33%), ethanol (EtOH, Sigma-Aldrich, $\geq 99.8\%$), rhodamine B isothiocyanate (RITC, Sigma-Aldrich, mixed isomers), (3-aminopropyl)trimethoxysilane (APS, Sigma-Aldrich, 97%) and 3-(trimethoxysilyl)propyl methacrylate (MPS, Sigma-Aldrich, 98%) were also used without further purification. As monomer, cross-linker and initiator in the seeded precipitation polymerizations *N*-isopropylacrylamide (NIPAM, Sigma-Aldrich, 97%), *N,N'*-methylenebisacrylamide (BIS, Fluka, $\geq 99.7\%$) and potassium peroxydisulfate (PPS, Fluka, $\geq 99\%$) were employed as received, respectively. For the Au overgrowth, ascorbic acid (Sigma-Aldrich, $> 99\%$) and cetyltrimethylammonium chloride (CTAC, Sigma-Aldrich, 25 wt% in H_2O) were used without further purification. Methacryloxyethyl thiocarbamoyl rhodamine B (MRB, Polysciences), hydrochloric acid (HCl, Bernd Kraft, 37 %), nitric acid (HNO_3 , Merck, 65 %), deuterium oxide (D_2O , Sigma-Aldrich, 99.9% atom D), isopropyl alcohol (Fischer Chemical, 99.97%), toluene (Fluka Analytical, 99.7%), *n*-decane (Sigma-Aldrich, $\geq 99\%$) and *n*-hexane (Sigma-Aldrich, 99%) were not purified prior to use. Water (H_2O) was purified using a Milli-Q system (Millipore) which resulted in a final resistivity of 18 M Ω cm.

3.2 Synthesis

3.2.1 Synthesis of Au-PNIPAM Particles

Synthesis and Functionalization of Gold Nanoparticles. Au nanoparticles were synthesized using an established protocol according to Turkevich *et al.*^[163] All glassware was cleaned with aqua regia and subsequently thoroughly rinsed with H₂O followed by EtOH. Finally, it was dried in a compartment dryer. 500 mL of an aqueous HAuCl₄ solution ($5 \cdot 10^{-4}$ M) were heated until boiling in an Erlenmeyer flask, before 25 mL of a preheated aqueous solution of sodium citrate dihydrate (1 wt%) were added quickly under continuous stirring. Boiling was continued for 25 min. A deep red Au nanoparticle dispersion was obtained. It was allowed to cool down to room temperature upon slow stirring.

Prior to the surface functionalization, 3 mL of an aqueous SDS solution (1 mM) were added dropwise to the Au nanoparticles under gentle stirring. SDS was added to prevent aggregation during the subsequent addition of the functionalization agent and to support colloidal stability during the following centrifugation cycles. After 20 min of stirring, the respective functionalizing agent was added. Typically, B-*en*-A was used to functionalize the Au nanoparticles. Therefore, 1.63 mL of an ethanolic B-*en*-A solution (1.4 mM) were added dropwise to the Au nanoparticle dispersion and stirred for another 20 min. Finally, the dispersion was concentrated and purified via centrifugation (1065 rcf, 14 h).

Additionally, the encapsulation was tested under the use of differently functionalized Au nanoparticles. Apart from B-*en*-A, functionalization with BA and MUA was performed. Moreover, Au nanoparticles without further functionalization, i.e., with citrate at their surface were employed. The functionalization with BA was conducted in the same manner as with B-*en*-A. In order to functionalize the particles with MUA, 15 mL of MUA solution (1 mM, isopropyl alcohol) were added to 500 mL of the citrate stabilized Au nanoparticle dispersion under vigorous stirring. Then, the pH was decreased to 1 by dropwise addition of HCl solution (1 M, aqueous) while stirring. This resulted in the sedimentation of the nanoparticles. The ongoing separation process was allowed to proceed for 12 h. Subsequently, the clear and colorless supernatant was discarded. The redispersion of the sediment was performed in 500 mL of H₂O and the pH was increased to 10 by dropwise addition of NaOH solution (0.5 M, aqueous). The precipitation and redispersion procedure were repeated once.

Seeded Precipitation Polymerization. The encapsulation of the functionalized Au nanoparticles was performed following a previously published protocol.^[55] The polymerizations were carried out in a three-neck round-bottom flask (1 L). The reaction setup was equipped with a reflux condenser and a magnetic stirrer. Typically, NIPAM and BIS were dissolved in H₂O in the flask at room temperature while continuous stirring. After-

wards, the clear, colorless solution was heated to 70°C while it was purged with nitrogen to remove oxygen from the reaction mixture. The solution was equilibrated at 70°C for 20 minutes. Then, the desired volume of a stock solution of functionalized Au nanoparticles was added dropwise. The reaction mixture was equilibrated for another 15 minutes. Subsequently, the polymerization was initiated by fast addition of the respective mass of PPS dissolved in 1 mL of H₂O. Within the first 15 min, after initiation the clear, red particle dispersion started to turn turbid. The reaction was allowed to proceed for 2 h. Finally, it was cooled to room temperature. The used quantities of chemicals for the synthesis of different Au-PNIPAM particles are summarized in Table 3.1.

Table 3.1: Quantities of NIPAM, BIS, PPS and Au seed stock solution as well as the concentration of Au⁰ of the seed solution for the preparation of different Au-PNIPAM particles.

CS system	V(H ₂ O) [mL]	m(NIPAM) [mg]	m(BIS) [mg]	c(Au ⁰) [mmol/L]	V(Au) [mL]	m(PPS) [mg]
Au _{citrate} -PNIPAM						
Au _{MUA} -PNIPAM	25	57	12	17	0.34	0.5
Au _{BA} -PNIPAM						
Au _{B-en-A} -PNIPAM						
Au _{B-en-A} -PNIPAM variation of the seed concentration	25	57	12	17	0-1.01	0.5
C ₁₅ S _{12.0} (10%)	750	849	116	26	6.84	15
C ₁₅ S _{15.7} (10%)	500	1132	154	26	4.50	10
C ₁₅ S _{16.2} (10%)	600	1697	231	25	6.70	12
C ₁₅ S _{16.5} (10%)	500	1697	231	23	5.22	10
C ₁₅ S _{12.5} (15%)	500	567	116	26	4.52	10
C ₁₅ S _{14.2} (15%)	500	1132	231	9	13.83	10
C ₁₅ S _{17.9} (15%)	500	1697	349	29	4.05	10
C ₁₅ S _{11.2} (25%)	700	792	270	19	8.50	14
C ₁₅ S _{14.6} (25%)	600	1697	578	23	7.23	12
C ₁₅ S _{14.7} (25%)	500	1132	385	15	7.80	10
C ₁₅ S _{16.0} (25%)	500	1697	578	23	5.19	10

Purification of the particles was conducted via centrifugation at 8422 rcf until the supernatant was clear (duration: 2-3 h). Centrifugation and redispersion of the residue in water were repeated three times. The final residues were redispersed in 5 mL of water and freeze-dried.

The reaction batches resulting in Au_{citrate}-PNIPAM, Au_{MUA}-PNIPAM, Au_{BA}-PNIPAM and Au_{B-en-A}-PNIPAM particles were prepared with differently functionalized Au nanoparticles. These experiments were performed in order to investigate the influence of the

functionalizing agent of the Au seeds on the encapsulation reaction. In these syntheses 340 μL of each differently functionalized Au seed solution ($c(\text{Au}^0) = 0.017 \text{ mol/L}$) were used. In addition, the influence of the Au seed concentration was investigated. Therefore, different volumes of the seed solution ($c(\text{Au}^0) = 0.017 \text{ mol/L}$) between 0 and 1013 μL were added. Here, Au nanoparticles functionalized with B-*en*-A were employed. The volumes and masses of chemicals for these syntheses are also listed in Table 3.1.

To study the crystallization of these Au-PNIPAM particles, large particle quantities were required. Therefore, larger batches were synthesized (500 to 750 mL, see Table 3.1). The synthesis procedure was similar to the small reaction batches. The quantities of the required chemicals for these syntheses are also included in Table 3.1. In these Au-PNIPAM syntheses, B-*en*-A functionalized Au nanoparticles were added to the reaction mixture. Throughout this thesis the following notation for the CS particles was used: $C_\sigma S_{\lambda_b}(X\%)$. Here, σ gives the diameter of the core. λ_b represents the shell-to-core ratio in bulk which is the quotient of the overall hydrodynamic diameter, $\lambda_b\sigma$, at ambient temperature divided by σ . $X\%$ indicates the nominal cross-linker content in mol% which refers to the employed concentration of NIPAM.

***In Situ* Monitoring of the Polymerization by LS.** A dustfree cylindrical quartz cuvette was filled with 1 mL of an aqueous NIPAM-BIS mixture ($c(\text{NIPAM}) = 0.01 \text{ M}$, 15 mol% BIS referred to $n(\text{NIPAM})$). This solution was degassed with nitrogen for 5 min. Subsequently, 14 μL of a B-*en*-A functionalized gold seed stock solution ($c(\text{Au}^0) = 0.017 \text{ M}$) were added. After mixing, the cuvette was placed in the decalin bath of the light scattering setup. The sample was allowed to equilibrate for 25 min at 70°C. In order to investigate the hydrodynamic dimension and the scattering intensity of the Au nanoparticles in the homogeneous monomer solution, intensity-time autocorrelation functions were measured at a scattering angle of 60°. Data for a single measurement was acquired for 15 s which corresponds to a time scale which is just long enough to guarantee convergence of R_h which was determined using live cumulant analysis. Afterwards, the sample was removed from the decalin bath and the initiator solution (0.5 mg of PPS in 68 μL of water) was added rapidly. After mixing and purging the solution quickly, it was returned to the bath and autocorrelation functions were recorded using the described settings for 1.2 h. After the LS measurements, the reaction mixture was allowed to cool to room temperature.

***In Situ* Monitoring of the Polymerization by UV-vis Absorbance Spectroscopy.** 1 mL of an aqueous solution containing NIPAM ($c(\text{NIPAM}) = 0.01 \text{ M}$) and BIS (15 mol% referred to $n(\text{NIPAM})$) was filled in a quartz cuvette with a light path of 1 cm. The solution was purged with nitrogen for 5 min. Next, it was equilibrated at 70°C for 10 min in the sample holder of the UV-vis spectrometer. A background spectrum was

recorded. Subsequently, 14 μL of a B-*en*-A functionalized Au nanoparticle stock solution ($c(\text{Au}^0) = 0.017 \text{ M}$) were added. After mixing the reaction mixture, a spectrum was measured. Figure 3.1 shows the recorded spectrum of the Au nanoparticles in the aqueous NIPAM-BIS mixture (solid black line) as compared to the Au nanoparticle spectrum in water (dashed red line). The spectra agree well highlighting that the Au nanoparticles were colloidally stable in the reaction medium and that aggregates were not present. Further, the LSPR position was not influenced by the presence of the monomer and the cross-linker. This indicates that the average refractive index of pure water and the reaction medium are similar. Afterwards, the reaction was initiated adding 0.5 mg of PPS dissolved in 68 μL of water rapidly. Mixing and purging with nitrogen was conducted. Subsequently, spectra were recorded in intervals of 20 s. After 1.65 h the reaction was aborted and allowed to cool to room temperature.

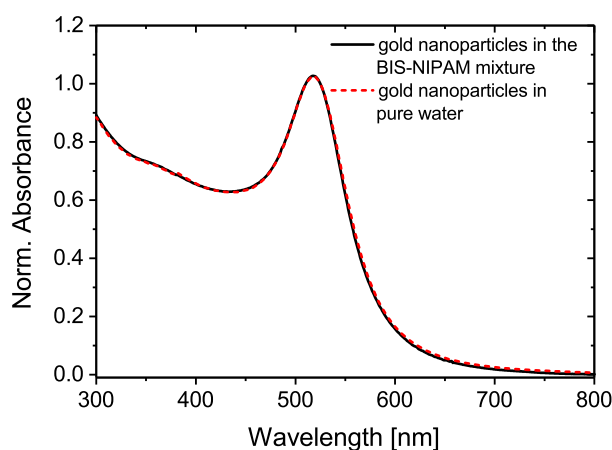


Figure 3.1: UV-vis absorbance spectra of the Au nanoparticles in the reaction medium with NIPAM and BIS (solid black line) and in aqueous medium (dashed red line). For better comparison, the two spectra were normalized to the absorbance at the plasmon resonance.

Semi-Batch Precipitation Polymerization. Au-PNIPAM particles with thick polymer shells were synthesized in a semi-batch fashion, i.e., by conducting the reaction in several polymerization steps. Initially, experiments that aimed for the formation of CS particles with thick polymer shells in a single polymerization step were performed. Here, purely organic microgel particles or aggregates were formed. Both observations are related to the presence of high monomer quantities during the polymerization. In order to circumvent these issues, several smaller monomer additions were conducted to prepare CS particles with thick shells. First, this protocol follows exactly the same procedure of the seeded precipitation polymerization as described previously. The mass of monomers and of the initiator used for the basis reaction which refer to a total volume of water of 50 mL are summarized in Table 3.2.

Table 3.2: Masses of monomers and of the initiator for the semi-batch synthesis of $C_{15}S_{31.5}(15\%)$ particles.

Synthesis step	m(NIPAM) [mg]	m(BIS) [mg]	m(PPS) [mg]
basis reaction	56.6	11.6	1
addition step 1	339.5	69.0	1.2
addition step 2	390.6	80.9	1.4
addition step 3	452.5	92.5	1.6

NIPAM and BIS were dissolved in water in a three-neck round-bottom flask equipped with a reflux condenser and magnetic stirring. 468 μL of a B-*en*-A functionalized Au seed solution with a concentration of Au^0 of 0.029 mol/L were added to the reaction mixture. After initiation, three sequential monomer additions were conducted in a semi-batch fashion as follows: 45 min after initiation, first a respective mass of BIS and afterwards a respective mass of NIPAM, both dissolved in 5 mL of water, were added dropwise. Then, 2.5 mL of a MRB solution (2.3 mg in 10 mL of water) were filtered using a 5 μm PTFE filter (Rotilabo, Carl Roth) and added dropwise to the reaction mixture within 5 min. During these additions, the reaction mixture was constantly purged with nitrogen. Subsequently, a respective amount of PPS, dissolved in 1 mL of water, was added quickly to start the polymerization. The reaction was allowed to proceed for 45 min until the next addition of reactants was conducted following the same procedure. In Table 3.2 the respective masses of the required chemicals of the different synthesis steps are listed. The volume of the MRB solution was kept constant in each addition step. As soon as the last initiation was performed, the synthesis was allowed to proceed for 2 h. After cooling to room temperature, the reaction mixture was purified by centrifugation at 8422 rcf until a clear supernatant was obtained (duration: 1.5 h). The residual particles were redispersed in water. In total, three centrifugation cycles were performed. The synthesis yielded the Au-PNIPAM particles $C_{15}S_{31.5}(15\%)$.

Post-Modification of Gold Cores. For the post-modification of the gold cores a recently published protocol was used.^[96] An aqueous 4 wt% precursor dispersion containing Au-PNIPAM particles $C_{15}S_{31.5}(15\%)$ (synthesis see previous paragraph) was prepared. Next, 10 mL of the precursor dispersion were diluted 1 : 1 with 10 mL of a CTAC solution (100 mM). Additionally, 800 mL of a 5 mM CTAC solution were added to the diluted precursor dispersion under stirring in a 3 L beaker. Subsequently, the reducing agent (ascorbic acid) as well as the feed solution (HAuCl_4 (0.5 mM) & CTAC (4.75 mM)) were added to this precursor dispersion at a ratio of ascorbic acid/ HAuCl_4 of 1.3. First, 8.3 mL of a freshly prepared solution of ascorbic acid (10 mM) were added. After that,

128 mL of the feed solution were added dropwise while constant stirring. Depending on the desired diameter of the Au nanoparticle cores the growth procedure was repeated. For this purpose, the reaction proceeded for 20 minutes until the next growth step was performed using the same amounts of ascorbic acid and feed solution. In the case of the $C_{15}S_{31.5}$ (15%) particles, 7 additions were performed. Purification was conducted by centrifugation at 3740 rcf until a clear supernatant was received. After removing the supernatant, the residue was redispersed in water. Then, centrifugation and redispersion were repeated three times. Finally, the particles were dialyzed for 7 days at 40°C in order to remove residual CTAC. The Au core overgrowth of the $C_{15}S_{31.5}$ (15%) Au-PNIPAM particles yielded the $C_{71}S_{6.6}$ (15%) particles.

Dissolution of the Au Nanoparticle Cores. To compare the crystallization of microgel particles with and without Au nanoparticle core, the Au cores of Au-PNIPAM particles ($C_{15}S_{16.2}$ (10%) and $C_{15}S_{14.6}$ (25%) in Table 3.1) were dissolved. Therefore, the respective aqueous particle dispersions were diluted to 0.25 wt%. The dissolution was performed with aqua regia that was prepared by mixing 7.5 mL H_2O , 12 mL HCl and 4 mL HNO_3 . 120 drops of aqua regia were added to 20 mL of the Au-PNIPAM dispersion. Within 15 minutes, the initial reddish color stemming from the LSPR of the Au cores disappeared indicating the dissolution of the Au cores. After shaking the dispersion for 2 h, it was purified by centrifugation (8422 rcf, 1.5 h). The supernatant was removed and the residue was redispersed in water to return to a neutral pH. This procedure was repeated twice. The last redispersion step was performed in D_2O . Subsequently, the samples were centrifuged at least twice and redispersed in D_2O . The pitted counterparts of the $C_{15}S_{16.2}$ (10%) and $C_{15}S_{14.6}$ (25%) particles are referred to as $C_dS_{16.2}$ (10%) and $C_dS_{14.6}$ (25%) particles.

3.2.2 Synthesis of SiO_2 -PNIPAM Particles

Synthesis and Functionalization of SiO_2 Nanoparticles. Dye-labeled SiO_2 particles were synthesized on the basis of a reported protocol.^[164] The functionalization of the dye molecules was performed prior to the SiO_2 synthesis. Therefore, the respective amount of APS was added to the ethanolic dye solution of RITC (10 mM) and stirred in the dark for 2 h. To guarantee covalent binding between functionalizing agent and dye molecules, APS was added in 10-fold excess. A certain volume of functionalized dye solution was diluted with ethanol (1:5 in the case of C_{125} and C_{351} , 1:1.5 in the case of C_{362} silica particles). The well-known Stöber method was used to prepare the SiO_2 particles.^[165] Briefly, EtOH, NH_3 (aq., 30-33%) and water were heated to 50°C under constant stirring in a three-neck round-bottom flask and equilibrated for 20 min (solution 1). In the meantime, a mixture of EtOH and TEOS was prepared which was equilibrated at 50°C while stirring (solution 2). After fast addition of solution 2 to solution 1, the clear reaction

mixture started to turn turbid indicating the formation of SiO₂ nuclei. At this point the dye solution was added dropwise within 5-15 minutes depending on the speed of the particle formation. The reaction rate passes a maximum with higher quantities of water, TEOS and NH₃ (aq.).^[166] The added volumes of diluted dye solution were: 2 mL (C₁₂₅), 2.5 mL(C₃₅₁) and 3.2 mL(C₃₆₂). The reaction proceeded for 24 h at 50°C. After that, it was allowed to cool to room temperature. Table 3.3 summarizes the used quantities of EtOH, NH₃ (aq., 30-33%), H₂O and TEOS which were required for the syntheses of C₁₂₅, C₃₅₁ and C₃₆₂.

Table 3.3: Respective quantities of EtOH, NH₃ (aq., 30-33%), H₂O and TEOS to synthesize the silica particles C₁₂₅, C₃₅₁ and C₃₆₂.

Silica particles	Solution 1			Solution 2	
	V(EtOH) [mL]	V(NH ₃ , aq.) [mL]	V(H ₂ O) [mL]	V(EtOH) [mL]	V(TEOS) [mL]
C ₁₂₅	125	10	/	5	20
C ₃₅₁	56.4	27.45	16.05	10.05	40.2
C ₃₆₂	112.8	54.9	32.1	20.1	80.4

The silica particles C₃₆₂ were overgrown by dropwise addition of 1.037 mL of water and 6.386 mL of TEOS. Prior and during these additions, the pH of the reaction mixture was adjusted to 9-10 by NH₃ (aq., 30-33%). In total four additions in intervals of 24 h were conducted. The first addition was performed at 50°C whereas the other additions were conducted at room temperature. The overgrowth of the SiO₂ particles C₃₆₂ resulted in the particles C₄₈₆. All synthesized SiO₂ particles were purified twice by centrifugation until a clear supernatant was obtained. The relative centrifugal force was adjusted depending on the particle size (90 min at 2599 rcf for C₁₂₅, 20 min at 1664 rcf for C₃₅₁/C₄₈₆). The supernatant was removed and redispersion was performed in EtOH. The allyl-functionalization of the different SiO₂ particles was conducted as follows: The obtained particles that were dispersed in EtOH were diluted to a volume which corresponded to half of the initial reaction volume in a two-neck round-bottom flask. The pH of the dispersion was adjusted to 9-10 by dropwise addition of NH₃ (aq., 30-33%) under constant stirring. MPS was used to functionalize the particles with an allyl group. The required volume of MPS, that referred to a surface density of 1 molecule per 40 Å², was dissolved in 1 mL of ethanol and added dropwise to the SiO₂ dispersion. The mixture was stirred for 24 h. Then, it was refluxed for 1 h to guarantee covalent binding of the functionalizing molecules. Afterwards, the dispersion was allowed to cool to room temperature. In the meantime, an ethanolic SDS solution (pH=9-10, adjusted by addition of NH₃ (aq., 30-33%)) was dropped to the suspension in order to stabilize the functionalized SiO₂ par-

ticles. The final SDS concentration in the reaction mixture was 0.2 mM. Typically the SiO₂ particles were purified three times using centrifugation (90 min at 2599 rcf for C₁₂₅, 20 min at 1664 rcf for C₃₅₁/ C₄₈₆). The clear supernatant was removed and the particles were redispersed in EtOH.

Seeded Precipitation Polymerization. Similar to the preparation of Au-PNIPAM particles, free radical seeded precipitation polymerization was used to prepare SiO₂-PNIPAM particles. The reaction was conducted in a three-neck round-bottom flask that was equipped with a magnetic stirrer and a reflux condenser. The respective amounts of NIPAM, BIS and SDS (0.2 mM) were dissolved in a certain volume of water while stirring. The reaction mixture was heated to 70°C and degassed using nitrogen. Equilibration was performed for 20 min. Next, the respective volume of functionalized SiO₂ particles that was dispersed in a small volume of EtOH was added. The reaction mixture equilibrated for another 15 min. Then, PPS dissolved in 1 mL of water was added. The reaction was allowed to proceed for 2 h and to cool to room temperature afterwards. Purification was performed via three centrifugation steps. The particles were centrifuged until a clear supernatant was received (90 min at 2599 rcf). Redispersion was conducted in water. Table 3.4 shows the respective amounts of chemicals needed for the encapsulation of the SiO₂ particles C₁₂₅ in cross-linked PNIPAM shells.

Table 3.4: Respective masses and volumes for the preparation of the different SiO₂-PNIPAM particle batches with varying shell thicknesses, i.e., shell-to-core ratios. All batches were synthesized using the silica particles C₁₂₅.

CS system	V(H ₂ O) [mL]	m(NIPAM) [mg]	m(BIS) [mg]	V(SiO ₂) [μL]	m(PPS) [mg]
C ₁₂₅ S _{1.4} (5%)	40	45	3	1125	4
C ₁₂₅ S _{2.0} (5%)	40	91	6	1125	4
C ₁₂₅ S _{2.2} (5%)	40	136	10	1125	4
C ₁₂₅ S _{3.0} (5%)	20	113	8	438	2
C ₁₂₅ S _{3.4} (5%)	20	113	8	250	2

The particle concentration of the stock dispersion of functionalized C₁₂₅ particles was 0.197 μM. It was determined in the following way: Using the particle volume and the density of SiO₂ (2.2. g/mL at 25°C), the mass of a single silica particle was calculated. As the mass concentration of the seed stock dispersion was available, the number of particles per volume and thus the particle number concentration was accessible.

Semi-Batch Seeded Precipitation Polymerization. Another series of SiO₂-PNIPAM particles with larger SiO₂ cores was also synthesized via seeded precipitation polymerization. In similarity to the Au-PNIPAM particles with thick polymer shells, a semi-batch fashion method was used to avoid agglomeration and the formation of purely organic microgel particles during the synthesis. The first steps of the semi-batch synthesis were exactly the same as in the standard synthesis route that was used to encapsulate the smaller SiO₂ particles (see previous paragraph). Then, 45 min after the initiation, sequential additions of SDS, NIPAM, BIS and PPS were conducted to grow larger shells. First, the respective amount of SDS in 2 mL water was added dropwise to the reaction mixture to stabilize the particles during the monomer additions. The respective amount of BIS was dissolved in 2 mL of water. NIPAM was dissolved in 4 mL of water. Then, the addition of the NIPAM solution was started using a syringe pump. This addition was performed within 30 min. 1 mL of the BIS solution was added dropwise starting simultaneously with the NIPAM addition. Afterwards, the polymerization was initiated with the respective amount of PPS dissolved in 1 mL of water. Next, the residual amount of BIS solution was added dropwise. 45 min after initiation the next monomer addition was performed in the same manner. The respective amounts of chemicals for the basis reaction and the addition steps are listed in Table 3.5 for C₃₅₁S_{1.5}(5%), C₃₅₁S_{2.2}(5%) and C₃₅₁S_{2.9}(5%). The particle concentration of the stock dispersion of the functionalized silicas C₃₅₁ was 0.0184 μM.

Apart from these CS particles, another batch of SiO₂-PNIPAM particles (C₄₈₆S_{1.7}(5%)) was synthesized via semi-batch fashion. These particles were employed for studies in the electric field. The reaction was performed similarly to the procedure described above. However, the respective amount of NIPAM, that was required for the addition steps, was dissolved in 5 mL of water. The cross-linker BIS was dissolved in 3 mL of water. The additions were conducted one hour after initiation. First, the SDS solution, then the BIS solution and finally the NIPAM solution were added dropwise before initiation. The respective quantities for this synthesis are as well summarized in Table 3.5. The particle concentration of the stock dispersion of the functionalized SiO₂ particles C₄₈₆ was 0.009 μM.

Table 3.5: Respective quantities of H₂O, NIPAM, BIS, SDS, silica seed stock dispersion and PPS for the synthesis of the SiO₂-PNIPAM particles C₃₅₁S_{1.5}(5%), C₃₅₁S_{2.2}(5%), C₃₅₁S_{2.9}(5%) and C₄₈₆S_{1.7}(5%).

Synthesis step	V(H ₂ O) [mL]	m(NIPAM) [mg]	m(BIS) [mg]	m(SDS) [mg]	V(SiO ₂) [μL]	m(PPS) [mg]
C ₃₅₁ S _{1.5} (5%)						
basis reaction	20	67.9	4.6	1.2	1018	2
C ₃₅₁ S _{2.2} (5%)						
basis reaction	20	113.2	7.7	1.2	1018	2
addition step 1	+ 8	113.2	7.7	1.2	/	2
C ₃₅₁ S _{2.9} (5%)						
basis reaction	20	113.2	7.7	1.2	1018	2
addition step 1	+ 8	169.7	11.6	1.7	/	3
addition step 2	+ 8	226.3	15.4	2.3	/	4
addition step 3	+ 8	282.9	19.3	2.9	/	5
addition step 4	+ 8	339.5	23.1	3.5	/	6
C ₄₈₆ S _{1.7} (5%)						
basis reaction	50	282.9	19.3	3.6	7000	5
addition step 1	+ 10	339.5	23.1	4.3	/	6
addition step 2	+ 10	396.1	27.0	5.0	/	7
addition step 3	+ 10	452.6	30.8	5.8	/	8

3.3 Sample Preparation

3.3.1 Samples for LS

The samples were measured in cylindrical quartz glass cells (Hellma Analytics) with a diameter of 1 cm. The cells were typically cleaned using ultrasonication treatments at low power (max. 50%) and 60°C for 20 min in different solutions/solvents (dilute Hellmanex solution, EtOH, acetone). Afterwards, the cells were rinsed with freshly distilled acetone using a home-built distillery setup to ensure that dust is fully removed. After drying, the cells were filled with dilute particle dispersions in a laminar flowbox to exclude contamination. Typically, the samples were filtered using a PTFE filter (Rotilabo, Carl Roth) with a pore size of 5 μm to remove dust or aggregates from the dispersions. The sample dilution was chosen so that a sufficient measurement signal was achieved and at the same time multiple scattering was avoided ($\phi_{eff} < 10^{-4}$).

3.3.2 Samples for SANS

The particles were dispersed in D₂O (Sigma-Aldrich, 99.9% atom D) to get a sufficient scattering contrast. Either freeze-dried material was dispersed in D₂O or particles from a dispersion in H₂O were centrifuged and redispersed in D₂O. In the latter case, centrifugation and redispersion were at least performed twice. The final dispersions were filled in quartz cells (Hellma Analytics) of 1 mm path length.

3.3.3 Crystalline Samples for UV-Vis Spectroscopy and SANS

Aqueous particle dispersions between 6 and 20 wt% were prepared. In Figure 3.2 A a quartz glass cuvette (Hellma Analytics) that was typically used for sample preparation is depicted. It consists of two halves. One half acts as cavity with a depth of 100 μm . The other half is a fully plane lid. Typically, an aqueous dispersion of CS particles was heated above the VPTT of the particles using a water bath at around 60°C. This reduced the viscosity of the dispersion and allowed to fill the cuvettes more easily. 40 μL of this particle dispersion were filled in the cavity and closed with the lid. This sandwich was placed in a cuvette holder. Subsequently, the sample was annealed in a compartment dryer at approximately 60°C. Annealing at these temperatures, i.e., above the VPTT of cross-linked PNIPAM, induces shrinkage of the particles due to the release of water. While the sample was allowed to cool to room temperature, it swelled again due to water uptake. During this process steric forces cause the particles to crystallize. In Figure 3.2 B a representative sample prior (non-crystalline state) and after (crystalline state) annealing is shown.

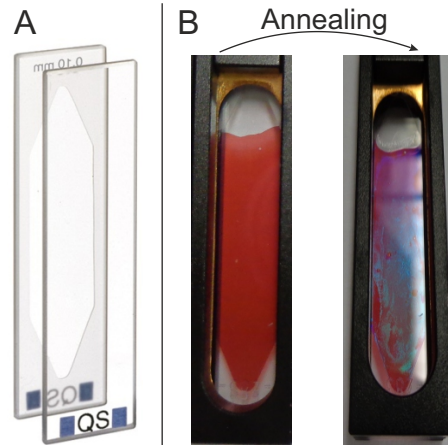


Figure 3.2: A. Two halves of a quartz glass cuvette with a cavity of $100\ \mu\text{m}$. Reprinted from reference^[167]. B. Quartz glass cuvette filled with an aqueous dispersion of Au-PNIPAM particles before (non-crystalline state) and after (crystalline state) the annealing of the sample.

3.3.4 Samples for CLSM

Crystalline Samples for CLSM. A $120\ \mu\text{m}$ thick adhesive spacer with a circular sample chamber (GRACE Bio-Labs, Secure-SealTM, diameter of the chamber: $9\ \text{mm}$) was fixed on a microscopy glass slide. About $7\ \mu\text{L}$ of an Au-PNIPAM particle dispersion ($\text{C}_{71}\text{S}_{6.6}$ (15%)) were filled in the chamber. Dispersions with weight concentrations between 5.6 and 9.9 wt% were investigated. Subsequently, a cover slip was placed on top of the spacer and the sample was investigated in the CLSM. To avoid contamination of the sample, the glass slides and cover slips were purified prior to the sample preparation. The glass ware was cleaned in a 1 wt% solution of Decon 90[®] using a 20 min ultrasonic treatment at low power (50%) and room temperature. Afterwards, the glassware was thoroughly rinsed with water and dried by a nitrogen jet. The annealing of the prepared sample was performed as described in Section 3.3.3 using a compartment dryer.

Samples for Electric Field Experiments. To investigate the influence of an alternating electric field on the particle dispersions, suitable sample cells were prepared. In these cells about $7\ \mu\text{L}$ of a particle dispersion were placed between two indium-tin oxide (ITO) coated cover slips (Diamond Coatings, $30\text{-}60\ \Omega/\text{sq.}$, $18 \times 18\ \text{mm}^2$, thickness 1.5, i.e., ≈ 0.16 to $0.19\ \text{mm}$). A multimeter was used to ensure that the sample was in contact with the conductive sides of the ITO slips. The distance between the ITO glasses was defined by an adhesive spacer with a circular chamber for the sample (GRACE Bio-Labs, Secure-SealTM, diameter of the chamber: $9\ \text{mm}$, thickness: $120\ \mu\text{m}$). $7\ \mu\text{L}$ of an aqueous SiO_2 -PNIPAM ($\text{C}_{486}\text{S}_{1.7}$ (5%)) dispersion (0.5 to 7.5 wt %) were filled in the sample chamber. Prior to the experiments, the dispersion was deionized for at least one week. Around 10 wt% of the resin Amberlite[®] IRN 150 (Sigma-Aldrich, hydrogen and hydroxide form, matrix

styrene/divinylbenzene (gel), 22-26 mesh) were added to the particle dispersion. During the deionization process the samples were shaken slowly. The resin was exchanged every day. After filling the chamber with the deionized sample, it was closed by another ITO cover slip. Both ITO cover slips were connected to a wideband amplifier (Krohn-Hite Corporation, Model 7602M) by thin wires. The amplifier was further connected to a wave generator from AIM-TTI instruments (Model TG315). The field direction in these experiments was perpendicular to the xy -image plane. A constant frequency of 100 kHz was applied. The samples were investigated at different voltages using CLSM. The setup is schematically illustrated in Figure 3.3.

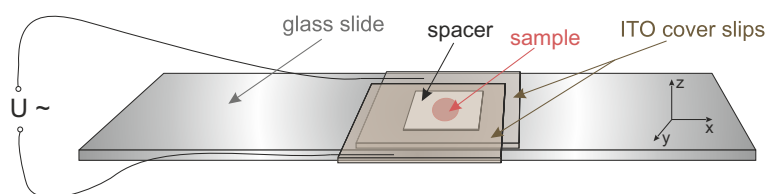


Figure 3.3: Schematic setup of a sample cell for experiments in an electric field. An aqueous dispersion of CS particles is filled in the sample chamber between the two ITO cover slips. An alternating electric field is applied between the cover slips. The z -direction corresponds to the direction of the electric field lines. The xy -plane is parallel to the cover slips. Adapted from reference^[168].

Samples for Confocal Differential Dynamic Microscopy. The respective particle dispersions were prepared from freeze-dried material of SiO_2 particles ($\text{C}_{351}\text{S}_{2.9}(5\%)$) by redispersion in water. To disperse them thoroughly, they were first ultra-sonicated for 10 minutes and subsequently mixed for about 12 h at 20°C using an Eppendorf ThermoMixer. Particle dispersions with weight concentrations between 0.3 and 8.4 wt% were prepared. The dispersions were filled into hollow rectangular glass capillary tubes (VitroCom) with dimensions of $100\ \mu\text{m} \times 50\ \text{mm} \times 2\ \text{mm}$ in thickness, length and width, respectively. Prior to filling, these capillary tubes were cleaned by rinsing them with EtOH, isopropanol and water. After filling the tubes, an UV-curable glue (Norland Optical Adhesive NOA 81) was used to seal the ends of the capillary and to attach it to a cover glass slide.

Monolayer Preparation for CLSM. The preparation of custom-made sample cells for the investigation of the interfacial monolayers was performed as follows: A thin cover glass (thickness 0, i.e., ≈ 0.085 to $0.13\ \text{mm}$, Thermo ScientificTM) with a hole (diameter: 10 mm) was fabricated. The hole was cut using a Hunst laser cutter equipped with a CO_2 laser with a wavelength of 10600 nm. This fabricated glass slide and an aluminium ring (inner diameter: 20 mm) were glued to another cover glass (diameter: 40 mm).

This sample construction allowed to obtain interfaces at a distance of 180 to 230 μm from the bottom cover glass. In order to prepare the Gibbs monolayers, aqueous particle dispersions with concentrations of $3 \cdot 10^{-3}$ wt% were filled into this cavity of the sample cells and an oil phase was added on top to establish an oil-water interface. The $\text{C}_{351}\text{S}_{2.9}$ (5%) particles were used for these experiments. The particles from the water phase adsorbed spontaneously at this interface resulting in a monolayer. Further sealing of the sample cell was realized by a cover glass slide to prevent convection.

3.3.5 Samples for EM and AFM

Either drop-casting, spin-coating, floating or LB depositions were used to prepare samples that were studied by SEM or AFM. In the case of drop-casting, a drop of a dilute particle dispersion was placed on top of a cleaned silicon wafer. The sample was dried until the solvent was fully evaporated.

Spin-coating was performed using a spin-coater from Speciality Coating Systems (type G3P-8). A dilute particle dispersion was spin-coated increasing the rotation speed from 1000 to 3000 rpm (settings: 1000 rpm for 2 s, 2000 rpm for 60 s using a ramp of 25.5 s and 3000 rpm for 30 s using a ramp of 2 s) on a silicon wafer.

In a floating experiment an ethanolic dispersion of particles was assembled at an air-water interface in a crystallizing dish. The water phase contained 0.05 mM SDS. The freely floating monolayers at the interface were transferred onto a silicon wafer and dried using a heatgun afterwards.

For the preparation of density gradients on a single substrate LB depositions were used. In Figure A.1 in the Appendix a photo of the setup is depicted. A custom-made LB trough made from teflon which was equipped with two moveable Delrin[®] barriers was used. The maximum and minimum surface areas were 197.5 cm^2 (barriers fully opened) and 57.5 cm^2 (barriers fully closed). The particle gradients were produced on a silicon substrate (1 x 2 cm^2) which was mounted on a moveable Teflon holder using a Delrin[®] screw. The function of this holder was to adjust the position of the substrate at the interface during the experiment, i.e., while the barriers moved closer. The substrate was fixed with an angle of 30° relative to the horizontal interface. Prior to the experiment, the wafer was cleaned by three ultrasonication treatments of 15 min in different solvents (toluene, isopropanol, H_2O). In order to remove remaining organic impurities and to hydrophilize the surface for the deposition experiment, the wafer was treated in an UV-ozone cleaner (Bioforce Nanosciences). In the beginning of each deposition experiment, the two barriers were fully opened and water was filled until the edge at which the oil-water interface is formed. Then, a Wilhelmy plate (1 x 2 cm^2) was mounted in a way so that one third of it was covered by water. Subsequently, the surface pressure was set to zero and a test run was conducted. The trough area was compressed

by the two barriers while the surface pressure was constantly checked to ensure a value below 0.2 mN m^{-1} . Higher surface pressures indicate the presence of contaminants which could affect the experiment. In this case, the water in the trough was removed using a pipette tip (Tip One) connected to a vacuum pump (Vacuum Brand PC3000) via tubing. These test runs were repeated until the required conditions were achieved. Then, the substrate was fixed on the dipper arm which was mounted in the trough so that the upper edge of the substrate was located at the air-water interface. 100 mL of *n*-hexane were added on top of the water phase and the surface pressure was set to zero. The dispersion consisting of 1 wt% particle dispersion, water and isopropanol in a ratio 1 : 7 : 2 was injected at the oil-water interface using a 100 μL Hamilton glass syringe. Finally, the experiment was started. The barriers compressed the trough area, while the substrate was lifted and the surface pressure was measured. To prepare the mentioned particle gradients, the barrier speed was constantly at 2.3 mm min^{-1} . Simultaneously, the dipper arm that controlled the position of the silicon wafer was lifted with a speed of 0.3 mm min^{-1} . These velocities allowed that the substrate passed fully through the interface while the compression was finished simultaneously. After the experiment, the two liquid phases were removed. All parts of the setup were rinsed with H_2O and EtOH and dried with a nitrogen jet.

In order to investigate the differently prepared samples by SEM, they were sputter-coated. Therefore, the silicon wafer was mounted on a sample stub (Plano) by a conductive adhesion graphite pad (Plano). The samples were sputter-coated with a layer of 1.3 nm platinum using a Cressington HR208 sputter-coater and a Cressington mtm20 thickness controller. In this way, the conductivity of the sample was increased and accumulation of electrostatic charge could be avoided.

For the preparation of transmission electron microscopy (TEM) samples, either drop-casting or floating techniques were used. Floating was performed in the same way as for the SEM samples except for the supporting substrate which was a copper grid (200 mesh, Electron Microscopy Sciences) in this case. In case of drop-casting two methods were applied: (1) 10 μL of a dilute dispersion were directly dropped onto a copper grid and left to dry. (2) 10 μL of a dilute dispersion were allowed to rest on a copper grid for 15 min before the excess of the particle dispersion was blotted with a filter paper from the bottom side of the grid. Drying occurred in both cases at room temperature over night.

3.3.6 Samples for Cryogenic SEM

Freeze-fracture shadow-casting cryo-SEM was performed to analyze the morphology of the particles at the interface. 0.5 μL of an aqueous 0.25 wt% dispersion were dropped at the bottom part of a custom-made copper holder to obtain a macroscopically flat interface. 3.5 μL of *n*-decane were placed on top of the first droplet, so that an oil-water interface was received. Then, the sample was sealed by the top part of the copper holder. The copper holder plus content was then shock-frozen using a liquid propane jet freezer at a cooling rate of 30000 K s⁻¹ (Bal-Tec/Leica JFD 030, Balzers/Vienna). Next, the sample was fixed on a double-fracture cryo-stage under liquid nitrogen. Subsequently, the sample was transferred under inert gas into a cryo-high vacuum airlock ($< 5 \times 10^{-7}$ mbar Bal-Tec/Leica VCT010) to a precooled freeze-fracture device at -140°C (Bal-Tec/Leica BAF060 device). The samples were fractured which typically occurred at the interface. As a result, two halves were obtained. One part included the water and the other part the oil phase. Each half was partially freeze-dried at -110°C for at least 1 min to remove ice crystals as well as deposited remaining water condensation. Afterwards, the sample was sputter-coated by unidirectional deposition of tungsten at an elevation angle of 30° at -120°C until a thickness of 2 nm was achieved. Next, further tungsten deposition was performed at varying angles between 90° and 45° .

3.4 Methods

3.4.1 LS

Angular-dependent DLS and SLS measurements were conducted on a 3D goniometer setup from LS instruments (Friburg, Switzerland) that operated in 2D mode. A HeNe laser was used as light source with a wavelength of 632.8 nm. The laser had a maximal constant power of 35 mW. For the detection of the scattered light two avalanche photodetectors in pseudocross-correlation mode were used. A decalin bath acted as refractive index matching bath. Additionally, it was used to adjust the temperature that was controlled by a Pt100 thermoelement which was placed in the bath and connected to a Julabo CF31 thermostat. The accuracy of the temperature was ± 100 mK. Angular-dependent SLS measurements were performed between angles of 20° and 150° in increments of 5° . 6 measurements per angle were recorded with an acquisition time of 30 s. DLS measurements were performed in the same range of angles, but with steps of 10° . Three intensity-time autocorrelation functions per angle with an acquisition time of 60 s were measured.

For temperature-dependent DLS measurements a standard goniometer setup by ALV (Langen, Germany) was used. The data were collected at a constant scattering angle of 60° between 20 - 50°C in increments of maximum 2°C . After adjusting the temperature,

the sample was allowed to equilibrate for 20 min. The device used a HeNe laser with a wavelength of 632.8 nm and a maximal constant output power of 35 mW as light source. The matching/temperature bath was filled with toluene in this setup. A Haake C25 thermostat with a Haake F6 control unit was used to control the temperature of the Pt100 thermoelement in the toluene bath and eventually of the sample. The final temperature stability was ± 100 mK. For each temperature three autocorrelation functions were recorded with an acquisition time of 60 s. The intensity-time autocorrelation functions received by angular and temperature-dependent measurements were analyzed by inverse Laplace transformations using the software *AfterALV* (Dullware, version 1.0d). The relaxation rate was determined for each autocorrelation function. The mean relaxation rates of three measurements were used for the calculation of the diffusion coefficient for translational diffusion D_T . R_h was determined by eq. 2.17. The standard deviation of the relaxation rate was used to calculate the deviation of the hydrodynamic radius by error propagation.

In some cases DLS measurements were performed using a Zetasizer Nano ZS from Malvern Instruments (Malvern, England). This device was equipped with a 4 mW HeNe laser ($\lambda = 633$ nm) as light source. The instrument provided a temperature-control jacket for the cuvette. The detector was positioned at a scattering angle of 173° . Either temperature-dependent swelling curves or measurements at a fixed temperature were performed. Temperature-dependent measurements between 20 - 60°C in intervals of 2°C were conducted using equilibration times of at least 20 min for each temperature. Apart from the temperature-dependent measurements, DLS data was collected at a fixed temperature using this device. Typically, these measurements were conducted at 25°C . As this temperature is close to ambient temperature, shorter equilibration times of 5 min were sufficient. Typically, three autocorrelation functions with an acquisition time of 60 s were performed per temperature. The analysis of the data was conducted by the cumulant method provided by the instrument software. The standard deviation of three measurements was used as error.

3.4.2 SANS

SANS experiments were conducted at the Institut Laue-Langevin (ILL) in Grenoble using the instrument D11. The schematic setup of the D11 is depicted in the Appendix in Figure A.2. Depending on the adjusted sample-to-detector (SD) distance the neutron wavelength was either 0.6 nm (SD distance: 1.2 m, 8 m, 28 m) or 1 nm (SD distance: 39 m). To detect the scattered neutrons, a ^3He CERCA gas multi-detector with an area of 96×96 cm² and a pixel size of 0.75×0.75 cm² was used. This detector was fixed on a moveable trolley in an evacuated tube. The dilute samples were measured at SD distances of 1.2 m, 8 m, 28 m and 39 m in order to collect data over a broad q -range (0.009

- 4.340 nm^{-1}). The acquisition time was extended for larger SD distance from at least 480 s, 600 s, 900 s and 1200 s, respectively. The measurements of the dilute samples were conducted in rectangular quartz glass cuvettes (Hellma Analytics) with a light path of 1 mm. The obtained 2D detector images were isotropic. Therefore, they could be averaged radially. The software *Large Array Manipulation Program* (LAMP, Version 8.1) provided by the ILL was used to merge the radially averaged profiles. Besides, this software was used to account for D_2O and empty cell scattering of the collected data. Eventually, the merged scattering profiles were analyzed using the software *SASfit* (Version 0.94.6) by Kohlbrecher.^[157] The concentrated, crystalline samples were measured at SD distances of 28 m and 39 m. At 28 m data were acquired for at least 900 s and at 39 m for at least 1200 s. The software *Scatter* by Förster and Apostol was used to evaluate the data.^[160] The lattice plane distance of the samples was analyzed using the first maximum of the radially averaged structure factor profiles. The qualitative profile of $S(q)$ was determined in the following manner: First, the radially averaged, merged profile of a dilute sample measured at 28 m and 39 m was multiplied with a q -independent factor. This factor was adjusted until an intensity overlap with the profile of the respective crystalline sample at large q -values was achieved. Then, the profile of the crystalline sample was divided by the data of the respective dilute sample.

3.4.3 SAXS

SAXS data was collected at the European Synchrotron Radiation Facility (ESRF) in Grenoble using the beamline BM26B DUBBLE. An aqueous, concentrated dispersion of Au-PNIPAM particles ($\text{C}_{71}\text{S}_{6.6}$ (15%), 7.5 wt%) was filled in a capillary cell with inner dimensions of 100 mm x 4 mm x 0.2 mm (W3520 Vitrocom). A microradian X-ray diffraction setup (similar to the one depicted in reference^[169]) was used. An X-ray beam (13 keV) with a wavelength of 0.095 nm was focused behind the sample at a charged coupled device X-ray detector from Photonic Science (4008 x 2671 pixels, $24 \times 24 \mu\text{m}^2$). Focusing was conducted using a set of compound refractive lenses. The measurements were performed at a SD distance of 8.3 m. The described setup allowed to collect data in a q -range between 0.01 - 0.08 nm^{-1} . The orientation of the capillary cells was vertically with their long axis (100 mm), so that their short axis (0.2 mm) was parallel to the X-ray beam. In order to perform rotational scans, the samples were rotated around their long axis (vertically) from $\omega = -60^\circ$ to $\omega = +45^\circ$ in intervals of 2.5° . At $\omega = 0^\circ$ the sample was in its initial position. An exposure time of 20 s was used. The software *Fit2D* (Version V13.008) allowed to take wedges of the measured SAXS patterns in order to get profiles of the q -dependent scattering intensity along different diffraction peaks.

3.4.4 UV-Vis Spectroscopy

An Agilent 8453 spectrophotometer or a Cary 5000 UV-vis-NIR spectrophotometer (Agilent Technologies) were used to measure absorbance spectra of dilute samples. The samples were measured in quartz glass cells (Hellma Analytics) with a path length of 1 cm. Absorbance spectra of crystalline samples were either measured by an Agilent 8453 or a Jasco V-630 spectrophotometer. Temperature-dependent measurements were conducted by the Agilent 8453 spectrophotometer. This device was equipped with a temperature-controlled sample holder. The temperature was controlled by a Pt100 thermoelement that was positioned in a cuvette filled with silicon oil. The temperature was adjusted by a circulating water bath (Thermo Haake C25P). Typically UV-vis absorbance spectra were measured in a wavelength range between 190 and 1100 nm. However, in some cases spectra were recorded in a wavelength range between 200 and 2500 nm (Cary 5000).

3.4.5 CLSM

CLSM Settings for Electric Field Experiments and for Crystalline Samples. An inverted confocal laser scanning microscope (Leica DM16000) was used to investigate the phase behavior of different concentrated CS dispersions in the presence or absence of an electric field. The device was equipped with a SP5 tandem scanner in the resonant mode. Since rhodamine derivatives were incorporated in the CS particles, an excitation wavelength of 543 nm was used for the measurements. Images were recorded with a 100x immersion objective with a numerical aperture of 1.4. In the case of crystalline samples, images were recorded in the xy -plane at different z -positions (see Figure 3.3 for explanation of the coordinates) in z -steps between 0.04 to 0.13 μm . Images were acquired at least four particle diameters away from the glass slide to reduce wall effects. At lower concentration, when the particles diffused quickly, time-lapse movies were recorded. Several hundreds of frames with 512 x 512 pixels at 17 frames per second were acquired per movie. Due to the fast resonant scanner, even quickly moving particles in the fluid state could be tracked. The instrument was placed in a thermostatted encasement which allowed a temperature control with an accuracy of $\pm 0.2^\circ\text{C}$. The measurements were performed at 20°C .

CLSM Settings for CDDM Measurements. CLSM was also implemented for differential dynamic microscopy (DDM) investigations. Here a Nipkow spinning disk confocal microscope (CSU-W1, 3i) was used. This microscope included a 561 nm diode-pumped solid state laser with a power of 200 mW and a Hamamatsu Orca-flash 4.0 V2 camera. Images were recorded using a 60x oil-immersion objective with a numerical aperture of 1.4. In order to collect the DDM data, time-lapse movies containing 10000 images with 300 x 300 pixels were acquired at 66.5 frames per second. Prior to the recording of these

movies, the samples were forcefully photo-bleached until the average image intensity was constant. Measurements were performed at room temperature.

In the present work, CDDM was used to characterize the dynamics and static structure properties of CS dispersions. Typically, the time series of real-space images measured by CLSM, $I(x, y, t)$, were Fourier transformed resulting in $\tilde{I}(\vec{q}, t)$ with \vec{q} denoting the wave vector. In order to calculate the dynamic image structure function (DISF) in dependence on the lag time Δt , time- and azimuthal-average operations were performed on $\tilde{I}(\vec{q}, t)$. The calculation of the respective DISF was performed by implementing an algorithm in MATLAB[®]. In the process of calculation, a Tesla K40c graphical processing unit allowed the parallelization of the time-average operations for each lag time Δt .

CLSM Settings for Experiments at the Interface. The same confocal microscope as described in the previous paragraph was used for measurements at an oil-water interface. The confocal measurements were conducted at a hexadecane-water interface at room temperature using a 60x water-immersion objective with a numerical aperture of 1.2. Images were recorded at 7 frames per second while the working distance of the objective was 0.32 mm.

3.4.6 TEM

TEM investigations were performed using a Zeiss CEM 902 transmission electron microscope. The device operated at an acceleration voltage of 80 kV. Images were recorded in bright-field mode. Particle size distributions were obtained measuring the particle diameter at different positions of the TEM images. The diameters of 150 particles (in the case of Au cores synthesized by Turkevich protocol) and the diameter of 65 particles (in the case of overgrown Au-PNIPAM particles $C_{71}S_{6.6}(15\%)$) was analyzed using the image processing software *ImageJ* (Version 1.48v).

3.4.7 SEM

A LEO Gemini scanning electron microscope from Carl Zeiss (Germany) with a Schottky field emission cathode operating at an acceleration voltage of 3 kV was used for SEM investigations. The samples, prepared by freeze-fracture described in Section 3.3.6, were transferred to a pre-cooled (-120°C) cryo-SEM (Zeiss Gemini 1530, Oberkochen) under high vacuum ($< 5 \times 10^{-7}$ mbar) operating at an acceleration voltage of 5 kV. Both devices used an in-lens detector and/or a secondary electron detector for imaging. Particle diameter distributions were determined measuring particle dimensions at different positions of SEM images. For the SiO_2 cores C_{486} 94 particle diameters and for the SiO_2 cores C_{125}

and C₃₅₁ at least 150 particle diameters were analyzed using the software *ImageJ* (Version 1.48v).

3.4.8 AFM

AFM investigations were performed using a Bruker Icon Dimension AFM. In this thesis, the substrates carrying gradients of microstructures obtained from LB deposition experiments were characterized by AFM. Height profiles were recorded along the main axis (in the direction of the gradient) of the wafer in intervals of 1 mm. The tapping mode was used for scanning with a speed of 0.2 Hz. A Micro Cantilever from Olympus with a theoretical spring constant of 26.1 N m⁻¹ was used working at a resonance frequency of 300 kHz. AFM images with a size of 20 x 20 μm² were taken acquiring 512 x 512 pixels. The software NanoScope Analysis 1.5 from Bruker was used to flatten (1st order) the collected height profiles. This should prevent the influence of any tilt of the sample position on the sample stage.

3.4.9 ζ-Potential Measurements

A Zetasizer Nano ZS from Malvern Instruments was used to measure the electrophoretic mobility μ_e . This device was equipped with a 4 mW HeNe laser ($\lambda = 633$ nm), a jacket to adjust the temperature and a detector which was positioned at 173° relative to the incident radiation. At least three measurements of dilute, aqueous dispersions without any addition of salt were performed at 25°C. The samples were equilibrated 5 min prior to the measurement. The respective ζ-potential values were calculated using the measured electrophoretic mobilities μ_e and the Smoluchowski equation ($\zeta = \mu_e \eta / \epsilon_0 \epsilon$ with η representing the viscosity of the solvent and $\epsilon_0 \epsilon$ denoting the permittivity of the dispersion).

3.4.10 TGA

Thermogravimetric analysis (TGA) was performed using a Mettler TGA/SDTA 85 device. Measurements were conducted in a nitrogen atmosphere between 30 and 700°C. Approximately 10 mg of freeze-dried particles were used for a measurement.

3.4.11 Refractive Index Measurements

The refractive index of dispersions consisting of CS particles at different concentrations (0-10 wt%) was determined using an Abbemat WR-MW refractometer from Anton Paar. Measurements were conducted at a wavelength of 633.2 nm. The temperature was controlled by a Peltier element and set to 25°C.

Chapter 4

Hard-Core/Soft-Shell Particles via Seeded Precipitation Polymerization

Within this work the self-assembly of hard-core/soft-shell particles in bulk and at the interface is studied. To reliably investigate the self-assembly of these particles, the CS particles need to fulfill three major prerequisites:

1. High degree of monodispersity
2. CS structure with a single nanoparticle core
3. High synthesis yield in quantities of grams

To accomplish these tasks, the synthesis of CS particles was analyzed in detail. As representative system Au-PNIPAM particles were used. In the next sections, the requirements of the surface functionalization of the Au nanoparticle cores (seeds) were studied. Additionally, the influence of the Au seed concentration was investigated. Apart from that, the polymerization was monitored *in situ* using UV-vis spectroscopy and LS to reveal insights in the reaction mechanism.

4.1 Influence of the Seed Surface Functionalization

Au-PNIPAM particles were synthesized by encapsulation of Au nanoparticles in cross-linked PNIPAM shells via free radical polymerization reaction in the presence of the monomer NIPAM and the cross-linker BIS. To achieve a successful encapsulation, the gold nanoparticles were modified prior to the polymerization. According to literature, they have been mostly functionalized with molecules providing a double bond (DB). The vinyl group has been assumed to enable a covalent link to the polymer shell in the radical polymerization.^[55,170–173] Apart from that, Singh *et al.* have followed a different approach: They used amine-terminated PNIPAM chains for the surface functionalization.

The authors have claimed that this modification renders the gold nanoparticle surface more hydrophobic. The gained hydrophobicity has been a prerequisite for the subsequent precipitation polymerization with NIPAM and BIS.^[174] Hence, so far, it has been still uncertain which properties the gold nanoparticle's surface has to fulfill for a successful encapsulation. To comprehend the requirements of the surface functionalization and its influence on the seeded precipitation polymerization, different surface functionalizing molecules were used in this thesis to modify the gold nanoparticles.

Figure 4.1 A shows a representative TEM image of the Au nanoparticles which were used for functionalization. The Au particles reveal a spherical shape with a low polydispersity. In Figure 4.1 B the respective histogram of the particle diameter is depicted. The diameter distribution could be fitted using a Gaussian size distribution. The narrow diameter distribution confirms the low polydispersity of the Au cores. An average diameter of 13.8 ± 1.6 nm was determined using the software ImageJ.

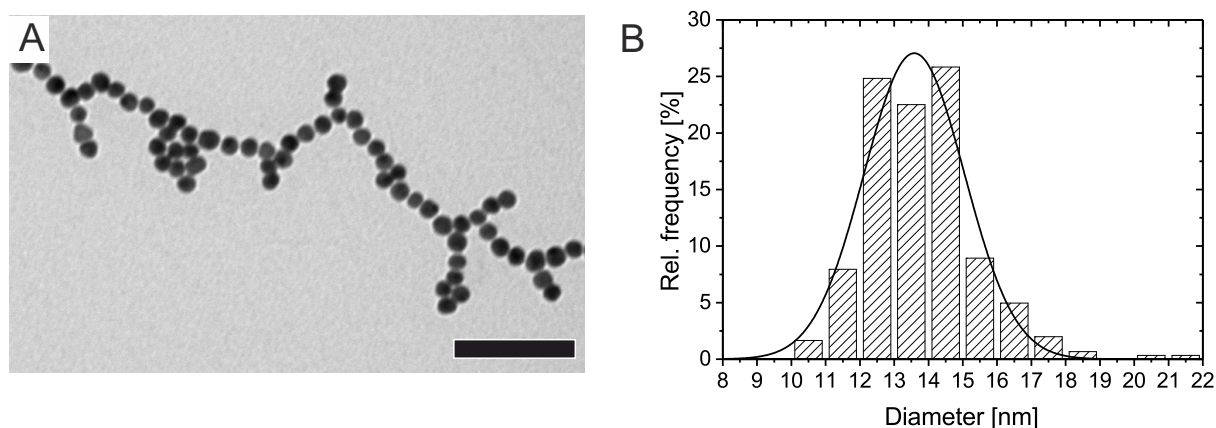


Figure 4.1: A. Representative TEM image of Au seeds prepared by Turkevich synthesis. The scale bar is 100 nm. B. Respective histogram displaying the diameter distribution of these Au nanoparticles. The black solid line is a Gaussian fit.

The following functionalizing molecules were used in order to determine the required Au nanoparticle modification: citrate, 11-mercaptoundecanoic acid (MUA), butylamine (BA) and butenylamine (B-*en*-A). The molecular structures of these four molecules are depicted in the top row of Figure 4.2. Below a sketch is illustrated showing a representative Au nanoparticle with the respective functionalization agents at its surface.

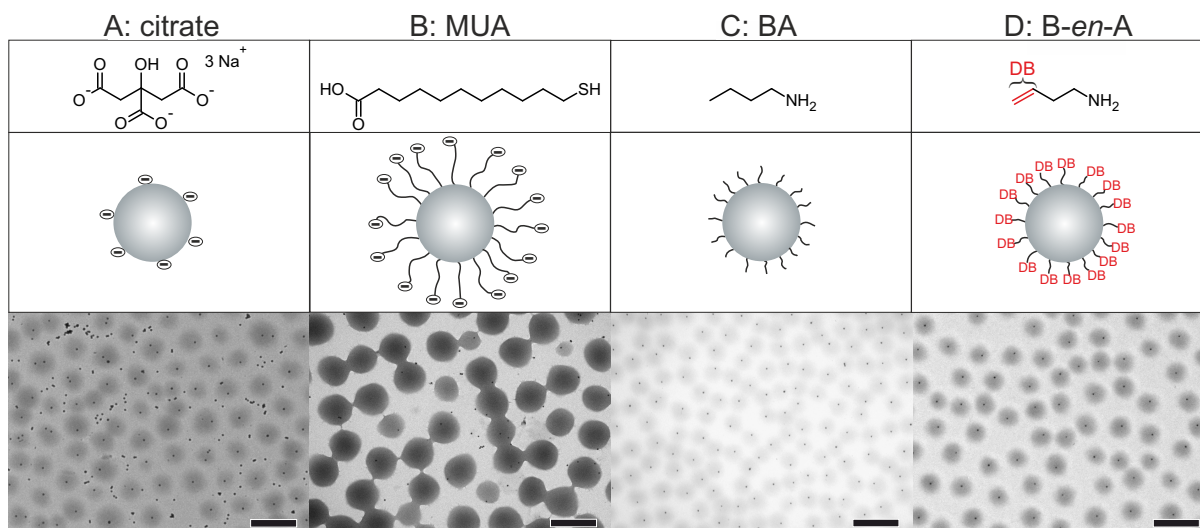


Figure 4.2: Functionalization of Au nanoparticles with different functionalizing agents: A. citrate, i.e., no functionalizing agent; B. 11-mercaptoundecanoic acid (MUA); C. butylamine (BA); D. butenylamine (B-*en*-A). From top to bottom, at first the molecular structures of the functionalizing molecules, then a scheme showing a functionalized Au nanoparticle and after that a TEM image (scale bar: 500 nm) of the reaction products prepared by encapsulation of differently modified Au nanoparticles are shown.

Citrate was used as stabilizer in the initial nanoparticle synthesis. Au nanoparticles carrying citrate on their surface have a negative surface charge in water at pH 5 (ζ -potential = -29 mV) due to their carboxy groups. Other molecules with an amine or thiol group can easily replace citrate, since citrate binds rather weakly to the Au nanoparticle surface.^[175] Therefore, MUA can coordinate more strongly to the surface due to its thiol group as compared to citrate. Apart from that, the increased surface charge (ζ -potential = -39 mV) and the longer aliphatic carbon chain of the MUA molecules support their colloidal stability. On the contrary, the functionalization with BA or B-*en*-A results in a more hydrophobic particle surface as compared to the initial stabilization with citrate. ζ -potential measurements were not reliable for these particles. Firstly, this is due to the excess citrate in solution. Secondly, this is related to the required addition of SDS prior to the functionalization with BA and B-*en*-A.^[55] Typically, concentrations of BA and B-*en*-A which result in a sub-monolayer on the Au nanoparticle surface were used for the functionalization. Thus, the Au nanoparticles are expected to exhibit some negative charges due to residual citrate. The main difference between BA and B-*en*-A is the presence of the double bond. The most important characteristics of the functionalizing molecules are schematically depicted in the mentioned sketches in Figure 4.2.

The differently functionalized Au nanoparticles were employed in seeded precipitation polymerizations in the presence of the monomer NIPAM and the cross-linker BIS. In all polymerizations the Au nanoparticle concentration was 2.8 nmol/L. TEM images of the

purified reaction products are shown in the last row Figure 4.2. Due to the different electron contrast Au and polymer are well distinguishable: Whereas the Au appears as a dark circular object, the hydrogel is brighter due to its lower electron contrast. Analyzing the images hydrogel particles were found for all four systems. However, not every synthesis yields only CS particles. In A the outcome of the synthesis using citrate functionalized Au nanoparticles is depicted. A mixture of CS particles and free Au nanoparticles was formed. Gold nanoparticles functionalized with MUA mostly resulted in hydrogel particles without Au cores (Figure 4.2 B) which were of distinctly larger size as compared to the other products. When the Au nanoparticles were functionalized with BA and *Ben-A* almost exclusively CS particles with a single encapsulated Au core (Figure 4.2 C and D) were obtained. To conclude, the encapsulation reaction with core particles that were functionalized with both amine derivatives was successful. This shows that the presence of polymerizable vinyl groups is not necessary. However, the hydrophobicity of the nanoparticle cores is crucial for the success of the encapsulation. Based on the suggested underlying mechanism of the seeded precipitation polymerization, that is illustrated in Figure 4.3, these results become clearer.

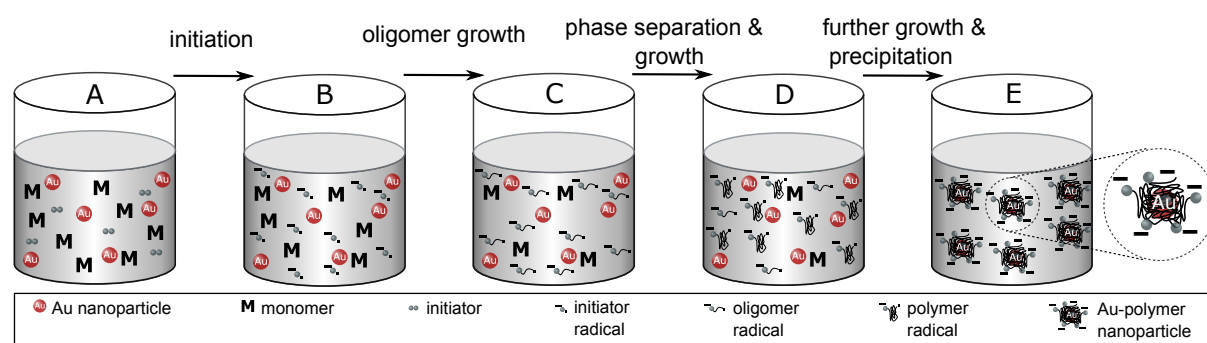


Figure 4.3: Scheme showing the mechanism of the seeded precipitation polymerization: A. Initially, the monomers (NIPAM and BIS), Au seeds and the initiator molecules are homogeneously distributed in solution. B. The initiator decomposes thermally. C. The initiator radicals grow to oligomer radicals. D. Further growth to polymer radicals takes place that induces phase separation at the reaction temperature. E. In the course of the reaction, these polymer/oligomer radicals grow further and/or precipitate onto the Au nanoparticle seeds.

In A the reaction mixture prior to initiation is depicted: NIPAM and BIS molecules are homogeneously dissolved in the presence of the functionalized Au nanoparticles and the initiator PPS. In B the initiator is already thermally decomposed into initiator radicals. These initiator radicals attack the monomers (NIPAM and BIS). As a result, oligomer radicals develop which can grow to polymer radicals (C). Subsequently, oligomer and polymer radicals grow further by monomer consumption. During this process, polymer precipitation begins as the polymer is formed under poor solvent conditions, i.e., above the lower critical solution temperature (LCST) of PNIPAM (D). The Au nanoparticles

serve as nucleation site. Thus, precipitation occurs almost exclusively onto their surface (E). This precipitation mechanism clarifies why polymerizable groups are redundant. Additionally, it explains why Au nanoparticles modified with MUA are not successfully encapsulated. This is due to electrostatic repulsion which prevents the negatively charged polymer/oligomer chains to precipitate onto the negatively charged seed surface. Therefore, the precipitation of polymer radicals proceeds similar to a seedless polymerization where purely organic hydrogel particles develop.^[176,177] Thus, the size of the particles is not controlled by the seed particle concentration but by the surface tension.^[178] This explains the difference in size of the reaction products shown in the TEM image in Figure 4.2 B as compared to the ones in Figure 4.2 A, C and D.

4.2 Influence of the Seed Concentration

Next, the influence of the Au seed concentration during the polymerization on the particle morphology and specifically on the shell thickness was investigated. Therefore, a series of seeded precipitation polymerizations was performed. In each reaction batch the volume of Au stock solution, i.e., the Au seed concentration was systematically varied between 0 and 8 nmol/L. The concentration of NIPAM (0.02 M) and BIS (15 mol% referred to the monomer NIPAM) were kept constant in all batches. The used Au nanoparticles were functionalized using *B-en-A*. Table 4.1 lists the different volumes of the stock solution, the corresponding concentration referred to Au^0 and to the Au particle number ($c(\text{seeds})$) in the total reaction volume as well as the overall particle surface $A(\text{seeds})$. The calculation of the values was performed using the diameter of the Au nanoparticles obtained by TEM as well as the Au concentration obtained from UV-vis measurements. The Au concentration was derived using the Beer-Lambert law and the extinction coefficient for Au particles of this size from literature.^[179]

After purification, the reaction products were investigated by TEM. In Figure 4.4 representative TEM images for each polymerization product are shown. Every reaction resulted in spherical microgels with narrow size distributions apart from the batch prepared with 8 nmol/L. For this highest seed concentration, polydisperse particles were obtained. Furthermore, the encapsulation of the Au core worked well for all batches. This concerns certainly only batches which were polymerized in the presence of Au nanoparticles and not the reference ($c(\text{seeds}) = 0$ nmol/L). Closer inspection of the TEM images revealed that neither aggregated Au nor free Au particles were formed. Most of the CS particles have a single Au core. Excluding the reference three categories of reaction products can be differentiated using the ranges of seed concentrations. For low seed concentrations (≤ 1.4 nmol/L), CS particles and purely organic microgel particles were formed. Intermediate seed concentrations (2.1 - 5.4 nmol/L) led to almost exclusively CS parti-

cles with a single Au core. At high seed concentrations (8 nmol/L), CS particles with a pronounced polydispersity were formed. TEM image analysis of the reaction products provided the fraction of particles with and without encapsulated Au nanoparticle. The respective results are summarized in Table 4.1.

Table 4.1: Summary of the conducted syntheses which were performed using different volumes of Au seed stock solution $V(\text{seed solution})$ ($[\text{Au}^0] = 0.017 \text{ mol/L}$). The resulting concentration of Au^0 ($c(\text{Au}^0)$), the Au nanoparticle concentration $c(\text{seeds})$ as well as the overall seed particle surface $A(\text{seeds})$ in the overall reaction mixtures are summarized. Furthermore, the percentages of particles with and without Au cores of the reaction products obtained from TEM image analysis are listed.

$V(\text{seed solution})$ [μL]	$c(\text{Au}^0)$ [$\mu\text{mol/L}$]	$c(\text{seeds})$ [nmol/L]	$A(\text{seeds})$ [cm^2]	Microgels with core [%]	Microgels without core [%]
0	0	0	0	0	100
42	28	0.4	33	52	48
84	56	0.7	65	75	25
169	112	1.4	130	84	16
253	168	2.1	195	92	8
338	223	2.8	261	97	3
422	278	3.4	326	97	3
506	332	4.1	390	95	5
591	387	4.8	456	98	2
675	440	5.4	521	99	1
1013	653	8.0	781	79	1

Up to seed concentrations of 1.4 nmol/L, the fraction of purely organic microgel particles is increased with decreasing seed concentrations. At these low seed concentrations, there is not enough Au seed surface provided, so that the oligomer and polymer radicals precipitate onto the seed surface, but as well freely in solution resulting in mixtures of microgels without core and CS particles. In the intermediate seed concentration range between 2.1 and 5.4 nmol/L the percentage of monodisperse CS particles is above 90%. In this concentration range, the nucleation is ruled by the provided excess area of the Au nanoparticles, i.e., the amount of seeds controls the number of CS particles. The monomer conversion during the reactions is assumed to be similar. Therefore, the seed concentration has a significant influence on the total particle size/ microgel shell thickness. A decreased particle size is obtained with increasing seed concentration. Indeed, this was noticed in the TEM images. In case of particles prepared with the highest seed concentration (8 nmol/L), the available surface is too high. Consequently, the precipitation is expected to occur rapid and uncontrolled and thus leading to polydisperse hydrogel shells. Here, it was difficult to assess if a polymer shell was present. For the image analysis only the particles with a

distinctly visible shell, i.e., of a certain thickness, were considered. Accordingly, the sum of particles with and without core in Table 4.1 is not equal to 100%.

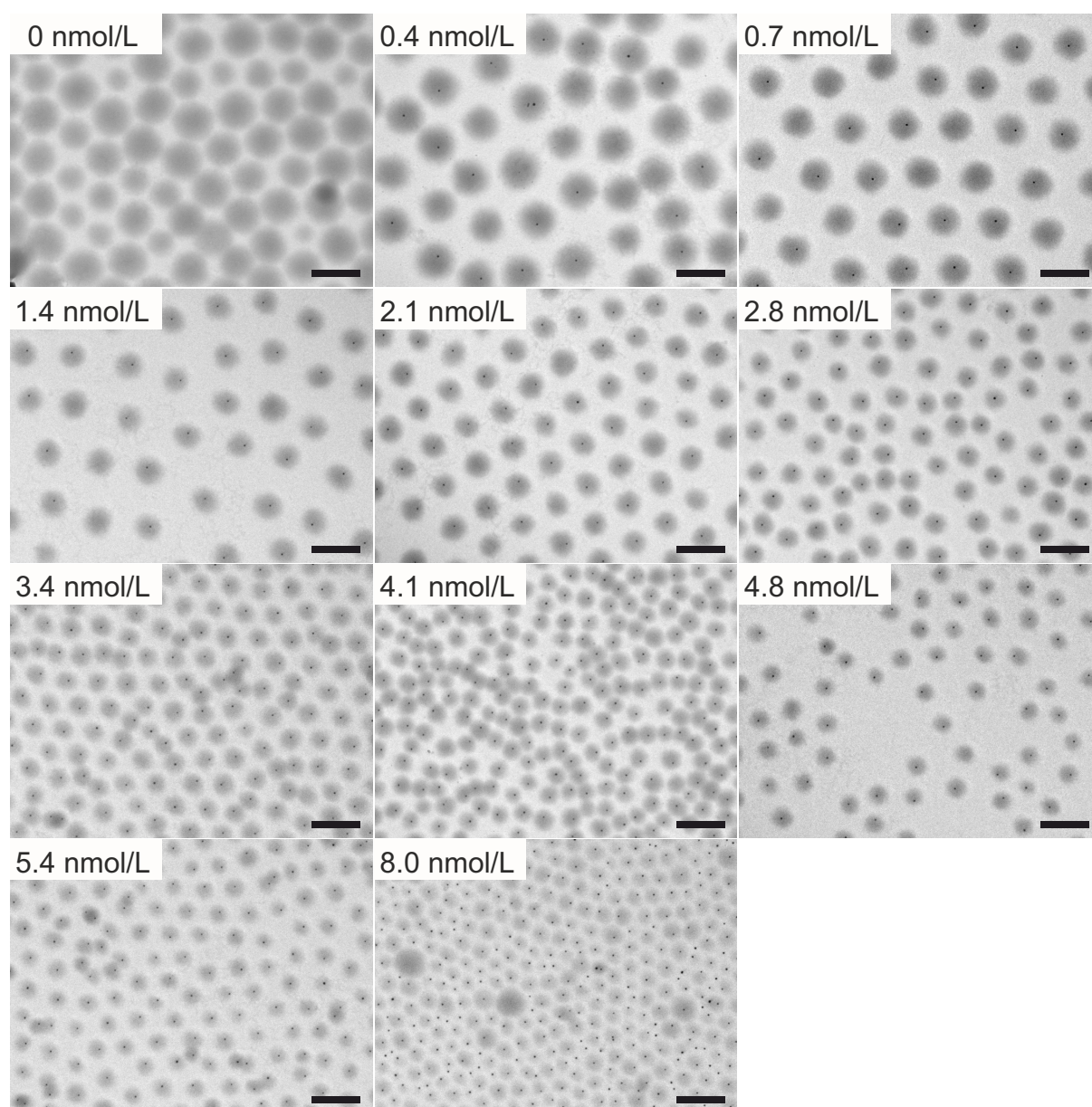


Figure 4.4: Representative TEM images of the reaction products prepared with different Au seed concentrations (0 - 8.0 nmol/L): microgels without Au cores (0 nmol/L), mixture of microgel particles with and without Au cores (0.4 - 1.4 nmol/L), monodisperse CS particles (2.1 - 5.4 nmol/L) and polydisperse CS particles (8.0 nmol/L). The scale bars correspond to 500 nm.

DLS was used to confirm the observed correlation between particle size and seed concentration. Figure 4.5 shows the evolution of the hydrodynamic radii with seed concentration in the swollen (20°C) and collapsed (60°C) state. The full swelling/deswelling curves between 20 and 60°C, are depicted in the Appendix in Figure A.3. In accordance with the TEM analysis, a constant decrease of the hydrodynamic radii with increasing seed concentration was measured at both investigated temperatures. Further, smaller radii are obtained at 60°C as compared to the dimensions received at 20°C. This can be ascribed to the volume phase transition behavior of cross-linked PNIPAM particles. Below the VPTT, at 20°C, the particles are highly swollen with water resulting in a large hydrodynamic volume. At temperatures distinctly above the VPTT, here 60°C, their volume is significantly reduced due to the release of water. The particles are in the collapsed state since polymer-polymer interactions are preferred in contrast to polymer-water interactions. In the range between 2.1 and 5.4 nmol/L, where solely CS particles were obtained, the seed concentration allowed a variation of the hydrodynamic radius at 20°C between 96 ± 1 nm (high $c(\text{seeds})$) and 123 ± 1 nm (low $c(\text{seeds})$). Hence, the seed concentration could be used to adjust the shell thickness to a certain extent. In some cases this might be an attractive alternative to the variation of the monomer feed concentration which is typically used to change the shell thickness.^[55] Summarizing the results of TEM and DLS, the seed concentration in the reactions has a significant influence on the particle morphology and size. It is a crucial parameter in order to achieve monodisperse CS particles with a single encapsulated core.

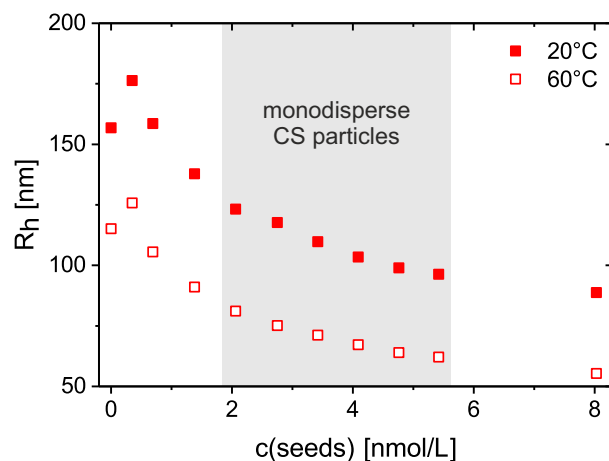


Figure 4.5: Evolution of the average hydrodynamic radius as a function of the seed concentration at 20°C and 60°C. The respective error bars are on the order of the symbol size. The seed concentration range, which resulted in monodisperse CS particles with a single encapsulated Au core, is indicated by a gray background.

The measured diameters of the particles are approaching the wavelength of the visible light. Thus, the prepared microgels are effective scattering objects in the wavelength range

of the visible light. This strongly influences their optical properties. In Figure 4.6 A a photograph of diluted aqueous dispersions (0.03 wt%) of the reaction products is shown. From left to right the seed concentration used in the polymerization was increased. The first sample on the left was prepared without any seeds. All polymerizations resulted in colloiddally stable dispersions, i.e., sedimentation or aggregation were not observed. Already the visual impression of the samples allows to draw conclusions on their optics. The purely organic microgel particle dispersion (very left) appears colorless and turbid. Once Au seeds were present in the polymerizations, a red color is noticeable in the dispersion of the reaction product stemming from the LSPR of the Au nanoparticles. The LSPR is caused by the interaction of the electromagnetic field of the incident light and the conduction electrons of the Au nanoparticle which causes collective electron oscillations.^[57,58] Increasing seed concentrations (in the photograph from left to right) lead to a more pronounced red color.

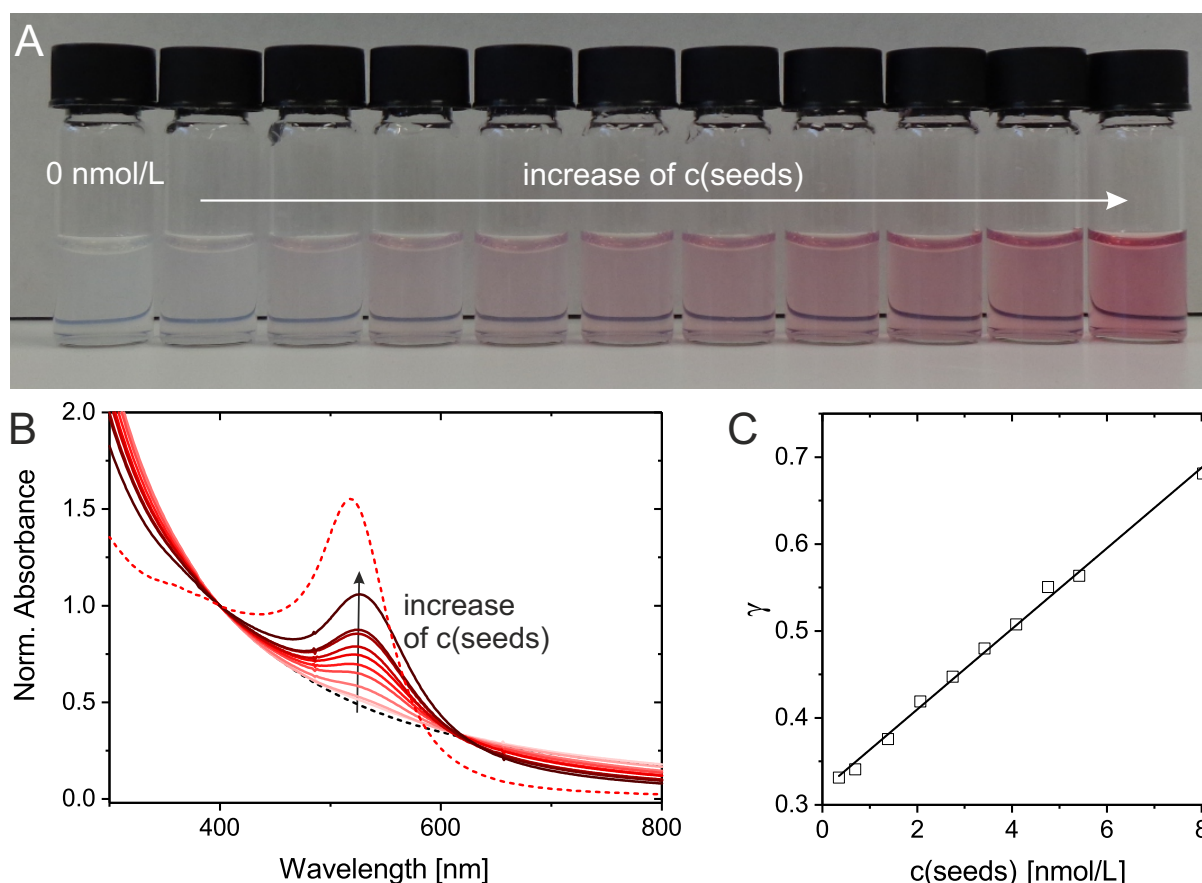


Figure 4.6: Analysis of the optical properties of the samples prepared with different Au seed concentrations (0 - 8.0 nmol/L). A. Photographs of these samples. B. Absorbance spectra normalized to the absorbance at 400 nm including a normalized spectrum of the pure Au seeds (dashed red line) measured at room temperature. C. The ratio γ in dependence on the Au seed concentration. The black solid line is a linear fit.

For a more quantitative study of the optical properties these dispersions were analyzed using UV-vis absorbance spectroscopy at room temperature. For reasons of comparability these spectra were normalized to the absorbance at 400 nm. The normalized spectra are depicted in Figure 4.6 B. For the sample prepared without any Au seeds (dashed black line) no distinct spectral features are visible. A constant rise in the absorbance towards decreasing wavelengths is noticed. This corresponds to the light scattering of microgel particles (Rayleigh-Debye-Gans (RDG) scattering).^[55] Further, a spectrum of the pure, *Ben-A* functionalized Au nanoparticles is shown as reference (dashed red line). As expected for Au particles in that size range, the maximum in the LSPR signal is at a wavelength position of 518 nm. The position of the LSPR of the microgel systems prepared with different seed volumes is on the order of 525 nm. As compared to the LSPR of the pure Au seeds, the plasmon resonance is significantly red-shifted. If the sensitivity of the LSPR position to the refractive index environment is considered, this difference is consistent, since water has a lower refractive index as compared to hydrogel.^[55,57] Hence, the encapsulation of Au seeds leads to an increase in refractive index of their immediate surrounding medium and thus to a red-shift of the LSPR. Comparing the reaction products prepared with different seed concentrations, the plasmonic contribution is increasing with higher Au content. Apart from the resonance positions, also the resonance widths match well. This indicates that single Au cores are encapsulated and that agglomeration of Au cores is absent. The scattering contribution shows the inverse trend than the LSPR with changing seed concentration. The slope below 400 nm in the absorbance spectra constantly increases with decreasing seed concentration. This can be attributed to an increased intensity of the scattered light for larger objects, i.e., for samples prepared with decreasing seed concentration.

A useful means to describe the balance between plasmonic and scattering contribution is the ratio γ .^[55] The absorbance at the LSPR $Abs(\lambda_{LSPR})$ (plasmonic contribution) is related to the absorbance at a wavelength at which scattering is dominating the spectrum (scattering contribution), e.g., $Abs(400\text{ nm})$. To calculate γ , the ratio of plasmonic and scattering contribution is divided by the respective ratio of the neat Au nanoparticles without polymer shell, i.e., $Abs_{Au}(\lambda_{LSPR})/Abs_{Au}(400\text{ nm})$:

$$\gamma = \frac{\frac{Abs(\lambda_{LSPR})}{Abs(400\text{ nm})}}{\frac{Abs_{Au}(\lambda_{LSPR})}{Abs_{Au}(400\text{ nm})}} \quad (4.1)$$

Consequently, an increasing scattering contribution as compared to a constant plasmonic contribution results in a decreased γ . Figure 4.6 C shows γ for the prepared samples as a function of the seed concentration. Increasing seed concentrations lead to a rise in γ indicating a decrease of the scattering contribution. The depicted evolution of γ with the seed concentration can be described by a linear trend line. The linear increase of the

absorbance with concentration is in accordance with the Beer-Lambert law. The increase of the scattering contribution is based on two effects: A decreasing Au seed concentration and an increasing thickness of the polymer shell. Hence, in order to recover the Beer-Lambert law, these effects have to be considered. Therefore, a normalization is performed using $Abs(400\text{ nm})$ in the calculation of γ in order to account for the changing scattering contribution.

4.3 In Situ Monitoring of the Seeded Precipitation Polymerization

To corroborate the proposed mechanism of the free radical seeded precipitation polymerization shown in Figure 4.3, a non-stirred polymerization was *in situ* monitored. These experiments were in similarity to a study of Richtering *et al.*^[176] They used DLS for *in situ* investigations of a seedless precipitation polymerization of PNIPAM. This way, they managed to draw conclusions on the kinetic rate law of the reaction. In addition to light scattering, UV-vis absorbance spectroscopy was used in this thesis to pursue the spectral developments in the course of the polymerization. A low monomer concentration was used for the experiments performed by both methods to eliminate the appearance of too high absorbance values in the UV-vis spectra and of multiple scattering in the LS experiment. The concentration of NIPAM was 0.01 M and the concentration of BIS was 15 mol% referred to the concentration of NIPAM. These monomer concentrations lead to monodisperse CS particles as known from previous studies.^[55] The Au seed concentration was 2.7 nmol/L. The reaction conditions were analogous to polymerizations in a three-neck round-bottom flask. However, constant degassing with nitrogen and stirring were not realizable. A detailed description of the sample preparation for the *in situ* studies is presented in Section 3.2.1. First, the changes in scattering intensity as well as the evolution of the hydrodynamic radius were analyzed by LS. Figure 4.7 A shows the scattering intensity as a function of reaction time. Up to 10 minutes after the initiation, the intensity of the scattered light is low and almost constant. Next, a steep rise in intensity is monitored up to 33 min reaction time. This corresponds to the precipitation of oligomer and polymer radicals. Afterwards, the scattered intensity reaches constant values. The scattered intensity is directly proportional to the radius of the scattering objects. Thus, a qualitative evolution of the radius with time can already be deduced using the results depicted in Figure 4.7 A. Figure 4.7 B verifies these assumptions. Here the evolution of the hydrodynamic radius R_h versus the polymerization time is shown. R_h is derived by evaluation of the time-dependent fluctuations of the scattering intensity. Initially, R_h of the scattering objects is about 10 nm which matches the size of the Au nanoparticle seeds.

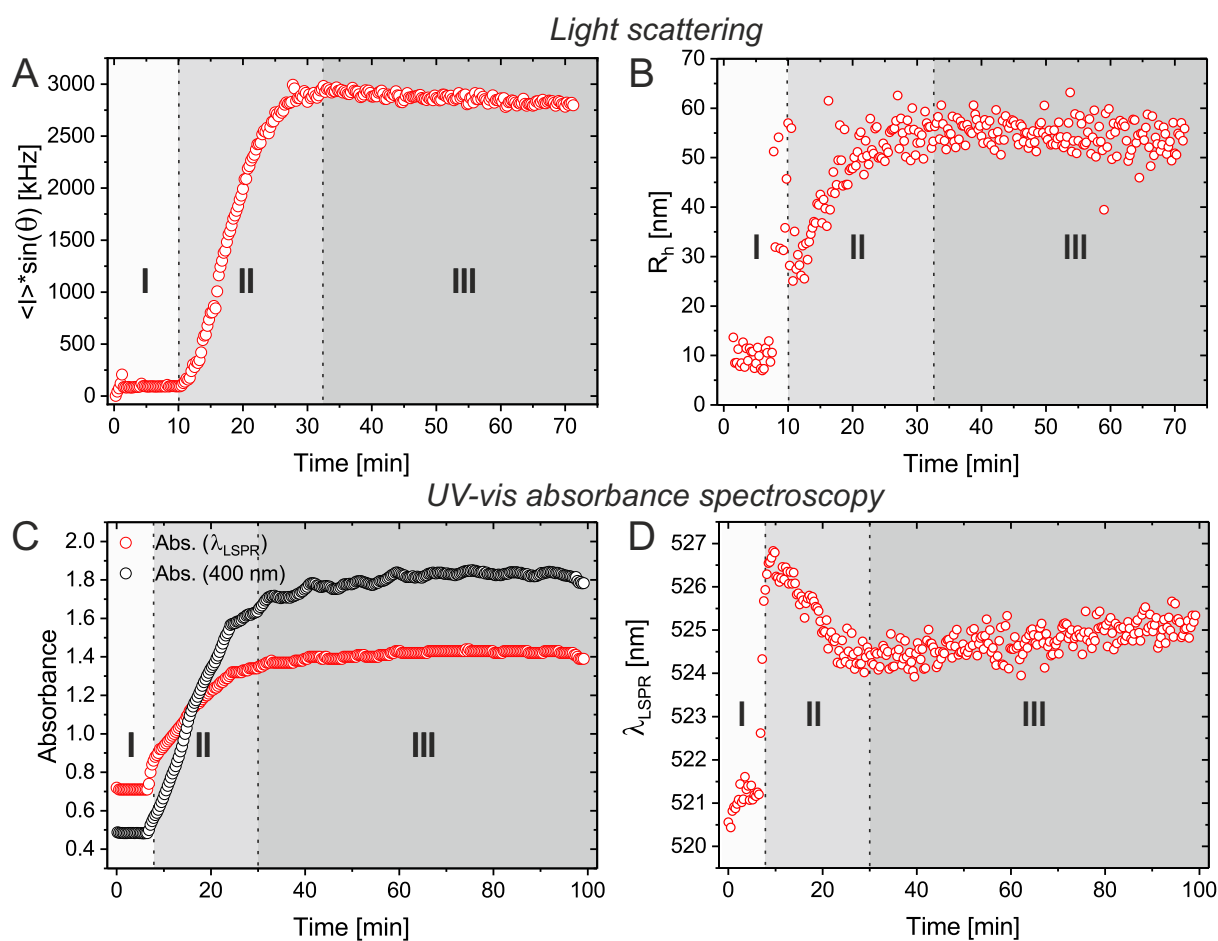


Figure 4.7: *In situ* monitoring of the polymerization by LS: The evolution of the average intensity of the laser light scattering (A) and the hydrodynamic radius (B) in dependence on the reaction time. *In situ* monitoring of the polymerization by UV-vis absorbance spectroscopy: The absorbance intensity at 400 nm and at the LSPR position λ_{LSPR} (C) as well as λ_{LSPR} (D) as a function of polymerization time. The data can be divided in three phases: I) the initiator decomposes and monomer consumption begins, II) oligomer and polymer radicals grow and precipitate, III) no further growth is visible after the precipitation of the radicals.

Usually, R_h for hard spheres is about 30% increased as compared to the radius obtained from TEM image analysis. Considering this, R_h agrees well with the radius R obtained by TEM ($R = 6.9$ nm). In accordance with the evolution of the scattered intensity, the hydrodynamic radius R_h steeply increases at around 10 min of reaction time. Within 1 min the radius jumps from 10 to 25 nm which is related to the precipitation of oligomer/polymer radicals onto the surface of the Au nanoparticle seeds. Within the next 22 min, growth of already precipitated radicals and free radicals in the reaction medium proceeds. At the same time further precipitation of oligomer/polymer radicals occurs. At this stage, the data fluctuates distinctly which can be related to the existence of differently sized objects during the growth. Finally, R_h approaches a plateau reaching a value of 55 nm after about 33 min. This indicates that polymerization and precipitation primarily take place

up to 33 min reaction time. To exclude multiple scattering during the experiment, the reaction product was diluted by a factor of four using water. Subsequently, intensity-time autocorrelation functions were recorded. The resulting hydrodynamic radius agreed with the value prior to dilution within the experimental error. Therefore, multiple scattering did not affect the *in situ* study.

Additionally, the evolution of the absorbance spectra was investigated by UV-vis spectroscopy. First, the spectrum of Au nanoparticles dispersed in the reaction medium including BIS and NIPAM prior to initiation coincided well with the spectrum measured of the aqueous dispersion of the pure Au nanoparticles (see Figure 3.1 in the Experimental Section). Thus, the Au nanoparticles are colloidally stable in the reaction medium and aggregation is not taking place. In Figure 4.7 C the changes in absorbance intensity at 400 nm and at the wavelength position of the LSPR (λ_{LSPR}) versus the polymerization time are plotted. The represented data shows the same progression as the light scattering data: In the course of the reaction, first low absorbances are measured. This is followed by a steep rise in absorbance starting at around 8 min which corresponds to the precipitation of oligomer/ polymer radicals. The evolution of the data agrees with the increase in scattered intensity (LS study), although it occurs at slightly shorter times (8 min instead of 10 min). The difference may be caused due to the different cell geometry. Furthermore, a slightly different sample preparation regarding degassing with nitrogen or sample mixing cannot be excluded. Both absorbance curves achieve constant absorbance values at about 30 min after initiation. Comparing the data at both wavelength positions the relative increase in absorbance is dominating at 400 nm as compared to the plasmon resonance position λ_{LSPR} . This difference correlates to the scattering contribution being more pronounced at lower wavelengths. Analyzing the absorbances at λ_{LSPR} in the time interval between 8 and 30 min, two different slopes in absorbance are measured. Around minute 8-10, i.e., in the beginning of the polymer precipitation, a much steeper slope as for the residual time up to 30 min is found. This observation is related to the precipitation of PNIPAM radicals onto the Au seed surface which has two consequences: Firstly, the absorbance at λ_{LSPR} augments due to an increasing scattering contribution. Secondly, the local refractive index rises resulting in an increase of the LSPR intensity. The latter consequence affects the absorbance solely in the first minutes of precipitation. Further growth of the hydrogel shell is not affecting the local environment of the Au nanoparticle anymore. As a result, the LSPR is only influenced in the initial phase of precipitation. After about 10 min, the steep increase in absorbance at λ_{LSPR} is only based on an increasing scattering strength related to the growth of scattering objects. Hence, a different slope is measured. In addition, the position of λ_{LSPR} is a convenient reporter for refractive index changes in the local surroundings of the Au nanoparticles surface. In Figure 4.7 D the position of λ_{LSPR} is shown as a function of the reaction time. Up to 8 min after initia-

tion, the LSPR position is at around 521 nm. Next, a rapid shift to longer wavelengths (527 nm) within 1 min is observed. This shift corresponds to the beginning precipitation of radicals onto the Au nanoparticles surface. In the progress of the reaction, a continuous blue-shift reaching constant values at 524 nm is monitored. This development is related to the growth of the polymer shell resulting in an increase of scattering. Due to an increasing scattering contribution with decreasing wavelength stemming from the power law dependence of scattering, λ_{LSPR} is located at shorter wavelengths for stronger scattering.^[55,154] Finally, the sample obtained from the UV-vis experiment was diluted and measured using DLS. The measurements were performed at 70°C which resembles the reaction temperature. This way the hydrodynamic radii of the CS particles obtained by both methods could be compared. The values coincided well: A R_h of 58 nm was measured for particles prepared in the UV-vis setup and a R_h of 55 nm for particles synthesized in the DLS setup. This justifies a direct comparison of the two *in situ* studies.

The analysis of the results of both methods allows to divide the seeded precipitation polymerization into three phase. In phase I (8-10 min after initiation) the thermal decomposition of the initiator and the attack of the monomers occurs. Phase II summarizes the next 22 minutes of the reaction, in which growth of radicals as well as growth and precipitation of oligomer/polymer radicals onto the Au nanoparticles surface take place. In the final phase, no further growth can be detected. In both methods the phase durations coincide apart from a slight mismatch in phase I. The gained knowledge about the reaction mechanism and kinetics allows to control the structure of the reaction products on a high level in order to get monodisperse CS particles with a single Au core encapsulated. This is exactly what is required for the self-assembly studies presented in the following.

4.4 Post-Modification of the Gold Cores

A neat method to influence the optical as well as the structural properties of the prepared Au-PNIPAM CS particles is the overgrowth of the Au cores encapsulated in the PNIPAM shells. Due to the porous, highly swollen structure of the microgel shells at room temperature, small molecules can diffuse to the Au core and enable a post-modification of the precursor particles. The PNIPAM shell guarantees colloidal stability during the overgrowth and allows a diffusion-controlled process.^[172,180] In order to overgrow the Au cores in the Au-PNIPAM particles with Au, a surfactant-assisted seeded growth protocol using mild reducing conditions is employed.^[96] This way a homogeneous overgrowth of the Au nanoparticle cores is ensured. Simultaneously, secondary nucleation is inhibited. According to previous studies, the nanoparticle morphology is strongly controlled by the ratio of reactants, temperature, pH, concentration of the surfactant and the type of halide counter ion of the surfactant.^[181,182] Here, CTAC was chosen, since this surfactant

is supposed to only promote the formation of spherical geometries. Apart from that the surfactant influences the redox potential of the metal salt by complexation. In order to achieve reduction solely at the metal surface, a mild reducing agent (ascorbic acid) was employed.^[183] Although the growth procedure of the Au cores can be performed in one step, a step-wise overgrowth by successive additions of ascorbic acid and feed solution (HAuCl_4 and CTAC) was conducted. In this way, the core dimension could be controlled precisely and the growth of cores with high monodispersity was favored. Au-PNIPAM particles which were prepared similarly to the previously described free radical seeded precipitation polymerization in a semi-batch fashion (see Section 3.2.1) were used as precursor particles. A 15 nm core was encapsulated in a cross-linked PNIPAM shell with a nominal cross-linker content of 15 mol%. The overall hydrodynamic particle diameter was 472 nm at 25°C. Applying the previously introduced notation to the precursor CS particles, they are referred to as $\text{C}_{15}\text{S}_{31.5}(15\%)$ particles. The overgrowth procedure was followed by UV-vis absorbance spectroscopy. In Figure 4.8 A the absorbance spectra recorded at room temperature after each addition of reducing agent and feed solution are shown. To allow an easier comparison the spectra were normalized to the absorbance at 400 nm.

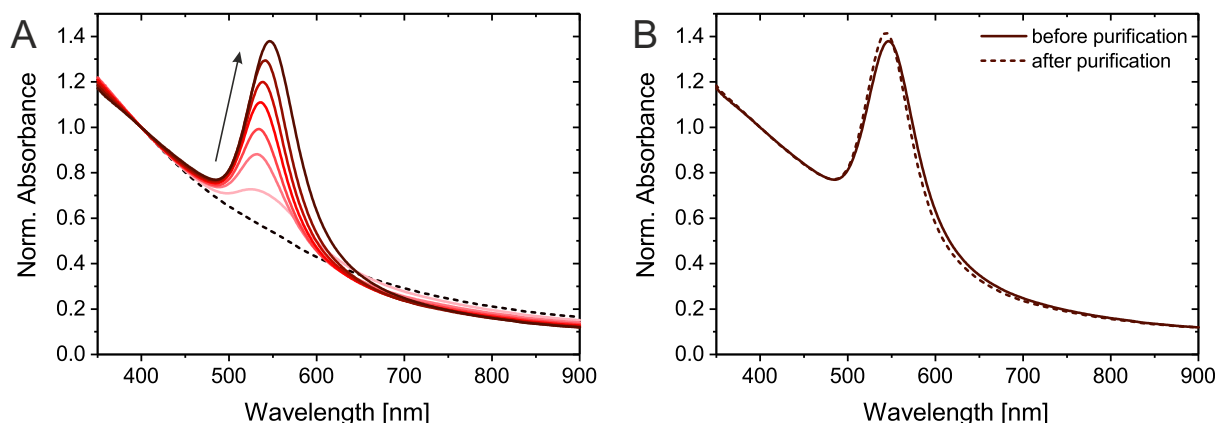


Figure 4.8: A. Absorbance spectra after each growth step normalized to the absorbance at 400 nm recorded room temperature (solid lines). The arrow indicates the shift of the LSPR as well as the significant increase of the LSPR intensity in the course of the overgrowth process. The black dashed line represents the extinction spectrum of the precursor particles. B. Absorbance spectra of the final, overgrown CS particles before (solid line) and after purification (dashed line) normalized to the absorbance at 400 nm.

The black dashed line depicts the spectrum of the precursor particles. Due to the large dimensions of these particles ($\lambda_b\sigma = 472$ nm at 25°C) the scattering dominates over the whole wavelengths range and the LSPR of the Au cores cannot be determined. All other spectra show a distinct extinction peak related to the plasmon resonance of the Au cores. Since only one single resonance is detected the formation of other non-spherical

Au nanoparticle shapes can be excluded to the greatest extent. All measured resonances display narrow widths indicating a low polydispersity of the overgrown Au nanoparticles. In addition, the position of the plasmon resonance λ_{LSPR} shifts continuously from 523 to 540 nm due to the increasing size of the Au cores. This evolution is highlighted by the arrow in Figure 4.8 A. Further, Table 4.2 lists the position of the plasmon resonance after each overgrowth step. The plasmonic properties are distinctly more pronounced for larger Au cores. The changes in the optical behavior of the CS particles can be fully attributed to the scattering and absorbance of the plasmonic Au cores. The scattering contribution of the hydrogel shell should remain nearly unaffected by the core growth. A suitable parameter to quantify the ratio of scattering to plasmonic contribution is the ratio γ . It is defined by eq. 4.1. In Table 4.2 the values for γ after each addition step are listed. A constant increase of this ratio during the growth procedure of the Au cores is revealed. This indicates a continuous increase in plasmonic properties which is significantly more pronounced as the growth of the scattering contribution of the Au cores. In Figure 4.8 B the absorbance spectra of the reaction product after purification is depicted. The purified reaction product shows a slight blue shift in the LSPR peak position due to the removal of residual chemicals (mainly the surfactant CTAC) from the reaction mixture.

Table 4.2: Wavelength position of the plasmon resonance λ_{LSPR} and values of the ratio γ after each addition of reducing agent and feed solution during the Au core overgrowth.

Overgrowth step	λ_{LSPR} [nm]	γ
before overgrowth	n.a. ^a	n.a. ^a
addition 1	530	0.47
addition 2	533	0.57
addition 3	534	0.64
addition 4	536	0.72
addition 5	539	0.78
addition 6	541	0.84
addition 7	547	0.89
addition 7(purified)	544	0.91

^a Scattering dominates over the whole absorbance spectrum. Therefore, the wavelength position of the LSPR λ_{LSPR} and γ cannot be reliably determined.

The success of the post-modification of the Au cores was further manifested by TEM. In Figure 4.9 the respective TEM images of the precursor particles (A) and the overgrown Au-PNIPAM particles (B) are shown. In both images the Au cores and the polymer shell can be well distinguished due to the higher electron contrast of Au as compared to the PNIPAM shell. Direct comparison of the particles before and after overgrowth reveals that the Au cores grew significantly. Each particle in A and B includes only one Au core.

Further, all Au cores show a spherical shape. Even after several addition steps neither non-spherical side products nor secondary nuclei were formed. In total 65 particles were analyzed using *ImageJ* resulting in an average particle diameter of 71 ± 6 nm.

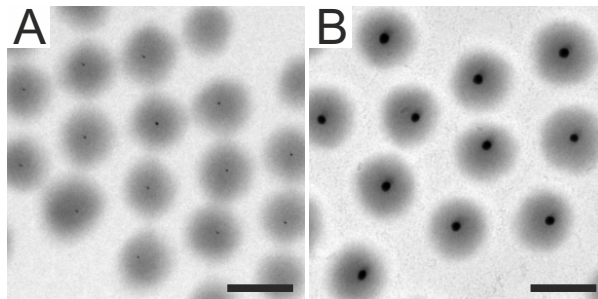


Figure 4.9: Representative TEM images of the CS particles prior (A) and after (B) Au overgrowth of the encapsulated Au nanoparticle. The scale bars are 500 nm.

In order to control, if the overgrowth has any significant influence on the swelling behavior of the particles, temperature-dependent DLS measurements were performed. In Figure 4.10 the hydrodynamic diameter $\lambda_b\sigma$ is shown as a function of temperature. The data of the precursor particles is compared to the results of the purified particles after the final addition step. For both samples the typical volume phase transition of cross-linked PNIPAM is observed with a VPTT at 35°C. Both temperature-dependent data sets match apart from slight deviations for temperatures smaller than the VPTT. This might be related to remaining CTAC in the microgel network that affects the swelling behavior.

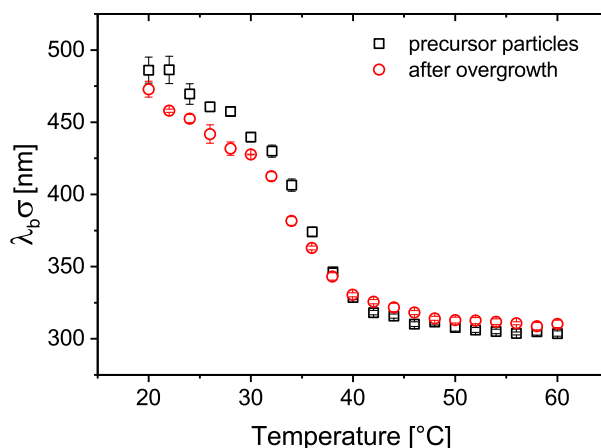


Figure 4.10: Temperature-dependent evolution of the hydrodynamic diameter $\lambda_b\sigma$ of the Au-PNIPAM particles prior and after the Au core overgrowth.

It is highlighted that upscaling of the overgrowth protocol^[96] was successful as the particles shown in Figure 4.9 were produced in a large batch synthesis (in total 1774 mL). This is

a great advance as large quantities of these CS particles are required for the self-assembly experiments in bulk.

Chapter 5

Self-Assembly of Hard-Core/Soft-Shell Particles in Bulk

In this chapter, the bulk self-assembly of hard-core/soft-shell particles for the formation of three-dimensional superlattices is explored. Their soft polymer shells consisting of cross-linked PNIPAM offer several advantages: (1) they allow to access high volume fractions exceeding the hard sphere limit for FCC packing of 0.74 due to their soft character, (2) they provide excellent stability even at such high volume fractions and (3) they allow to precisely tune the inter-particle distances by adjusting the volume fraction.^[56] Their soft character allows ordering at different length scales ranging from core-core to shell-shell contacts in one sample (see Figure 1.1). When CS particles are in shell-shell contact, their polymer shells are swollen and just in contact. Core-core contacts correspond to CS particles that are in contact in the compressed state, i.e., when the soft shells are maximally compressed. The appearance of these two length scales is predicted to result in a rich phase behavior for soft colloidal particles or hard-core/soft-shell particles according to theoretical studies.^[15,16,53] In order to additionally study interesting optical phenomena in the self-assembled superlattices, gold was chosen as core material due to its extraordinary optical properties. In the following, the fabrication of the self-assembled structures is shown. The self-assembly of CS particles was studied in dependence on the volume fraction and on structural properties of the particles. Regarding the particle structure the cross-linker content, i.e., the softness, the overall size and the Au core presence as well as size were varied. This allowed to study correlations between the particle structure as well as structural and optical properties of the prepared superlattices.

5.1 Influence of Cross-Linker Content and Particle Size

The self-assembly of Au-PNIPAM particles with different cross-linker contents, i.e. softnesses, and overall particle dimensions was studied. Both parameters influence the accessible inter-particle distances in the self-assembled structure. The objective hereby was to manipulate the self-assembly by varying the cross-linker content and the particle dimension. First, the particle morphology and softness of the different particle types were analyzed. Further, their optical properties in the dilute regime and at highly concentrated states were investigated. In the case of crystalline, self-assembled structures, conclusions on their crystal lattice could be drawn.

5.1.1 Particle Structure and Softness

Nine types of Au-PNIPAM particles with different cross-linking densities and/or dimensions were synthesized. Large batches (500-750 mL) were prepared, since high particle quantities were needed for the self-assembly studies. Due to the structural differences of the synthesized CS particles, they were expected to cover a large range of lattice constants in their self-assembled superstructures. An elegant way to control the size of these CS particles is given by variation of the monomer feed concentration.^[55] In total three different NIPAM feed concentrations (0.01, 0.02 and 0.03 M) were used for this study. To control the cross-linking in the polymer shells, different cross-linker contents referred to the monomer concentration were employed. Combining each of the three NIPAM feed concentrations with three different cross-linker contents (10, 15 and 25 mol%) resulted in nine different CS systems (see Table 5.1). Au nanoparticles with a diameter of 15 nm were

Table 5.1: Core diameter σ , overall diameter $\lambda_b\sigma$ and shell-to-core ratio λ_b of the different particle types synthesized with varying monomer feed concentrations and cross-linker contents.

CS system	σ [nm]	$\lambda_b\sigma$ ^a [nm]	λ_b
C ₁₅ S _{12.0} (10%)	15 ± 2	180 ± 1	12
C ₁₅ S _{15.7} (10%)	15 ± 2	235 ± 5	15.7
C ₁₅ S _{16.5} (10%)	15 ± 2	248 ± 2	16.5
C ₁₅ S _{12.5} (15%)	15 ± 2	188 ± 2	12.5
C ₁₅ S _{14.2} (15%)	15 ± 2	214 ± 2	14.2
C ₁₅ S _{17.9} (15%)	15 ± 2	268 ± 5	17.9
C ₁₅ S _{11.2} (25%)	15 ± 2	168 ± 1	11.2
C ₁₅ S _{14.7} (25%)	15 ± 2	220 ± 4	14.7
C ₁₅ S _{16.0} (25%)	15 ± 2	240 ± 2	16

^a As determined by dynamic light scattering at 25°C using Cumulant analysis.

encapsulated in the different polymer shells. As mentioned, CS particles prepared with the same NIPAM concentration are in the same size range. Slight deviations may arise due to the different cross-linker contents in these samples. CS particles with a higher cross-linker density are more rigid and thus result in slightly smaller dimensions as compared to less cross-linked CS particles. Table 5.1 lists the core diameter σ , the hydrodynamic diameter $\lambda_b\sigma$ at 25°C determined using DLS and the shell-to-core ratio λ_b . The previously introduced notation for the CS systems is used. Note that increasing values of λ_b at a constant core size are related to thicker shells. In Figure 5.1 representative TEM images of each particle type are shown.

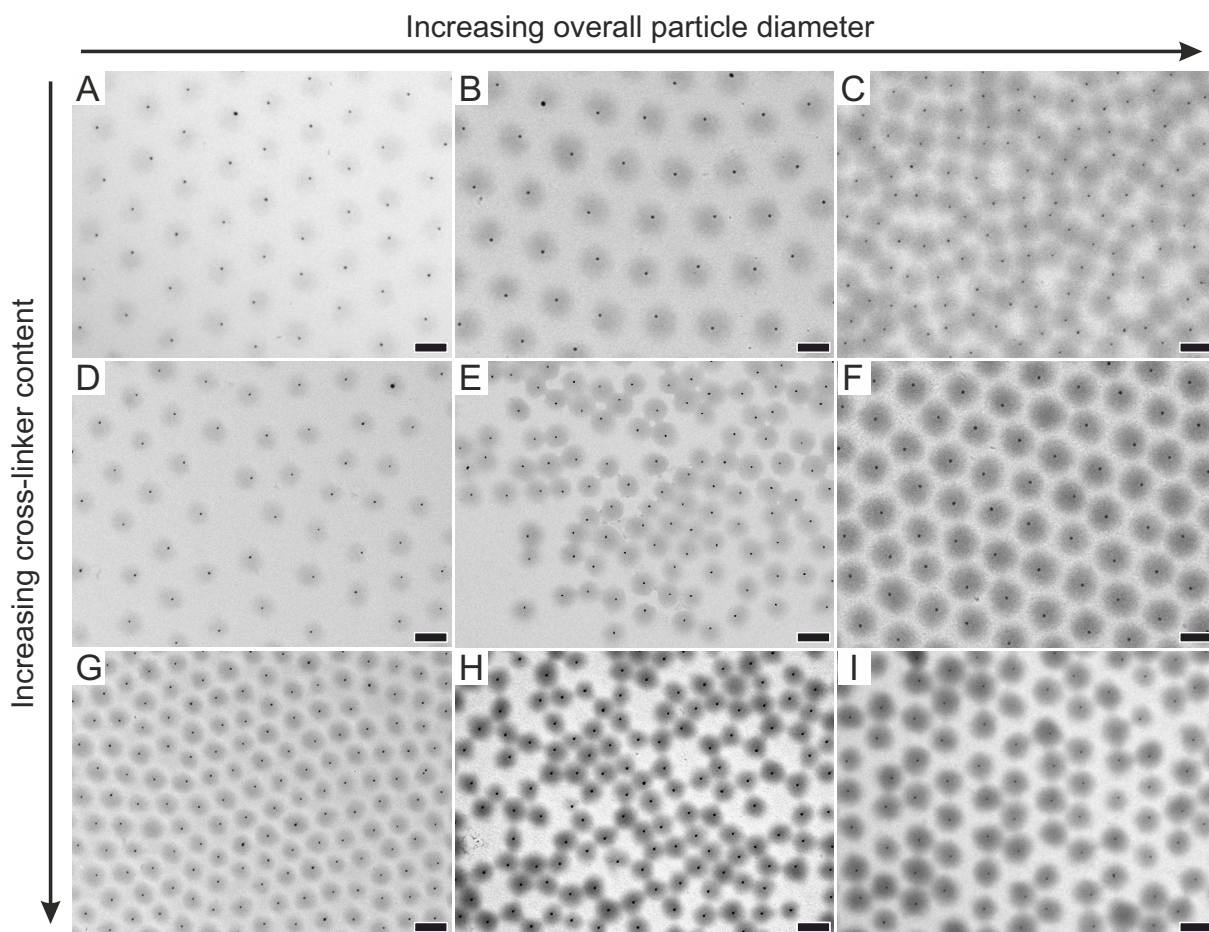


Figure 5.1: TEM images of the different Au-PNIPAM particles which differentiate in size and/or cross-linker content: A. $C_{15}S_{12.0}(10\%)$, B. $C_{15}S_{15.7}(10\%)$, C. $C_{15}S_{16.5}(10\%)$, D. $C_{15}S_{12.5}(15\%)$, E. $C_{15}S_{14.2}(15\%)$, F. $C_{15}S_{17.9}(15\%)$, G. $C_{15}S_{11.2}(25\%)$, H. $C_{15}S_{14.7}(25\%)$, I. $C_{15}S_{16.0}(25\%)$. The scale bars correspond to 250 nm.

Since Au has a higher electron density than the cross-linked PNIPAM shell both components can be easily distinguished, so that the CS structure is distinctly visible. All particles are monodisperse and a single Au nanoparticle per microgel particle is encapsulated. This highlights the reliability of the synthesis protocol even for larger batch sizes as

realized here. Au cores encapsulated in highly cross-linked polymer shells are located in the center of the polymer network. In contrast to this, the Au cores are more decentered for lower cross-linked samples. This is related to the mechanism of the seeded precipitation polymerization. As shown in Chapter 4, the polymer radicals precipitate onto the modified, hydrophobic Au nanoparticle surface. Hence, there is a weak attraction, but not a covalent link between the polymer shell and the Au nanoparticle. Therefore, the cross-linker density of the polymer network significantly influences the position of the Au core. Highly cross-linked samples that include smaller mesh sizes and size distributions in their polymer network are more effective in fixing the core in the center of the network structure as compared to samples with low cross-linker content. The position of the Au cores in the polymer network might additionally be influenced by the strong collapse of the shell due to drying of the sample in the course of the sample preparation and by the high-vacuum conditions in the TEM chamber. Further, a gray scale analysis of the cross-linked polymer shells revealed how the cross-linking density is correlated to the electron density or the appearance of the samples, respectively. The gray value of the background, i.e., the grid, was set to zero and the gray value of the Au core was taken as maximum. Comparing the gray values of the polymer shells, higher gray values were obtained for more rigid shells with increased cross-linker content. This is related to an increasing electron contrast and thus a darker appearance with higher cross-linker content. In addition, particles with increased cross-linker content seem to be more rigid in their shell structure as they cannot shrink to the same degree on the TEM grids as similar sized particles with a decreased cross-linker content. As the CS particles were monodisperse, they often arranged in hexagonally ordered areas as visible in the TEM images.

The crystallization of these particles strongly depends on their softness as it influences the pair interaction potential (see Section 2.1.2). To draw conclusions on the softness, swelling curves measured by temperature-dependent DLS were recorded. At temperatures below the VPTT, the particles are highly swollen with water. Above their VPTT, polymer-polymer interactions are favored leading to a collapse in their particle volume. This transition is well visible for all synthesized Au-PNIPAM particles on the lefthand side in Figure 5.2. The cross-linker density increases from A to C. Analyzing the swelling curves using a sigmoidal fit, transition temperatures between 33.5 and 36.5°C are obtained. These values coincide with VPTT in the literature measured for similar particles.^[55] Increasing values for the VPTT are achieved with decreasing particle diameter and increasing cross-linker content. The respective values of the VPTT of the different samples are listed in Table 5.2. Lowly cross-linked particles show their transition from the swollen to the collapsed state within a smaller range of temperatures as compared to higher cross-linked particles. This results in a steeper transition. Further, they release a larger volume of water which is related to their increased swelling capacity. This becomes

even clearer, if the evolution of the de-swelling ratio α (eq. 2.19), i.e., the hydrodynamic volume of the particles at a respective temperature $V_h(T)$ divided by the hydrodynamic volume of the particles in the swollen state, $V_h(20^\circ\text{C})$ is analyzed. The respective diagrams are shown on the right in Figure 5.2.

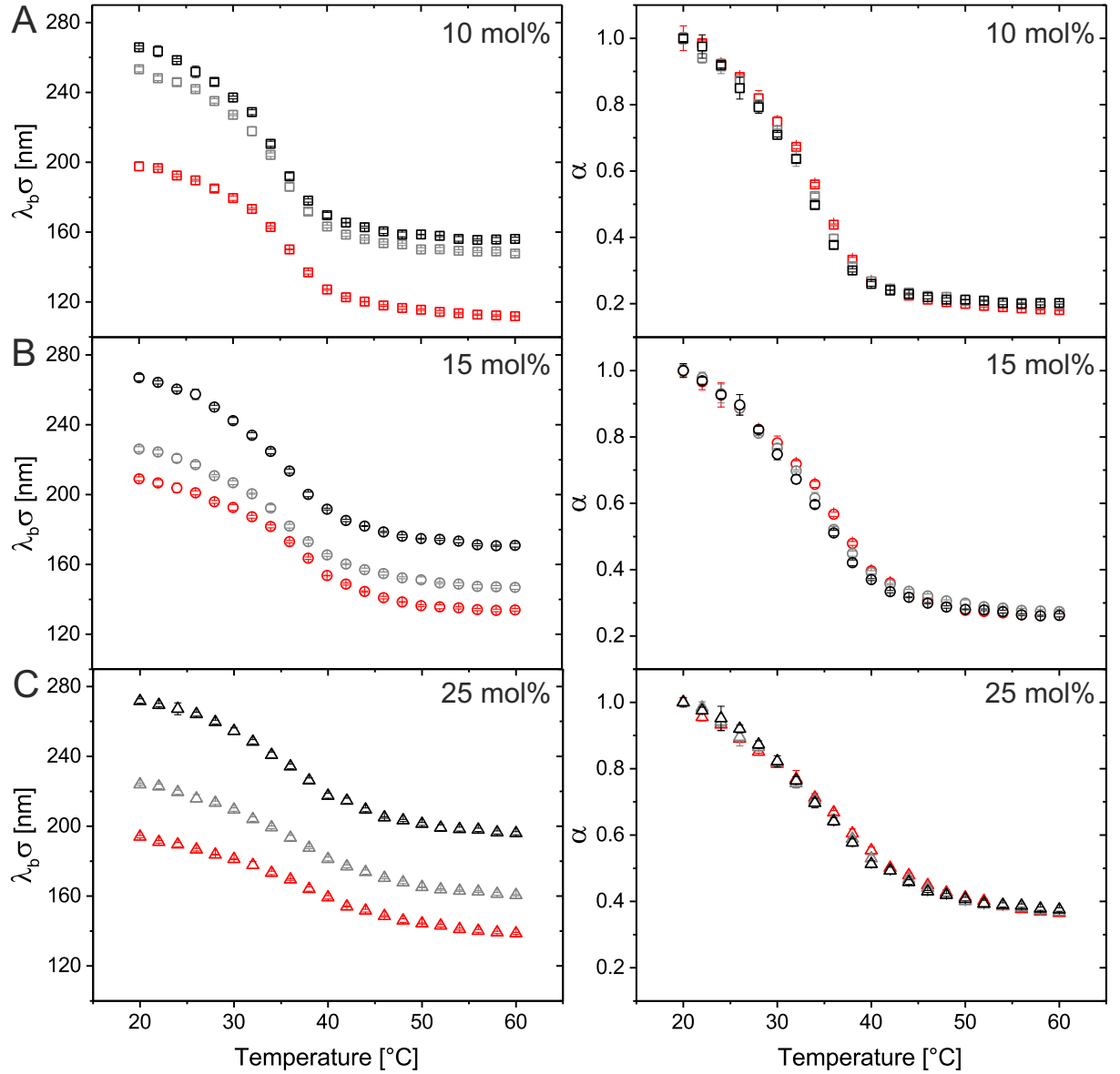


Figure 5.2: Results from temperature-dependent DLS experiments: A. samples with 10 mol% cross-linker content: $C_{15}S_{12.0}$ (10%), $C_{15}S_{15.7}$ (10%), $C_{15}S_{16.5}$ (10%), B. samples with 15 mol% cross-linker content: $C_{15}S_{12.5}$ (15%), $C_{15}S_{14.2}$ (15%), $C_{15}S_{17.9}$ (15%), C. samples with 25 mol% cross-linker content: $C_{15}S_{11.2}$ (25%), $C_{15}S_{14.7}$ (25%), $C_{15}S_{16.0}$ (25%). On the left, the temperature-dependent evolution of the hydrodynamic diameter $\lambda_b\sigma$ is shown. On the right, the de-swelling ratio α , i.e., $V_h(T)/V_h(20^\circ\text{C})$, is plotted versus the temperature. Identical colors correspond to the same NIPAM monomer feeds during synthesis for each cross-linker density: 0.01 M (red), 0.02 M (gray), 0.03 M (black).

Samples with a similar cross-linking, i.e., a similar softness, reveal a similar maximum swelling capacity. Indeed, this is visible in the depicted diagrams. The temperature-dependent evolution of α for samples with similar cross-linker content overlaps well and approaches similar de-swelling ratios at temperatures well above the VPPT. The maximum de-swelling ratios α calculated using the collapsed volume of the particles at 60°C are summarized in Table 5.2. Samples with 10, 15 and 25 mol% cross-linker content achieve average values of α around 0.19, 0.26 and 0.37, respectively. Particles prepared with different monomer feed concentrations, but the same nominal cross-linker content, show similar maximum de-swelling ratios. Hence, it can be assumed that their softness is similar and thus independent of their size. These results indicate again the robustness of the synthesis protocol even at large scales leading reliably to particles with similar swelling behavior, i.e., softness, if the nominal cross-linker content referred to the monomer NIPAM is kept constant. To conclude, the preparation of different sized particles displaying the same softness was successful allowing the investigation of their self-assembly in dependence on softness and size.

Table 5.2: VPPT and maximum de-swelling ratio α of the different CS systems.

CS system	VPPT [°C]	$\alpha = V_h(60^\circ\text{C})/V_h(20^\circ\text{C})$
C ₁₅ S _{12.0} (10%)	35.1	0.18
C ₁₅ S _{15.7} (10%)	34.0	0.20
C ₁₅ S _{16.5} (10%)	33.5	0.20
C ₁₅ S _{12.5} (15%)	35.9	0.26
C ₁₅ S _{14.2} (15%)	35.0	0.27
C ₁₅ S _{17.9} (15%)	34.2	0.26
C ₁₅ S _{11.2} (25%)	36.2	0.36
C ₁₅ S _{14.7} (25%)	35.7	0.37
C ₁₅ S _{16.0} (25%)	35.4	0.38

5.1.2 Optical Properties in the Dilute Regime

Both, the size as well as the cross-linker content of the particles influence the optical properties significantly.^[56] Initially, the optical properties in the dilute regime were studied in order to understand the absorbance properties of the single particles before self-assembled, crystalline samples were investigated which show additionally collective effects that influence the optics further. Figure 5.3 shows absorbance spectra of dilute aqueous dispersions of particles synthesized using different NIPAM feeds and cross-linker contents that are referred to the NIPAM concentration: 10 mol% (A), 15 mol% (B) and 25 mol% (C). For reasons of comparison, the spectra were normalized to the absorbance at 400 nm.

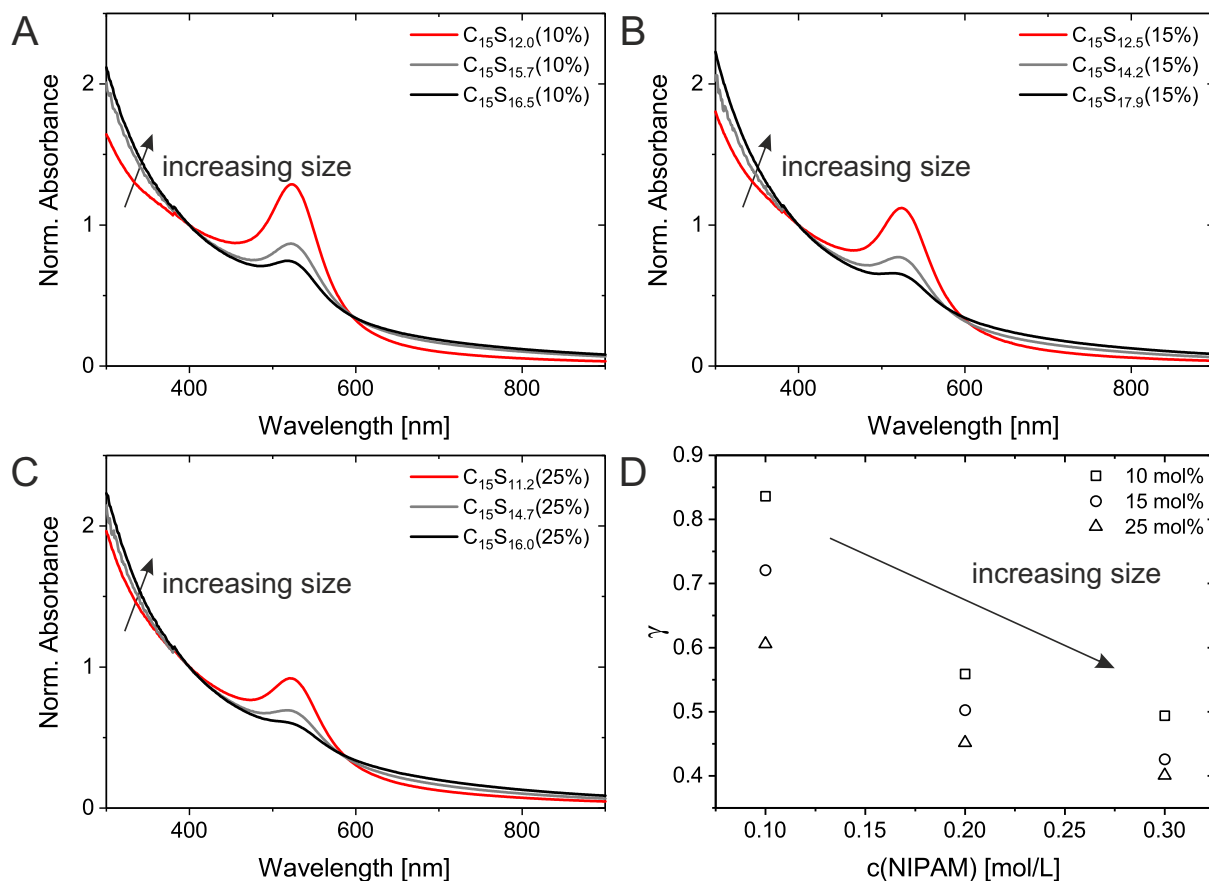


Figure 5.3: Absorbance spectra of dilute dispersions from Au-PNIPAM particles with different sizes and cross-linker densities (A. 10 mol%, B. 15 mol%, C. 25 mol%) measured at room temperature. All spectra are normalized to the absorbance at 400 nm. In D γ is plotted versus the monomer concentration of NIPAM that was employed in the different syntheses.

The spectra are influenced by two contributions which is on the one hand a scattering and on the other hand a plasmonic contribution originating from the LSPR of the Au nanoparticles. The scattering contribution which can be described by RDG scattering follows a power law dependence.^[55] Thus, it is more pronounced at low wavelengths. The maximum of the plasmonic contribution is located at wavelengths between 520 to 524 nm. Slightly different values are correlated to the magnitude of the scattering contribution: The scattering contribution is increased by increasing cross-linker contents as well as by larger overall particle sizes. A stronger scattering contribution results in a slight blue shift of the plasmon resonance position which is based on the mentioned power law dependence of scattering. As the encapsulated Au cores are only 15 nm in diameter, it can be assumed that their contribution to the spectrum is purely absorptive and that their scattering cross-section is negligible.^[184] Therefore, the scattering contribution can be clearly assigned to the polymer shell and the absorption contribution solely to the Au nanoparticles. As introduced in Chapter 4, γ is a suitable means to describe the balance of these two

contributions. Therefore, γ was calculated according to equation 4.1. In Figure 5.3 the resulting values are plotted versus the monomer concentration which was employed in the syntheses. This diagram indicates two main trends: First, there is a decrease in γ with larger particle dimension or monomer concentration (indicated by an arrow), respectively. This is related to the increase in scattering for increasing overall particle size but constant cross-linker content. Second, decreasing values of γ with increasing cross-linker contents were observed for samples with similar particle diameter. Again, this can be attributed to a stronger scattering contribution as compared to the plasmonic contribution in case of an increasing cross-linker content.

5.1.3 Optical Properties in the Crystalline State

Concentrated, aqueous dispersions of CS particles with weight concentrations ranging from 7 to 20 wt% were prepared. Note that in the following the volume fraction ϕ is used to compare the samples. The reason for this is as follows: The weight concentrations only give the solid content. Hence, they are not suited to compare self-assembled structures prepared of different particle types. In order to compare the samples, a molar mass independent quantity like the volume fraction is required. The volume fractions can be derived from absorbance spectra of the self-assembled samples as will be shown later on. The dispersions of different volume fractions were filled in quartz cells with a thickness of 100 μm . Some CS systems directly displayed strong iridescence after filling the cells. Subsequently, the thermoresponsive nature of the particles was used to induce/improve the crystallization by applying several annealing steps. Therefore, the dispersions were heated slightly above the VPTT. At these temperatures, polymer-polymer interactions become favored, so that the CS particles release water and collapse. Upon slow cooling to room temperature, water-polymer interactions are preferred resulting in the incorporation of water in the microgel network of the particles. During swelling, steric forces come into play which force the particles to crystallize/recrystallize at high enough volume fractions. This was directly visible by a strong iridescence. Repeating the annealing procedure usually supported the reduction of crystal defects and increased the overall crystal fraction.

Photographs prior (A) and after (B) the annealing procedure of a representative particle type ($\text{C}_{15}\text{S}_{15.7}(10\%)$) are shown in Figure 5.4. In contrast to A, the samples after the annealing procedure in B show iridescence which is already visible with the naked eye. This indicates a successful crystallization. Crystalline structures in the cm range were easily obtained without applying shear forces. UV-vis absorbance spectra recorded at room temperature are depicted below the photographs. Following the Beer-Lambert law, higher absorbances are measured with increasing volume fraction ϕ . The evolution of the absorbance spectra in A is similar to the results of the dilute samples, i.e., a scattering contribution and a plasmonic contribution are observed as previously discussed. The

spectrum (solid green line) of the sample with the lowest volume fraction ($\phi = 0.57$) shows additionally a diffraction (Bragg) mode at 567 nm. At this volume fraction, the viscosity of this sample is already sufficiently low. Hence, the colloids possess a high degree of freedom, so that they are able to order independently of the annealing step. After annealing (Figure 5.4 B), each of the different concentrated samples shows this additional feature in the absorbance spectrum. Increasing the volume fraction, this diffraction peak shifts towards shorter wavelengths which corresponds to smaller inter-particle distances in the crystalline superstructure. The depicted set of samples consisting of $C_{15}S_{15.7}(10\%)$ particles allows to shift the Bragg peak from the green/yellow wavelength range (550-575 nm) to the dark blue range (375-400 nm) of the visible spectrum. The colors used to describe the spectra in Figure 5.4 are related to the wavelength position of the Bragg peak in the visible spectrum, i.e., to the color of the sample.

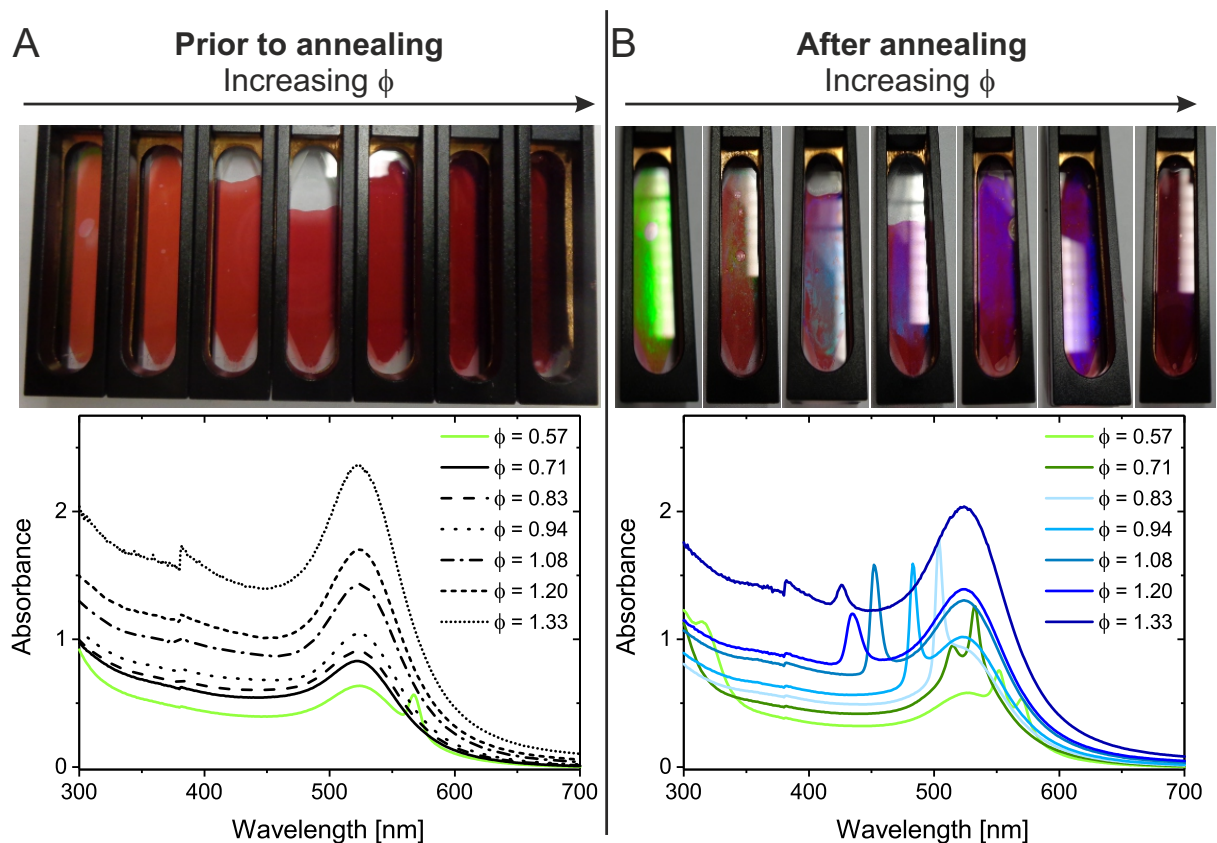


Figure 5.4: Crystal preparation for different concentrated dispersions of $C_{15}S_{15.7}(10\%)$ particles. Photographs and absorbance spectra before (A) and after (B) the annealing procedure which induces crystallization. The colors that are assigned to the absorbance spectra are related to the wavelength position of the Bragg mode in the visible spectrum.

The reversibility of the temperature-induced melting/recrystallization process is depicted in Figure 5.5 for a representative sample consisting of $C_{15}S_{14.7}$ (25%) particles ($\phi = 0.52$ at 25°C).

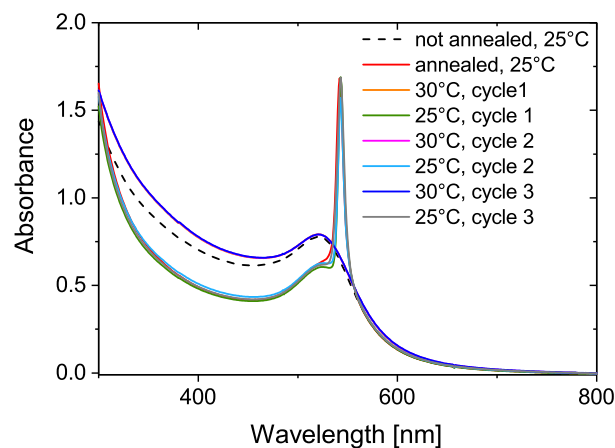


Figure 5.5: UV-vis absorbance spectra showing the reversibility of the crystallization process upon application of several heating (30°C)/cooling (25°C) cycles. The spectra were recorded using a dispersion containing $C_{15}S_{14.7}$ (25%) particles. Note that the spectra recorded at 30°C overlap.

A spectrum (dashed black line) prior to the first annealing step at 25°C is represented. A Bragg peak is not present which confirms the absence of iridescence that is notable by visual inspection. Annealing was performed at temperatures above the VPTT. After slow cooling to room temperature, the spectrum (solid red line) that displays a sharp Bragg mode could be recorded. All other spectra in Figure 5.5 were recorded upon applying three further annealing cycles. For this sample annealing at 30°C was sufficient to achieve volume fractions below the critical volume fraction that is necessary to induce crystallization. Increasing the temperature from 25 to 30°C caused a reduction of the hydrodynamic radius from 110 nm to 105 nm. However, the volume of each particle decreased by about 13% by increasing the temperature from 25 to 30°C , since the volume of the particle is correlated with R^3 . The spectra recorded after each annealing cycle (25°C) showed a sharp Bragg diffraction whereas the spectra during each annealing cycle (30°C) did not display a Bragg mode. Thus, switching between 25 and 30°C allowed to change the volume fraction and to switch between the crystalline and non-crystalline state of these particles, respectively. The difference in absorbance at wavelengths below 500 nm for spectra recorded at 30°C compared to the spectrum prior to annealing at 25°C is mainly related to an increased scattering contribution as a result of an increasing refractive index of the particles at higher temperatures. All spectra of the sample in the crystalline state display sharp diffraction peaks that overlap nicely representing the high reproducibility of this process. However, increasing numbers of annealing cycles result in a slight shift of the Bragg peak (≈ 1 nm) to longer wavelengths. Further, the full widths at

half maximum (FWHM) is slightly smaller. Both observations were previously reported in literature^[56] and are related to the reduction of crystal defects.

The absorbance spectra of dispersions at different volume fractions for all particle types recorded at room temperature are depicted in Figure 5.6.

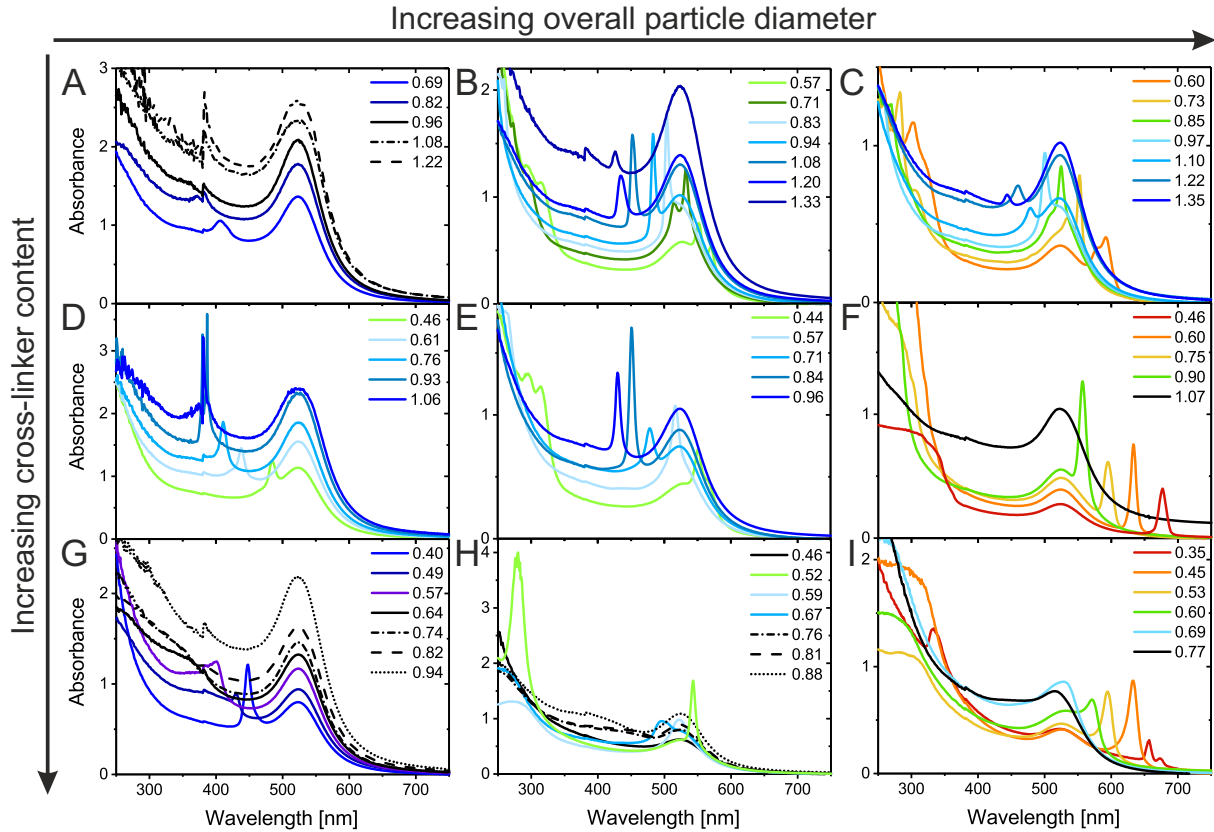


Figure 5.6: UV-vis absorbance spectra of self-assembled samples at different volume fractions ϕ (see diagram captions) consisting of Au-PNIPAM particles with different dimensions and cross-linker contents recorded at room temperature: A. $C_{15}S_{12.0}(10\%)$, B. $C_{15}S_{15.7}(10\%)$, C. $C_{15}S_{16.5}(10\%)$, D. $C_{15}S_{12.5}(15\%)$, E. $C_{15}S_{14.2}(15\%)$, F. $C_{15}S_{17.9}(15\%)*$, G. $C_{15}S_{11.2}(25\%)$, H. $C_{15}S_{14.7}(25\%)$, I. $C_{15}S_{16.0}(25\%)$. The colors used to describe the spectra correspond to the wavelength position of the Bragg peak in the visible spectrum, i.e., to the color of the sample.

* The spectrum of $C_{15}S_{17.9}(15\%)$ in Figure 5.6 F at $\phi = 0.46$ was recorded at 15°C .

First of all, it is highlighted that all particle types crystallize in a certain range of volume fractions which is indicated by diffraction peaks. The spectra highlight that the photonic bandgap can be easily tuned over the whole visible wavelength range by adjusting particle size, cross-linker content and volume fraction. The diffraction peaks are narrow displaying FWHM on the order of 10 nm. In agreement with the Beer-Lambert law, the absorbances increase with increasing volume fraction considering the spectra of a specific particle type. At wavelengths below the Bragg mode, the single-particle scattering which is very pronounced in the dilute state (see Section 5.1.2) is significantly decreased. This is related to a very efficient space allocation of the particles at high volume fractions. The particles

are in contact or even deform and/or interpenetrate. As a result, the Au nanoparticles are surrounded by a polymer matrix and scattering at the single particle interface can be neglected. The Bragg peak arises due to periodicity in the self-assembled structure which is mainly caused by refractive index modulations. These modulations arise due to the regular arrangement of gold nanoparticles and due to refractive index variations in the polymer matrix caused by the decreasing cross-linking density in the network structure of the single particles. Using the wavelength position of the Bragg peak λ_{diff} , characteristic parameters of the crystal lattice can be calculated. Assuming that all samples crystallize in a FCC structure which is justified by SANS measurements of similar particles in Section 5.2.4, d_{hkl} can be determined using eq. 5.1 with hkl representing the Miller indices. The (111) plane of the FCC lattice is expected to be oriented parallel to the flat walls of the sample cell leading to a scattering angle $\theta = 0^\circ$ and to $h = k = l = 1$. Apart from λ_{diff} , the average refractive index of the crystal $n_{crystal}$ is needed for this calculation. In contrast to λ_{diff} which can be determined with a low error of ± 1 nm leading to a relative error smaller than 0.3%, the average refractive index of the self-assembled samples $n_{crystal}$ is more defective and influences the calculation of d_{111} . $n_{crystal}$ is expected to be between the refractive index of H₂O ($n = 1.33$) and the refractive index of highly swollen particles ($n = 1.36$). The refractive index of highly swollen particles was calculated using two assumptions. First, the cross-linked PNIPAM reveals a refractive index of 1.53 which was determined for similar particles by a refractometer (see Section A.9 in the Appendix). Second, SANS measurements of similar particles revealed a water content of 85% in the PNIPAM shell (see Section 5.2.1). Accordingly, an average refractive index of the crystalline medium $n_{crystal}$ of 1.345 ± 0.015 was used for the calculation of d_{111} :

$$m_{diff} \lambda_{diff} = 2 \cdot d_{hkl} \cdot \sqrt{n_{crystal}^2 - \sin^2 \theta} \quad (5.1)$$

Here, m_{diff} is the diffraction order which is unity in this case. The lattice constant a for cubic systems can be determined using equation 2.34.

It is not easy to precisely access the volume fraction of soft particles.^[118] Here, it could be estimated using the results of the absorbance spectra. As previously mentioned, a FCC lattice could be assumed. Hence, eight particles are allocated at the corners of the unit cell, i.e., they participate to 1/8 in the unit cell. Another six particles are positioned at the planes and contribute to 50% to the unit cell. The number of particles per unit cell, the lattice constant a as well as the radius of the particles allows to calculate the volume fraction ϕ of each sample:

$$\phi = \frac{(3 + 1) \frac{4}{3} \pi R^3}{a^3} \quad (5.2)$$

The radius determined from DLS data, R_h , was used for this calculation, since it was the

most reliable particle radius from ensemble, even though this led to a slight overestimation of the volume fraction. Further, it was not clear if and how the particle dimension changes at very high volume fractions. Due to the soft character of the particles even volume fractions above the hard sphere limit for FCC packing of 0.74 are feasible since the particles can interpenetrate and/or deform at high concentrations.^[13] Nevertheless, using eq. 5.2 and R_h reasonable estimations of the volume fractions of the crystalline samples were accessible. Yet, volume fractions for concentrated dispersions which were not displaying a diffraction peak were not available by this method. Such dispersions were either fluid-like (lower volume fraction limit) or glassy (upper volume fraction limit). To ascribe volume fractions to these dispersions, the linear relationship between the weight concentrations and the calculated volume fractions could be used. The respective plots that show this procedure are depicted in the Appendix in Figure A.4.

Further, the inter-particle distances between the colloids in the crystal lattice could be calculated using equation 5.3 and the lattice constant a .

$$d_{cc} = a/\sqrt{2} \quad (5.3)$$

The results from the analysis of the absorbance spectra that include λ_{diff} , the FWHM of the Bragg peaks, d_{111} , the lattice constant a , the volume fraction ϕ_{UV-vis} determined from UV-vis spectra as well as the one determined using the regression curve ϕ_{fit} and d_{cc} are listed in Tables A.1 to A.3 in the Appendix. Increasing volume fractions lead to a shift of the Bragg mode to shorter wavelengths, i.e., to smaller lattice constants, for each sample. This implies as well a smaller inter-particle and lattice plane distance for increasing values of ϕ . Figure 5.7 exemplarily shows the influence of the size and of the cross-linker content of the CS particles on the self-assembled structures. Cross-sections of CS colloids at two different volume fractions, i.e., two different states of compression, are illustrated. On the left, the inter-particle distance for particles in contact is depicted and, on the right, the inter-particle distance at maximum compression is shown. First, the effect of particle size on the self-assembled structure is discussed. CS particles with larger dimensions show Bragg modes that are shifted to longer wavelengths as compared to smaller particles in a similar volume fraction range. This can be observed by comparing accessible positions of the Bragg modes in Figure 5.6 A to C, D to F and G to I. Increasing the dimensions of the colloids that assemble in a crystalline lattice, larger inter-particle distances can be achieved in the superstructures. This is schematically depicted in Figure 5.7 A and B. Comparing small (A) and large (B) particles with similar cross-linker density, it is quite obvious that larger particles can access increased inter-particle distances in a self-assembled crystalline lattice. As compared to smaller particles of the same softness, the large particles approach the glassy state at increased inter-particle distance (see righthand side in Figure 5.7 A and B). To conclude, different sized particles with similar cross-linker content show diffraction

modes over a similar range of wavelengths. However, the wavelength positions of the Bragg peaks, that they can access, are significantly influenced by their size. Hence, the particle diameter is a crucial parameter to manipulate the diffraction behavior of the samples.

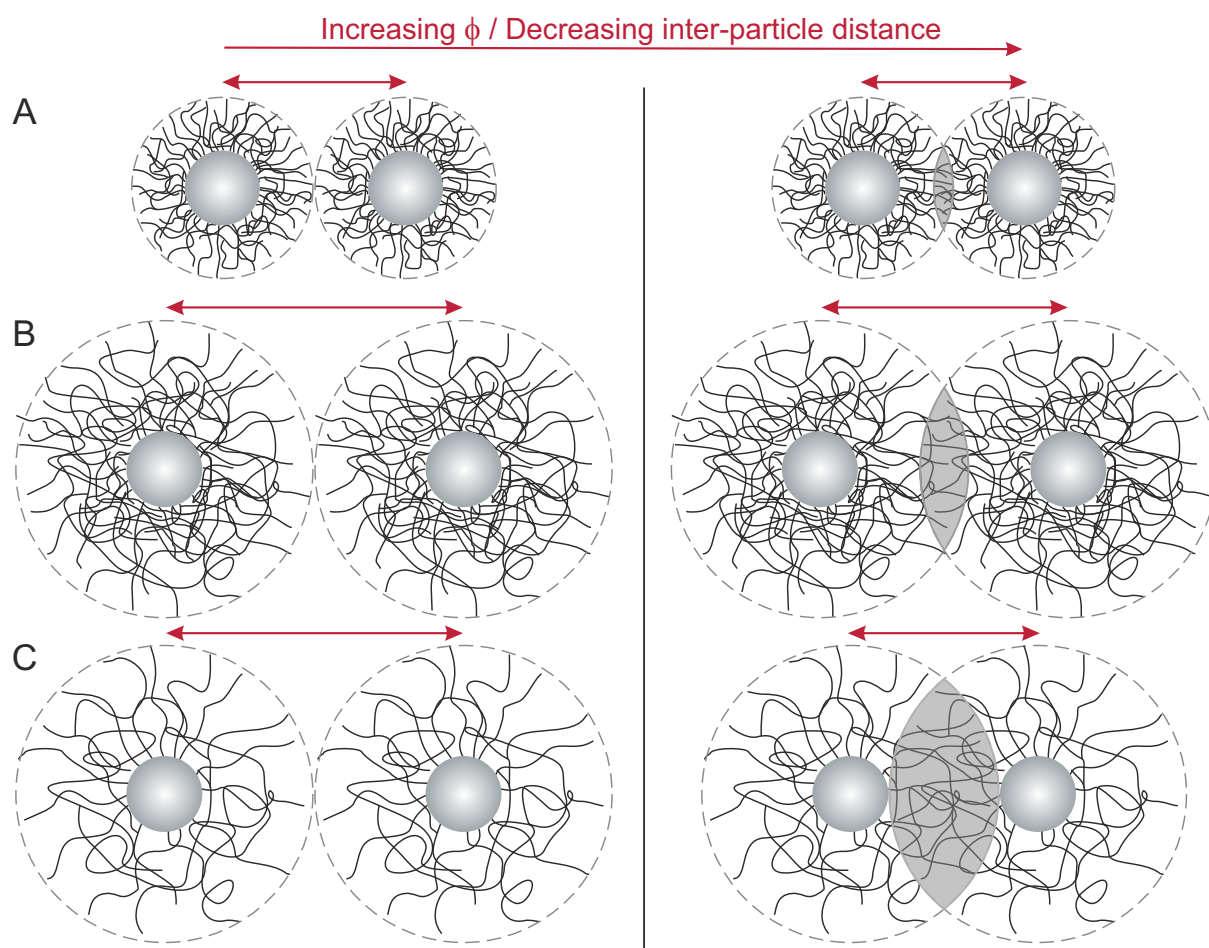


Figure 5.7: Scheme showing the cross-section of two representative CS particles at low (left) and at high (right) volume fraction in a self-assembled structure: The CS particles in A have a smaller dimension, but similar cross-linker density as the CS particles in B. The CS particles in B and C have a similar dimension. However, the CS particles in C exhibit a lower cross-linker content as the CS particles in B. The red arrows indicate the inter-particle distance. The overlap volume is indicated by the gray-shaded area.

In addition to these observations, the cross-linker density, i.e., the softness, has an effect on the self-assembly. The cross-linked PNIPAM shells display a radial density profile with a higher cross-linker density in the inner volume element and a decreasing cross-linker density towards the periphery which contains loosely- or non-cross-linked chains. This is caused by the faster consumption of the cross-linker BIS compared to the monomer NI-PAM in the synthesis.^[110,111] The distribution of the cross-linker content is also indicated in Figure 5.7. Particles with a low cross-linker density crystallize over a broad range of

volume fractions as shown in the spectra in Figure 5.6 B and C. Their softness enables lowly cross-linked particles to increase the range of realizable inter-particle distances, i.e., length scales in the crystal structure, as they can strongly interpenetrate. This is schematically illustrated in Figure 5.7 B and C. The particles in B and C have the same dimension, but the cross-linker density is increased in the case of the CS particles in B. This scheme illustrates that lowly cross-linked samples (C) can interpenetrate over a greater extent as compared to highly cross-linked samples (B). The analysis of the recorded absorbance spectra revealed that the lowly cross-linked samples crystallized at volume fractions far beyond the hard sphere limit of 0.74 achieving values of $\phi=1.35$ ($C_{15}S_{16.5}(10\%)$). In contrast to this, highly cross-linked samples already reached the glass phase, i.e., the state of a frustrated, glassy system, at volume fractions of $\phi = 0.88$ (Figure 5.6 H) and $\phi = 0.77$ (Figure 5.6 I). In addition, the lowly cross-linked samples are assumed to be more tolerant regarding defects in the crystal structure due to their soft character. Further, the Bragg modes recorded for lowly cross-linked samples are often sharper and thus indicate smaller values of FWHM (see Tables A.1 to A.3 in the Appendix).

Moreover, at low volume fractions of 0.3-0.4 (highly cross-linked) or 0.5-0.6 (lowly cross-linked) some samples display two diffraction peaks which are in close vicinity. These samples are assumed to display a liquid crystalline character. This implies that the particles could arrange in crystalline lattices with two different lattice constants, i.e., in lattices of different inter-particle distances. This is supported by the appearance of the samples, since areas of iridescence with different colors could be identified by the naked eye. Therefore, these two Bragg modes might be an indication for the coexistence of two crystalline phases. In addition, in some spectra a second Bragg peak is observed at low wavelengths. This mode corresponds to the second-order Bragg mode which appears at approximately $\lambda_{diff}/2$. For some samples this peak appears below 300 nm in the ultraviolet range of the spectrum. However, due to the spectral limit of the cuvettes extinctions of the sample below 300 nm cannot be reliably measured. Hence, in some cases the second peak is cut off.

Figure 5.8 A represents the position of the diffraction peak of the different particle types as a function of $c^{-1/3}$. In the literature, this plot is used to draw conclusions on the crystalline lattice.^[56,185] Note that $c^{-1/3}$ is directly proportional to ϕ . In order to draw further conclusions on this plot, the parameters that influence the diffraction peak need to be investigated in dependence on the volume fraction. According to eq. 5.1 these are: n , m_{diff} , θ and d_{hkl} . Increasing volume fractions slightly increase the refractive index within the sample. However, the influence on λ_{diff} is negligible. The scattering angle and the diffraction order are independent of $c^{-1/3}$ or the volume fraction. Hence, λ_{diff} is mainly influenced by d_{hkl} , since d_{hkl} decreases with increasing ϕ . Figure 5.8 A shows a linear relationship of λ_{diff} and $c^{-1/3}$ for each particle system. Due to the direct proportionality

of λ_{diff} and d_{hkl} , it can be assumed that the lattice type remains similar with increasing volume fraction for each particle system.

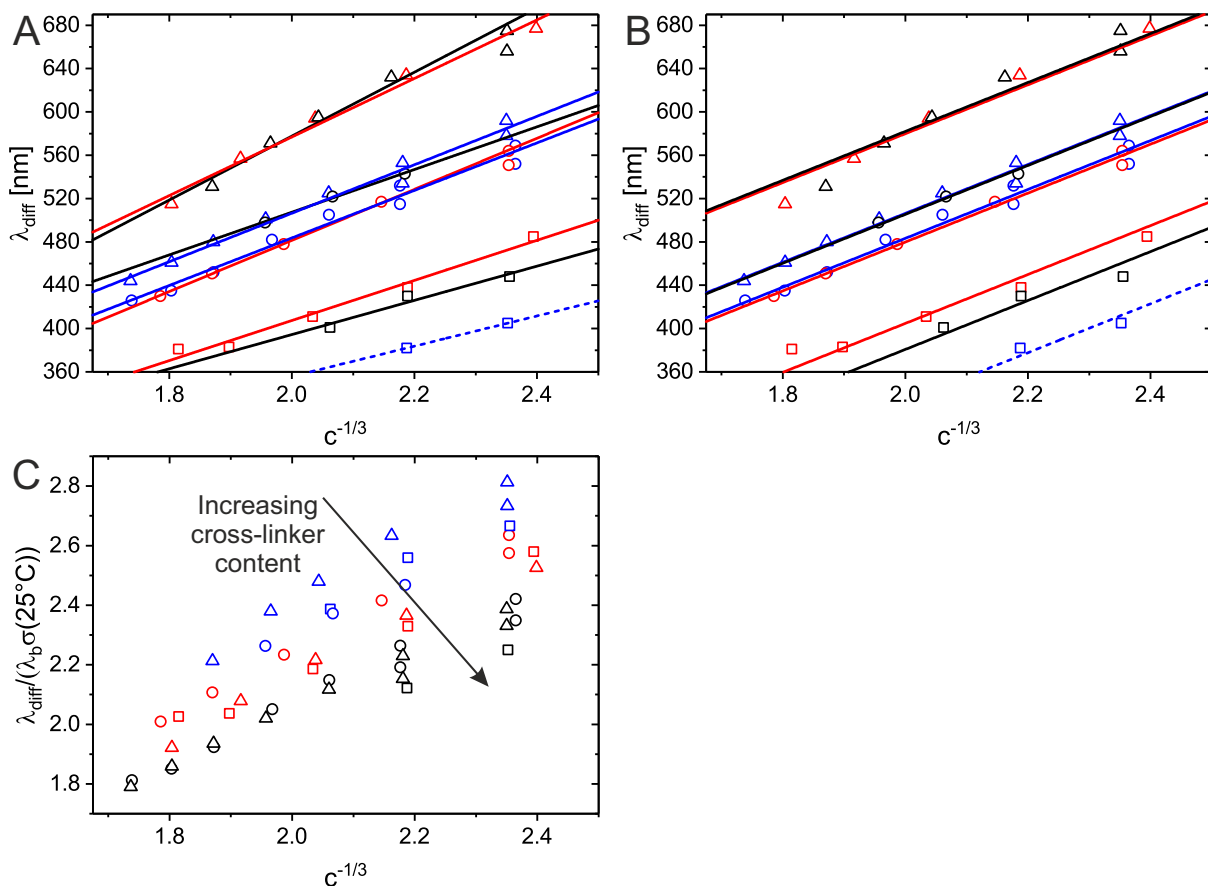


Figure 5.8: A. Position of the diffraction peak of the respective samples as a function of $c^{-1/3}$. The solid lines are linear fits to the data. B. Same plot as in A, however, a constant slope was applied in order to fit the data (solid lines). C. Position of the diffraction peak of the respective particles normalized by the hydrodynamic diameter at 25°C as a function of $c^{-1/3}$. The blue symbols display the samples with 10 mol% cross-linking: square ($C_{15}S_{12.0}(10\%)$), circle ($C_{15}S_{15.7}(10\%)$), triangle ($C_{15}S_{16.5}(10\%)$). The red symbols label the 15 mol% cross-linked samples: square ($C_{15}S_{12.5}(15\%)$), circle ($C_{15}S_{14.2}(15\%)$), triangle ($C_{15}S_{17.9}(15\%)$). The black symbols correspond to the 25 mol% cross-linked samples: square ($C_{15}S_{11.2}(25\%)$), circle ($C_{15}S_{14.7}(25\%)$), triangle ($C_{15}S_{16.0}(25\%)$). The regression curves in A and B considering the data points of $C_{15}S_{12.0}(10\%)$ might be defective as they are only based on two data points. To highlight this uncertainty, they are described by a dashed line. Note that the fit curves of $C_{15}S_{16.5}(10\%)$ and $C_{15}S_{14.7}(25\%)$ in B overlap.

Comparing the data of all different particle types in Figure 5.8 A, they could be fitted using regression curves with similar slopes. In Figure 5.8 B these data was reasonably fitted using a uniform slope for all regression curves. Again, the influences of n , m_{diff} , θ and d_{hkl} on λ_{diff} were considered for a reasonable comparison between the different particle types. First, it was focused on the refractive index n . Figure A.9 in the Appendix shows the refractive index determination of similar Au-PNIPAM particles with different degree

of cross-linking. Despite the varying cross-linker content, the refractive index was similar for these samples. Therefore, the refractive indices of the samples in Figure 5.8 B were assumed to be also similar. θ and m_{diff} are as well not influenced by the particle type. Consequently, λ_{diff} is again mainly influenced by d_{hkl} . As the data of all different particle types could be fitted using regression curves with a uniform slope, the samples can be assumed to crystallize in the same crystal lattice in the range of investigated volume fractions.

In Figure 5.8 C the same plot is depicted whereas the position of the Bragg peak is here normalized using the hydrodynamic diameter of the particles at 25°C in order to achieve a master curve. Since the normalization using R_h is not fully correct, a master curve could not be obtained. R_h overestimates the interaction particle radius. The radius of the particles in the superstructures depends on the volume fraction as the particles might shrink, interpenetrate and/or deform particularly in the highly concentrated samples.^[13] Even though the presented plot could not be normalized correctly, it gives a rough estimation of the position of the Bragg peak for a respective particle type.

5.2 Influence of the Gold Core

To get insights in the role of the absorbing nanocrystal Au core, the photonic and structural properties of 3D superstructures composed of CS particles and their respective pitted counterparts were studied. For this purpose, two types of Au-PNIPAM particles $C_{15}S_{16.2}(10\%)$ and $C_{15}S_{14.6}(25\%)$ were synthesized. The shells included different contents of cross-linker and thus revealed different softnesses. Their pitted counterparts $C_dS_{16.2}(10\%)$ and $C_dS_{14.6}(25\%)$ served as non-plasmonic reference. The subscript d implies dissolved, indicating the dissolution of the Au core. The core size and the bulk shell-to-core ratio λ_b are similar for the two particle types with different cross-linking. Hence, they are not always mentioned in the particle notations in the following. Figure 5.9 schematically illustrates the CS particles with two different cross-linker contents and their pitted analogues, C_dS particles, after the dissolution of the Au cores.

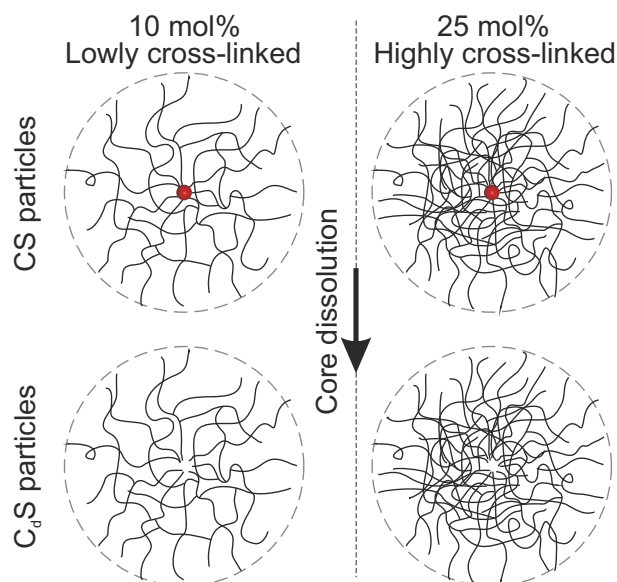


Figure 5.9: Schematic sketch that depicts the CS particles $C_{15}S_{16.2}(10\%)$ and $C_{15}S_{14.6}(25\%)$ and their respective pitted counterparts $C_dS_{16.2}(10\%)$ and $C_dS_{14.6}(25\%)$.

Initially, it was focused on the success of the Au core dissolution using microscopic and spectroscopic methods. Further, scattering techniques like SLS, DLS and SANS were employed to establish that the size, swelling behavior and network morphology were not affected by the harsh dissolution process of the Au core. Electrophoretic mobility measurements allowed to exclude changes in the surface charge of CS and the respective C_dS particles. The accordance of the mentioned properties was a prerequisite for the subsequent comparison of the crystallization behavior of CS particles and their pitted counterparts. Regarding the analysis of the crystalline structures, it was focused on the photonic properties using far-field extinction spectroscopy and on the structural charac-

terization employing SANS. Combining both methods, correlations between the particle structure, the optical properties and the superlattice structure could be deduced.

5.2.1 Structural Prerequisites of Core-Shell and Pitted Particles

The structure of the CS particles and their pitted analogues was analyzed using TEM. Representative TEM images of the CS particles are shown in Figure 5.10 A (CS(10%)) and B (CS(25%)).

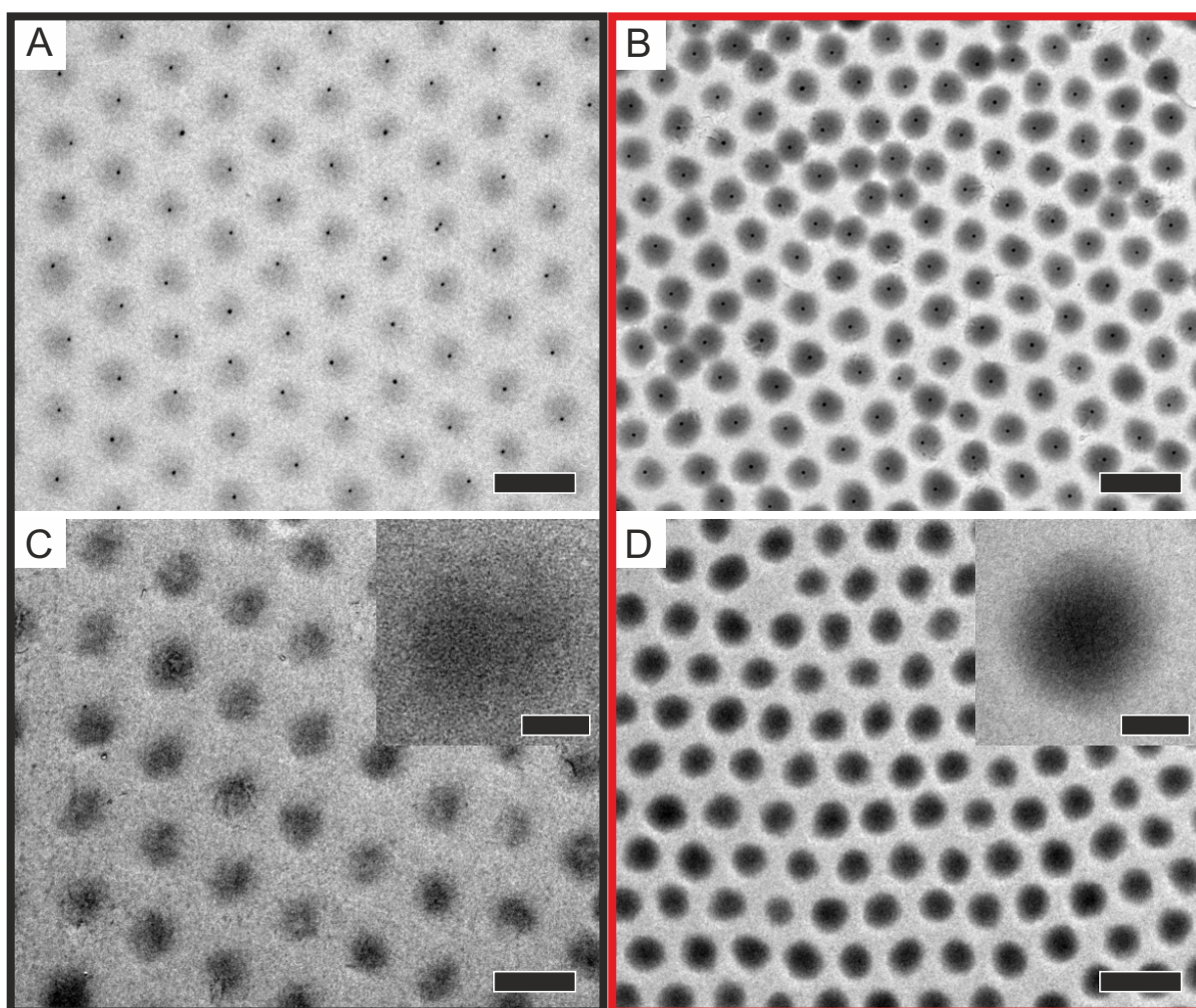


Figure 5.10: Representative TEM images of CS and C_dS particles with 10 mol% (black frame) and 25 mol% (red frame) cross-linker content: A. $C_{15}S_{16.2}(10\%)$, B. $C_{15}S_{14.6}(25\%)$, C. $C_dS_{16.2}(10\%)$, D. $C_dS_{14.6}(25\%)$. The scale bars are 500 nm. In the insets in the upper right corners in C and D magnified images of single particles after the dissolution of the gold core are shown. Here, the scale bars are 100 nm.

The CS structure is well visible as a result of the difference in electron contrast between Au and cross-linked PNIPAM. Analyzing different positions on the TEM grids, it is found that 99.6% of the CS(10%) and 98.3% of the CS(25%) particles have a single Au core

encapsulated. Regarding the different cross-linker contents of the particles, the same observations as discussed in detail in Section 5.1.1 are made. A lower cross-linker content of the microgel shell (CS(10%)) results in a more decentered Au core and a decreased electron contrast, i.e., a brighter appearance of the shell as compared to an increased cross-linker content (CS(25%)). Subsequently, half of the CS(10%) or CS(25%) material was treated with aqua regia to dissolve the gold core. TEM images of the resulting pitted microgel particles are shown in Figure 5.10 C ($C_dS(10\%)$) and D ($C_dS(25\%)$). The images clearly reveal that the dissolution was successful. This is particularly evident in the magnified TEM images in the upper right corner of C and D. It should be noted that contrast and brightness were adjusted more drastically for the images in C and D as for the residual ones. As expected the stronger cross-linked, pitted particles $C_dS(25\%)$ appear more distinct (darker) due to their enhanced electron contrast as compared to the $C_dS(10\%)$ particles. For all particles shown in Figure 5.10 A-D two-dimensional lattices with regular inter-particle distances and hexagonally ordered domains are observed indicating the low polydispersity of the particles. The non-close-packed character of these lattices corresponds to sample drying and the high-vacuum conditions in the TEM leading to collapsed PNIPAM shells.

In the following, the particle properties in the dilute regime are evaluated. Therefore, the particles were compared regarding their network structure, size and surface charge. Figure 5.11 shows the temperature-dependent evolution of the hydrodynamic diameter $\lambda_b\sigma$ between 20 and 50°C.

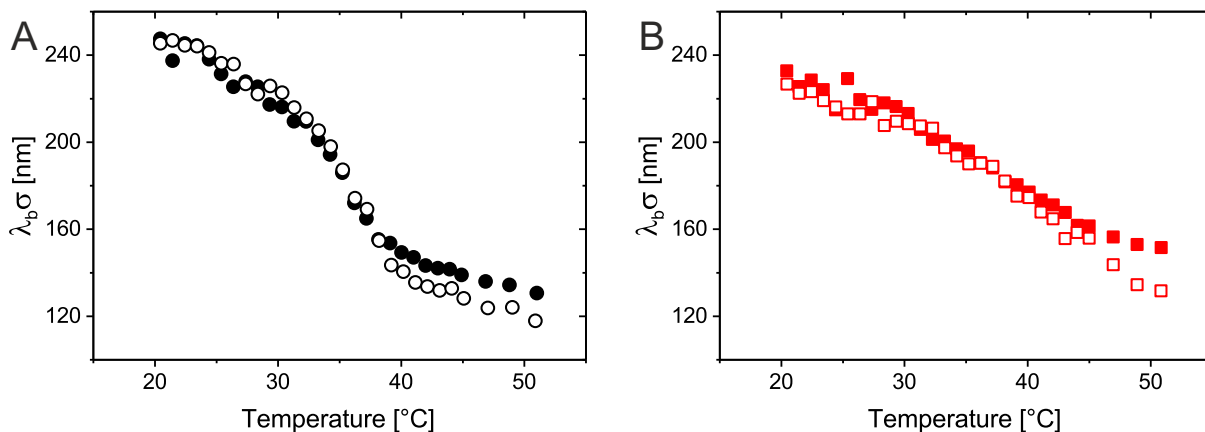


Figure 5.11: Temperature-dependent evolution of the hydrodynamic diameter $\lambda_b\sigma$ of dilute dispersions in D_2O : A. CS(10%) (filled black circles) and $C_dS(10\%)$ (empty black circles), B. CS(25%) (filled red squares) and $C_dS(25\%)$ (empty red squares). The error bars are on the order of the symbol size.

All samples reveal the typical volume phase transition behavior as already discussed in the previous chapters with VPTT between 35 to 37°C. Further, the evolution of the volume phase transition agrees very well for CS particles and their pitted analogues with

the same cross-linker content except for slight deviations at high temperatures. Thus, it can be concluded that the volume phase transition is not affected by the harsh etching procedure of the Au cores. Consequently, the chemical composition of the network must be still similar and oxidation of the amide groups as well as degradation can be excluded, otherwise the thermoresponsiveness would be clearly changed. These results enable the comparison of the optical and structural properties in the crystalline structures later on. Comparing the different cross-linked particles, the transition to decreased diameters occurs over a smaller temperature range with a very clear inflection point for the lowly cross-linked samples in contrast to the highly cross-linked ones. The latter ones are more rigid resulting in a transition over a broader temperature range. In addition, they display a reduced swelling capacity as compared to softer particles with 10 mol% cross-linker content. In Figure 5.12 the relation between swelling capacity and cross-linker content is even more evident.

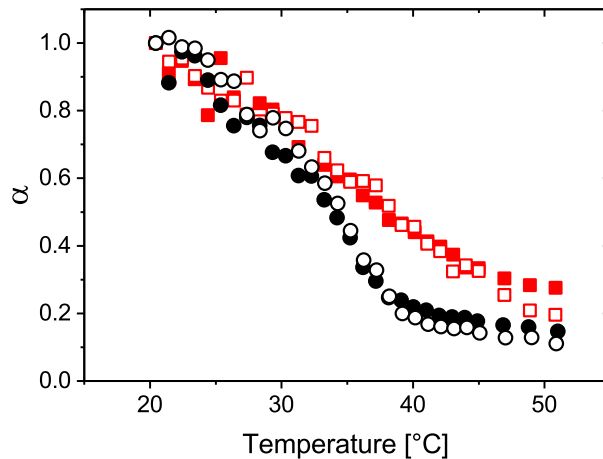


Figure 5.12: Temperature-dependent evolution of the de-swelling ratio α of $C_{15}S_{16.2}$ (10%) (filled black circles), $C_dS_{16.2}$ (10%) (empty black circles), $C_{15}S_{14.6}$ (25%) (filled red squares) and $C_dS_{14.6}$ (25%) (empty red squares). The error bars are in the range of the symbol size.

It shows the temperature-dependent evolution of the de-swelling ratio α in the temperature range between 20 and 50°C. α is the ratio of the hydrodynamic volume $V_h(T)$ at certain temperature in the mentioned temperature range divided by V_h in the swollen state, i.e., at 20°C (eq. 2.19). All particles display a constant decrease of α indicating a continuous de-swelling as function of the temperature. The maximum decrease of α at the highest measured temperature is more pronounced for samples with lower cross-linker content ($\alpha(50^\circ\text{C}) \approx 0.15$ for 10 mol% samples, $\alpha(50^\circ\text{C}) \approx 0.24$ for 25 mol% samples). Further, the evolution of α for CS particles (filled symbols) and C_dS particles (empty symbols) matches very well. This highlights again that the polymer network structure is neither affected by the dissolution procedure nor by the absence or presence of the Au cores.

In addition, angular-dependent dynamic and static light scattering experiments of dilute dispersions of CS and C_dS particles with both cross-linker contents were performed at 25.6°C. The recorded intensity-time autocorrelation functions obtained by DLS were analyzed using the CONTIN algorithm. The resulting average relaxation rates are plotted versus q^2 in Figure 5.13.

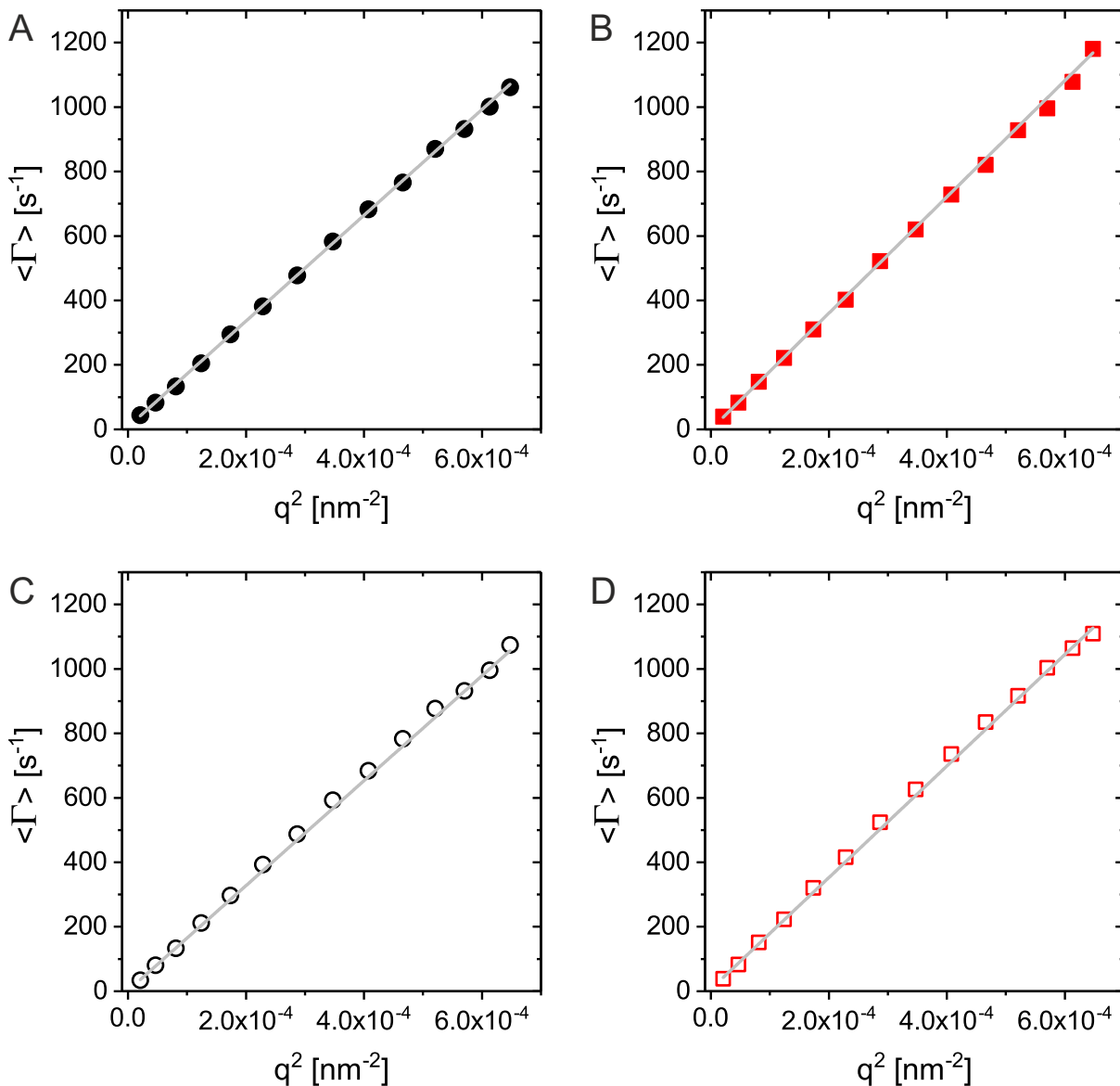


Figure 5.13: Average relaxation rates $\langle \Gamma \rangle$, that were obtained from CONTIN analysis of the intensity-time autocorrelation functions measured at 25.6°C, as a function of q^2 : A. $C_{15}S_{16.2}$ (10%), B. $C_{15}S_{14.6}$ (25%), C. $C_dS_{16.2}$ (10%), D. $C_dS_{14.6}$ (25%). The solid gray lines are linear fits to the data. The error bars are in the range of the symbol size.

Linear regression curves with intercepts close to zero (solid gray lines) were used to fit the data. This indicates that only translational diffusion is probed. The translational diffusion coefficient D_T is calculated using the slope of the fits. Inserting D_T in the Stokes-

Einstein equation (eq. 2.17) provides the hydrodynamic radius R_h listed in Table 5.3. The respective Guinier plots obtained by SLS are depicted in Figure 5.14. Here, $\ln(I)$ is plotted as a function of q^2 .

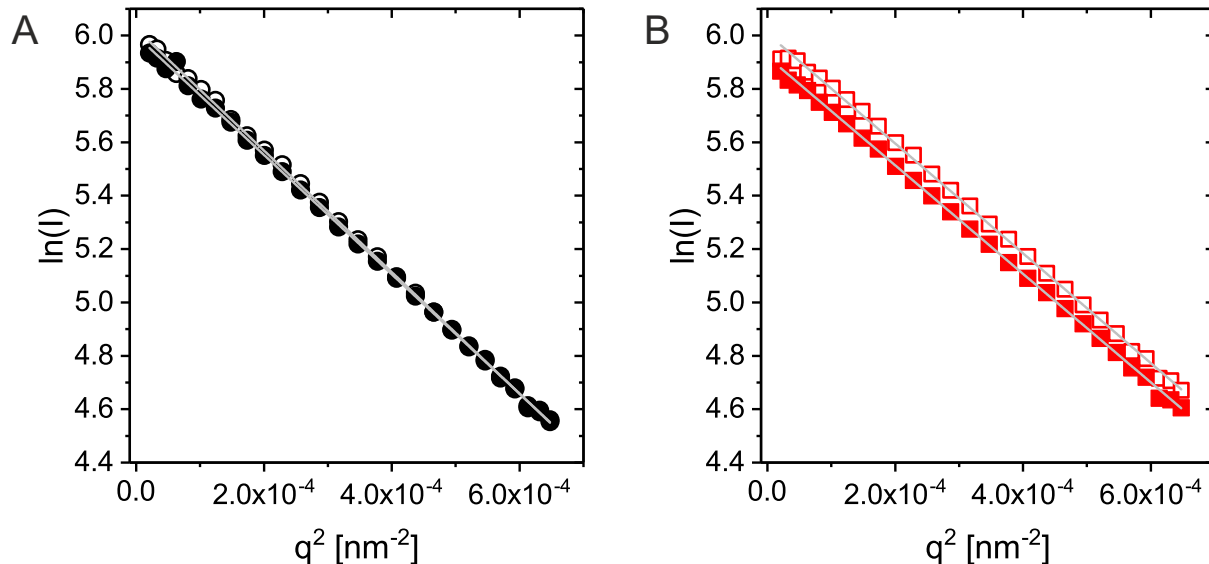


Figure 5.14: Guinier analysis depicted for data recorded at 25.6°C: A. $C_{15}S_{16.2}(10\%)$ (filled black circle) and $C_dS_{16.2}(10\%)$ (empty black circle), B. $C_{15}S_{14.6}(25\%)$ (filled red square) and $C_dS_{14.6}(25\%)$ (empty red square). The gray solid lines are linear regression curves. The error bars are in the range of the symbol size.

Due to the linear evolution of $\ln(I)$ versus q^2 , the Guinier approximation (eq. 2.20) could be used in the whole measured q -range. The slope of these fits allowed to calculate the radius of gyration R_g for the different samples. The results are summarized in Table 5.3. Within the experimental error R_g agreed very well for samples with the same cross-linker contents. Comparing the values of R_g and R_h for samples with different cross-linker content, it is noticed that the radii are slightly reduced for stronger cross-linked samples. Since all particles were prepared with the same monomer concentrations, the smaller dimension can be attributed to the denser network of highly cross-linked samples. Further, a comparison of the ratio R_g/R_h of the samples with the theoretically expected value for hard spheres, $\sqrt{\frac{3}{5}} = 0.775$, was performed. Here, all calculated ratios of the samples are very similar, however, higher cross-linked samples result in slightly larger values. All in all, the calculated ratios are smaller than the value found for hard spheres. This can be ascribed to the inhomogeneous network structure in the PNIPAM shell with a decreasing cross-linker density from the center to its periphery. The density gradient affects R_h more than R_g . This finding is in agreement with previous studies of these particles in the literature.^[154] Summarizing, the etching of the Au core had no influence on the dimensions of the particles.

Table 5.3: The hydrodynamic radius R_h , the radius of gyration R_g and the ratio of both R_g/R_h as determined from angular-dependent DLS and SLS measurements at 25.6°C as well as the results from electrophoretic mobility μ_e measurements at 25°C from salt-free dispersions at neutral pH and the respective ζ -potentials derived using the Smoluchowski model.

Sample	R_h [nm]	R_g [nm]	R_g/R_h	μ_e [$\mu\text{mcm/Vs}$]	ζ -potential [mV]
C ₁₅ S _{16.2} (10%)	123 ± 1	82 ± 1	0.67	-3.2 ± 0.1	-41 ± 1
C _d S _{16.2} (10%)	123 ± 1	83 ± 1	0.67	-2.8 ± 0.1	-35 ± 1
C ₁₅ S _{14.6} (25%)	111 ± 1	78 ± 1	0.70	-3.0 ± 0.1	-38 ± 1
C _d S _{14.6} (25%)	116 ± 1	79 ± 1	0.68	-3.1 ± 0.1	-40 ± 1

In the following, electrophoretic mobility μ_e measurements are presented. The measurements allow to draw conclusions on the particle charge which has a major impact on the interaction potential and thus on the self-assembly of the particles. However, μ_e is not directly linked to the surface charge, it only shows the same tendencies. The values of μ_e are used to calculate the ζ -potential according to the Smoluchowski model. The respective results are listed in Table 5.3. As an anionic radical initiator (PPS) was used, all measured values for μ_e are negative and in a range between -3.2 and -2.8 $\mu\text{mcm/Vs}$. Thus, the calculated ζ -potentials are also negative and in a range of -(35-41) mV for all samples. Further, the values are typical for Au-PNIPAM particles prepared by the used synthesis protocol.^[186] Consequently, the similar ζ -potentials of the samples allow to conclude that the particles' surface charges were not changed during the etching procedure of the Au. Because of the relatively small dimensions of the particles, SLS resolves solely the Guinier region and not the form factor $P(q)$ of the particles. Additionally, the wavelength in light scattering experiments is too long to gain insight into the internal network structure of the objects. In contrast to this, the smaller wavelengths available in neutron scattering experiments allow to measure larger q -values which reveal details on the network structure of the particles. Radially averaged SANS profiles of all particles in the dilute regime dispersed in D₂O at 25.6°C are shown in Figure 5.15. A first comparison of all samples already displays the similar evolution of the scattering intensity: At low q -values, the Guinier plateau is visible, i.e., constant scattering intensities are measured. In the medium q -range, two form factor minima are identified. Finally, at large q -values, the profiles achieve again a plateau. Particularly, the scattering profiles of CS and C_dS particles with the same cross-linker content agree very well showing no remarkable distinctions. The software *SASfit* by Kohlbrecher was employed to analyze the data using equation 2.32.^[157] Theoretical background regarding the fit model is described in Section 2.4.2.2. The determined hydrodynamic radii served as start values for the fit parameters in *SASfit*. Scattering contrasts were extracted from literature.^[154] The used

model described in equation 2.32 comprises a form factor contribution and an Ornstein-Zernike (OZ) contribution. To gain maximal accordance of fit and experimental data, the method of minimizing χ^2 was performed. Several iterations were conducted for each fit parameter until minimal values for χ^2 were obtained. Next, all decisive fit parameters for each contribution were optimized until again minimal values of χ^2 were received. This process was repeated until no changes of the fit parameters were observed anymore. The fits (solid gray lines) depicted in Figure 5.15 A and B were obtained using equation 2.32 and considering a Gaussian polydispersity of the particle dimension.

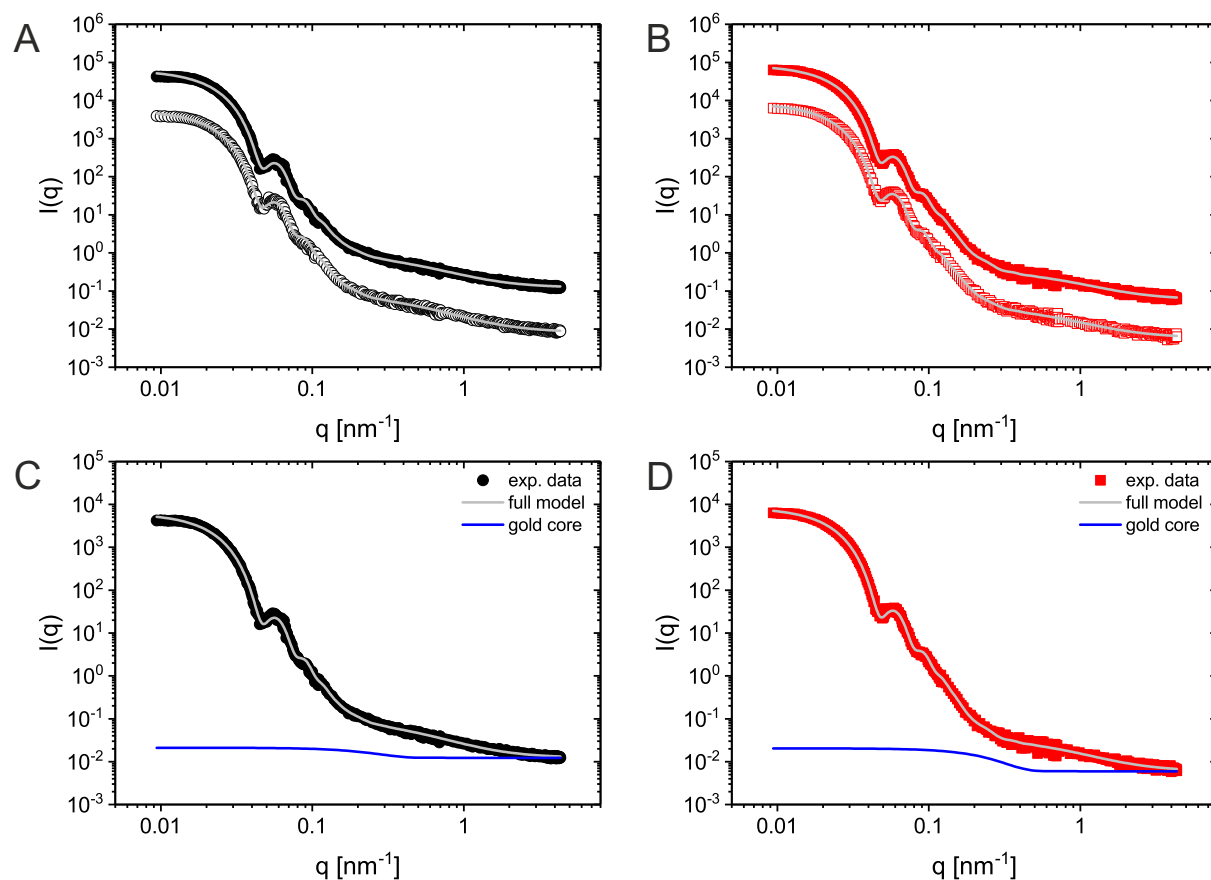


Figure 5.15: Radially averaged SANS profiles and their respective fits (solid gray line) from dilute dispersions: A. $C_{15}S_{16.2}$ (10%) (filled black circles) and $C_dS_{16.2}$ (10%) (empty black circles), B. $C_{15}S_{14.6}$ (25%) (filled red squares) and $C_dS_{14.6}$ (25%) (empty red squares). The error bars are in the order of the symbol size. For the sake of clarity, the intensities in the profiles of the CS particles were multiplied by a factor of 10 to shift them vertically. In C (10 mol%) and D (25 mol%) the profiles and the respective fits of the CS particles are shown using the same color coding as in A/B. The data is compared to a simulated scattering profile of the Au cores (solid blue line).

The good match between the experimental data and the fit was confirmed by the small residuals shown in the Appendix in Figure A.5. In Figure A.5 the mentioned two main contributions are separately represented. At low q -range, the form factor contribution is

more pronounced whereas at medium to high q -range the OZ contribution is dominating. The fits of the CS particles were performed without accounting for the scattering of the Au nanoparticles. This simplification is reasonable, since the volume of the Au core constitutes only 0.2% to the overall particle volume. To elucidate that the Au core scattering is effectively negligible referred to the total scattering intensity, simulations revealing the impact of the Au core scattering were conducted. For this purpose, the particle size including the respective standard deviation derived from TEM, the scattering length density of Au and the number density ρ_N resulting from fits of the experimental data from the CS particles were used.^[154] The corresponding profiles are shown in Figure 5.15 C and D. A comparison with the scattering profiles of the CS particles indicates that the scattering intensity of the Au cores is several orders of magnitude smaller in the q -range that is decisive for the form factor of the CS particles and at least by a factor of 10 smaller in the q -range used for the analysis of the OZ contribution. Hence, this confirms that the scattering of the gold cores can be neglected in the investigated q -range. In Table 5.4 selective fitting parameters are listed.

Table 5.4: Correlation length ξ , the amplitude of the OZ contribution normalized by the number density ($I(0)/\rho_N$), radius of the inner homogeneous volume segment R_{hom} and thickness ΔR of the outer volume element with an exponentially decaying density obtained by fitting the SANS profiles of the dilute particle dispersions using *SASfit*.

Particle system	ξ [nm]	$I_L(0)/\rho_N$ [cm ²]	R_{hom} [nm]	ΔR [nm]
C ₁₅ S _{16.2} (10%)	1.9	1.0	39	64
C _d S _{16.2} (10%)	1.9	1.0	38	66
C ₁₅ S _{14.6} (25%)	1.2	0.2	47	52
C _d S _{14.6} (25%)	1.4	0.3	51	49

An overview of all fit parameters is given in Table A.4 in the Appendix. The form factor contribution allows the determination of the radius R_{hom} of the inner volume element with a constant density and an outer volume region exhibiting an exponentially decaying density with a thickness ΔR . CS and C_dS particles with similar cross-linker contents show similar values of R_{hom} and ΔR . This demonstrates that the presence or absence of the Au core as well as the dissolution procedure are not affecting the internal network morphology. In addition, a correlation between the cross-linker content and the morphology was found. Stronger cross-linked samples result in a larger inner volume element with homogeneous density and a reduced outer volume element with an exponentially decaying density. This is in contrast to the less cross-linked samples that show the inverse relation regarding the dimension of the volume elements. Consequently, higher cross-linked samples reveal an overall more homogeneous density. These findings are in line with results

from Varga *et al.*^[113] They investigated microgels using light scattering and reported a rather homogeneous network structure for microgels with increased cross-linker contents. Furthermore, the authors proposed a CS morphology with a shell of decreasing density for more loosely cross-linked microgels.

Further, the fit parameters that describe the OZ contribution of the different samples were compared. The correlation length ξ of CS and of C_dS particles with the same cross-linker content are very similar. As expected, larger values of ξ were obtained for samples with lower cross-linker contents indicating a more flexible network. To draw conclusions on the dynamic fluctuations in the network, the amplitude of the OZ contribution $I_L(0)$ was normalized by the particle number density ρ_N . In accordance with previous studies, $I_L(0)/\rho_N$ is larger for the CS(10%) and C_dS (10%) than for the CS(25%) and C_dS (25%) particles (here: around 4 times).^[187]

In conclusion, the results from light and neutron scattering clarify that the network structure and the volume phase transition behavior remained unaffected by the dissolution of the gold core. Another important finding of these studies is that higher cross-linked samples reveal a more homogeneous and more rigid network structure.

5.2.2 Optical Properties in the Dilute State

Finally, the optical properties of the particles in the dilute regime were investigated. These results are crucial to allow a comprehension of the photonic properties in the crystalline state, that are discussed later on. In Figure 5.16 A photographs of the dilute samples with a concentration of 0.03 wt% are illustrated.

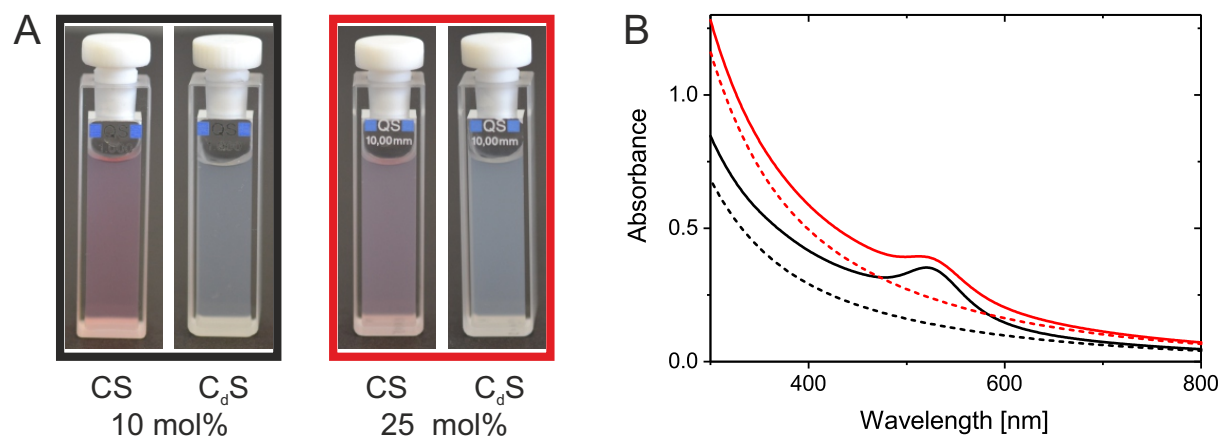


Figure 5.16: A. Photographs of dilute dispersions (0.03 wt%) in D₂O of the CS and C_dS particles with 10 mol% (black frame) and 25 mol% (red frame) cross-linker content. B. Absorbance spectra of these dispersions measured at room temperature: C₁₅S_{16.2}(10%) (solid black line), C_dS_{16.2}(10%) (dashed black line), C₁₅S_{14.6}(25%) (solid red line) and C_dS_{14.6}(25%) (dashed red line).

Already by the naked eye, it is evident which particles contain a Au core. The CS dispersions possess a typical reddish color which is related to the LSPR of the Au nanoparticles. In contrast to this, the C_dS dispersions are colorless. Owing to the scattering of the particles, all dispersions are turbid. In Figure 5.16 B the respective absorbance spectra recorded at room temperature are shown. The corresponding normalized absorbance spectra are depicted in Figure A.6 in the Appendix. The spectra of the C_dS particles are dominated by RDG scattering. This results in a constant increase of the absorbance particularly towards low wavelengths caused by the power law dependence of the RDG scattering.^[55] The absorbance spectra of the CS particles are based on two main contributions : 1) In similarity to the C_dS particles, the spectra are influenced by RDG scattering. 2) A peak at around 522 nm appears which describes the LSPR of the Au particles.^[55] Since the Au particles are only around 15 nm in diameter, they can be assumed to be purely absorptive, i.e., their scattering cross-section is negligible.^[184] Therefore, the optics of the CS particles can be separated into two contributions. The absorption is solely attributed to the Au cores and the scattering is fully assigned to the PNIPAM shell. To allow a direct comparison of the measured extinction properties of the different samples, the molar extinction coefficients ϵ_M were calculated. Therefore, the Beer-Lambert law was used:

$$Abs_\lambda = \epsilon_M \cdot c \cdot d \quad (5.4)$$

Here, Abs_λ denotes the extinction at a specific wavelength, d is the pathlength of the sample in m and c the concentration of the sample in mol/m³. In order to determine the molar concentration, the weight concentration (0.03 wt%) and the molar mass of the particles were used. Regarding the weight concentration, the residual water content (5.7% in the case of CS(10%), 5.3% in the case of CS(25%)) was considered. These values were determined by TGA data which are shown in Figure A.8 in the Appendix. As previously depicted for similar particles, the molar mass can be derived from absorbance spectra.^[56,154] Therefore, the extinction coefficient at 400 nm is used to calculate the concentration of the particles and to eventually draw conclusions on the molar mass. The details of these calculations are explained in Section A.7 in the Appendix. ϵ_M was determined considering the extinction at the plasmon band (CS(10%) & C_dS (10%): 522 nm, CS(25%) & C_dS (25%): 521 nm) of the corresponding CS particles. The values for ϵ_M are summarized in Table 5.5. ϵ_M is for both cross-linking densities twice (10 mol%) or even three times (25 mol%) higher if CS and C_dS particles are compared.

To comprehend the different values of ϵ_M , the ratio γ (eq. 4.1) was used. This ratio allows further quantification of the two main contributions that are scattering (based on the particle size) and absorption (here, determined by the Au cores). γ was already introduced in Chapter 4. Briefly, it reveals whether the absorption or the scattering contribution

dominates. If scattering is more pronounced, γ reaches small values approaching zero. In contrast to this, it approaches unity if the sample is mainly influenced by absorption. To get an idea of the lower limit of γ , it was also determined for the C_dS samples which demonstrate purely scattering particles. Therefore, their absorbances at wavelength positions of 521 and 522 nm corresponding to the plasmon peak position of the CS particles were inserted in eq. 4.1. $\gamma = 0.31$ was calculated for both types of pitted particles revealing that their wavelength-dependent scattering contribution is similar. This is appropriate since the particles have comparable dimensions (see Table 5.3). In the case of the CS particles, γ is distinctly increased indicating the influence of the plasmonic/ absorptive contribution. Comparing the CS particles, γ is higher for the lowly cross-linked sample as compared to the CS(25%) particles. This can be attributed to the reduced scattering cross-section of the CS(10%) particles. CS(25%) particles scatter stronger due to the increased effective average refractive index of the PNIPAM shells which is related to their denser network.^[55]

Table 5.5: Results from analysis of the absorbance spectra of the different dilute dispersions: The position of the plasmon resonance λ_{LSPR} , the molar extinction coefficient ϵ_M at λ_{LSPR} and the ratio γ .

Sample	λ_{LSPR} [nm]	$\epsilon_M(\lambda_{LSPR})$ [m ² /mol]	γ
$C_{15}S_{16.2}(10\%)$	522	$1.86 \cdot 10^7$	0.54
$C_dS_{16.2}(10\%)$	-	$0.64 \cdot 10^7$ ^a	0.31 ^b
$C_{15}S_{14.6}(25\%)$	521	$2.67 \cdot 10^7$	0.42
$C_dS_{14.6}(25\%)$	-	$1.49 \cdot 10^7$ ^a	0.31 ^b

^a These values were determined using the respective absorbances at 522 nm ($C_dS_{16.2}(10\%)$) or 521 nm ($C_dS_{14.6}(25\%)$), respectively.

^b These values were determined using the respective absorbances at 400 nm and at 522 nm ($C_dS_{16.2}(10\%)$) or 521 nm ($C_dS_{14.6}(25\%)$), respectively.

5.2.3 Photonic Properties of the Superstructures

Knowing the optical properties in the dilute regime, it is now focused on the photonic properties of self-assembled superstructures from CS and C_dS particles. The fabrication of these superstructures was performed as described in Section 5.1.3. In order to prepare superstructures, particle dispersions at high weight fractions between 6 and 11 wt% were filled in quartz cells with pathlengths of 100 μm . For comparison of the crystalline samples of CS and their respective C_dS particles, samples with similar volume fractions were prepared. Directly after filling the cells, the samples showed a distinct iridescence indicating a successful crystallization. Particularly, after several annealing steps, i.e.,

increasing the temperature carefully above the VPTT and slowly cooling to room temperature, the overall crystal fraction was enhanced and the defects in the structures were reduced. Thereby, it was focused on achieving a spectral overlap of plasmon band and Bragg diffraction mode of the CS particles since, in the case of 2D lattices, it resulted in coupling between the two modes.^[61,62] In Figure 5.17 the respective absorbance spectra are shown. Crystalline samples with low volume fractions are labeled in gray (10 mol%, A) and rose (25 mol%, B) whereas samples with higher volume fractions are depicted in black (10 mol%, A) and red (25 mol%, B).

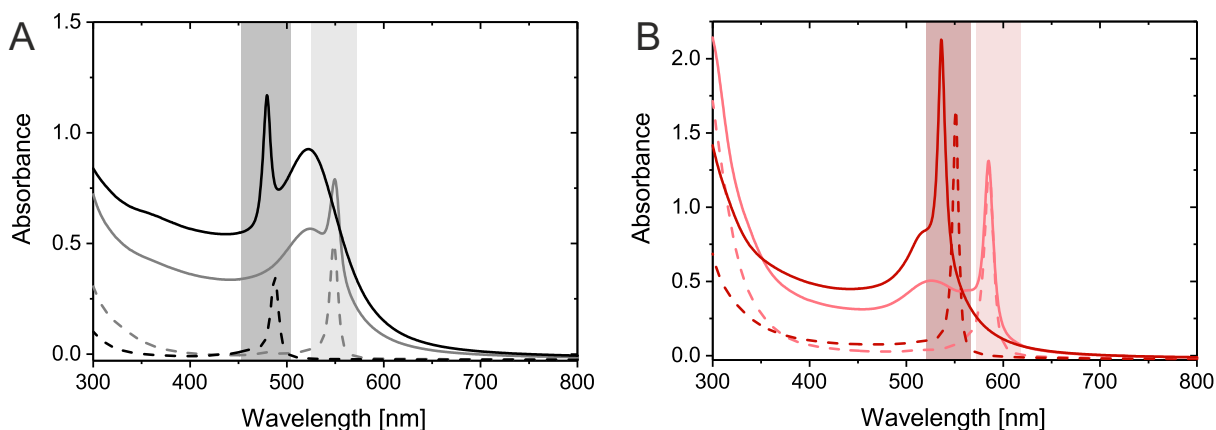


Figure 5.17: Absorbance spectra of the crystalline samples measured at room temperature: A. samples with 10 mol% cross-linker content at low (gray lines) and high (black lines) volume fractions; B. samples with 25 mol% cross-linker content at low (rose lines) and high (red lines) volume fraction. The solid lines describe the spectra of CS particles and the dashed lines represent the data of C_dS particles. The colored background shading highlights the similar position of the Bragg modes of superstructures consisting of CS and C_dS particles at similar volume fractions.

In all absorbance spectra a narrow Bragg diffraction peak is visible with narrow FWHM in the range of 7-14 nm that reveal the high order of the superstructures. The position of the Bragg peak λ_{diff} in the spectrum shifts to decreased wavelengths with increasing volume fraction which corresponds to a smaller lattice constant a . λ_{diff} can be used to calculate the lattice constant a of the superlattices as described in Section 5.1.3. Therefore, the particles can be assumed to crystallize in a FCC lattice which is proven later on (Section 5.2.4). A medium refractive index $n_{crystal}$ of 1.345 ± 0.015 was derived using the assumption that the volume fraction of D_2O in the particles is 85%, as determined by SANS in Section 5.2.1, and the refractive index of cross-linked PNIPAM ($n = 1.56$). The latter value was determined by refractive index measurements that are shown in Figure A.9 in the Appendix. Moreover, it is expected that the (111) plane of the FCC lattice is oriented parallel to the cuvette wall, so that $\theta = 0^\circ$. Using the position of the Bragg mode λ_{diff} , $n_{crystal}$ and $\theta = 0^\circ$, the lattice plane distance d_{111} could be determined by eq. 5.1. d_{111} allows access to the lattice constant a and the volume fraction ϕ_{UV-vis}

according to eq. 2.34 and 5.2. For the calculation of ϕ_{UV-vis} the hydrodynamic radius was used. The results for d_{111} , a and ϕ_{UV-vis} are listed in Table 5.6. For all samples crystalline lattices were obtained which is in line with previous studies on comparable particles shown in Section 5.1.3. Analyzing the results of ϕ_{UV-vis} , volume fractions far beyond the hard-sphere limit of 0.74 are found (e.g. 1.04 and 1.02 for superstructures of CS and C_dS particles with a cross-linker content of 10 mol%). As previously discussed, soft particles can deform and/or interpenetrate at high volume fractions so that very high volume fractions are accessible.^[13] The inter-particle distances in the crystal lattice are between 218 to 267 nm as determined using eq. 5.1. In fact, the preparation of samples at similar volume fractions for CS particles and their respective pitted counterparts was successful. A comparison of the corresponding particle pairs at similar volume fractions showed indeed an almost identical diffraction behavior, i.e., a good match regarding the Bragg peak position and its width. Apart from the similar volume fraction, this is certainly as well related to comparable surface charges, radii and network structures of the CS and the respective C_dS particles, as discussed in Section 5.2.1.

Table 5.6: Results from the analysis of the absorbance spectra of the superstructures: Position of the diffraction peak λ_{diff} , FWHM of the diffraction peaks, distance between the lattice planes d_{111} , the lattice constant a , the volume fraction ϕ_{UV-vis} and the ratio γ .

ϕ	Sample	λ_{diff} [nm]	FWHM [nm]	d_{111} [nm]	a [nm]	ϕ_{UV-vis}^a	γ
low	$C_{15}S_{16.2}(10\%)$	548	13.9	204 ± 2	353 ± 4	0.70 ± 0.02	1.0
	$C_dS_{16.2}(10\%)$	548	10.4	204 ± 2	353 ± 4	0.72 ± 0.02	-
	$C_{15}S_{14.6}(25\%)$	585	10.7	217 ± 2	377 ± 4	0.43 ± 0.01	0.85
	$C_dS_{14.6}(25\%)$	585	10.6	217 ± 2	377 ± 4	0.49 ± 0.02	-
high	$C_{15}S_{16.2}(10\%)$	480	10.2	178 ± 2	309 ± 3	1.04 ± 0.03	1.05
	$C_dS_{16.2}(10\%)$	487	10.1	181 ± 2	314 ± 3	1.02 ± 0.03	-
	$C_{15}S_{14.6}(25\%)$	536	8.9	199 ± 2	345 ± 4	0.56 ± 0.02	1.10
	$C_dS_{14.6}(25\%)$	551	7.2	205 ± 2	355 ± 4	0.59 ± 0.02	-

^a The volume fractions ϕ_{UV-vis} were calculated assuming FCC lattices (number of particles per unit cell is 4 and the unit cell volume is given by a^3) using the lattice constant a and the hydrodynamic radius R_h at 25°C.

Superstructures consisting of CS particles show a distinct maximum at 522 nm in their spectra in Figure 5.17 which can be ascribed to the plasmon resonance. The LSPR can thus be found at a similar wavelength as in the dilute state. However, the plasmon resonance is more distinct in the superstructures than in dilute solution. Moreover, it is noticed that the scattering contribution at lower wavelengths is distinctly suppressed in the spectra of crystalline samples of CS and C_dS particles compared to the dilute state. Spectra of superstructures with C_dS particles, i.e., without plasmonic contribution,

show absorbances of almost zero at wavelengths between the Bragg peak position and 350 nm. These samples are nearly transparent in the visible wavelength range except for the wavelength position of the Bragg peak. Hence, the spectra mainly compose of strong interference resulting from Bragg diffraction whereas single-particle scattering is significantly reduced. This can be explained as follows: The deformable polymer network leads to deformation and/or interpenetration if the particles come into close contact leading to a very efficient space filling in contrast to hard spheres. This efficient space allocation and the low refractive index of the highly swollen particles lead to a very homogeneous medium at high ϕ . Interestingly, the samples still show Bragg peaks. The main reason for this is that the refractive index in the overall crystal structure of the samples shows a certain periodicity which can be attributed to the gradual decrease in density of the network structure in a single particle.^[110,111] Typically, the network structure of cross-linked PNIPAM particles is more dense, i.e., reveals an increased refractive index, in the central region of the particle. The outer volume element of the shell ranging from this central region to the periphery of the particle indicates a decreasing cross-linking density and thus a decay in the refractive index. Considering these observations, microgels with a homogeneously cross-linked shell would not lead to pronounced Bragg diffractions at similar ϕ .

Further, the influence of the plasmonic core on the spectra was analyzed. The mathematical superpositions of the absorbance spectra of the respective crystalline C_dS sample (Figure 5.17) and the spectrum of the gold nanoparticles prior to encapsulation in dilute dispersion were compared to recorded spectra of crystalline CS samples at comparable ϕ . In other words, a spectrum describing the diffractive contribution only (Bragg peak only) and a spectrum revealing solely the gold core contribution were superimposed. The resulting spectra are depicted in Figure 5.18. A very good match between the spectra of crystalline CS samples and the corresponding superimposed spectrum is found with only slight deviations regarding the position of the LSPR and the Bragg peak. The minimal mismatch in the Bragg peak position refers to a slight distinction of the volume fractions of the samples consisting of CS and C_dS particles. In addition, the refractive index environment of the gold nanoparticles is changed from an aqueous medium (superimposed spectrum) to a cross-linked PNIPAM matrix (measured spectrum of the crystalline samples from CS particles). As the plasmon resonance position is sensitive to refractive index changes in the vicinity of the gold particles, a small shift to longer wavelengths is observed in the measured spectra as compared to the superimposed spectra.^[57]

To get further insights into the photonic properties of the samples, the ratio γ was determined as already introduced for these samples in the dilute regime. γ gives the ratio of scattering to absorbing contribution of the sample (eq. 4.1). The plasmonic character of the CS superstructures, which can be fully described by the absorptive contribution,

is significantly enhanced as compared to the dilute samples. Values of γ achieving the theoretical maximum of unity were determined as listed in Table 5.6.

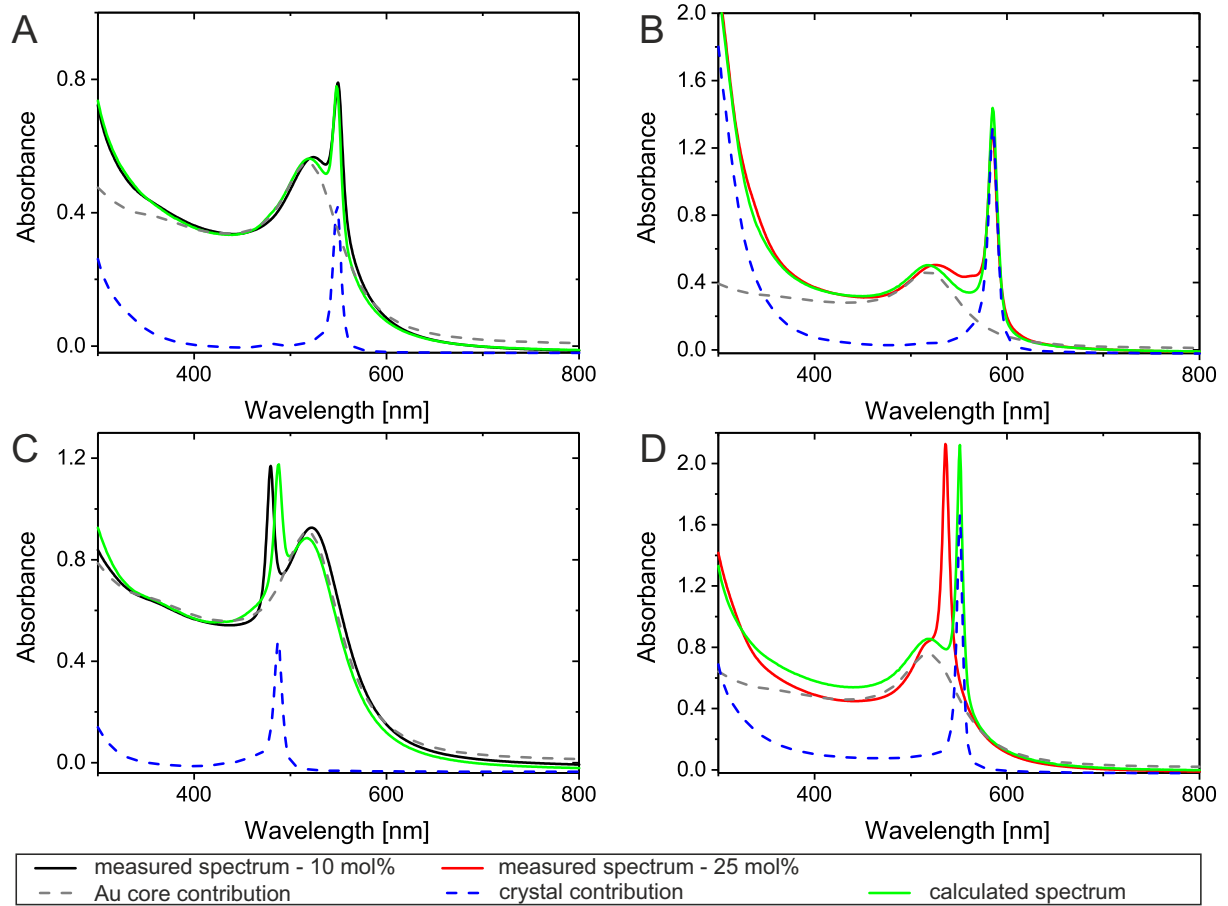


Figure 5.18: Calculated superposition spectra as compared to the recorded UV-vis absorbance spectra for the crystalline samples of CS(10%) (A. $\phi_{UV-vis} = 0.70 \pm 0.02$, C. $\phi_{UV-vis} = 1.04 \pm 0.03$) and of CS(25%) (B. $\phi_{UV-vis} = 0.43 \pm 0.01$, D. $\phi_{UV-vis} = 0.56 \pm 0.02$).

This is related to the absence of any scattering in the low wavelength region resulting in dominating plasmonic properties. These findings support the very unique properties of this material which combines the plasmonic absorption of the core with a mostly transparent matrix apart from the sharp diffraction peak which position can be adjusted by tuning the volume fraction.

In addition, this is significant for future studies dealing with coupling between plasmon and diffraction peak in 3D plasmonic superstructures. Here, no indication for plasmonic/diffractive coupling nor for plasmonic near-field coupling was observed. The latter type of coupling is mainly absent due to the small size of the nanocrystal cores in the investigated system which eventually corresponds to the center-to-center distance of the gold nanoparticles that is too large for this gold nanoparticle sizes. Apart from that, plasmonic/diffractive coupling is additionally impeded through the deviations of the core positions from the particle center. In particular, for samples with lowly cross-linked shells

the cores were distinctly decentered. To promote plasmonic/diffractive coupling in 3D plasmonic superstructures in future studies, larger gold cores that provide enhanced extinction cross-sections should be encapsulated and highly cross-linked shells should be preferably used to locate the gold nanocrystals in the center of the CS particles.

5.2.4 Crystal Structure

The results of the absorbance spectra allow to determine the position of the Bragg peak, however, they do not provide information about the type of crystal lattice. In order to identify the crystal lattice of the superstructures, SANS measurements were performed. These investigations were conducted at 25.6°C. The neutron beam was parallel to the [111] direction of the crystal in these measurements, i.e., in the radial beam direction. The lattice of a FCC crystal is exemplarily illustrated in Figure 5.19 A. The (111) planes, i.e., the planes in the radial beam direction, are highlighted with different colors indicating the A, B and C layers of a colloidal crystal. A theoretical map of possible combinations of Miller indices h , k and l considering the selection rule for a FCC lattice which requires either that all h , k and l are even integers or that all h , k and l are uneven integers is represented in Figure 5.19 B.^[188] In Figure 5.19 C a representative experimentally received SANS 2D pattern of a colloidal crystal consisting of C_dS particles at a SD distance of 28 m is shown.

Analyzing this scattering pattern further several orders of Bragg peaks with a six-fold symmetry are noticed revealing the high crystallinity of the sample. Figure 5.19 D shows the same measurement with indexed Bragg peaks. The differently colored circles are used to label the peaks. The colors correspond to the Miller indices shown in the map in Figure 5.19 B with the same color code. Thus, the gray, blue, red and green circles depict the different orders of Bragg peaks located at perfect hexagons. Occasionally there are slight deviations between the position of the circles located at a perfect hexagon for each diffraction order and the experimentally measured Bragg peaks. Other examples showing the indexing of the Bragg peaks are depicted in Figure A.12 in the Appendix. Further analysis was performed using the relative positions of the Bragg peaks to draw conclusions on the size and shape of the unit cell. To reveal the position of the colloids in the unit cell, the relative intensities of the Bragg peaks are investigated. For the simulation of the measured 2D patterns the software *Scatter* by Förster and Apostol was used.^[189] Details on the analysis are presented in Section 2.4.2.2.

In Figure 5.20 the measured scattering patterns of colloidal crystals from CS(10%) and C_dS (10%) are shown. These measurements were conducted at a SD distance of 28 m providing access to a q -range from 0.02 to 0.19 nm⁻¹. The respective measurements of colloidal crystals consisting of CS(25%) and C_dS (25%) are depicted in Figure 5.21. In both figures the upper row shows results of the crystals at low volume fraction and the bottom

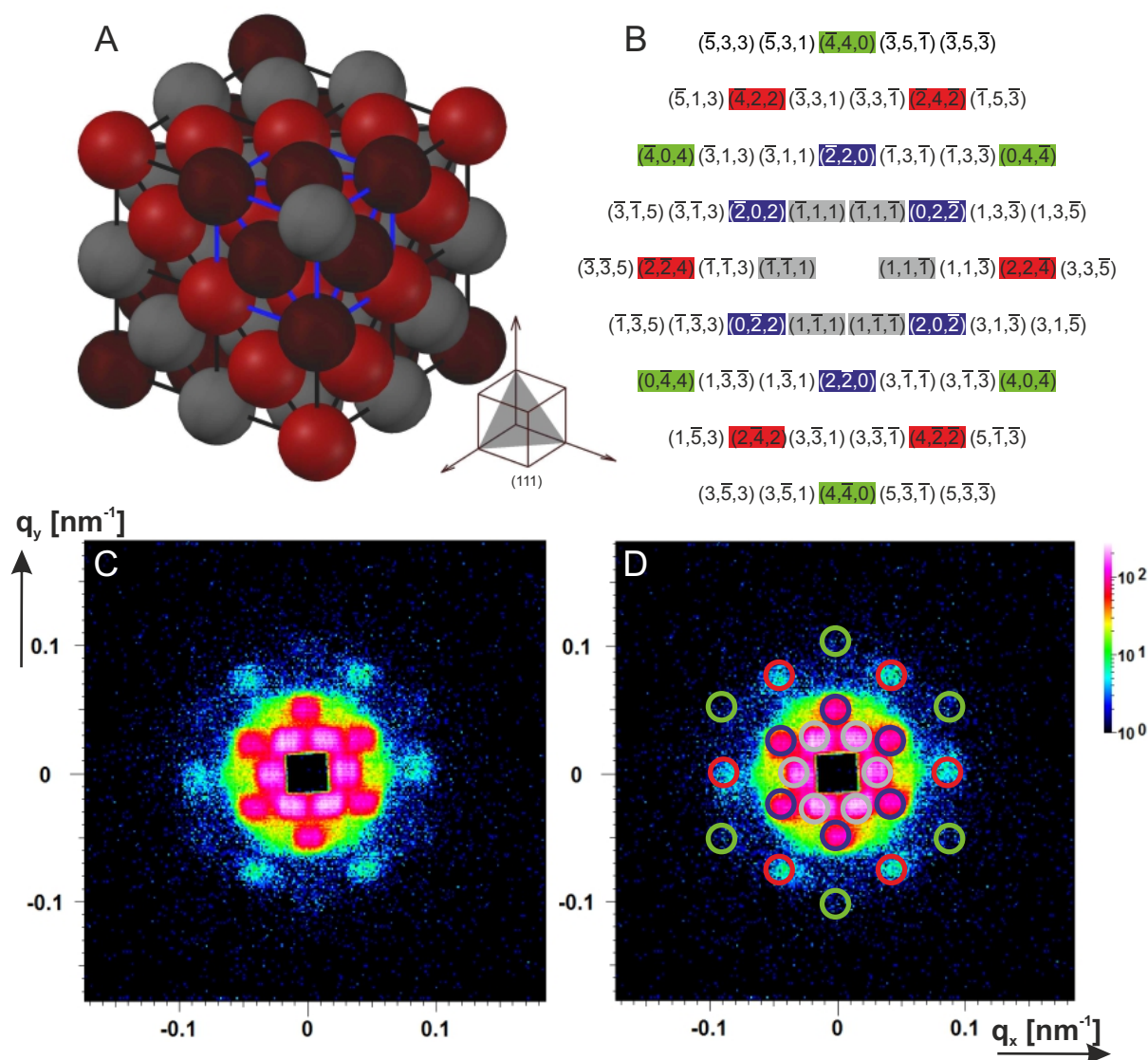


Figure 5.19: A. Schematic illustration of a FCC crystal lattice with the (111) planes A, B and C labeled using gray, red and brown spheres. The blue lines highlight a unit cell in the FCC lattice. The direction of the neutron beam in the performed experiments was parallel to the [111] direction. For the sake of clarity, the (111) plane is shown in a schematic unit cell in the bottom right corner. B. Miller indices of the theoretically available diffraction peaks in a FCC lattice. C. Measured 2D SANS scattering pattern of a representative crystalline sample ($C_dS(10\%)$, $\phi_{UV-vis} = 0.72$). D. Indexing of the experimentally received Bragg peaks using the same color code as in B. The circles used to label the Bragg peaks are arranged on perfect hexagons.

row the results at high volume fraction. The left half of each scattering pattern shows the experimentally measured data whereas on the right the simulation is represented. The corresponding results of measurements performed at a SD distance of 39 m are depicted in the Appendix (Figures A.10 and A.11). All samples are highly ordered resulting in several diffraction orders of peaks. Further, a characteristic six-fold pattern was always observed.

Peak arrangement as well as the peak spread match very well between simulation and experimental data. In all cases a FCC lattice with a space group $Fm\bar{3}m$ was obtained by indexing. Slight deviations between simulation and experiment are caused by geometric smearing in the SANS experiment and by wavelength distributions ($\Delta\lambda/\lambda$) of around 9%.

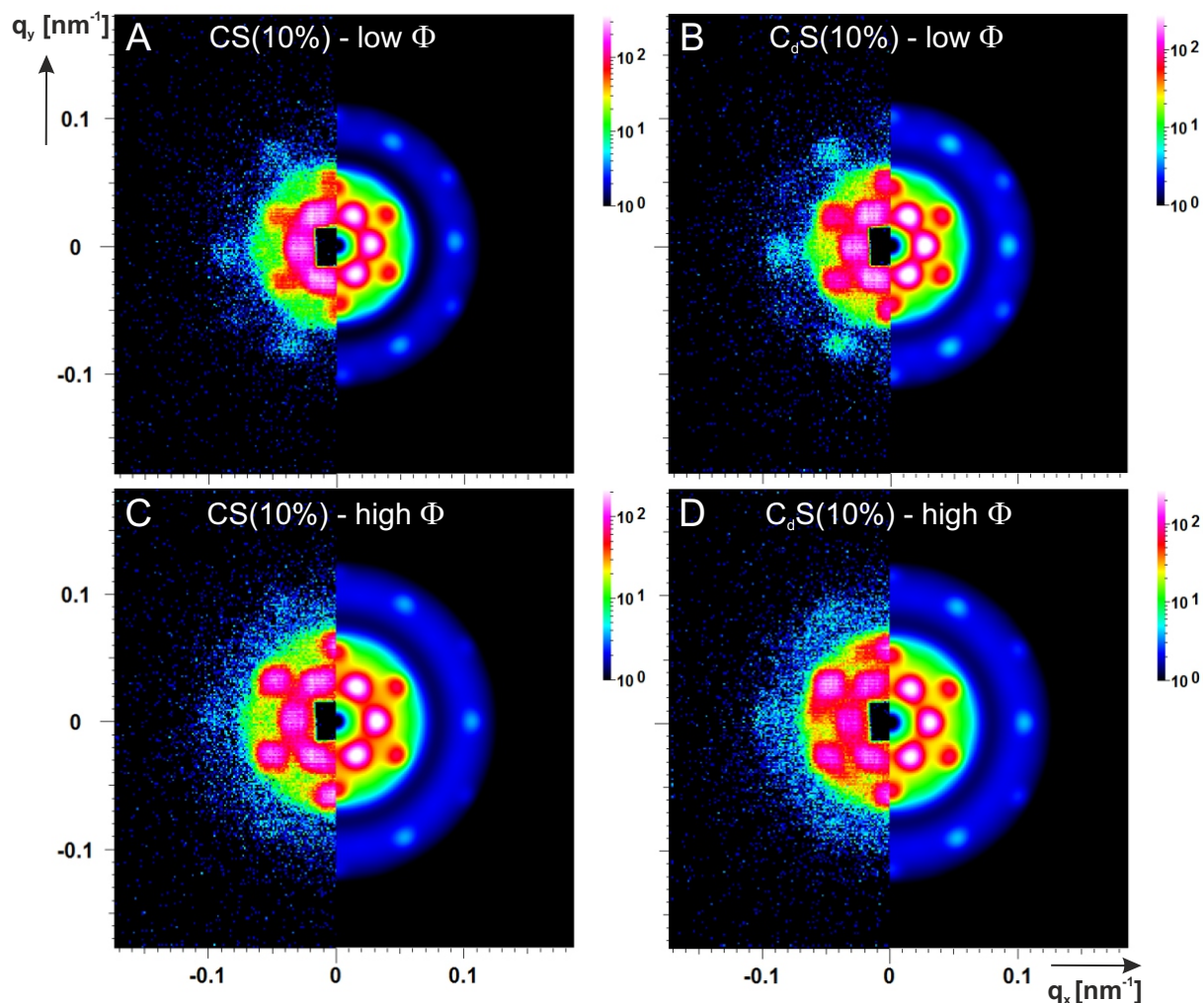


Figure 5.20: Experimentally obtained 2D SANS patterns (left half) and calculated SANS patterns (right half) in the radial beam direction [111] for the samples CS(10%) and CdS(10%) at low (A, B) and high (C, D) volume fraction measured at a SD distance of 28 m. Adapted with permission from "Role of Absorbing Nanocrystal Cores in Soft Photonic Crystals: A Spectroscopy and SANS Study.", by Rauh, A.; Carl, N.; Schweins, R.; Karg, M. *Langmuir* **2017**, DOI: 10.1021/acs.langmuir.7b01595. Copyright 2017 by American Chemical Society.

Crystals built up from soft colloids often show crystallographically forbidden, secondary Bragg peaks which are attributed to their small longitudinal and transverse coherence lengths resulting in typically large peak width.^[190] Hence, crystallographically forbidden peaks like the $\langle 111 \rangle$ (highlighted in gray in Figure 5.19 D) or the $\langle 311 \rangle$ reflections (see Figure A.12 in the Appendix) are detected in addition to allowed, primary Bragg peaks like the $\langle 220 \rangle$, $\langle 422 \rangle$ and the $\langle 440 \rangle$ reflections. Generally, most of the detected peaks are

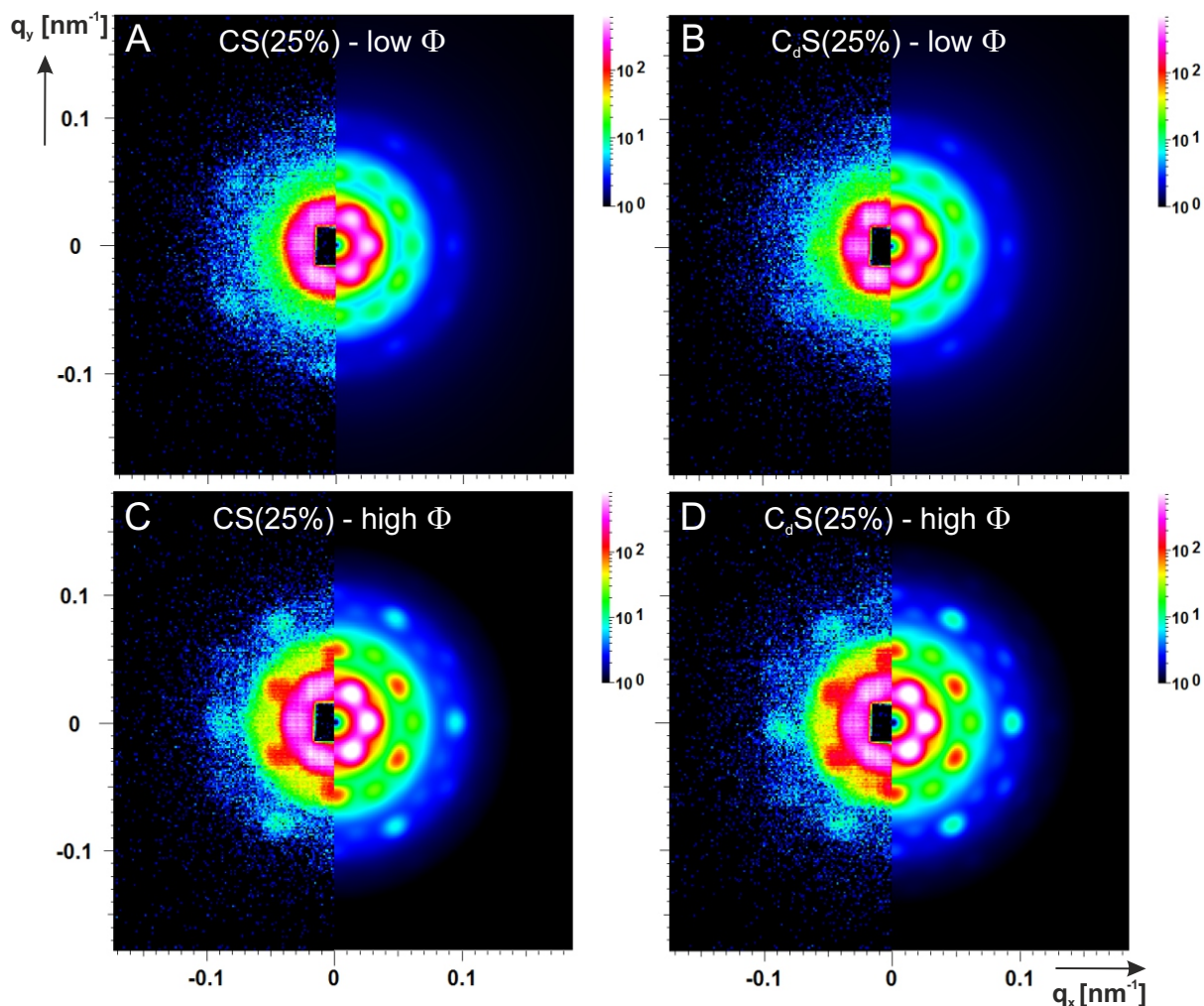


Figure 5.21: Experimentally obtained 2D SANS patterns (left half) and calculated SANS patterns (right half) in the radial beam direction [111] for the samples CS(25%) and C_dS(25%) at low (A, B) and high (C, D) volume fraction measured at a SD distance of 28 m. Adapted with permission from "Role of Absorbing Nanocrystal Cores in Soft Photonic Crystals: A Spectroscopy and SANS Study.", by Rauh, A.; Carl, N.; Schweins, R.; Karg, M. *Langmuir* **2017**, DOI: 10.1021/acs.langmuir.7b01595. Copyright 2017 by American Chemical Society.

primary, allowed reflections.

Simulations of the scattering patterns of CS(10%) and C_dS(10%) agreed best with the experimental data using an inhomogeneous core-shell model. This model considers an inner volume element of the particle with a homogeneous density profile and an outer volume element with a decreasing cross-linking density from the center to the periphery. Hence, it is similar to the model applied for the dilute samples. The samples with a higher cross-linking density in the shell could be successfully simulated using a simple hard sphere model. Both models are introduced in Section 2.4.2.2. The results obtained by the *Scatter* simulations are summarized in Table 5.7.

Comparing the total particle radii R_{total} from these simulations and the radii obtained

Table 5.7: Results from the simulation of the experimentally obtained 2D SANS patterns (SD distance: 28 m) of the superstructures at different volume fractions: Lattice constant a , the longitudinal (D_l) and azimuthal (D_Ψ) domain size, the overall radius (R_{total}), the radius of the core R_{hom} , $\alpha_{Scatter}$ indicating the algebraic density decay in the shell, the contrast ratio of the core and corona at the core-corona interface $\eta_{core-corona}$ as well as the displacement $s_{Scatter}$ from the ideal lattice points.

ϕ	Sample	ϕ_{UV-vis}	a [nm]	D_l [nm]	D_Ψ [nm]	R_{total} [nm]	R_{hom} [nm]	$\alpha_{Scatter}$	$\eta_{core-corona}$	$s_{Scatter}$ [nm]
low	CS(10%)	0.70 ± 0.02	335	450	450	95	30	1.2	0.95	5
	$C_dS(10\%)$	0.72 ± 0.02	335	450	450	95	30	1.25	0.95	5
	CS(25%)	0.43 ± 0.01	340	375	375	99	-	-	-	25
	$C_dS(25\%)$	0.49 ± 0.02	340	375	375	100	-	-	-	25
high	CS(10%)	1.04 ± 0.03	290	450	450	85	30	1.25	0.95	10
	$C_dS(10\%)$	1.02 ± 0.03	295	450	450	85	30	1.25	0.95	5
	CS(25%)	0.56 ± 0.02	320	400	400	99	-	-	-	20
	$C_dS(25\%)$	0.59 ± 0.02	325	400	400	100	-	-	-	15

from simulation of the scattering profiles in the dilute regime, the values coincide well except for the lower cross-linked samples at high volume fractions. Here, slightly smaller radii were obtained (CS(10%) at $\phi_{UV-vis} = 1.04$ / $C_dS(10\%)$ at $\phi_{UV-vis} = 1.02$). This might be due to deformation and/or shrinkage of the particles at these high volume fractions. Note, that the scattering patterns are strongly dominated by the structure factor, so that the form factor of the particles and thus their size cannot be identified reliably. The analysis of the lattice using the SANS data provides the lattice constant a (see Table 5.7). The lattice constant a is in good accordance with the lattice constants obtained from UV-vis measurements for these samples (see Table 5.6).

Further, surprisingly small domain sizes ranging from 375 to 450 nm and thus being only in the order of the particle diameter are found. This is again typical for soft crystals since the measurements are affected by limited coherence resulting in reduced values of D_l and D_Ψ . A detailed description of factors leading to limited coherence is described in the theory part in Section 2.4.2.2. The presence of instrumental limitations is confirmed analyzing the SANS data collected at a SD distance of 39 m (see Figures A.10 and A.11 in the Appendix). Simulations for these data led to narrower peak shapes, i.e., to larger domain sizes which clearly indicate that limited transversal and longitudinal coherence lengths resulting from instrumental limitations affect the measurements. Besides, a certain polydispersity (here: around 10%) as well as slight deviations from the ideal lattice points (here: $s_{Scatter}=5-25$ nm) give strong evidence for lattice imperfections influencing the coherence lengths as well.

Comparing crystals built up from particles with different cross-linking at similar volume fractions (CS(25%) at $\phi_{UV-vis} = 0.56$ as compared to CS(10%) at $\phi_{UV-vis} = 0.70$), the simulations result in similar domain sizes and diffraction orders of Bragg peaks revealing that the crystallinity is similar. However, the displacement from the ideal lattice points is reduced for the sample with lower cross-linking implying that these samples manage to compensate defects more effectively than more rigid particles.

As the crystal lattice of all samples is now proved to be FCC, the first maximum of the structure factor $S(q)$ profile can be used to approximate the volume fraction from SANS data. Therefore, the radially averaged scattering profile of the concentrated sample $I(q)_{concentrated}$ is divided by the corresponding radially averaged profile of the dilute sample $I(q)_{dilute}$ to determine $S(q)$. One should note that this is only an approximation, since the size and shape of the particles are assumed to remain constant with changing concentration. The respective profiles of $S(q)$ of the superlattices are presented in Figure 5.22.

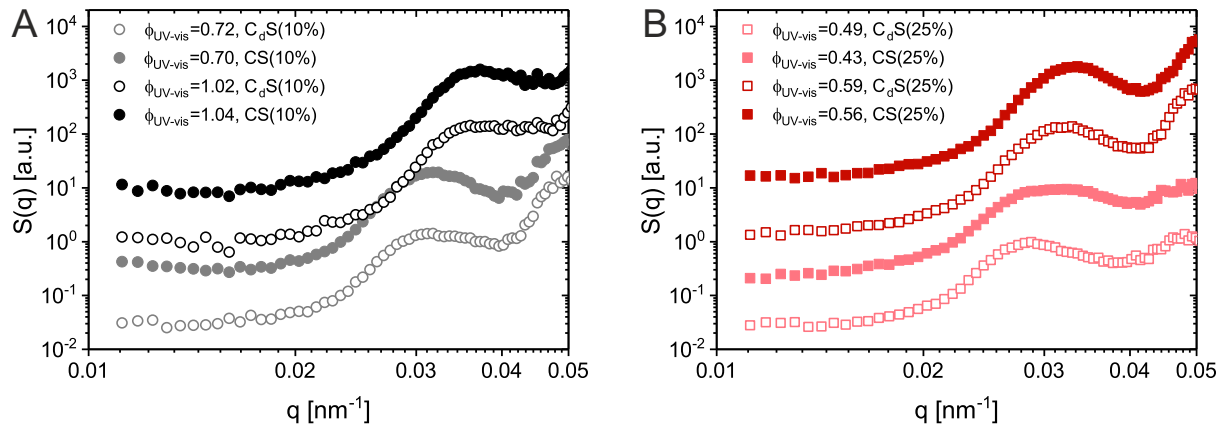


Figure 5.22: Radially averaged scattering profile of the structure factor of the samples with 10 mol% cross-linker content (A) and with 25 mol% cross-linker content (B) at different volume fractions. For the sake of clarity, the profiles of $S(q)$ are shifted vertically by multiplying the intensity using the factors 1, 10, 100 and 1000 from bottom to top, respectively.

The position of the first maximum of $S(q)$, q_{max} , is used to calculate d_{111} according to eq. 2.33. Table 5.8 lists the resulting values as well as the lattice constant a and volume fraction ϕ_{SANS} derived using eq. 2.34 and 5.2, respectively. Moreover, conclusions on the inter-particle distances in the crystalline structures can be drawn by means of eq. 5.3. The values of d_{cc} are between 210 and 250 nm. Comparing the values of ϕ obtained by analysis of the $S(q)$ profiles and the absorbance spectra, a reasonable agreement is found considering their errors. However, ϕ_{SANS} is always larger which is mainly attributed to the defectiveness of q_{max} based on the following error sources: First, the form factor of the dilute systems is used to determine $S(q)$. This assumption affects ϕ_{SANS} , since the size and shape of the particles in the crystalline state can deviate from the dilute state. If

this is the case, $S(q)$ and thus also q_{max} would be influenced. Second, the first maximum which is used to access q_{max} is rather broad due to instrumental parameters affecting the resolution. Hence, q_{max} cannot be determined as precisely as the position of the Bragg peaks λ_{diff} in the absorbance spectra which display very narrow peak widths.

Table 5.8: Position of the first maximum q_{max} of $S(q)$, the lattice plane distance d_{111} , the lattice constant a and the volume fraction derived from absorbance spectra ϕ_{UV-vis} and from SANS data ϕ_{SANS} .

ϕ	Sample	ϕ_{UV-vis}^a	q_{max} [nm ⁻¹]	d_{111} [nm]	a [nm]	ϕ_{SANS}^a
low	CS(10%)	0.70 ± 0.02	0.0311 ± 0.0006	202 ± 4	350 ± 7	0.72 ± 0.04
	C _d S(10%)	0.72 ± 0.02	0.0311 ± 0.0006	202 ± 4	350 ± 7	0.73 ± 0.04
	CS(25%)	0.43 ± 0.01	0.0308 ± 0.0006	204 ± 4	353 ± 7	0.53 ± 0.03
	C _d S(25%)	0.49 ± 0.02	0.0288 ± 0.0006	218 ± 5	379 ± 8	0.49 ± 0.03
high	CS(10%)	1.04 ± 0.03	0.0366 ± 0.0006	172 ± 3	297 ± 5	1.17 ± 0.06
	C _d S(10%)	1.02 ± 0.03	0.0358 ± 0.0006	176 ± 3	304 ± 5	1.12 ± 0.06
	CS(25%)	0.56 ± 0.02	0.0326 ± 0.0006	193 ± 4	334 ± 6	0.62 ± 0.03
	C _d S(25%)	0.59 ± 0.02	0.0316 ± 0.0006	199 ± 4	344 ± 7	0.64 ± 0.04

^a The volume fractions were calculated assuming FCC lattices (number of particles per unit cell is 4 and the unit cell volume is given by a^3) using the lattice constant a and the hydrodynamic radius R_h at 25°C.

5.3 Core-Shell Particles with a Small Shell-to-Core Ratio

The interaction potential of CS particles can be manipulated by the shell-to-core ratio. CS particles with distinctly smaller shell-to-core ratios as the ones investigated in the previous sections are expected to interact differently. The shell-to-core ratio is a decisive parameter regarding the control of the accessible range of inter-particle distances. Particles, displaying a step interaction potential and possessing shell-to-core ratios between 1 and 2, are expected to induce several different crystal phases including quasicrystalline structures according to simulations.^[15] However, the shells of these objects have not been exhibiting a gradually decreasing density in their shells. Instead, their shells have been fully permeable. Hence, the hard cores of these particles can approach contact. This is in contrast to the used CS particles with cross-linked shells as shown in Figure 1.1 C. To approach similar core-core and shell-shell length scales as in the described simulations, CS particles with slightly larger shell-to-core ratios than 1-2 were prepared. This is related to the fact that the actual core of the used CS particles is the hard core plus the inner highly cross-linked, rigid area of the polymer network.

In addition to the potential of such CS particles to induce different crystal lattices, their self-assembled structures might have extraordinary optical properties. Due to interactions of the diffraction and the plasmon mode in such structures, surface lattice resonances (SLR) might develop. This has already been observed for similar particles in 2D lattices.^[61] As shown in Section 5.2, SLRs were not observed for particles with small gold cores as their scattering cross-section was too small. Hence, particles with larger gold cores and thus an increased scattering cross-section are promising.

$C_{71}S_{6.6}(15\%)$ particles which were previously introduced in Section 4.4 were used for the described studies. CLSM and SAXS measurements were performed to analyze the crystal structure of the self-assembled structures. The optical properties were investigated by UV-vis absorbance spectroscopy.

5.3.1 Crystal Structure

Initially, dispersions from $C_{71}S_{6.6}(15\%)$ particles at different weight concentrations ranging from 5.6 to 19.9 wt% were prepared. The fabrication of the self-assembled structures was performed as described in Section 5.1.3. Visual inspection of the prepared samples revealed strong iridescence over the whole range of volume fractions. This already indicated that all samples were crystalline. Due to the large overall size of these particles ($\lambda_b\sigma = 472$ nm at 25°C), additional analysis methods were accessible apart from scattering methods. As the polymer shells were fluorescently labeled with methacryloxyethyl thiocarbamoyl rhodamine B (MRB), confocal laser scanning microscopy (CLSM) was a suitable technique. However, CLSM is only suitable for a limited range of concentra-

tions/volume fractions of the samples which is related to two circumstances: (1) The excitation wavelength of the dye (543 nm) is in vicinity of the LSPR (544 nm) of the encapsulated gold nanoparticle cores so that a large part of the laser light is absorbed by the gold cores. (2) Since the shells are labeled, the particles are hard to distinguish as soon as their shells touch or interpenetrate. Consequently, volume elements of the crystalline samples could only be investigated in the concentration range between 5.6 and 9.9 wt%. These weight concentrations correspond to volume fractions ϕ between 0.33 and 0.49. Therefore, 2D images in the xy -plane were recorded at planes separated by maximal $0.13 \mu\text{m}$ in order to get a good resolution in z -direction of the 3D volume element.

The volume fraction ϕ_{CLSM} can be derived from the number of particles in the investigated volume element, i.e., the average number density ρ_N , using the following relation:^[12,13]

$$\phi_{CLSM} = \rho_N \cdot \frac{4}{3}\pi R^3 \quad (5.5)$$

The number of particles in the investigated volume element was determined using a custom-written software that was programmed in *Python*. The software implemented the particle tracking code by Crocker and Grier.^[142] Further, the hydrodynamic radius R_h was used as it can be determined very reliably. However, one should note that this leads to a slight overestimation of ϕ_{CLSM} . The obtained values range from 0.33 to 0.49 and are listed in Table 5.9.

Table 5.9: Summary of the results obtained from the 3D $g(r)$ functions calculated of the crystalline samples at weight concentrations c ranging from 5.6 to 9.9 wt%: The position of the first maximum of the radial distribution function r_{max} , the lattice plane distance d_{111} , the lattice constant a and the volume fraction $\phi_{g(r)}$ obtained from analysis of $g(r)$ as well as the volume fraction ϕ_{CLSM} derived using the number density in the volume element.

c [wt%]	r_{max} [nm]	d_{111} [nm]	a [nm]	$\phi_{g(r)}^a$	ϕ_{CLSM}^a
5.6	625 ± 30	510 ± 25	884 ± 42	0.32 ± 0.05	0.33 ± 0.01
6.5	589 ± 32	481 ± 26	833 ± 45	0.38 ± 0.06	0.36 ± 0.02
7.5	567 ± 26	463 ± 21	802 ± 37	0.43 ± 0.06	0.40 ± 0.01
9.9	512 ± 70	418 ± 57	724 ± 99	0.58 ± 0.24	0.49 ± 0.02

^a For the calculation of the volume fraction R_h at 25°C was used as particle radius.

In Figure 5.23 representative 2D CLSM images of the xy -plane and the respective Fast Fourier transformations at these four volume fractions are depicted. All images show a hexagonal arrangement of particles which is confirmed by the six-fold symmetry obtained in the Fourier transformations. Further, several orders of peaks are visible in the Fast Fourier transformations which highlight the good order in the samples. The described

limitations are well visible for the CLSM image recorded for the sample at $\phi = 0.49$. Here, the particles are more densely packed as compared to samples at smaller ϕ . Hence, it is already hard to distinguish them.

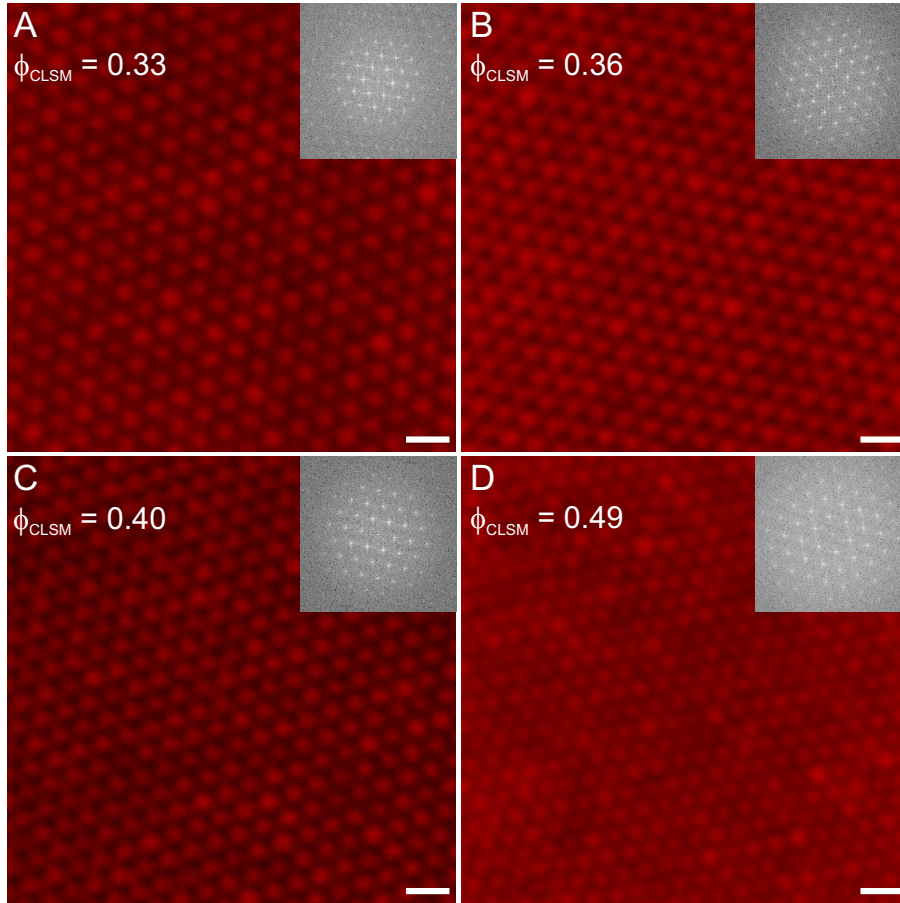


Figure 5.23: CLSM images of dispersions from $C_{71}S_{6.6}(15\%)$ particles at different volume fractions ϕ_{CLSM} : A. $\phi_{CLSM}=0.33$, B. $\phi_{CLSM}=0.36$, C. $\phi_{CLSM}=0.40$, D. $\phi_{CLSM}=0.49$. The images were recorded at least 4 particle diameters away from the glass slide. The scale bars are $1 \mu m$. The insets show the respective Fast Fourier transformations of the CLSM images.

Analyzing the measurements of the recorded volume elements using the custom written software, the particle coordinates could be extracted so that the 3D structure was accessible. Sections of the crystalline structures obtained at these four volume fractions are depicted in Figure 5.24. Side views (left) and perspective views (right) of the crystal structures at $\phi = 0.33 - 0.49$ are illustrated. For the sake of clarity the xy -planes are labeled using different colors. These 3D views highlight the good order in the samples. Slight dislocations in the structures might arise due to drift of the particles.

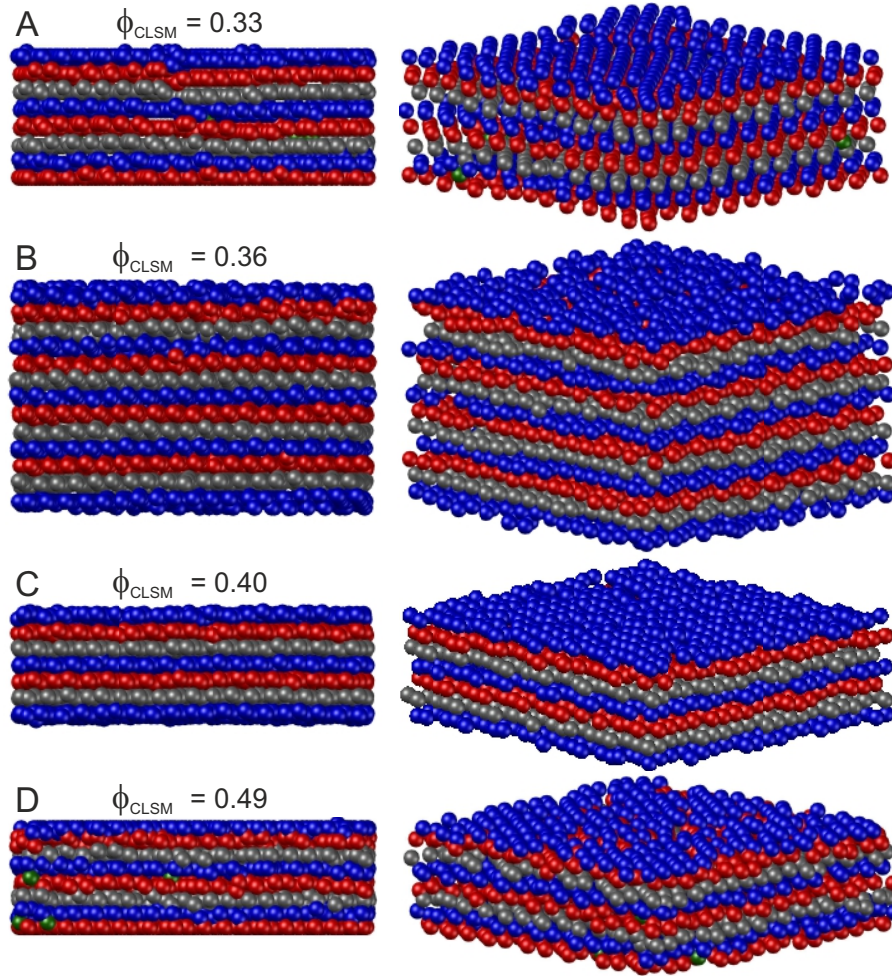


Figure 5.24: 3D crystal structures as measured by CLSM for samples at different volume fractions ϕ_{CLSM} : A. $\phi_{CLSM}=0.33$, B. $\phi_{CLSM}=0.36$, C. $\phi_{CLSM}=0.40$, D. $\phi_{CLSM}=0.49$. Side views (left) and perspective views (right) are shown. The particles are indicated as spheres with a diameter of 472 nm which corresponds to $\lambda_b\sigma$ at 25°C. For the sake of clarity, the particle layers in the xy -plane are labeled using different colors. Particles which could not clearly be assigned to a xy -plane are labeled as green spheres.

The respective 3D average radial distribution functions were calculated for the whole image sequence of the volume elements. Figure 5.25 depicts representative 3D $g(r)$ functions normalized by the position of their first maximum at $\phi_{CLSM} = 0.33 - 0.49$. The $g(r)$ functions without normalization are depicted in Figure A.13 in the Appendix. All $g(r)$ functions show several oscillations that confirm a good order in the samples and a first pronounced maximum. The position of the first maximum r_{max} in Figure A.13 gives the average inter-particle distance in the structures. The values of r_{max} are listed in Table 5.9. As expected, the determined inter-particle distances decrease with increasing volume fraction from 625 ± 30 nm to 512 ± 70 nm. Hence, the particles in the studied samples were not in contact. This explains why imaging using CLSM was still possible. The $g(r)$ functions display some characteristic features of a FCC lattice which is revealed

analyzing the peak positions. The theoretical peak positions are included using red lines in Figure 5.25. However, it was not possible to unambiguously manifest the crystal type as some signals that are usually present in a FCC lattice are missing in the experimental data. This is clearly due to detection problems and drift of the CLSM. Hence, it was not possible to get further information on the stacking order in the crystal.

If a FCC lattice is assumed, r_{max} can be used to calculate the lattice constant a , the lattice plane distance d_{111} and the volume fraction ϕ using eq. 2.34, 5.1 and 5.2. Again, one should note that the hydrodynamic radius was used for the calculation of the volume fraction which results in an overestimation of $\phi_{g(r)}$. Considering the errors, the volume fraction, $\phi_{g(r)}$, agrees well with the volume fraction ϕ_{CLSM} determined by eq. 5.5. Increasing the volume fraction leads to a decrease of a and d_{111} .

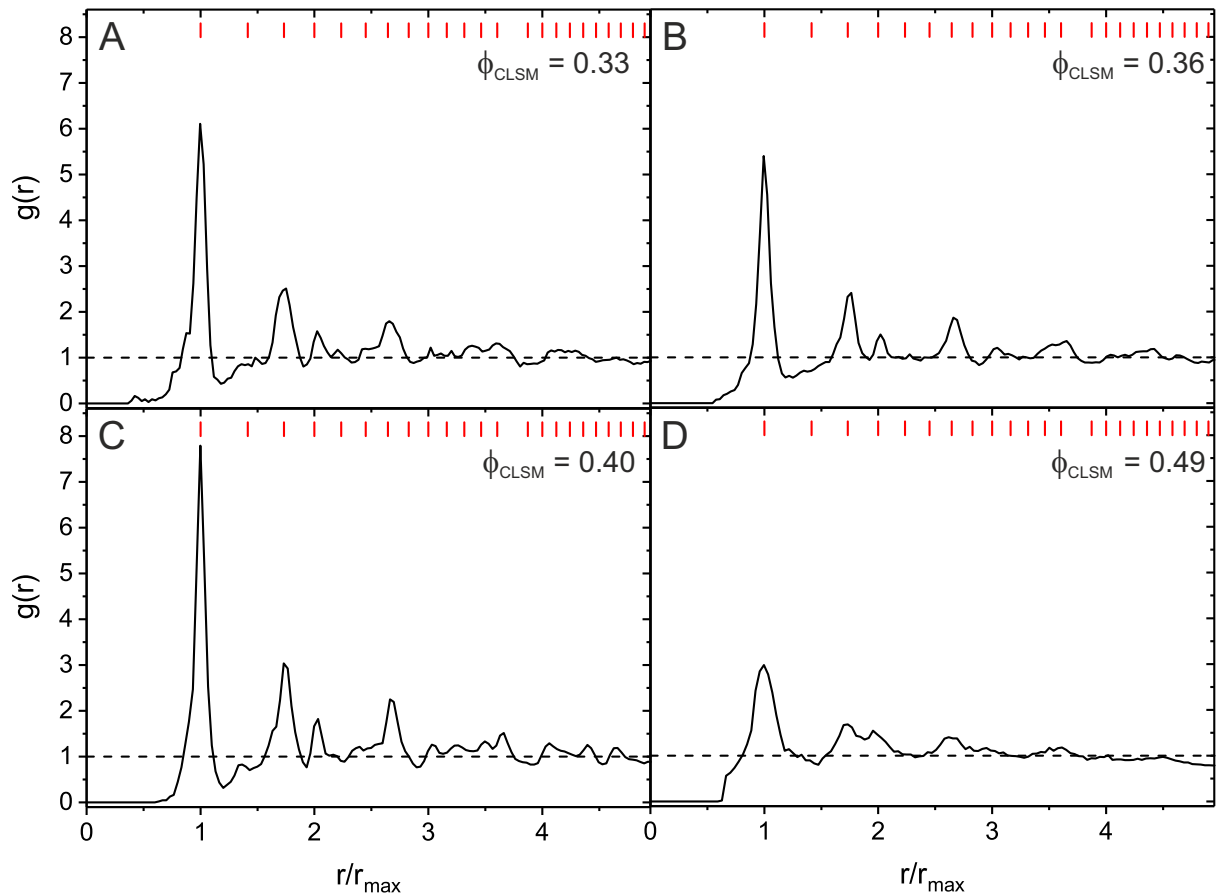


Figure 5.25: Normalized 3D average radial distribution functions calculated from image sequences describing a volume element in the samples consisting of $C_{71}S_{6.6}(15\%)$ particles at different volume fractions ϕ_{CLSM} : A. $\phi_{CLSM}=0.33$, B. $\phi_{CLSM}=0.36$, C. $\phi_{CLSM}=0.40$, D. $\phi_{CLSM}=0.49$. The distance r is normalized by the average inter-particle distance r_{max} in the structure. The red lines indicate theoretical peak positions in a 3D $g(r)$ of a FCC lattice.

To obtain further information on the crystal lattice, microradian SAXS was used. This method provides average information on the whole bulk sample structure in contrast to the CLSM measurement which gives only local structure details. Using the microradian setup, instrumental limitations are quite small as the beam is focused on the detector. Therefore, sharp Bragg peaks are obtained, if the sample includes large single crystalline domains. The sample was rotated by a rotational angle ω with respect to the incident X-ray beam direction, so that measurements along different orientations of the crystalline sample were possible. $\omega = 0^\circ$ corresponds to the initial sample position. At this position the close-packed hexagonal planes are aligned parallel to the capillary wall as seen before in the CLSM measurements. Thus, the initial beam position is parallel to the $[111]$ direction of the crystalline sample. Representative scattering patterns of the sample dispersion with a weight concentration of 7.5 wt% at different rotational angles ω (A: $\omega = 0^\circ$, B: $\omega = -55^\circ$, C: $\omega = +35^\circ$) are depicted in Figure 5.26.

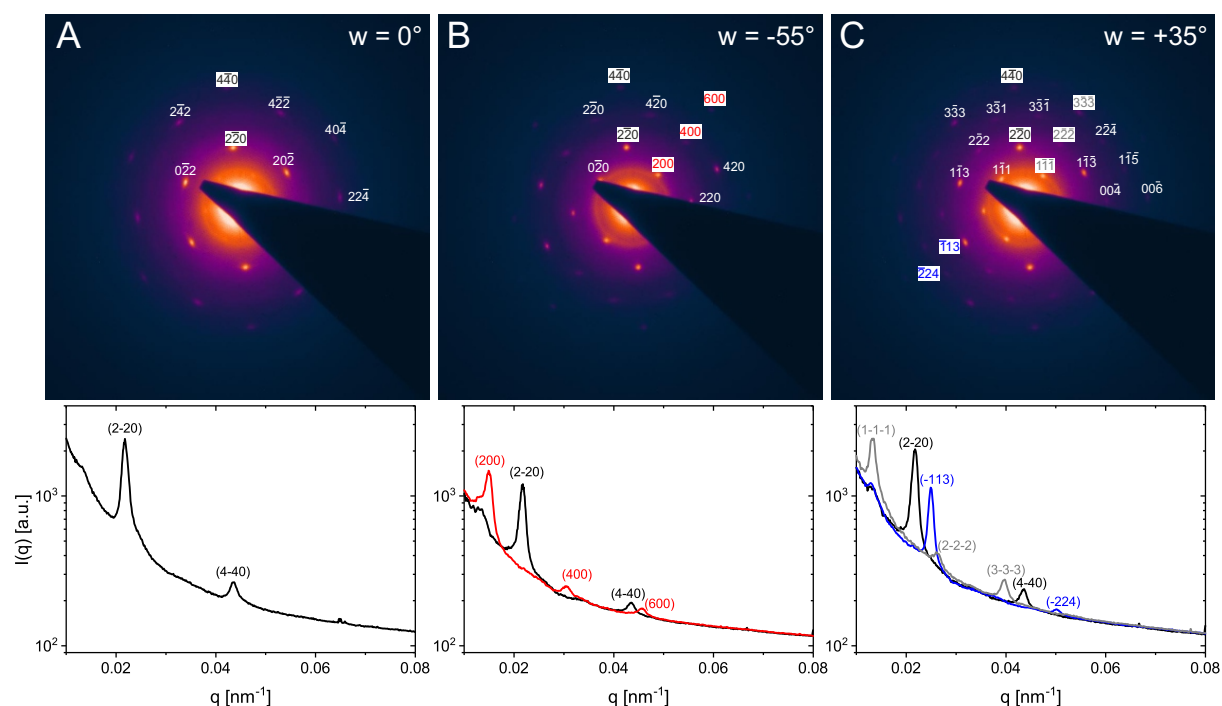


Figure 5.26: Scattering patterns recorded at different rotational angles ω : A. 0° , B. -55° , C. $+35^\circ$. Below the scattering patterns, scattering profiles are shown, which were extracted from selected wedges of the scattering patterns. Peaks belonging to a specific wedge are labeled with the same color as the resulting profile of this wedge.

The scattering pattern at $\omega = 0^\circ$ reveals a six-fold symmetry of the samples and pronounced Bragg peaks of several orders. The diffraction peaks of all scattering patterns are sharp as peak broadening in radial or azimuthal direction is mostly absent. The narrow peak widths point to the pronounced long-range order of the sample. This is in particular remarkable, since the beam cross-section was large ($500 \times 500 \mu\text{m}^2$). Hence,

single crystals with areas of at least $500 \times 500 \mu\text{m}^2$ were present and the crystal orientation was perfectly preserved over $500 \mu\text{m}$. In B and C the respective scattering patterns recorded at a rotational angle ω of -55° and $+35^\circ$ are depicted, respectively. These include as well sharp Bragg peaks of several orders. The diffraction peaks in A, B and C can be assigned to the reciprocal lattice representing either a FCC or a RHCP lattice. Exemplarily, a few peaks are indexed in the scattering patterns shown in Figure 5.26.

To analyze the scattering patterns further, wedges which contain different orders of Bragg peaks were converted into the respective scattering profiles. Bragg peaks belonging to the same selected wedge are labeled using the same color for their Miller indices. Below each 2D scattering pattern, the scattering profiles corresponding to the selected wedges are shown using the same color code. The stacking independent (2-20) and (4-40) diffraction peaks are visible at all three rotational angles and are located at similar values of q . This shows that the crystal planes are very well aligned to the capillary wall. The q -positions of the maxima (Bragg peaks) are required to determine the interplanar distance d_{hkl} of the crystal lattice which were calculated according to eq. 2.33.

For this purpose, the background intensity that can be derived if a small wedge without diffraction peaks is analyzed was subtracted from the scattering profiles shown in Figure 5.26. Fitting the background corrected scattering profiles with a Gaussian fit curve, the q -positions of the maxima were extracted and d_{hkl} was calculated. A FCC lattice was assumed for these calculations. These values allowed to derive the lattice constant a , the inter-particle distance d_{cc} and the volume fraction ϕ_{SAXS} using eq. 2.34, 5.3 and 5.2. The analysis of all Bragg peaks led to similar results for a , d_{cc} and ϕ . Averaging the results, the following mean values including their standard deviation as errors were obtained: $a = 821 \pm 7 \text{ nm}$, $d_{cc} = 580 \pm 5 \text{ nm}$ and $\phi = 0.40 \pm 0.01$. The resulting values for each analyzed Bragg peak are listed in Table A.7 in the Appendix. Considering the errors of the respective parameters, the results agree with the ones derived from analysis of the CLSM images.

In Figure 5.27 scattering patterns at a rotational angle ω of $+35^\circ$ and -35° are depicted. Contrary to expectations, the 2D scattering patterns at opposite angles are similar. This implies that peaks, that are forbidden in a pure FCC crystal, appear and hence stacking disorder is present. The forbidden peaks are exemplarily indicated with white circles in Figure 5.27. Further investigations have to be conducted to clarify if either twinning, i.e., the appearance of ABCABC as well as ACBACB stacking is present, or if a random hexagonal close packed (RHCP) lattice exists. If twinning is the case, the ratio of both stacking types should be around 1 as the diffraction peaks are of similar intensity at negative and positive rotational angles. For further analysis in this thesis a FCC lattice is assumed.

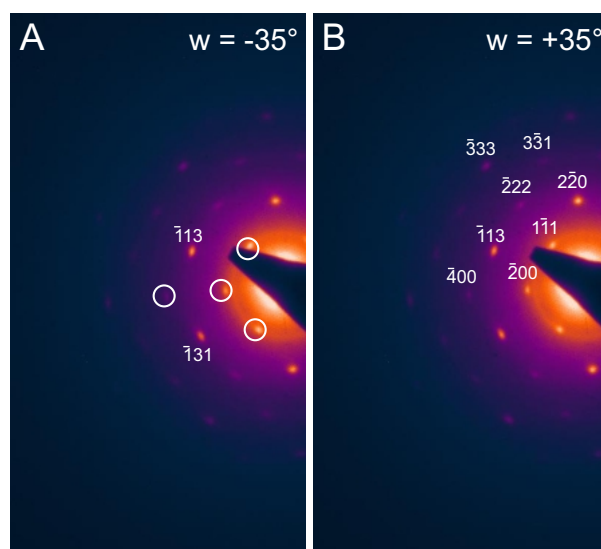


Figure 5.27: Scattering patterns at $\pm 35^\circ$: A. -35° , B. $+35^\circ$. The white circles exemplarily indicate forbidden reflections which should not arise at the given rotational angle ω .

5.3.2 Optical Properties

Apart from the structural investigations, the optical properties of the crystalline samples were studied. Figure 5.28 A shows the absorbance spectra of the samples at different volume fractions.

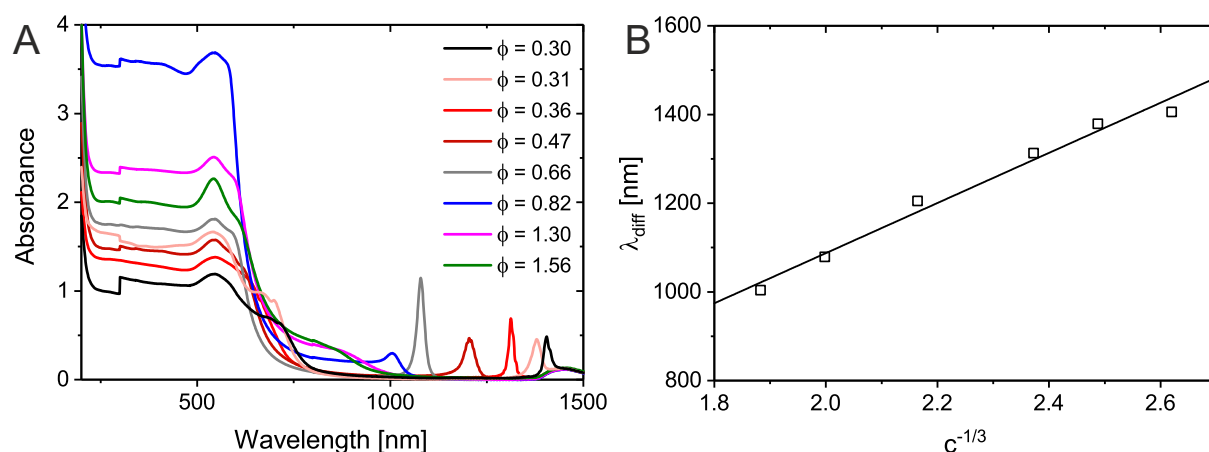


Figure 5.28: A. UV-vis absorbance spectra of crystalline samples from $C_{71}S_{6.6}(15\%)$ particles at different volume fractions ϕ_{UV-vis} recorded at room temperature. B. Position of the diffraction peak as a function of $c^{-1/3}$ of dispersions consisting of $C_{71}S_{6.6}(15\%)$ particles.

In similarity to the dilute dispersion of these particles, the concentrated dispersions show a plasmon resonance at 544 nm. Additionally, a narrow diffraction peak is visible in most of the spectra indicating a crystalline character of the samples. Only for the highest

volume fractions ($\phi = 1.30$ and $\phi = 1.56$) the diffraction peak is not distinctly visible. In these spectra it appears as shoulder close to the plasmon resonance. As expected, the Bragg peaks shift from longer to shorter wavelengths with increasing volume fraction. Due to the larger dimension of these particles, their diffraction covers a completely different wavelength range as compared to smaller Au-PNIPAM particles discussed in Sections 5.1.3 and 5.2.3. Diffraction peaks reaching the near-infrared spectral range (800-1400 nm) could be obtained for the investigated volume fractions of the $C_{71}S_{6.6}(15\%)$ particles. Based on the results of CLSM and SAXS, a FCC lattice was assumed for the different samples, although further investigations would be needed to clearly manifest the type of crystal lattice. So far, only samples with low volume fractions were investigated by CLSM and SAXS. To show that the same crystal lattice is present for samples at $\phi = 0.30 - 0.82$, the position of the Bragg mode, λ_{diff} , at each volume fraction was plotted versus their concentration $c^{-1/3}$ as shown in Figure 5.28 B.

A linear relationship as indicated by the solid black line is found. As previously derived in Section 5.1.3, the linear evolution allows to conclude that the sample crystallizes in the same crystal lattice over the whole range of investigated volume fractions.^[185,191] λ_{diff} at $\phi = 1.30 - 1.56$ was not plotted as it could not be reliably determined. The (111) plane of the samples is assumed to be oriented parallel to the glass slide of the sample cell ($\theta = 0^\circ$). Using the position of the Bragg peak, λ_{diff} , and assuming an average refractive index of 1.345 of the superstructure as derived in Section 5.2.3, the lattice plane distance d_{111} can be calculated according to eq. 5.1. d_{111} allows to derive a , d_{cc} and ϕ using eq. 2.34, 5.3 and 5.2. These values as well as the FWHM of the Bragg modes are summarized in Table 5.10.

Table 5.10: Summary of the results obtained from UV-vis absorbance spectra analysis: The position of the diffraction peak λ_{diff} , the full width at half maximum FWHM, the lattice plane distance d_{111} , the lattice constant a , the volume fraction ϕ_{UV-vis} and the inter-particle distance d_{cc} .

$C_{71}S_{6.6}(15\%)$						
c [wt%]	λ_{diff} [nm]	FWHM [nm]	d_{111} [nm]	a [nm]	ϕ_{UV-vis}^a	d_{cc} [nm]
5.6	1406	17	523 ± 2	905 ± 4	0.30 ± 0.01	640 ± 3
6.5	1379	31	513 ± 2	888 ± 4	0.31 ± 0.01	628 ± 3
7.5	1313	16	488 ± 2	845 ± 4	0.36 ± 0.01	598 ± 2
9.9	1205	36	448 ± 2	776 ± 3	0.47 ± 0.01	549 ± 2
12.5	1079	23	401 ± 2	695 ± 3	0.66 ± 0.01	491 ± 2
15.0	1004	70	373 ± 2	646 ± 3	0.82 ± 0.01	457 ± 2

^a The volume fractions ϕ_{UV-vis} were calculated assuming FCC lattices (number of particles per unit cell is 4 and the unit cell volume is given by a^3) using the lattice constant a and the hydrodynamic radius R_h at 25°C.

Increasing volume fractions result in smaller values of d_{111} , a and d_{cc} . Above volume fractions ϕ_{UV-vis} of 0.82 the inter-particle distance is smaller as the measured hydrodynamic diameter $\lambda_b\sigma$ (472 nm at 25°C) of the particles in the dilute regime. If the particles are assumed to have a diameter in the range of $\lambda_b\sigma$ in the crystal lattices, it can be concluded that the particles already interpenetrate. The FWHM of the diffraction modes in the absorbance spectra in Figure 5.10 are increased as compared to the CS particles including a 15 nm gold core, but still narrow. Further, some samples show a secondary order diffraction mode which appears at $\lambda_{diff}/2$. In a few cases ($\phi_{UV-vis} = 0.36, 0.47, 0.66$) the secondary Bragg peak is at a similar position as the plasmon resonance of the particles. Here, coupling between the plasmon resonance and the Bragg mode might occur. However, future investigations on these samples including simulations are needed to interpret the spectra further. Apart from that, the single-particle scattering is significantly reduced at wavelengths smaller than the Bragg mode. This agrees well with the results presented in Section 5.2.3. The values for d_{111} , a and ϕ listed in Table 5.10 are in the same range as the ones from CLSM and SAXS (at $c = 7.5$ wt%). To conclude, the use of three complementary methods (CLSM, SAXS and UV-vis absorbance spectroscopy) provided full insight into the structural and optical properties of superstructures from CS particles with a small core-to-shell ratio.

Chapter 6

Influence of an Electric Field on Hard-Core/Soft-Shell Particles in Bulk

Up to now, the crystallization of CS particles was investigated in dependence on structural aspects like the cross-linker content, total dimension and core size or presence, respectively. Tuning the mentioned properties led to crystal phases in the equilibrium state. A promising route that can lead to crystal phases beyond equilibrium is directed self-assembly. This is realized, e.g., by application of an external electric field to a colloidal dispersion. The particles acquire a dipole moment in the electric field. For hard colloids it is known that this dipole is the result of the mismatch in permittivity of colloid and solvent while they are exposed to the electric field. The dipole moment creates a different type of force symmetry. At low volume fractions, it has been observed that the colloids preferentially align in chain-like structures (strings) in direction of the electric field.^[63] In principle, different phase transitions can be observed that are influenced by the applied electric field strength, the colloid type and the volume fraction of the investigated dispersions. In this chapter, the field-induced structural transitions of SiO₂-PNIPAM particles were investigated in dependence on the field strength and the volume fraction. Hard-core/soft-shell particles combine the properties of hard spheres and soft colloids. Therefore, it is of significant interest to explore their field-induced behavior. The CS particles may offer the possibility to tune the electric field response between the one of hard and the one of soft colloids by tailoring the CS structure. For now, it is focused on a detailed characterization of one specific CS system.

6.1 Characterization of SiO₂-PNIPAM Particles in the Dilute Regime

For the experiments in the presence of an electric field, colloids which are easily polarizable are needed. Among others, the size of the particle is crucial to ensure a sufficient polarizability.^[192] Therefore, SiO₂-PNIPAM CS particles with diameters in the μm range were prepared. The SiO₂ particles were prepared using the known Stöber process.^[165] SEM images of the rhodamine labeled SiO₂ cores prior to encapsulation are depicted in Figure 6.1 A. The Stöber synthesis led to monodisperse, spherical particles. The diameter of 94 particles was analyzed at different positions of the deposited particle monolayer on the substrate using the software *ImageJ*. The respective histogram is depicted in Figure 6.1 B. An average diameter of 486 ± 23 nm was determined. In similarity to the synthesis route of the Au-PNIPAM particles, the encapsulation of the SiO₂ cores was performed using free radical seeded precipitation polymerization. In order to allow the preparation of particles with larger polymer shells, the synthesis was performed in a semi-batch fashion using several sequential polymerization steps (see Section 3.2.2).

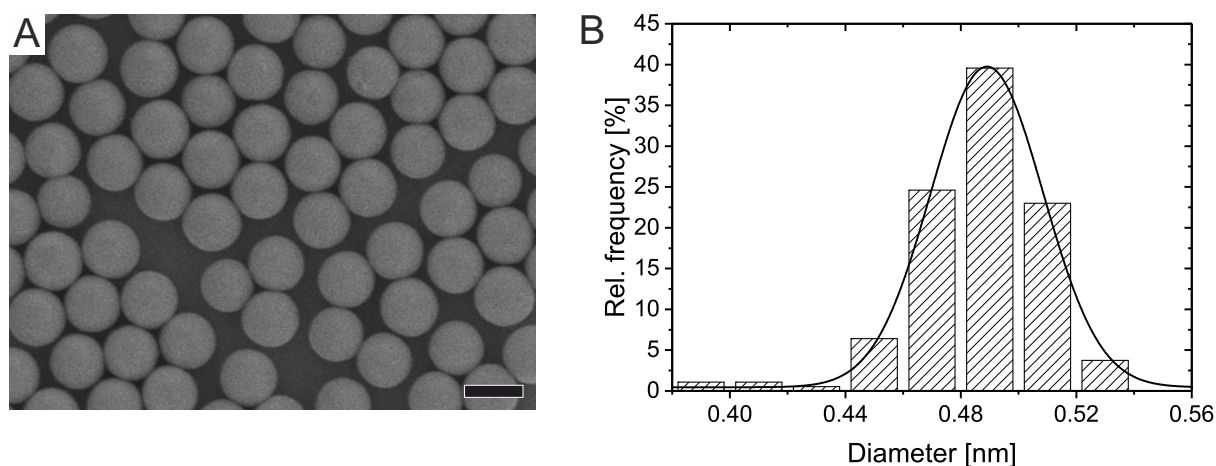


Figure 6.1: A. Representative SEM image of the silica particles C₄₈₆ prior to encapsulation. The scale bar is 500 nm. B. Histogram illustrating the distribution of analyzed particle diameters. The solid black line is a Gaussian fit to the data.

The success of the synthesis was confirmed by TEM and LS. A respective TEM image that shows the CS structure of the particles is depicted in Figure 6.2.

The SiO₂ cores are clearly visible as circular objects because of their high electron contrast. The cross-linked PNIPAM shells are surrounding the SiO₂ cores. They are less recognizable as compared to the cores due to their low electron contrast which is related to their low nominal cross-linker content (5 mol% referred to NIPAM). Furthermore, one should note that the TEM images are not showing the actual dimension of the shell. The shells are collapsed due to the high vacuum atmosphere in the TEM and due to drying

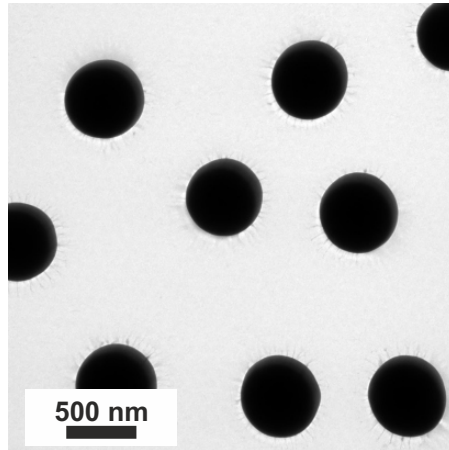


Figure 6.2: Representative TEM image of the SiO₂-PNIPAM particles C₄₈₆S_{1.7}(5%).

effects as a result of the sample preparation. The dimension of the CS particles in the swollen state was determined by angular-dependent SLS and DLS measurements at 25°C. The large size of the CS particles leads to form factor minima in the angle range from 30° to 150°. It is reasonable to analyze the data obtained from SLS first in order to reveal positions of the form factor minima of the particles. Then, these positions can be considered in the DLS analysis. Figure 6.3 A shows the non-solvent corrected, recorded scattering intensity $I(q)$ in dependence on the scattering vector q .

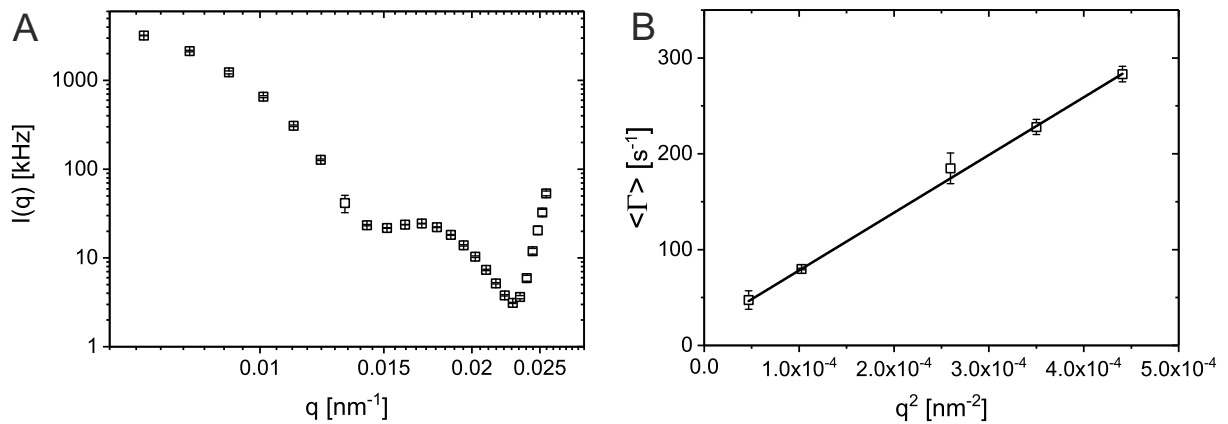


Figure 6.3: A. Non-solvent corrected scattering profile of C₄₈₆S_{1.7}(5%) particles. The scattering intensity $I(q)$ in dependence on the scattering vector q at 25°C is shown. B. Average relaxation rate $\langle \Gamma \rangle$ as function of q^2 . The black solid line is a linear fit.

At low q -values, the scattering intensities approach constant values indicating the Guinier plateau. Further, two pronounced form factor minima at $q = 0.014$ and 0.023 nm^{-1} appear. At the position of the first minimum (q_{min}), the relation $qR = 4.493$, that is valid for hard, monodisperse colloids, can be used as an approximation to estimate the particle radius.^[155] Accordingly, a radius of 321 nm was determined. In Figure 6.3 B the

angular-dependent DLS data are depicted. The mean relaxation rate, $\langle\Gamma\rangle$, as function of q^2 is shown. Data collected at angles at or in the vicinity of the form factor minima are not reliable and thus not plotted in the diagram. The data could be fitted using a linear regression curve indicated by the solid line with an intercept close to zero. This allows to conclude that purely translational diffusion was probed. The translational diffusion coefficient D_T can be calculated via $\Gamma = D_T \cdot q^2$. R_h was determined to be 405 ± 5 nm using D_T and the Stokes-Einstein equation (eq. 2.17). According to the introduced nomenclature, these particles are denoted as $C_{486}S_{1.7}(5\%)$ particles.

6.2 Overview of the Electric Field-Induced Phase Transitions

Herein, the electric field-induced behavior of different concentrated dispersions of the core-shell system $C_{486}S_{1.7}(5\%)$ is explored. Aiming for dispersions at volume fractions including fluid-like as well as crystalline samples, the $C_{486}S_{1.7}(5\%)$ particles were dispersed in water at different weight fractions (1-10 wt%). As analyzed later on, these weight fractions correspond to a volume fraction range between 0.16 and 0.40. The experimental setup that is schematically shown in Figure 6.4 was used to investigate the electric field-driven phase transitions.

The sample was placed between two ITO cover slips which acted as electrodes. An uniaxial sinusoidal electric field with field strengths ranging from 0 to $0.21 V_{rms}/\mu\text{m}$ at a constant frequency of 100 kHz was applied to the samples in z -direction. The frequency was chosen to be just high enough to avoid electrohydrodynamic flow. Monitoring of the field-induced transitions was performed by an inverted confocal laser scanning microscope in the xy -plane. The measurements were conducted at 20°C . Note, that the recorded CLSM images visualize the dye labeled SiO_2 core whereas the polymer shell is not visible in the images. The selective labeling of the particles was performed to distinguish them even at high volume fractions when they are in contact or interpenetrate/overlap. Further, the measurements were conducted at least 10 particle diameters away from the ITO cover slips in the xy -plane. For all samples several frames (around 1000) in dependence on the time were recorded at a fixed z -position. At low volume fractions, it can be assumed that these measurements are valid for the whole volume. At high volume fractions, i.e., in the crystalline state, volume elements were additionally analyzed. This was performed by collecting image sequences in the xy -plane at planes separated by maximal $0.13 \mu\text{m}$ in z -direction. Bleaching can be challenging, although not at the time scales needed for these measurements. The volume fractions were estimated using the average number density multiplied by the particle volume (eq. 5.5). The

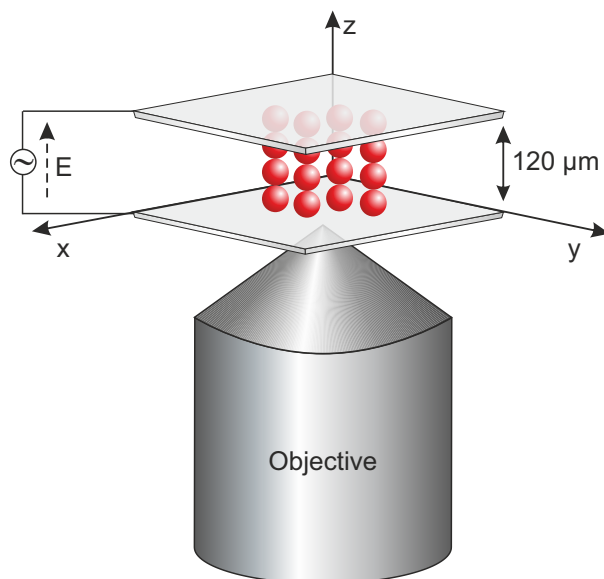


Figure 6.4: Schematic depiction of the setup used to investigate the influence of an applied electric field on the dispersion. The sample is placed between two ITO cover slips that act as electrodes. The distance between them is defined by a spacer with a thickness of $120\ \mu\text{m}$. In these experiments an alternating electric field at a constant frequency of 100 kHz was applied along the z -direction. Images were recorded in the xy -plane. Adapted with permission from "Electric Field Driven Self-Assembly of Ionic Microgels", by Nöjd, S; Mohanty, P.S.; Bagheri, P; Yethiraj, A.; Schurtenberger, P. *Soft Matter* **2013**, *9*, 9199-9207. Copyright 2013 by The Royal Society of Chemistry.

hydrodynamic dimensions ($R_h = 405 \pm 5\ \text{nm}$ at 25°C) of the particles were used to calculate the particle volume. Again, one should note that this results in an overestimation of the volume fraction. The average number of particles was counted per volume for the image sequences describing a volume element of the sample. In the case of the time-dependent measurements, it was counted per area. In order to count the particles, a custom-written software was used. The volume fraction of the crystalline samples can be calculated with much higher precision as compared to the fluid sample. This is achieved using the number density for an entire volume element with a thickness of several particle diameters in z -direction. In the case of the liquid-like samples, it was only possible to access the number of particles per xy -plane as the particles were continuously diffusing. The volume of the xy -plane was used as thinnest possible volume slice. The height of this slice corresponded to the particle diameter. The length and width were given by the area of the image. However, this determination is defective. Not every particle which is visible in the xy -plane has its center of gravity in the plane. Therefore, the number density and thus the volume fraction are overestimated. Yet, this derivation provides a reasonable approximation for the volume fraction, since a linear evolution between the determined volume fractions and the respective weight concentrations of the investigated dispersions was obtained. This correlation is depicted in Figure 6.5.

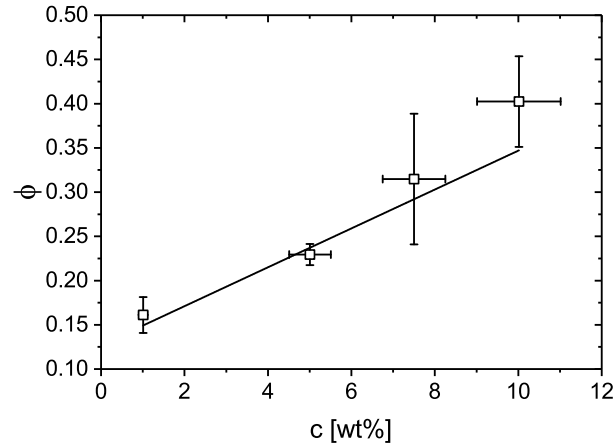


Figure 6.5: Volume fractions determined directly from the CLSM data versus the weight concentrations of the different concentrated dispersions. The black solid line is a linear fit.

The standard deviation of several measurements ($\phi = 0.16$ (36 measurements), $\phi = 0.23$ (10 measurements), $\phi = 0.32$ (19 measurements), $\phi = 0.40$ (17 measurements)) was used as error for the volume fraction. Regarding the weight concentration an error of 10% was assumed. Before the observed field-induced transitions are discussed in detail, a short overview of the different phases in dependence on volume fraction and electric field strength E is given in Figure 6.6.

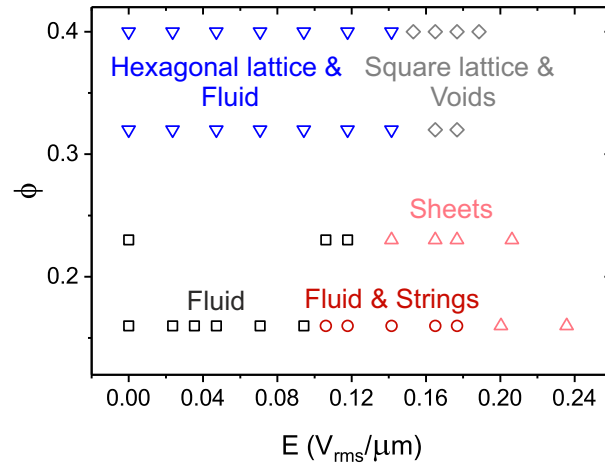


Figure 6.6: Phase diagram of $C_{486}S_{1.7}(5\%)$ particles showing different transitions in dependence on the volume fraction and the electric field strength E . At low volume fractions either a fluid (black squares), a mixture of a fluid and string phase (red circles) or sheets (rose triangles) are obtained. In contrast to this, a phase that shows a coexistence of fluid and hexagonally ordered domains (blue inverted triangles) or a square lattice separated by voids (gray rhombuses) are formed at higher volume fractions.

Representative CLSM images showing aqueous dispersions of $C_{486}S_{1.7}(5\%)$ particles between volume fractions of 0.16 and 0.40 for zero-field and after field-induced transition are presented in Figure 6.7. At $\phi = 0.16$, a field-induced transition from a fluid to a string phase was observed as depicted in Figure 6.7. Increasing the field strength further at $\phi = 0.16$, created a sheet phase at this volume fraction. A field-driven transition from a fluid-like to a sheet phase was found at $\phi = 0.23$. These sheets assembled, so that domains of particles arranged in a square lattice were observed in the xy -plane. These domains are shown in the CLSM image in Figure 6.7. At higher volume fractions of 0.32 and 0.40 the sample was in a fluid-crystalline state, i.e., a coexistence of a hexagonally ordered lattice and a fluid phase was revealed at zero-field or at low to medium field strengths, respectively. Areas that crystallized in a square lattice separated by voids were observed at high field strengths. The described transitions typically occurred within a few seconds.

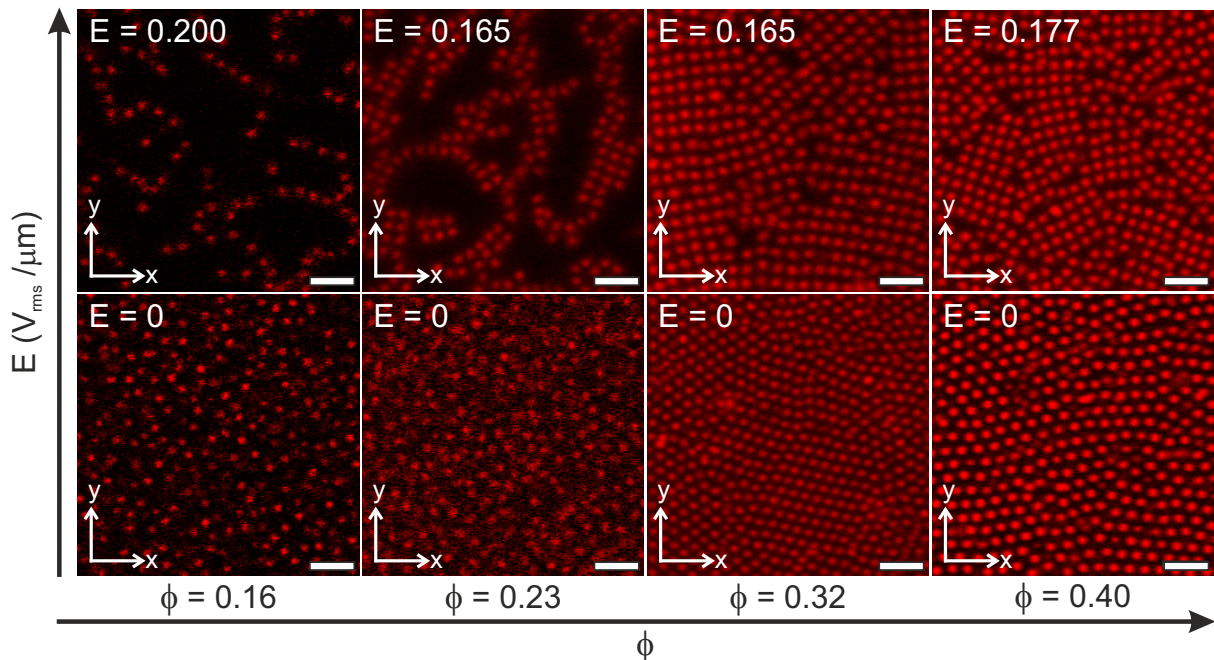


Figure 6.7: Representative 2D CLSM images (xy -plane) recorded at least 10 particle diameters away from the ITO cover slip. The images give an overview of the observed electric field-induced transitions for dispersions consisting of $C_{486}S_{1.7}(5\%)$ at different volume fractions and field strengths. The electric field was applied in z -direction, i.e., perpendicular to the image plane. The electric field strength E is given in $V_{rms}/\mu\text{m}$. The scale bars are $3 \mu\text{m}$.

6.3 Analysis of the Electric Field-Driven Transitions

In this section, the field-induced transitions are discussed in more detail. A quantitative analysis using radial distribution functions $g(r)$ is shown. The $g(r)$ functions were calculated by averaging the $g(r)$ of at least 100 frames of a time-lapse series in order to get enough statistics. First, the phase behavior of the sample with $\phi = 0.16$ is studied precisely.

In Figure 6.8 average radial distribution functions and corresponding representative CLSM images for this sample are depicted at different field strengths. In the absence of an electric field (Figure 6.8 A), the particles diffuse homogeneously in the field of view. This phase is referred to as isotropic liquid-like phase, i.e., as fluid. The phase behavior is still fluid-like if field strengths in the range of 0.024 to 0.094 $V_{rms}/\mu\text{m}$ were applied. Between field strength of 0.11 and 0.18 $V_{rms}/\mu\text{m}$, a transition to a string phase is observed. Strings are chains of touching particles which align in the z -direction of the electric field. Thus, they are not directly visible in the xy -plane. However, the decrease in 2D particle density visible in Figure 6.8 B and C as compared to Figure 6.8 A and B as well as the observed deceleration of the particle diffusion are typical signs for the presence of strings in the xy -plane according to several studies.^[65,66] Typically, these strings differ in their lengths. In order to visualize the chain-like structures, the electric field can be applied in x direction, so that the strings align in x direction as previously studied by Mohanty *et al.*^[66] In the performed experiments, the field is applied in z -direction, so that strings are aligned in z -direction (schematically shown in Figure 6.4). This leads to the appearance of single particles in the xy -plane and coincides well with the observed results. Within the range of 0.11 and 0.18 $V_{rms}/\mu\text{m}$ the strings approach each other. At even higher field strength of 0.20 to 0.24 $V_{rms}/\mu\text{m}$, a mixture of strings and sheets has been observed. Sheets are 2D assemblies of chains aligned in the field direction which are typically hexagonally ordered.^[63] In the field of view (xy -plane), they are visible as chains of particles. To ultimately prove the presence of these sheets, studies in which the field is applied in x direction would be necessary. The observed sheets start to arrange in a labyrinthine structure of chains in the xy -plane which has been previously observed for hard-sphere systems.^[63]

The reported observations are in accordance with the tendencies observed in the calculated $g(r)$ functions. Figure 6.9 depicts these tendencies by showing the evolution of the peak height of the first maximum g_{max} (left) and its position r_{max} (right), i.e., the average inter-particle distance, with increasing field strengths. The data at $\phi = 0.16$ is indicated using black squares. At low field strengths, the $g(r)$ shows a maximum at around 1 μm and a peak height of around 1.4. Increasing the field strengths leads first to a decrease in the height of the first maximum g_{max} until a field strength of 0.12 $V_{rms}/\mu\text{m}$. This can be

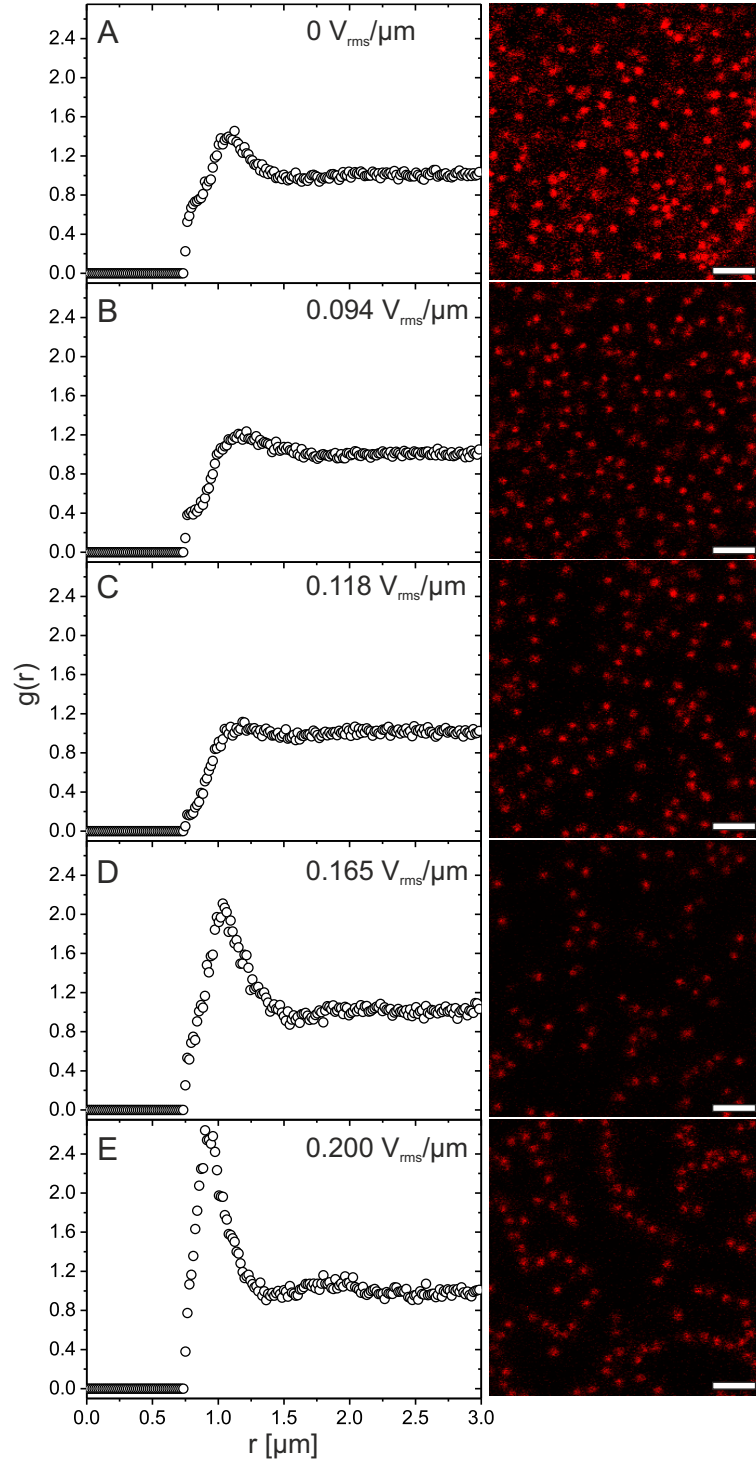


Figure 6.8: Representative average 2D radial distribution functions $g(r)$ and the corresponding 2D CLSM images describing the xy -plane for a dispersion of $C_{486}S_{1.7}(5\%)$ with $\phi = 0.16$ at different field strengths. The scale bars are $3 \mu\text{m}$.

attributed to the decrease in the spatial correlation as soon as the string formation starts. At this stage, the particle number density in the xy -plane is reduced. Further increasing the field strengths ($0.13 - 0.18 \text{ V}_{\text{rms}}/\mu\text{m}$) these strings approach each other which results

in a constant increase of the peak height g_{max} . Field strengths of 0.2 and 0.24 $V_{rms}/\mu\text{m}$ enhance the amplitude of g_{max} further. At the same time, increasing the electric field strength results initially in an increasing average inter-particle distance r_{max} . This is related to a decreasing particle density in the xy -plane that indicates the beginning of string formation. As soon as these strings start to approach each other in the xy -plane, a constant decrease of the inter-particle distance is observed. At high field strengths (0.2/ 0.24 $V_{rms}/\mu\text{m}$), when the strings transform to sheets, a further reduction of r_{max} is observed. This is related to the chain formation in the xy -plane when the sheet formation takes place.

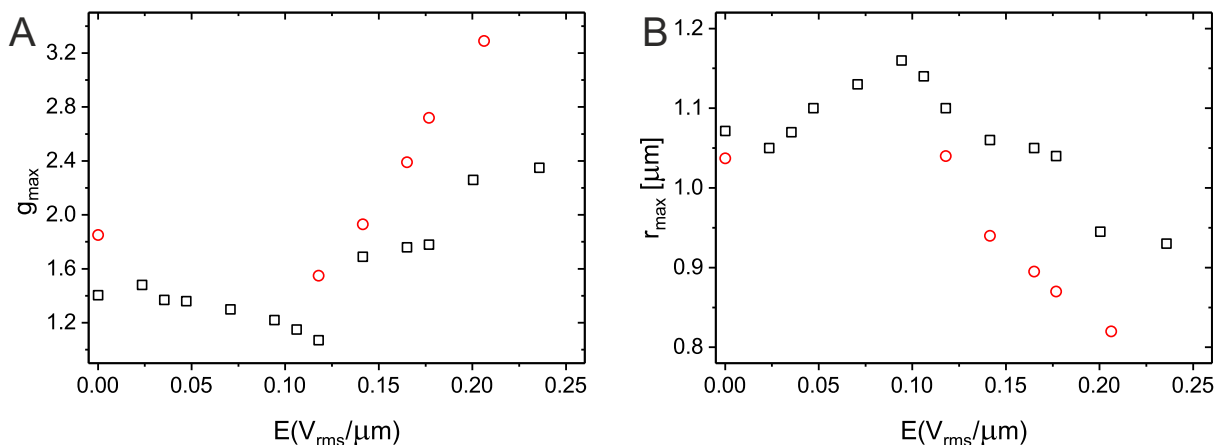


Figure 6.9: Evolution of the first maximum of the average 2D $g(r)$ function in dependence on the electric field strength E at volume fractions of 0.16 (black squares) and 0.23 (red circles). On the left the data describing the amplitude of the first maximum in the $g(r)$ and on the right the corresponding average inter-particle distance r_{max} is shown.

In Figure 6.10 the CLSM images and the corresponding average radial distribution functions at different field strengths are depicted for $\phi = 0.23$. A fluid phase is found below $E = 0.14 V_{rms}/\mu\text{m}$. Sheets are formed at field strengths between 0.14 to 0.19 $V_{rms}/\mu\text{m}$. These sheets form an interconnected labyrinth of chains in the field of view (xy -plane). Interestingly, a direct transition to sheets seems to be preferred and no intermediate phase consisting of strings is found. This observation is in contrast to the data recorded at $\phi = 0.16$. The formed sheets quickly form an interconnected labyrinthine network in the xy -plane. Increasing the field strengths further the sheets approach each other within this labyrinthine network and form interconnected domains that show a square symmetry. These areas of square lattices still retain in the labyrinthine shape of the sheets. Additionally, the analysis of the position and peak height of the radial distribution functions is shown in Figure 6.9 using red circles. The following observations are made: At low E up to 0.12 $V_{rms}/\mu\text{m}$, the particles are freely diffusing. At this stage the peak height of the $g(r)$ is slightly decreasing while the inter-particle distance is almost constant with increasing E . As soon as sheets are formed, the peak height g_{max} of the first maximum is

increasing and a second peak at larger distances appears. Both observations are related to the formation of chain-like structures in the xy -plane. Further enhancement of the electric field causes the sheets to assemble, i.e., an assembly of the chain-like structures in the xy -plane is found, resulting in an increasing spatial correlation. Hence, the peak height g_{max} increases further. During the formation of sheets and their subsequent assembly, the average inter-particle distance r_{max} decreases constantly.

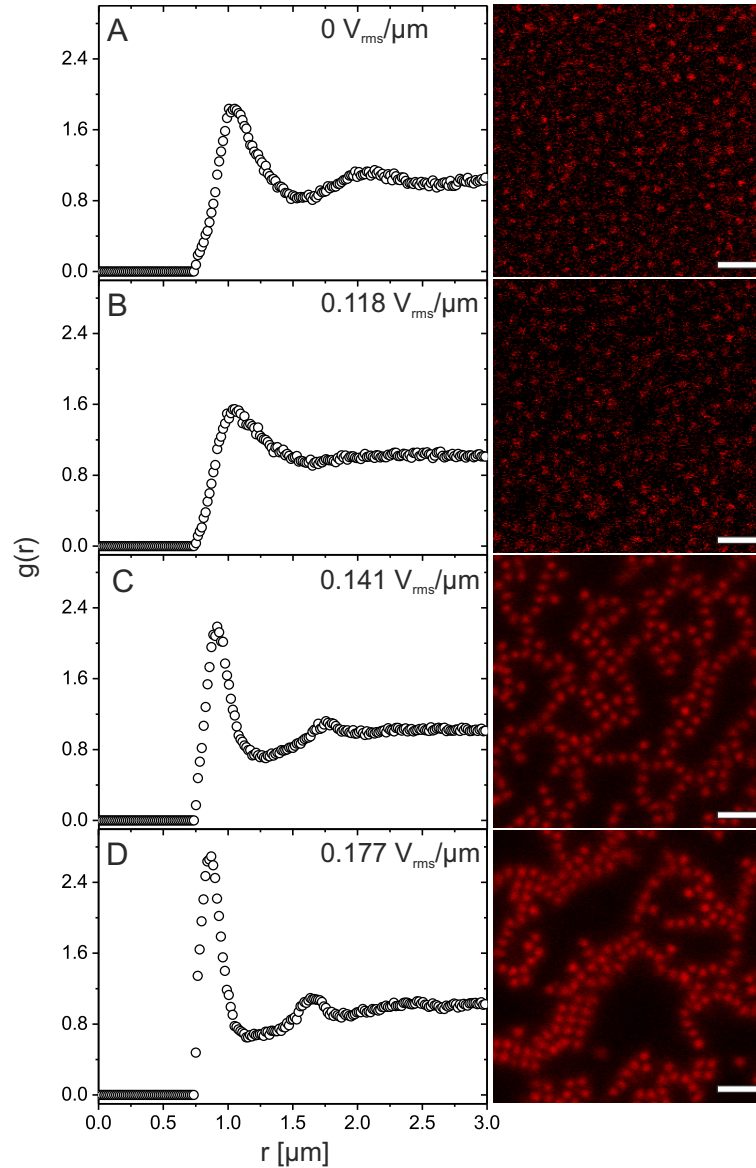


Figure 6.10: Representative average 2D radial distribution functions $g(r)$ and the corresponding 2D CLSM images describing the xy -plane for a dispersion of $C_{486}S_{1.7}(5\%)$ with $\phi = 0.23$ at different field strengths. The scale bars are $3 \mu\text{m}$.

At higher volume fractions of 0.32 and 0.40, a mixture of a fluid phase and hexagonally arranged domains is observed at zero-field up to $E = 0.14 V_{rms}/\mu\text{m}$. The coexistence of these two phases might be related to the volume fraction of the samples which is slightly

below the volume fraction which would lead to a stable crystalline phase. However, also contaminations can disturb the hexagonally ordered lattice and thus lead to coexistence of fluid and crystalline phases. Representative CLSM images as well as a respective radial distribution function at $\phi=0.32$ and $\phi=0.40$ recorded at zero-field conditions are depicted in Figure 6.11 and 6.12, respectively.

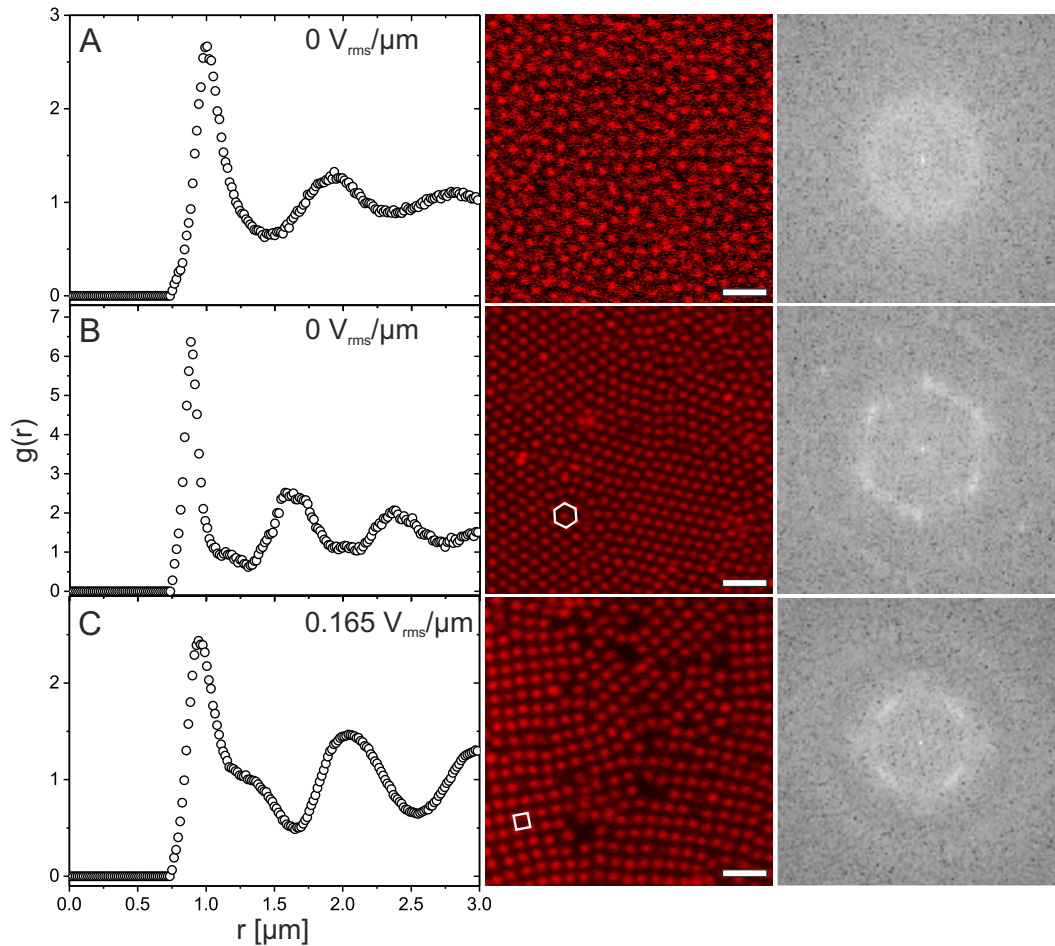


Figure 6.11: Representative average 2D radial distribution functions $g(r)$ (left), corresponding 2D CLSM images describing the xy -plane (middle) and Fast Fourier transformations (right) for a dispersion of $C_{486}S_{1.7}(5\%)$ with $\phi = 0.32$ at different field strengths. The scale bars are $3 \mu\text{m}$.

The six-fold symmetry in Figure 6.11 B and 6.12 B is exemplarily highlighted using a white regular hexagon. In both Figures, 6.11 and 6.12, A shows images at a sample position where the particles are in a fluid phase whereas in B hexagonally arranged domains are dominating. On the righthand side in Figure 6.11 and 6.12 Fast Fourier transformations of the CLSM images are shown that confirm the existence of both phases. In Figure 6.11 A and 6.12 A the Fast Fourier transformation patterns show concentric circles with equal intensity indicating the presence of a disordered fluid. In Figure 6.11 B and 6.12 B the Fast Fourier transformations indicate a six-fold symmetry which is typical for hexagonally arranged systems. Due to the coexistence of fluid and

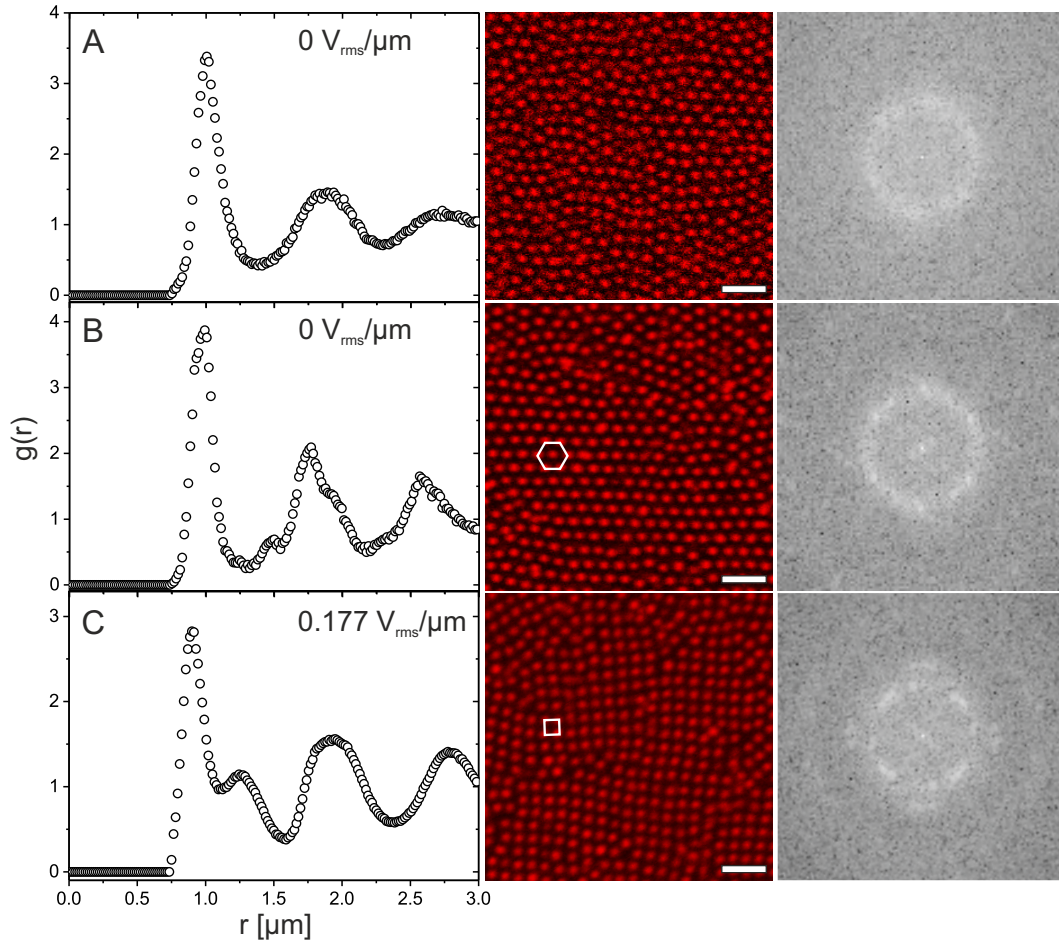


Figure 6.12: Representative average 2D radial distribution functions $g(r)$ (left), corresponding 2D CLSM images describing the xy -plane (middle) and Fast Fourier transformations (right) for a dispersion of $C_{486}S_{1.7}(5\%)$ with $\phi = 0.40$ at different field strengths. The scale bars are $3 \mu\text{m}$.

hexagonally ordered domains, the radial distribution functions differ strongly at different sample positions at low field strengths up to $0.14 \text{ V}_{rms}/\mu\text{m}$ at $\phi=0.32$ and $\phi=0.40$. Hence, the inter-particle distance varies between $1 - 2 \mu\text{m}$ and the amplitude of the first peak ranges from ≈ 2 to 5 . At field strengths up to $0.14 \text{ V}_{rms}/\mu\text{m}$, no significant influence of the electric field strength on the phase behavior of the colloidal dispersions could be noted at $\phi=0.32$ and $\phi=0.40$.

Between $E = 0.16$ and $0.18 \text{ V}_{rms}/\mu\text{m}$ at $\phi = 0.32$ and between $E = 0.15$ and $0.19 \text{ V}_{rms}/\mu\text{m}$ at $\phi = 0.40$, a field-induced transition to a square symmetry in the xy -plane is found. A representative CLSM image as well as the corresponding $g(r)$ function and a Fast Fourier transformation are represented in Figure 6.11 C and 6.12 C at $\phi=0.32$ and $\phi=0.40$, respectively. The square symmetry in both samples is exemplarily indicated using white squares. The four-fold symmetry is confirmed by the Fast Fourier transformations that show four distinct peaks. The area fractions of particles in the field of view which are

ordered in this square pattern are separated by voids. A homogeneous square lattice without voids was not observed for the range of investigated field strengths and volume fractions. However, the space of the voids is significantly decreased at $\phi = 0.40$ as compared to $\phi = 0.32$. Further, a significant degree of polycrystallinity is observed at both volume fractions. Both samples show domains with square symmetry of several orientations leading to a large number of grain boundaries. Particularly, the sample at $\phi = 0.32$ is distinctly polycrystalline which may be additionally supported by the increased area fraction of voids. Thus, the amplitude in the first peak of the $g(r)$ functions in C is reduced at both volume fractions as compared to the phase that showed the coexistence of fluidic and hexagonally arranged domains (see Figure 6.11 and 6.12 A and B, respectively). Analyzing the position of the first peak in the $g(r)$ functions, r_{max} , at field strengths above $0.17 V_{rms}/\mu\text{m}$ provides values of around $0.9 \mu\text{m}$ at $\phi = 0.40$ in contrast to increased values of around $0.94 \mu\text{m}$ at $\phi = 0.32$. This difference can be attributed to an increased particle density at higher volume fraction as well as to the decreasing area fraction of voids at larger ϕ . As previously mentioned, image sequences separated by small z -intervals were also recorded to visualize volume elements in the samples at $\phi = 0.32$ and 0.4 . However, both samples were not fully static, i.e., a slight particle motion was observed from image to image in the recorded image sequences. Hence, it was not possible to obtain reliable informations on their ordering in z -direction in order to reconstruct the crystal lattice, so that the crystal structure could not be unambiguously determined. For similar particles a body-centered tetragonal (BCT) lattice, i.e., a stretched BCC lattice, has been found.^[65] Here, the unit cell spacings a and b are equal. The unit cell spacing c is different. Assuming a BCT lattice for the $\text{C}_{486}\text{S}_{1.7}$ (5%) particles in which the unit cell spacing a and b correspond to the average inter-particle distance r_{max} , the unit cell spacing c can be estimated. Therefore, the equation $c = 2a/\sqrt{6}$ is used providing a value of $0.77 \mu\text{m}$ at $\phi = 0.32$ and $0.73 \mu\text{m}$ at $\phi = 0.40$ for the unit cell spacing c .

6.4 Comparison with Hard Colloids and Microgel Systems

So far, electric field-driven phase transitions of hard-core/soft-shell particles were not investigated in the literature. As the CS structure combines hard, spherical colloids and soft microgel shells, it is hard to predict how dipolar interactions arise in these systems. Several studies on field-induced transitions for hard colloids^[63,64,122–127] and negatively charged microgel particles^[65–67,123] exist in the literature. These transitions are based on dipolar interactions which rise in these systems in the presence of an electric field. As discussed in Section 2.1.3, the dipolar interactions of spherical, hard colloids are influenced by the applied frequency of the electric field.^[65] In the case of hard colloids in aqueous medium, the dipolar interaction at low frequencies in the kHz regime consists of the fol-

lowing two main contributions: (1) Ionic polarization that develops due to surface charges in the double layer and (2) dielectric polarization based on the different dielectric constant between particles and solvent.^[65,130,131] At frequencies approaching the MHz regime, which is mostly investigated with charged, hard colloids in both aqueous and low polar solvents, ionic polarization is decreased and dielectric polarization dominates.^[63,65,124,132] In contrast to this, negatively charged microgels are supposed to follow another mechanism: As their shell is highly swollen with water (around 80%), the dielectric polarization is probably quite small because no significant difference in the dielectric constant between particles and solvent is present. Since these ionic microgels contain more counterions as compared to the number of surface charges, it is assumed that the dipolar interactions arise from the polarization of the confined counterions.^[65]

The investigated CS particles include only a small number of negative charges that originate from the anionic initiator PPS. Hence, the dipolar interaction is probably more similar to that of hard, spherical colloids. However, further investigations would be needed to verify the exact interaction mechanism.

In the following, the presented experimental results are compared to studies on hard SiO₂ colloids and negatively charged microgels in the presence of an electric field in dependence on the volume fraction.^[63,65] Dassanayake *et al.* investigated the electric field-driven self-assembly of SiO₂ particles in a water-glycerol mixture.^[63] These results coincide with the observations on CS particles. At low volume fraction ($\phi=0.1$) and with increasing field strength, the authors observed a transition from a fluid-like phase to chains in z -direction which start to assemble. At the same time, sheets were formed by a small percentage of particles which transformed into BCT structures after annealing them for a few hours. These observations conform to results of CS particles at $\phi = 0.16$ although the transformation to BCT domains was not observed at such low volume fractions for CS particles. However, this might be related to the fact that the structures from CS particles were not annealed. A transition from sheets to domains with square symmetry was observed for CS particles at increased $\phi = 0.23$. At larger volume fractions (>0.15), the formation of sheets and only a few chains has been reported for the SiO₂ particles. This agrees well with the C₄₈₆S_{1.7}(5%) particles at $\phi = 0.23$. In similarity to the findings on CS particles, the authors also observed that the chains in the xy -plane form complex labyrinthine structures. They describe that this structure was not changing for hours until it transformed into domains ordered in a BCT lattice. The longterm effects (hours to days) of the field influence for CS particles were not investigated as all transitions occurred very fast (seconds to minutes). The transition from the chain phase to small square areas in the image plane was observed within seconds. However, it could be interesting for future studies to investigate the influence of time more thoroughly. At high volume fractions (>0.4), Dassanayake *et al.* found a FCC lattice for the particles at zero-field conditions.

In the presence of an electric field, they observed a martensitic transition to domains of BCT crystals which started from defects in the hexagonal lattices. This is similar to the observations on CS particles at high volume fractions ($\phi = 0.32$ and 0.40), although no pure FCC phase was observed. Instead, a coexistence of hexagonal and fluidic domains was revealed up to field strengths of around $0.15 V_{rms}/\mu\text{m}$. At larger field strengths, a square lattice was found for the SiO_2 -PNIPAM particles.

Nöjd and Mohanty *et al.* investigated the field-induced transitions for negatively charged microgels in water.^[65,66] Identically to the observations on CS particles, the authors observed the formation of chains along the field direction with increasing field strengths. In their systems, the chains attracted each other with further increasing E and domains ordered in BCT lattices were reported even at very low volume fractions of 0.07 . For the SiO_2 -PNIPAM CS particles the chains that formed in z -direction also attracted each other. However, a BCT ordering at low ϕ was not obtained. At medium volume fractions ($\phi = 0.33$) in the microgel dispersions of Nöjd and Mohanty *et al.*, the density of chains along the field direction was increased. This led to larger domains ordered in BCT lattices at sufficient field strength. At high ϕ , when the particles already crystallize at zero-field, a transition from a FCC to a BCT phase was observed. In contrast to the CS system, a sheet phase has not been observed for these ionic microgels. Nöjd *et al.* directly reported a transition of chain-like structures (in z -direction) to BCT domains. In the case of CS particles, the chain-like structures approached each other. Yet, a direct transition to BCT domains was not observed. Instead, they either transformed into disordered domains of chains or into sheets with increasing field strengths ($\phi = 0.20$). Areas including square lattices were first observed at sufficient volume fractions of 0.32 and 0.40 and field strengths above $E = 0.15 V_{rms}/\mu\text{m}$. These square lattices developed from a phase that consisted of hexagonally ordered and fluid domains.

Chapter 7

Self-Assembly of Hard-Core/Soft-Shell Particles at Oil-Water Interfaces

The Chapters 5 and 6 focused on the phase behavior of hard-core/soft-shell particles in bulk. This chapter deals with the self-assembly of these particles at oil-water interfaces. Interactions at oil-water or air-water interfaces can be different than in bulk which is often underestimated.^[24,25] Thus, colloids that are stable in bulk can show a different behavior when they are adsorbed at fluid interfaces.^[26] These contradictory observations are related to additional interactions such as attractive capillary forces that exist at the interface and are not present in bulk.^[27] Additionally, the magnitude and effect of interactions like van der Waals^[28] and electrostatic interactions^[29] may be altered at the interface as compared to the bulk phase. Therefore, detailed investigations on the microstructures of the interfacial monolayers were performed. The self-assembly at the oil-water interface of CS particles with two different core sizes encapsulated in polymer shells of different thicknesses was investigated. CLSM and FreSCa cryo-SEM^[139] were used to study the interfacial microstructures *in situ*. The latter method was also suited to reveal the interfacial morphology of the particles at low surface coverage. Further, LB experiments were conducted to study the development of the microstructures upon compression, i.e., at increasing surface coverage. The results allowed to draw correlations between the different CS particle structures and the resulting interfacial microstructures upon compression. Apart from that, significant differences were found in the microstructures for CS particles and purely organic microgel particles without inorganic core. Finally, the structural behavior of a specific CS model system at an oil-water interface was directly compared to the bulk phase.

The same notation as previously introduced for the CS particles is used, except for a different supplement regarding the shell-to-core ratio and the diameter at the interface. As discussed in this chapter, both parameters are different at the interface as compared to the bulk phase. In order to highlight this difference, the subscript i for interface is introduced in terms of the shell-to-core ratio and the diameter resulting in λ_i and $\lambda_i\sigma$.

Still, the subscript b is applied with respect to the bulk phase.

7.1 Particle Morphology in Bulk

Based on a well established protocol, five different types of CS particles were synthesized via free radical seeded precipitation polymerization.^[191] All CS particles included a single SiO₂ core that was encapsulated in a soft hydrogel shell. Within this chapter, two series of CS particles are differentiated: One series including particles with a 125 nm silica core in diameter (C₁₂₅). Another series of CS particles incorporating a SiO₂ core with a diameter of 351 nm (C₃₅₁). These cores were encapsulated in shells of different thicknesses. The interfacial self-assembly of these CS particles was analyzed with respect to the different particle structures with varying core sizes and polymer shell thicknesses. Further, the results of the CS particles were compared to purely organic microgel particles without a solid core.

The two batches of different sized SiO₂ nanoparticle cores were prepared using the Stöber method.^[165] In Figure 7.1 a representative SEM image and a respective histogram of the diameter distribution are shown for the SiO₂ particles C₁₂₅ and C₃₅₁. In both cases, the particles are spherical and monodisperse. The diameter of the particles was determined by analyzing at least 150 particles using the software *ImageJ*. In total, five different CS systems were prepared. Table 7.1 summarizes the diameter σ of the SiO₂ particle cores as obtained by SEM, the overall hydrodynamic diameter $\lambda_b\sigma$ at 20°C in bulk and the shell-to-core ratio λ_b . The hydrodynamic diameters were obtained by Cumulant analysis of the DLS data. The standard deviation of three measurements gives the error of $\lambda_b\sigma$. The small error values highlight the monodispersity of the synthesized CS particles.

Table 7.1: Core diameter σ , overall hydrodynamic diameter $\lambda_b\sigma$ and shell-to-core ratio λ_b of the different CS systems.

Parameter	Small cores			Large cores	
	C ₁₂₅ S _{2.2}	C ₁₂₅ S _{3.0}	C ₁₂₅ S _{3.4}	C ₃₅₁ S _{2.2}	C ₃₅₁ S _{2.9}
$\sigma^{\#}$ [nm]	125 ± 10	125 ± 10	125 ± 10	351 ± 16	351 ± 16
$\lambda_b\sigma^*$ [nm]	281 ± 2	376 ± 5	429 ± 2	779 ± 14	1028 ± 9
λ_b	2.2 ± 0.2	3.0 ± 0.2	3.4 ± 0.3	2.2 ± 0.1	2.9 ± 0.1

As determined by analysis of SEM images, see Figure 7.1.

* As determined by Cumulant analysis of the DLS data recorded at 20°C.

Independent of core size and shell thickness, the same nominal cross-linker content of 5 mol% was employed. Consequently, similar cross-linking densities were expected for all

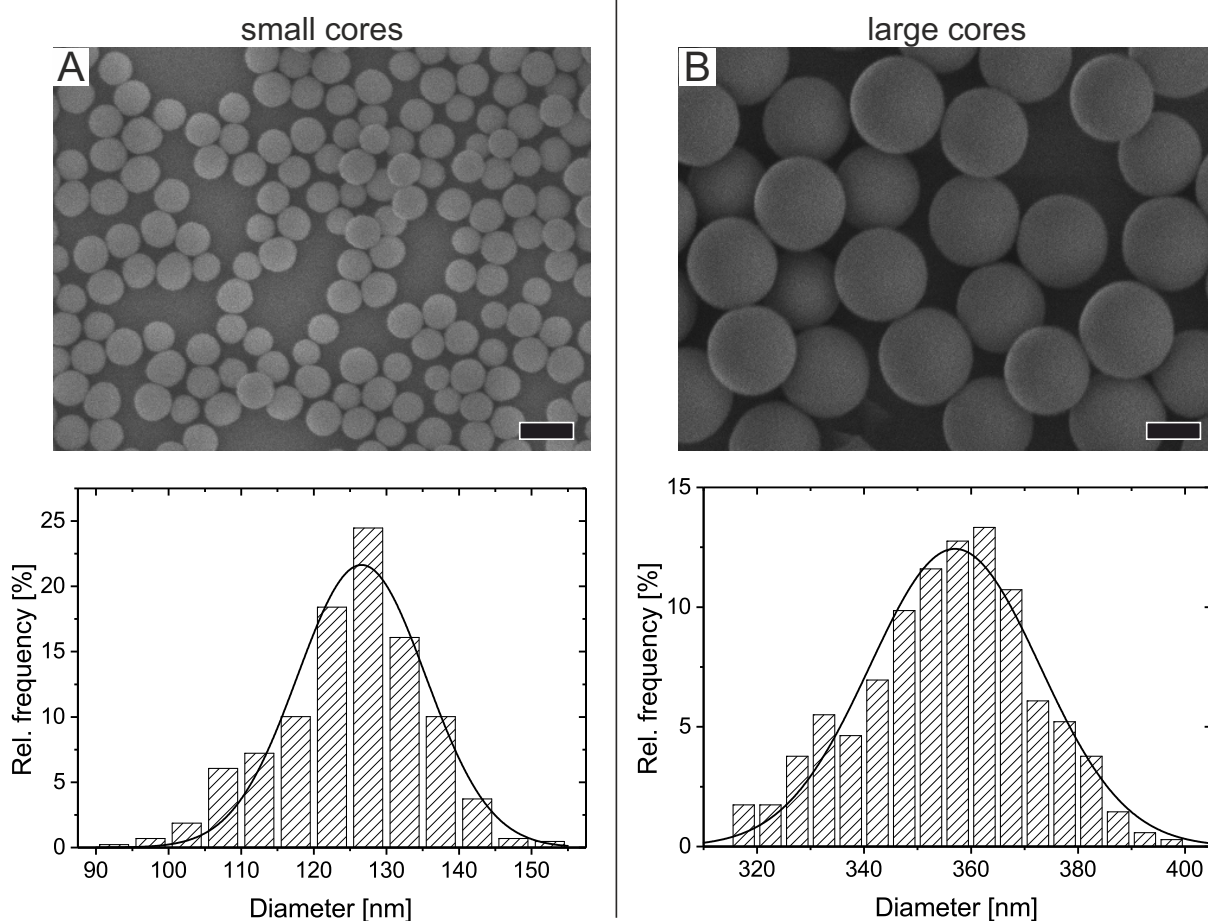


Figure 7.1: Representative SEM images of the silica particles and respective histograms that show their particle diameter distribution. The data of silica cores with different average diameters is shown: A. 125 nm; B. 351 nm. The scale bars are 200 nm. The solid black line in the histograms is a fit using a Gaussian size distribution.

CS particle batches. As described in Section 2.1.2, the hydrogel shells exhibit a radial density profile with a decreasing density from the center to the periphery.^[110,111] Section 5.1.1 revealed that the temperature-dependent swelling behavior is connected with the cross-linking density of the particles. Therefore, it can be used as suitable measure for the softness of the CS particles. Consequently, temperature-dependent DLS measurements were performed between 20 and 60°C of dilute dispersions from SiO₂-PNIPAM particles. In Figure 7.2 A the temperature-dependent evolution of the hydrodynamic diameter $\lambda_b\sigma$ is depicted. Independent of core and shell size a VPTT was observed between 32 and 34°C which is typical for hydrogel particles with a nominal cross-linker content of 5 mol%.^[191] In Figure 7.2 B the swelling ratio β is plotted versus the temperature. β is the ratio of the total CS particle volume at a temperature T ($V_{CS}(T)$) and the respective volume at 60°C ($V_{CS}(60^\circ\text{C})$) corresponding to the shell in its fully collapsed state (eq. 2.18). Hence, β is a convenient measure for the swelling capacity of the CS particles.

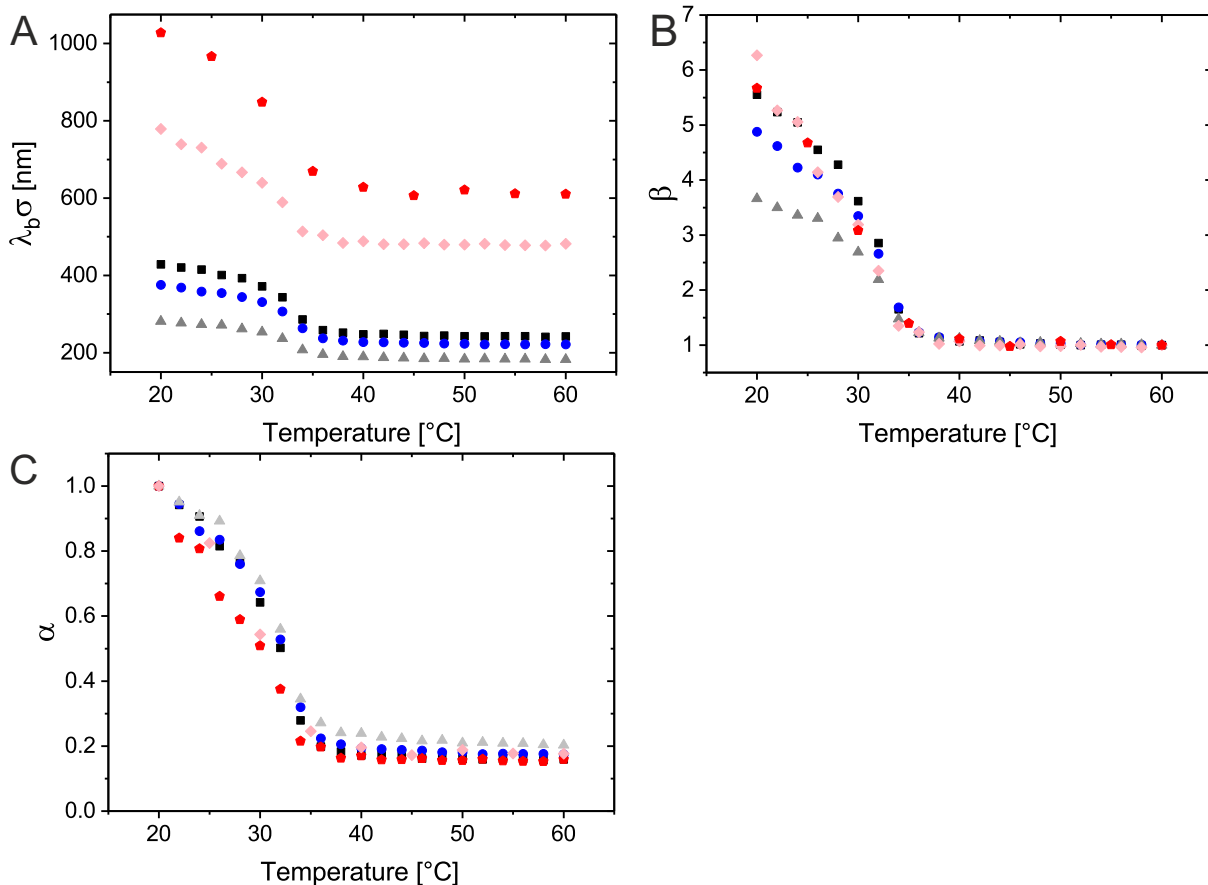


Figure 7.2: Results obtained from temperature-dependent DLS investigations for the different CS particles: C₁₂₅S_{2.2} (gray triangles), C₁₂₅S_{3.0} (blue circles), C₁₂₅S_{3.4} (black squares), C₃₅₁S_{2.2} (rose rhombuses) and C₃₅₁S_{2.9} (red pentagons). A. Temperature-dependent evolution of the hydrodynamic diameter $\lambda_b\sigma$. B. Swelling ratio $\beta = V_{CS}(T)/V_{CS}(60^\circ\text{C})$ versus temperature. C. De-swelling ratio α of the PNIPAM shells as a function of the temperature with $\alpha = V_S(T)/V_S(20^\circ\text{C})$. For all presented data the error bars are within the symbol size.

Particles with an increasing λ_b result in larger values of β at temperatures below the VPTT. Thus, thicker shells lead to an increased total degree of swelling. This is accompanied with an increasing relative water uptake. Consequently, CS particles with larger values of λ_b reveal an increased volume of the swellable shells. Certainly, this is only valid if these particles encapsulate a SiO₂ core of the same size. For the particles with large cores similar values of β are obtained for temperatures below the VPTT. This might be attributed to slight deviations in the hydrodynamic dimensions determined for these particles. Due to the larger particle size, an influence of sedimentation or non-random particle diffusion to the DLS data cannot be fully excluded. Therefore, the values of β below the VPTT might be slightly defective.

As all hydrogel shells were prepared with the same nominal cross-linker content, a similar maximum swelling capacity is expected. In order to verify this assumption, the de-swelling ratio α was determined according to $V_S(T)/V_S(20^\circ\text{C})$. V_S describes the volume of the

hydrogel shell without considering the volume of the SiO₂ particle (V_c), i.e., $V_S = V_{CS} - V_C$. The core volume V_C was calculated using the radius determined using SEM images. The reference volume $V_S(20^\circ\text{C})$ was calculated using the hydrodynamic radius at 20°C. The temperature-dependent development of the de-swelling ratio is shown in Figure 7.2 C for the different CS particles. Similar values of α are obtained for all particles. At temperatures well above the VPTT, all particles approach a value for α of 0.2. This demonstrates that the cross-linker content and thus the softness in the polymer network is similar for all CS particles. Summing up, the morphology of the hydrogel shell in bulk is almost independent of the shell thickness as well as on the size of the SiO₂ core. This is a significant requirement in order to compare the compression behavior of the particles at the oil-water interface later on.

7.2 Particle Morphology at the Interface

The morphology, i.e., the position, contact angle and shape, of the CS particles at the oil-water interface was determined using FreSCa cryo-SEM.^[139] This method was already used to describe the particle morphology of purely organic microgels by Geisel *et al.*^[83] The surface activity of the polymer chains has been found to support the spreading of the microgel until there is a compensation between deformation and internal elasticity (see Section 2.2.2). Typically, this interplay results in particle diameters that are larger than in bulk. Similar observations are expected for the CS particles due to their microgel shells. In order to visualize their interfacial morphology, FreSCa measurements were carried out at low surface coverage corresponding to a low surface pressure. Apart from the analysis of the particle morphology at the interface, conclusions on the interfacial microstructures could be drawn at low surface coverages. In the following sections, at first, the basics of the method are explained. After that, it is focused on the particle morphology at the interface and finally the interfacial microstructures of the submonolayers are analyzed. Details on the FreSCa procedure are described in Section 3.3.6. Briefly, a submonolayer of particles at the oil-water interface is prepared and shock-frozen. Next, the two phases are separated by fracturing. These two halves are freeze-dried in order to remove ice crystals and condensed water. Afterwards, the water phase is imaged from the top side using cryo-SEM. Figure 7.3 shows the resulting FreSCa cryo-SEM images. Additionally, respective SEM images of a dry particle layer consisting of the respective CS particles on a silicon wafer are depicted. The blue circles in Figure 7.3 represent the areas calculated using the average diameters of the SiO₂ cores as obtained by SEM analysis. The white circles in Figure 7.3 show the areas determined using the hydrodynamic diameter $\lambda_b\sigma$ of the CS particles derived from DLS data. The CS structure can be easily identified in these images as a "fried-egg" morphology with a fuzzy boundary.

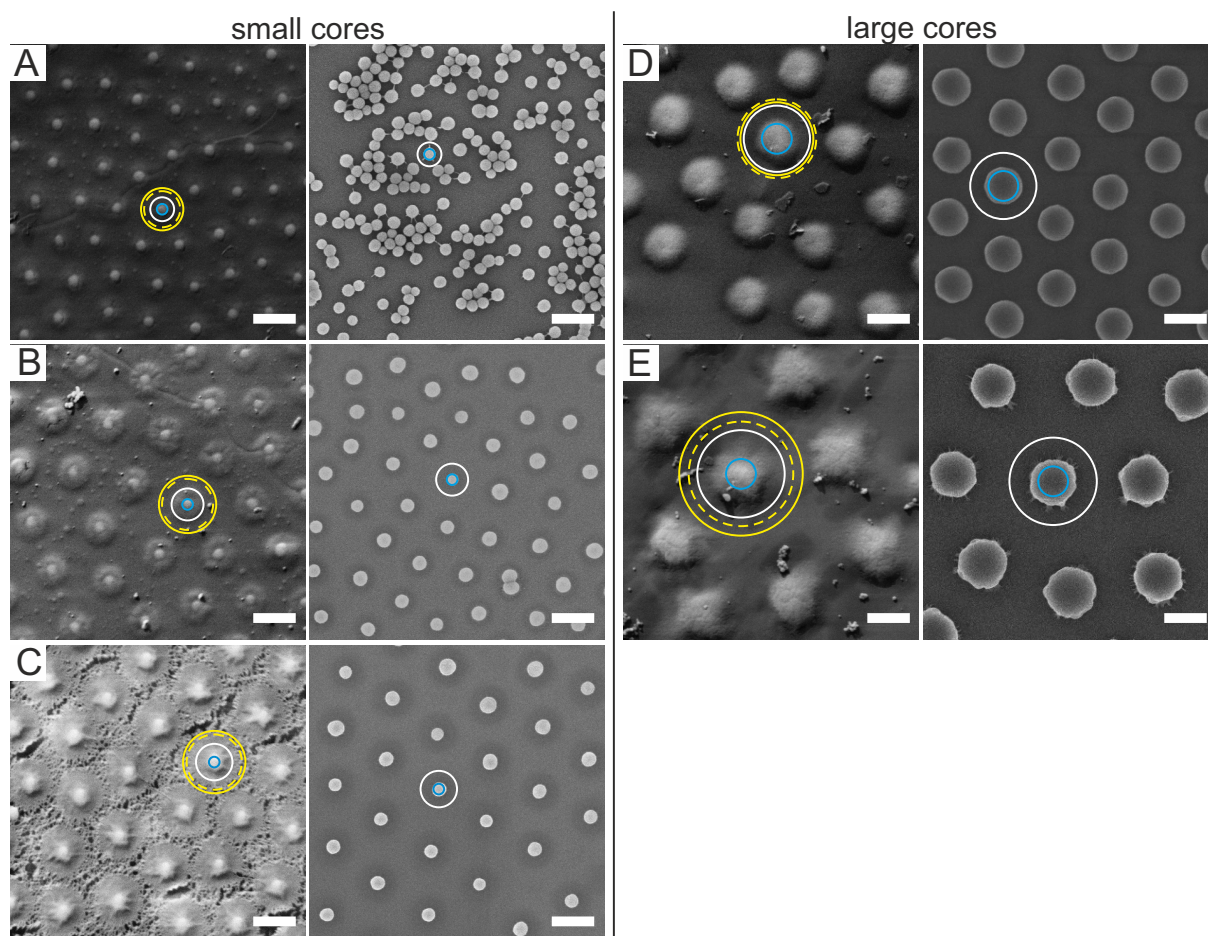


Figure 7.3: SEM images of the different CS systems: A. $C_{125}S_{2.2}$, B. $C_{125}S_{3.0}$, C. $C_{125}S_{3.4}$, D. $C_{351}S_{2.2}$, E. $C_{351}S_{2.9}$. The left column at each side shows the FreSCa cryo-SEM images of the exposed particles at a fractured *n*-decane/water interface. The right column depicts SEM images of dried particles on silicon wafers. The blue solid circle indicates the area of the SiO_2 cores. The white labeling reveals the area that the particles occupy in bulk. The inter-particle distances obtained from FreSCa and compression-deposition (C-D) experiments at low surface coverage were used to calculate the area that the particles cover at the interface. The areas are highlighted using a yellow dashed (FreSCa) and a yellow solid (C-D) circle. In all images the scale bar is 500 nm.

This morphology has also been observed for purely organic microgels at the interface.^[83,84] Specifically, the images of the $C_{125}S_{3.4}$ particles (Figure 7.3 C) distinctly show the exposed polymer shells. This sample was recorded under rougher freeze-etching conditions that leads to a very effective removal of the water. The shells come into contact at inter-particle distances which are distinctly increased as compared to the hydrodynamic diameter in bulk (white circle).

Prior to imaging, the samples were typically sputter-coated from an elevation angle of 30° . The shadow trace of the particles allows to draw conclusions on their contact angle at the interface. In the cryo-SEM images of the CS particles with small SiO_2 cores a shadow was not visible (lefthand side in Figure 7.3). Hence, the portion of the particle

protruding into the oil forms an effective contact angle below 30° . This indicates that the hydrogel shell adsorbs at the interface while it prefers to stay hydrated in the water phase to a large extent. The position of the particles at the interface is determined by a balance of maximal deformation and hydration. On the righthand side in Figure 7.3, the results for the CS particles with large silica cores are depicted. Here, a tiny halo can be identified. The appearance of a shadow implies that the particles form an effective contact angle defined from the water phase larger than 30° . To quantify this further, a detailed analysis of the geometric shape of the shadow would be necessary. However, the shadow is very diffuse, without clear borders which impedes an analysis of the contact angle. Considering this undefined, small halo, it can be estimated that these particles are slightly more hydrophobic as their analogues with small SiO_2 cores. Yet, they are still hydrophilic. Their contact angles should be still close to 30° .^[83] Consequently, the values of the contact angle are in a similar range as compared to the CS particles with small cores. Albeit, further experiments on particles with different core sizes and similar shell-to-core ratios are necessary to analyze their position and contact angle at the interface more precisely.

In difference to purely organic microgels without solid cores, the CS particles include a rigid, non-deformable core. Due to the covalent link between core and microgel shell, the flexibility of the shell is limited. As a result, an upward deformation of the interface is observed in the surroundings of the particles which is well visible in Figure 7.3 A and B. In D and E, i.e., for CS particles with larger SiO_2 cores, the mentioned upward deformation is not clearly observed. However, the results presented in the following sections are an indirect proof for the existence of these upward deformations. The results of the LB experiments in Section 7.3/7.4 show that CS particles with larger SiO_2 cores sit in a similar way at the interface than their analogues with small cores.

Analyzing the microstructures at low surface coverage, similar microstructures were formed independent of the core size of the CS particles. The upward deformation of the shells results in attractive capillary inter-particle interactions. These forces drive the particles into contact already below complete coverage of the interface. The interactions are actuated by a reduction of the deformations themselves.^[193] Such deformations are termed as capillary monopoles in the literature. Characteristically, they appear due to gravity for much heavier and larger particles or due to electro-dipping in the case of small colloids.^[24] Here, a completely new mechanism for such capillary monopoles is revealed: They arise due to the wetting of a deformable, surface-active hydrogel shell grafted onto a solid core. These attractive interactions drive the particles into contact already below complete coverage of the interface. The average inter-particle distance at low surface coverage $\lambda_i\sigma$ equals the interfacial diameter of the particles at a non-compressed surface. In Figure 7.3 the area the particles occupy at the interface, that was determined using

$\lambda_i\sigma$, is represented by a dashed, yellow circle. Particularly, Figure 7.3 C highlights that the yellow circles agree well with the shell diameter. Besides, the same quantity could be extracted from the C-D experiments as it will be discussed later in Section 7.3. The area calculated using $\lambda_i\sigma$ obtained from C-D experiments is depicted as solid, yellow circle. Table 7.2 lists the results of FreSCa and C-D experiments for $\lambda_i\sigma$ and the relative size increase at the interface as compared to bulk defined by the ratio λ_i/λ_b .

Table 7.2: Overall particle diameter $\lambda_i\sigma$ at the interface and relative size increase at the interface as compared to bulk, λ_i/λ_b , as determined by FreSCa and compression-deposition (C-D) experiments of the different CS systems.

Parameter	Small cores			Large cores	
	C ₁₂₅ S _{2.2}	C ₁₂₅ S _{3.0}	C ₁₂₅ S _{3.4}	C ₃₅₁ S _{2.2}	C ₃₅₁ S _{2.9}
$\lambda_i\sigma$ [nm] (FreSCa)	425 ± 50	600 ± 50	650 ± 50	926 ± 118	1230 ± 173
$\lambda_i\sigma$ [nm] (C-D)	498 ± 37	674 ± 50	734 ± 30	858 ± 45	1453 ± 177
λ_i/λ_b (FreSCa)	1.51 ± 0.17	1.59 ± 0.11	1.51 ± 0.11	1.19 ± 0.13	1.20 ± 0.16
λ_i/λ_b (C-D)	1.77 ± 0.12	1.79 ± 0.11	1.71 ± 0.06	1.10 ± 0.04	1.41 ± 0.16

Comparing the ratio λ_i/λ_b of both methods (C-D experiments and FreSCa) within a series of CS particles with SiO₂ cores of the same size, a good match is found. Slight deviations may arise due to a small precompression occurring upon spontaneous adsorption in the FreSCa experiments which results in underestimated values of λ_i . Indeed, this was found in previous studies which claim that spontaneous adsorption may cause an internal compression of the monolayer.^[88] Shells of CS particles with the same core size deform to a similar extent at the interface with respect to their shell thickness. This means that all systems with SiO₂ cores of the same size revealed a similar proportional size increase at the interface as evident by the ratio λ_i/λ_b . If CS particles with a similar shell-to-core ratio but a different silica core size (C₁₂₅S_{2.2} and C₃₅₁S_{2.2}/ C₁₂₅S_{3.0} and C₃₅₁S_{2.9}) were compared, it is found that λ_i/λ_b is smaller for CS particles with larger cores. Consequently, they deform less strongly at the interface as compared to their analogues with small SiO₂ cores. This coincides with the findings from FreSCa which revealed that the particles with large cores are slightly more hydrophobic, i.e., a larger portion of their volume protrudes into the oil phase. This different position of the SiO₂ cores certainly influences the spreading of the PNIPAM shells, since the microgel shells are covalently linked to the SiO₂ cores. Hence, smaller values for λ_i/λ_b are obtained for CS particles with larger cores. However, further investigations are needed to support these findings.

Apart from that, there might be differences in the grafting density between CS particles with small and large SiO_2 cores, that could additionally affect these results.

In addition to the FreSCa experiments, an *in situ* investigation was conducted by CLSM to directly visualize the assembly of particles at low surface coverage. As representative CS system the $\text{C}_{351}\text{S}_{2.9}$ particles were used. In similarity to the FreSCa experiments, the particles were not spread directly at the interface, but adsorbed spontaneously from the bulk aqueous subphase. During this process, the *in situ* analysis was carried out. Representative CLSM images which demonstrate the progress of a single adsorption event at the interface are shown in Figure 7.4.

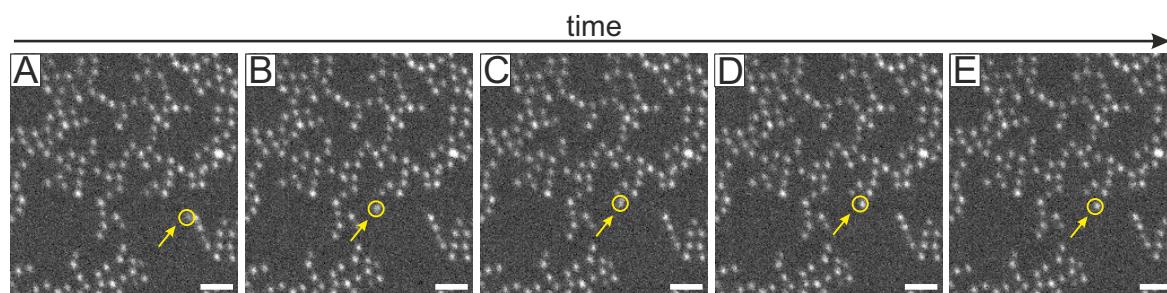


Figure 7.4: CLSM image sequence that visualizes a single adsorption event at the oil-water interface in dependence on the time. As representative system the $\text{C}_{351}\text{S}_{2.9}$ particles are used. The observed particle is labeled using a yellow circle and an arrow. At the beginning (0 s) (A), the particle is freely diffusing in the water subphase below the interface. After 3.9 s (B), it adsorbs at the interface and gets attracted by an existing aggregate after 4.8 s (C). The particle rearranges slightly at 5.3 s (D) before it occupies a stationary position after 11.5 s (E). The scale bars are $4 \mu\text{m}$.

From the very beginning, a certain number of particles are unavoidably already adsorbed at the interface which can be attributed to the sample preparation (see Section 3.3.4). Areas of particle clusters separated by voids were found. This has to be a consequence of the attractive forces discussed in the course of the FreSCa analysis. The time-dependent series of CLSM images in Figure 7.4 confirms this further. Here, a single adsorption event can be pursued. Therefore, the particle which is labeled with a yellow circle and an arrow is in focus. At $t = 0$ s, the particle is freely diffusing (A). Within the next 3.9 s, the particle disappears from the focal plane. Next, it reappears again and adsorbs at the interface (B). Subsequently, it is attracted by a present particle cluster within less than one second. This happens from B to C. It rearranges slightly (D). Eventually, it stays in a stationary position (E).

7.3 Influence of Compression

Up to now, the particle microstructures at low interface coverage were evaluated. In this section, the interfacial microstructures at different states of compression, i.e., surface coverage, were investigated. A modified version of the LB deposition at an oil(*n*-hexane)-water interface was performed.^[89] The setup is schematically shown in Figure 7.5.

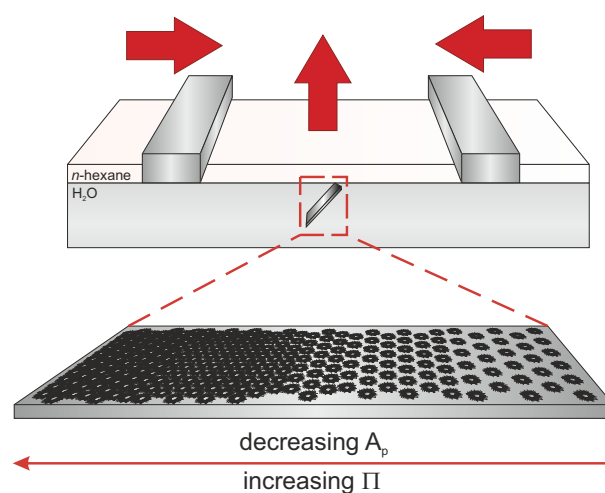


Figure 7.5: Schematic depiction of the compression of a monolayer and its deposition onto a substrate in the LB trough. The interface is compressed by two barriers and a wafer is withdrawn simultaneously through the oil-water interface. This procedure results in a substrate carrying a density gradient of CS particles. In the direction of the main axis of the wafer, the area per particle A_p decreases while the surface pressure Π increases.

A silicon wafer was used to continuously collect the interfacial microstructures from the interface upon compression. The experiment was performed as follows: The upper edge of a silicon wafer was placed exactly at the oil-water interface. The orientation of the silicon substrate was 30° with respect to the interface. A certain volume of the CS particle dispersion was injected at the oil-water interface in the trough. Upon constant compression of the two barriers in the trough, the wafer moved upwards through the interface. In the meantime, the particle monolayer was transferred onto the surface of the wafer. During this procedure, the surface pressure was measured using a Wilhelmy plate. Finally, a substrate was obtained which carried particle microstructures deposited at varying compression states along its main axis. Since the area of the LB trough is limited, several deposition experiments using different dispersion volumes are typically required in order to receive a complete compression curve of one particle system. The microstructures on each substrate were analyzed systematically taking SEM or AFM images in intervals of 1 mm along the main axis of the substrate. The area per particle A_p was determined by counting the number of particles per area of the recorded image. The evolution of the surface pressure Π with decreasing A_p gives the compression curves

shown in Figure 7.6 for samples with different shell-to-core ratio.

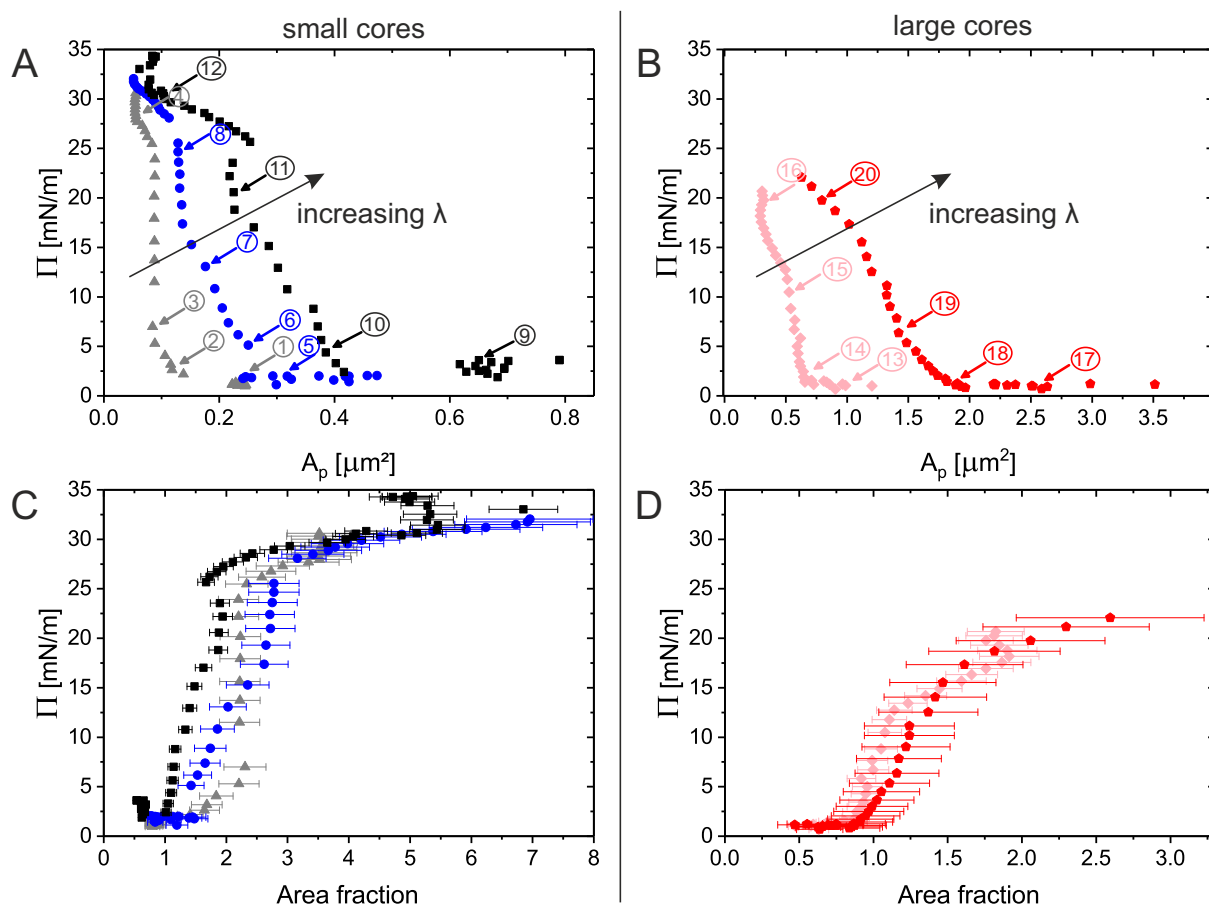


Figure 7.6: Compression curves of the different CS systems: $C_{125}S_{2.2}$ (gray triangles), $C_{125}S_{3.0}$ (blue circles), $C_{125}S_{3.4}$ (black squares), $C_{351}S_{2.2}$ (rose rhombuses) and $C_{351}S_{2.9}$ (red pentagons). In A and B the evolution of the surface pressure versus A_p upon compression is shown. The data points labeled with an arrow and a number correspond to the accordingly numbered images in Figure 7.7. In C and D the normalized compression curves are depicted revealing the surface pressure as a function of the area fraction.

Every single data point in these compression curves corresponds to a different location at a wafer. Figure 7.6 shows the compression curves collected for CS particles with small (A) and large (B) SiO_2 cores. Initially, the data seemed to be identical as for purely organic microgels without solid cores (see Section 2.2.2). In the context of purely organic microgels, it is important to note that the inner strongly cross-linked region is meant by "core" in contrast to CS particles that include a solid, inorganic core. The loosely cross-linked part of microgel particle is termed as „shell“ in the following. Rey *et al.* studied the microstructures upon compression of purely organic microgels.^[89] Briefly, they found the following evolution: At large A_p , microgels are not in contact and randomly distributed (gas phase). In this state, low surface pressures are measured. Upon further compression, the particles approach each other until they are in contact. This leads to a step rise

of Π . Typically this stadium is followed by a quasi-plateau of Π . Within this range of constant Π , a phase transition of shell-shell to core-core contacts is observed for microgels. Subsequently, a small compression of the close-packed phase followed by monolayer failure or buckling takes place.^[89] Considering the behavior of microgels, significant differences to CS particles could be revealed along the compression curves. This was done by closer inspection of the microstructures along the recorded compression curves. The respective microstructures of the CS particles are shown in Figure 7.7. In this figure representative microstructures from low to high surface coverage are depicted from left to right, respectively. The same color code as for the compression curves (Figure 7.6) is used. From top to bottom, the results of $C_{125}S_{2.2}$ (gray), $C_{125}S_{3.0}$ (blue), $C_{125}S_{3.4}$ (black), $C_{351}S_{2.2}$ (rose) and $C_{351}S_{2.9}$ (red) are represented. The images correspond to the accordingly numbered data points that are indicated by arrows in Figure 7.6.

At low surface coverage, i.e., low surface pressure (see first column in Figure 7.7 and the arrows 1, 5, 9, 13 and 17 in Figure 7.6 A and B), a random distribution of particles was not found for the five CS systems which is in contrast to microgels. Instead, areas in which the particles are arranged in local hexagonal lattices separated by voids were observed. This is related to the presence of attractive capillary forces as discussed in Section 7.2. These attractions develop through local deformations of the interface caused during the wetting of the CS particles. The particles are attracted by capillarity and come into contact at a defined distance corresponding to their effective size at the interface. Therefore, the inter-particle distance at these low compressions was used to estimate $\lambda_i\sigma$ (C-D), which is listed in Table 7.2.

AFM/SEM images of the microstructures at the beginning of the rise in Π (indicated by the arrows 2, 6, 10, 14 and 18 in Figure 7.6 A and B) are shown in the second column of Figure 7.7. In accordance to purely organic microgels, the CS particles form a regular, space-filling hexagonal particle lattice at this stage. In this lattice the particles are in shell-shell contact. The order of the monolayer is confirmed by several oscillations and a well-defined first maximum in the $g(r)$ functions (black line) in Figure 7.8. Note that the $g(r)$ functions in Figure 7.8 correspond to the accordingly numbered data points highlighted by arrows in Figure 7.6. The first maximum in the $g(r)$ functions can be used to estimate the average inter-particle distance. For samples with the same core size but larger shells the rise in surface pressure is measured at larger A_p (indicated by the arrows 2, 6, 10, 14 and 18 in Figure 7.6 A and B). This is simply related to the different particle dimensions. An even more interesting observation is that the slope in the rise of the surface pressure is distinctly steeper for smaller λ_i . This is a direct consequence of the different shell thicknesses. Although the shells have a similar cross-linking density, the range of distances over which the shells can be compressed until hard repulsion occurs is increased for thicker shells.

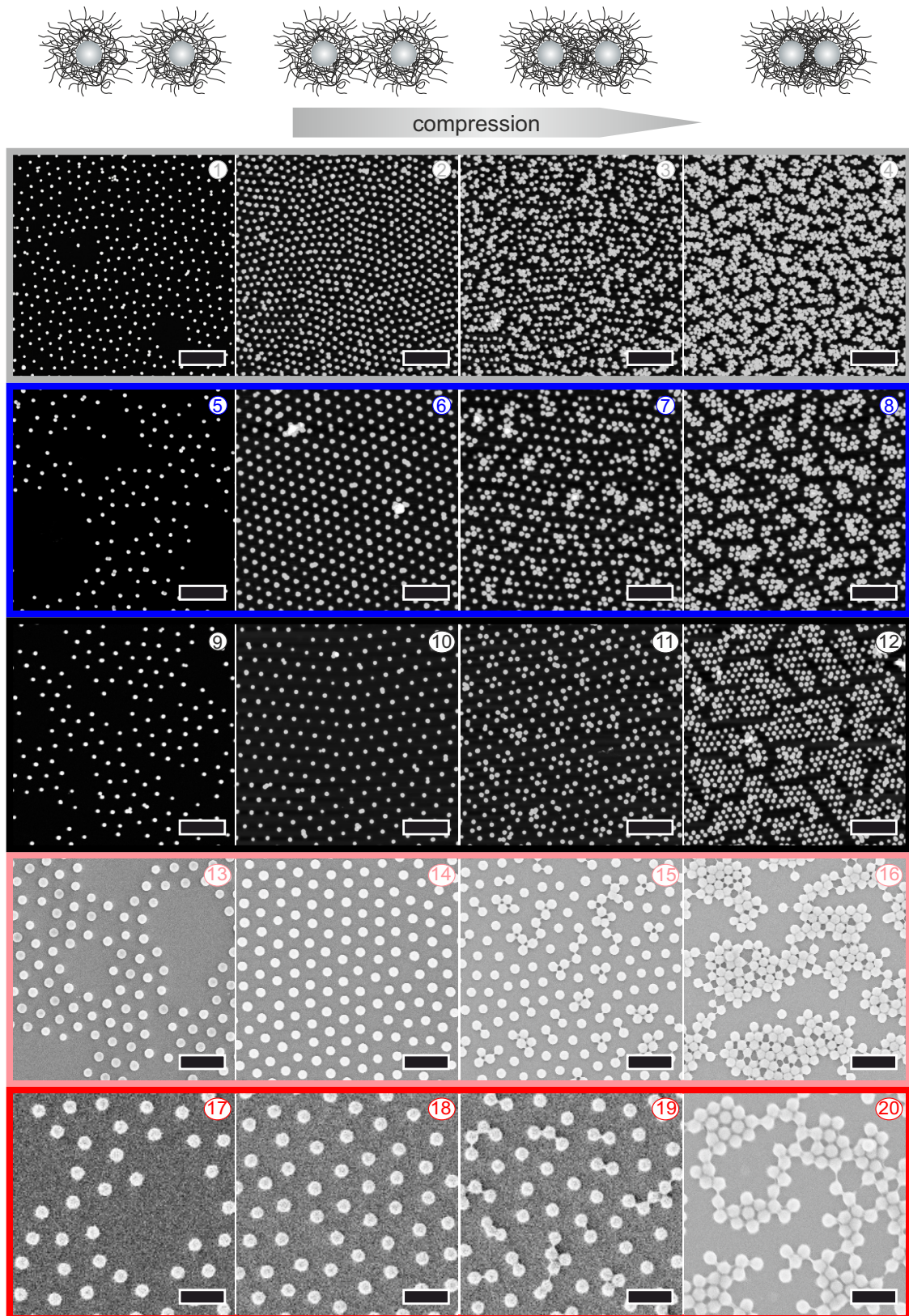


Figure 7.7: AFM/SEM images of the transferred microstructures of the CS particles with increasing compression/surface pressure from left to right. Each series is highlighted by a differently colored frame: $C_{125}S_{2.2}$ in gray, $C_{125}S_{3.0}$ in blue, $C_{125}S_{3.4}$ in black, $C_{351}S_{2.2}$ in rose and $C_{351}S_{2.9}$ in red. The same color code as in Figure 7.6 is used. The images correspond to the accordingly numbered data points highlighted by arrows in Figure 7.6 A and B of the respective CS system. The scale bars in all images are $2 \mu\text{m}$.

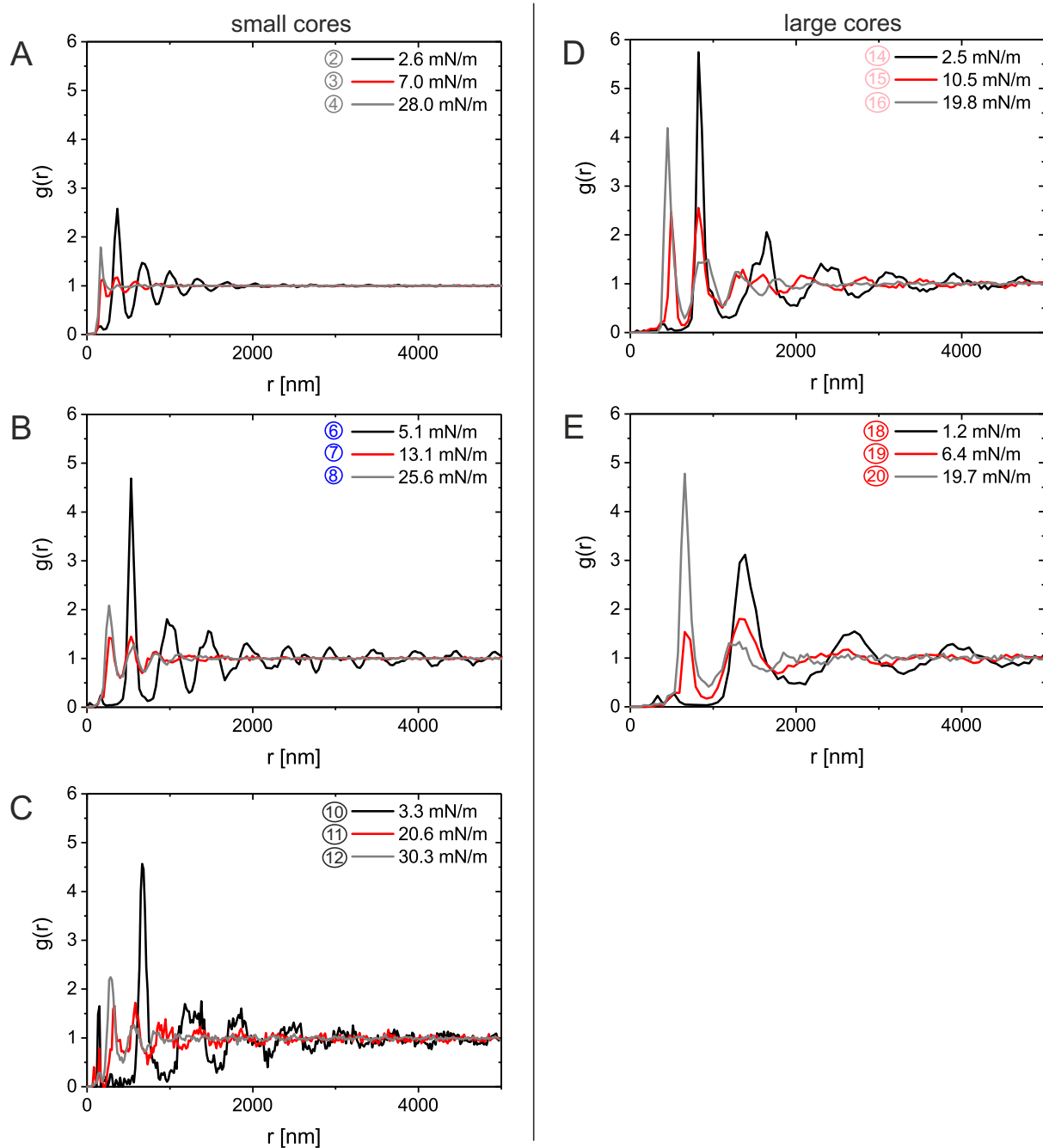


Figure 7.8: Representative radial distribution function $g(r)$ calculated for the deposited monolayers of the CS particles with small cores (left) and with large cores (right) at different surface pressures Π : A. $C_{125}S_{2.2}$, B. $C_{125}S_{3.0}$, C. $C_{125}S_{3.4}$, D. $C_{351}S_{2.2}$, E. $C_{351}S_{2.9}$. The numbers that are assigned to the $g(r)$ functions correspond to the numbered data points labeled by arrows in Figure 7.6 and to the accordingly numbered SEM/AFM images in Figure 7.7.

This means that the absolute degree of compressibility is different for the samples and depends on the shell-to-core ratio for samples with similar cross-linking density as shown here. Samples characterized by a lower shell-to-core ratio are less swollen (Figure 7.2 B) and deform less at the interface (Figure 7.3, Table 7.2).

Upon further compression shell-shell contacts start to fail. This results in close-packed particle clusters. This phase corresponds to the third column in Figure 7.7 and the red lines in the $g(r)$ functions (Figure 7.8) at intermediate surface pressure. The first and second maximum of the $g(r)$ function approach the same intensities. Thus, both inter-particle distances are equally probable. Additionally, the position of the second maximum coincides well with the initial first maximum at smaller surface pressure (black lines). This indicates that the initial inter-particle distance of particles in shell-shell contact has barely shifted during compression. The $g(r)$ functions show that the probability of finding a particle in a non-close-packed lattice (particles in shell-shell contact) or a close-packed cluster (particles in core-core contact) is similar. In fact, upon compression the particles rather aggregate to clusters instead of constantly deforming the whole lattice. This explains the sudden evolution of the second maximum at smaller inter-particle distances (core-core contacts). This happens already at surface pressures substantially below the quasiplateau (arrow 3, 7, 11, 15 and 19 in the compression curves in Figure 7.6 A and B). This is a strong difference to purely organic microgels. For CS particles the range of Π and A_p over which this transition occurs depends on the shell-to-core ratio. The transition takes place at larger values of Π with increasing shell-to-core ratio for CS particles with small SiO_2 cores. This points out that the larger shells are more tolerant towards the nucleation of defects in the clusters. The opposite trend was found for the CS with large cores. According to the results from FreSCa, the position of the CS particle seems to be influenced by the core size. Certainly, the location of the particles alters the inter-particle interactions. The altered interactions may explain this observation. However, the influence of the core size deserves further work. Furthermore, the region over which two distinct inter-particle distances are notable in the $g(r)$ functions seems to be influenced by the core size. It is less pronounced in the case of large CS particles as compared to smaller CS particles with a similar shell-to-core ratio or to purely organic microgels. In addition, large CS particles with similar shell-to-core ratios as compared to their small analogues show the transition to close-packed clusters separated by voids at much lower surface pressures. This is related to the fact that their monolayers are compressed over a narrower region of A_p . Presumably, this correlates to the difference in the absolute core size which influences the mechanical response at the interface. However, the relation between absolute core size and compressibility is complex and needs further investigation.

The images in the fourth column of Figure 7.7 correlate to the stage at which the transition to the cluster phase is finished. The particles are arranged in close-packed clusters which are separated by voids. The dimension of the voids is similar to the nearest neighbor distance of the non-close-packed phase. The gray line in Figure 7.8 describes the corresponding $g(r)$ functions at this stage. The nearest neighbor spacings in the clusters are still the same as compared to the red line in the same diagram. However, the peak

height is increased, i.e., core-core contacts are more likely than shell-shell contacts. This implies that more particles are in the cluster phase at this stage. This region reveals again pronounced contrasts as compared to microgels. First, microgels can minimize the energy used for their deformation as they can fully reorganize their shape. In contrast to this, the cores of CS particles cannot come into contact within the close-packed phase at the interface. The shell is prevented to squeeze out in the contact region as it is covalently connected to the SiO₂ core. As a result, the minimum inter-particle distance equals a CS particle with a fully compressed shell. The thickness of the compressed shell increases with larger values of the shell-to-core ratio which is qualitatively visible in the AFM images of the CS particles with small cores in the fourth column in Figure 7.7. In the case of the CS particles with larger SiO₂ cores, this is barely visible in Figure 7.7 as the polymer shells form "bridges" between the SiO₂ cores. However, to reveal that the inter-particle distance in the compressed state is similar to the diameter of fully compressed CS particles, the results shown in Figure 7.2 can be used. As an estimation of the inter-particle distance in the compressed state, the achieved bulk hydrodynamic diameters $\lambda_b\sigma$ at temperatures well above the VPTT, i.e., in the collapsed state, can be assumed. The determined values of $\lambda_b\sigma$ above the VPTT coincide well with the core-core inter-particle distances at high surface coverage.

A second difference to microgels is that the monolayers cannot reach a state of full clustering without voids (fourth column in Figure 7.7). Before a complete transition to a non-close-packed lattice could be reached, failure and buckling of the monolayer occurred. The latter events describe the last data points of the compression curve when the surface pressure rises constantly with reducing A_p .

For a better comparison of the compression curves the surface pressure was plotted versus the area fraction. The respective evolutions are shown in Figure 7.6 C and D. The area fraction was calculated as follows: The interfacial diameter $\lambda_i\sigma$ (C-D) determined using the results of the C-D experiments at low Π was used to calculate the area, that a CS particle occupies at the interface. Dividing this value by A_p provides the area fraction. This normalization allows to compare the data independent of the shell thickness. The error of the area fraction was calculated using error propagation considering the error of $\lambda_i\sigma$, that was determined by C-D experiments (Table 7.2). A_p can be determined very precisely, so that its error is negligible in the mentioned error propagation. Due to the soft character of the particles, area fractions above the two-dimensional close packing value of 0.91 can be achieved upon compression. For all particles a pronounced rise in the surface pressure at area fractions around 1 was observed.

7.4 Microstructure Characteristics

In this section, the evolution of the nearest neighbor distance d_{NN} and the hexagonal order parameter Ψ_6 in the monolayers as a function of area fraction is addressed. First, it is focused on the evolution of d_{NN} upon compression of the monolayers. Every AFM/SEM image in Figure 7.7 corresponds to a respective Π or A_p as accordingly labeled by numbers in Figure 7.6 and Figure 7.7. Each image was analyzed using Voronoi tessellations to approximate the nearest neighbor distribution. Next, this distribution was fitted using a Gaussian size distribution to determine the nearest neighbor distance d_{NN} . The maximum of the fit curve is equivalent to the mean nearest neighbor distance. The standard deviation is used to describe the error of the single data points. The error for the area fraction was determined as described in Section 7.3. In this way, Figure 7.9 was obtained. Here, the development of d_{NN} with increasing area fraction is shown.

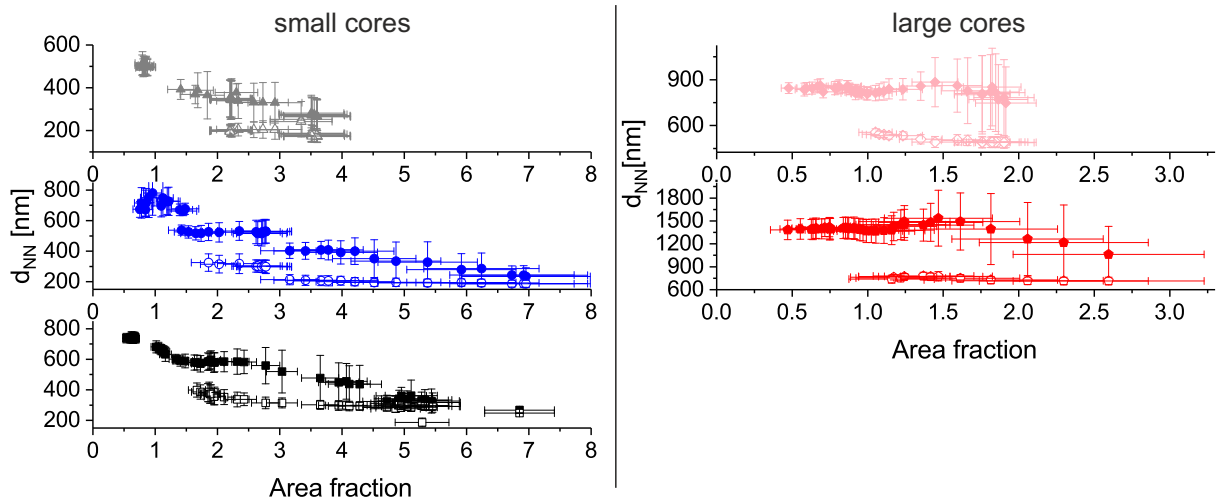


Figure 7.9: Nearest neighbor distances d_{NN} plotted versus the area fraction for the CS systems with different core sizes. For small cores (left) and large cores (right) the shell-to-core ratio is increasing from top to bottom. The different CS particles are labeled with different symbols and colors: $C_{125}S_{2.2}$ (gray triangles), $C_{125}S_{3.0}$ (blue circles), $C_{125}S_{3.4}$ (black squares), $C_{351}S_{2.2}$ (rose rhombuses) and $C_{351}S_{2.9}$ (red pentagons). Filled symbols are used to indicate average nearest neighbor distances corresponding to the non-close-packed phase. Accordingly, empty symbols indicate the average nearest neighbor distances of the close-packed phase.

At low area fractions up to 1.0, d_{NN} remains constant for all particle systems (first column in Figure 7.7). The inter-particle distance in the local lattices is not changing while the area filled with voids decreases upon compression of the monolayer. This is related to the presence of the previously described attractive capillary forces driving the particles together to a fixed distance already at low area fractions/surface coverage. Hence, d_{NN} of this region in Figure 7.9 is ideally suited to define the interfacial size $\lambda_i\sigma$ (C-D). Particularly convenient is the average value of d_{NN} at area fractions below 0.91 as it

was measured at large A_p . Accordingly, this value was used to determine $\lambda_i\sigma$ (C-D) in Table 7.2. Next, the nearest neighbor distances corresponding to the representative images shown in the second column of Figure 7.7 are analyzed. Upon compression d_{NN} in the non-close-packed lattice reduced slightly over a small range of area fractions. This compression proceeds over a much narrower range of area fractions for CS particles with similar shell-to-core ratios and larger cores as compared to small cores ($C_{351}S_{2.2}$ compared to $C_{125}S_{2.2}/C_{351}S_{2.9}$ compared to $C_{125}S_{3.0}$). In the case of $C_{351}S_{2.2}$ particles (rose rhombuses), the region in which this transition occurs is even almost not existent.

In the next region, the cluster transition begins (third column of Figure 7.7). A second distance which is constant for the investigated range of area fractions is observed. In Figure 7.9 this distance is indicated by open symbols. The distance equals the inter-particle distance of particles with fully compressed hydrogel shells. In the course of the clustering transition, the larger inter-particle distance which corresponds to the non-close-packed d_{NN} (particles in shell-shell contact) is not changing up to an area fraction of 2.5 for CS particles with small cores. Afterwards, it reduces until it reaches the close-packed d_{NN} (particles in core-core contact) at the largest area fraction (fourth column in Figure 7.7). This reduction corresponds to the decrease of the distance between the clusters which approximates the distance between particles with fully compressed hydrogel shells. In contrast to this observation, the non-close-packed d_{NN} of the CS particles with large cores reduces at distinctly smaller area fractions of 1.4. Due to the smaller range of collected data points, a complete transition to the close-packed d_{NN} is not visible. Again, this observation is connected to the larger core size of the CS particles. The core size influences the position of these particles at the interface and, thus, also the inter-particle interactions. Generally, all particles demonstrate a similar qualitative behavior. Changing the shell-to-core ratio as well as the core size allows to manipulate the accessible range of inter-particle distances.

Furthermore, the hexagonal order parameter Ψ_6 was investigated as a function of area fraction. A definition of Ψ_6 is given in Section 2.4.1.2. Ψ_6 is introduced to evaluate the degree of hexagonal order in the monolayers. The respective evolution of Ψ_6 plotted versus the area fraction is shown in Figure 7.10. At low area fractions, Ψ_6 stays constant. At this low surface coverage, capillary attraction is present. This results in locally ordered domains separated by voids (first column in Figure 7.7). Upon compression, when complete surface coverage is reached (second column in Figure 7.7), Ψ_6 increases to a maximum value. In the case of the CS particles with small SiO_2 cores, Ψ_6 achieves larger values for thicker shells, i.e., for an increasing shell-to-core ratio. Thicker shells seem to be more tolerant towards defects increasing the degree of order in the monolayers. As soon as the cluster formation (third column in Figure 7.7) sets in, a sharp drop of Ψ_6 is found. This is mainly related to particles at the edges of the clustered regions which are

no longer positioned in a hexagonally ordered lattice. Upon further transition, a second increase of Ψ_6 is observed which can be attributed to the ordering within the growing clustered regions (fourth column in Figure 7.7). At this stage (highest area fractions), particles with thicker shells reach higher values of Ψ_6 . CS particles with large SiO_2 cores show a similar evolution of Ψ_6 as compared to CS particles with small cores. In contrast to the described observations for the particles with small SiO_2 cores, Ψ_6 of $\text{C}_{351}\text{S}_{2.2}$ achieves increased values as compared to $\text{C}_{351}\text{S}_{2.9}$. This could be related to the different interfacial interactions of CS particles in dependence on their core size. To derive further conclusions, additional investigations are needed.

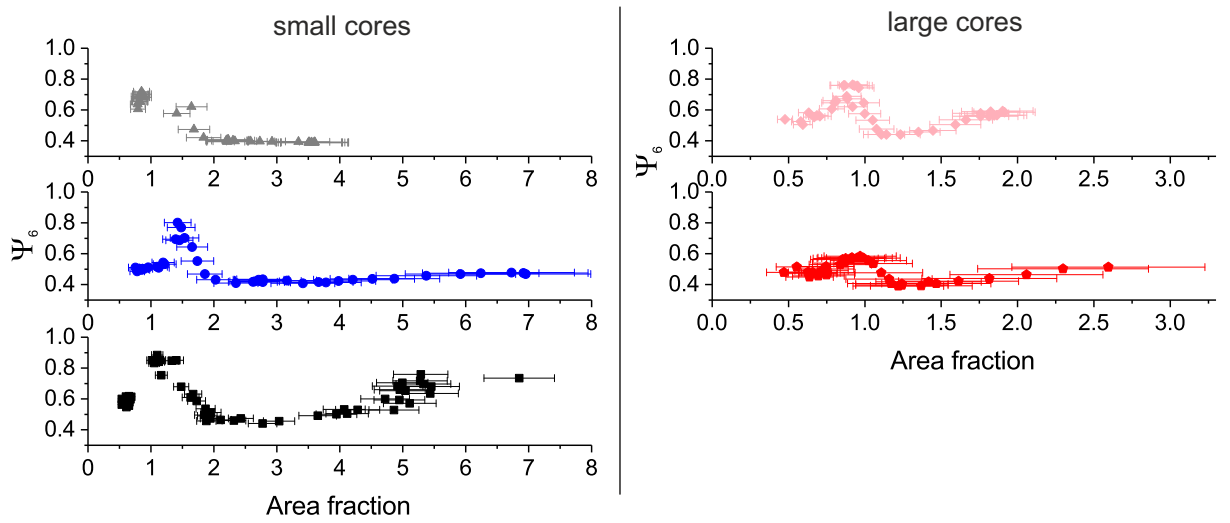


Figure 7.10: Evolution of the hexagonal order parameter Ψ_6 with increasing area fraction: On the left, Ψ_6 is shown for particles with small cores ($\text{C}_{125}\text{S}_{2.2}$ (gray triangles), $\text{C}_{125}\text{S}_{3.0}$ (blue circles), $\text{C}_{125}\text{S}_{3.4}$ (black squares)). On the right, it is depicted for particles with large cores ($\text{C}_{351}\text{S}_{2.2}$ (rose rhombuses) and $\text{C}_{351}\text{S}_{2.9}$ (red pentagons)). The error bars of the hexagonal order parameter are in the range of the symbol size.

As already described, the compliance of the shells changes with their thickness. Besides, the compliance directly influences the formation of the clustered phase. In Figure 7.11 the orientation of the hexagonal clusters at high area fractions with respect to the initial non-close-packed lattice at low area fractions is shown. The color scale in the figure gives the orientation derived from the phase angle of Ψ_6 in the range of $-\pi$ to $+\pi$ for each particle. Thus, the initial non-close-packed lattice corresponds to a phase angle of Ψ_6 equal to zero. This state is indicated by a green color. The results are exemplarily shown for the CS particles with small SiO_2 cores. The orientation of the crystal lattice is less distorted with increasing shell thicknesses. A uniform green color coding in the figure means that all particles in the field of view have the same orientation as in the initial non-close-packed phase. The CS particles with the smallest PNIPAM shell, $\text{C}_{125}\text{S}_{2.2}$, shown in Figure 7.11 A, reveal that the local hexagonal order is not restored at all. Instead, every

possible orientation is found indicating that the orientation of the initial non-close-packed phase is not existing anymore. An intermediate state is found for $C_{125}S_{3.0}$ depicted in Figure 7.11 B. Here, several orientations indicated by different colors are present. Some of them coincide with the orientation of the initial non-close-packed phase. In the case of $C_{125}S_{3.4}$, the underlying crystal lattice is almost not twisted/distorted. This is already visible by comparing image 10 and 12 outlined in black in Figure 7.7. Therefore, the cluster phase in Figure 7.11 C can be described by a uniform green color coding (phase angle of $\Psi_6 \approx 0$). In conclusion, the transition and the resulting structure is again drastically different than for purely organic microgels.^[89]

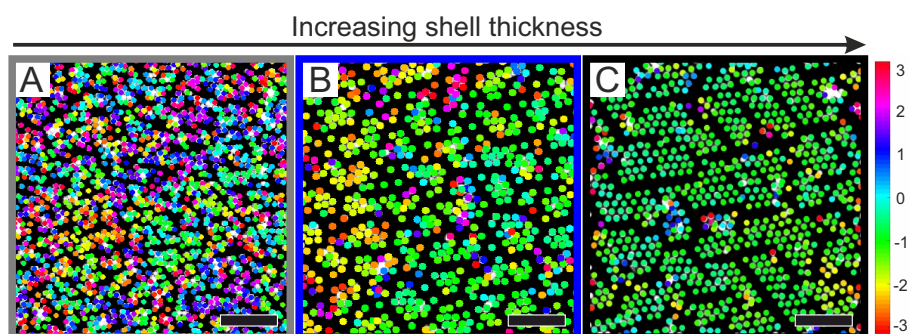


Figure 7.11: Local orientation of the hexagonal clusters with respect to their initial non-close-packed lattice at low surface coverage: A. $C_{125}S_{2.2}$ (gray frame), B. $C_{125}S_{3.0}$ (blue frame), C. $C_{125}S_{3.4}$ (black frame). The colors give the orientation derived from the phase angle of Ψ_6 for each particle in the range of $-\pi$ to $+\pi$. The images shown here coincide with the AFM images 4, 8 and 12 in the fourth column of Figure 7.7. The scale bars are $2 \mu\text{m}$.

7.5 Core-Shell Particles with a Small Shell-to-Core Ratio

Apart from the CS particles used for the studies shown above, CS particles with smaller shell-to-core ratios were synthesized. The same two types of silica cores (C_{125} and C_{351}) were used as core materials. The results from C-D experiments of these CS particles allowed to draw further conclusions on the adsorption prerequisites of CS particles at oil-water interfaces. Table 7.3 gives an overview of the synthesized particles.

Table 7.3: Core diameter σ , overall diameter $\lambda_b\sigma$ and shell-to-core ratio λ_b of the CS systems with small shell-to-core ratios.

Parameter	Small cores		Large cores
CS system	$C_{125}S_{1.4}$	$C_{125}S_{2.0}$	$C_{351}S_{1.5}$
$\sigma^{\#}$ [nm]	125 ± 10	125 ± 10	351 ± 16
$\lambda_b\sigma^*$ [nm]	169 ± 2	244 ± 2	530 ± 5
λ_b	1.4 ± 0.1	2.0 ± 0.2	1.5 ± 0.1

[#] As determined by analysis of SEM images, see Figure 7.1.
^{*} As determined by Cumulant analysis of the DLS data recorded at 20°C.

It summarizes the core diameter σ , the overall hydrodynamic diameter $\lambda_b\sigma$ of the CS particles and their shell-to-core ratio λ_b . Shell-to-core ratios between 1.4 and 2.0 could be achieved which means that the SiO_2 cores are encapsulated in very thin polymer shells. Note that the minimum value of λ_b is unity which implies that the cores are not encapsulated in a PNIPAM shell. Interestingly, these CS systems did not result in stable monolayers. In a typical compression-deposition experiment with those particles, a fluctuation in the particle density per unit area was observed. Exemplarily, this is shown in Figure 7.12.

Here, the evolution of the microstructures upon compression is shown using $C_{125}S_{2.0}$ and $C_{351}S_{1.5}$ as representative CS systems with different core sizes. In the images the microstructures, that are deposited at consecutive positions along the long axis of the wafers upon compression of the trough area, are depicted from left to right. As shown in the Section 7.3, the surface pressure and the surface coverage usually increase upon compression along the main axis of the substrate for similar CS particles with larger shell-to-core ratios, i.e., thicker shells. In contrast to these observations, the surface coverage fluctuated randomly upon compression of the trough area for the CS particles with smaller shell-to-core ratios. Hence, reliable compression curves could not be measured. This is related to the instability of CS particles with small λ_b at the interface which causes the particles to sink into the water phase during the experiment. The observations reveal that the stability of the particles at the interface is strongly influenced by the hydrogel

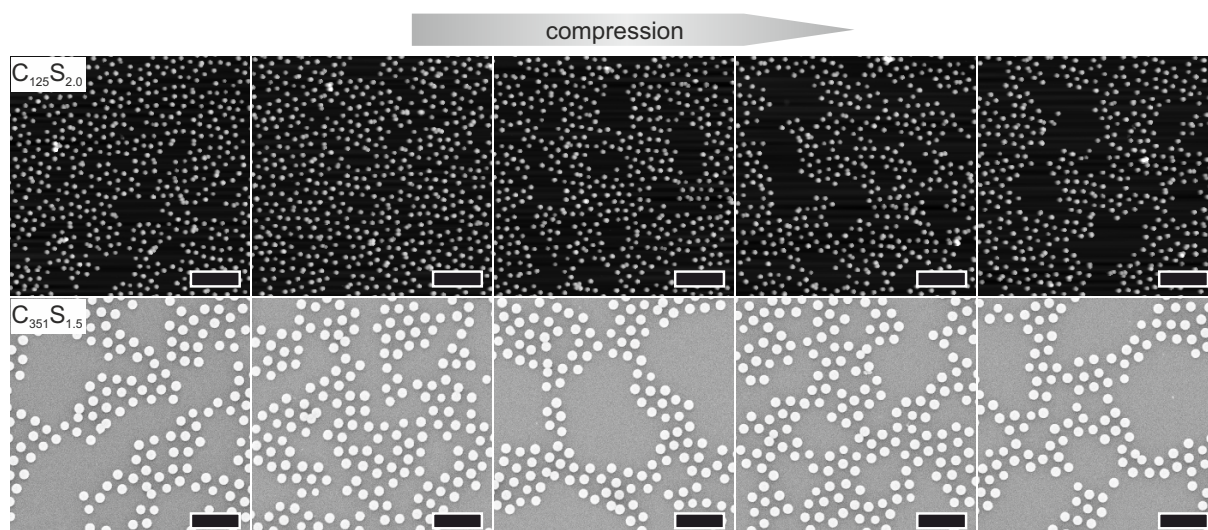


Figure 7.12: Images of transferred microstructures of CS particles with small shell-to-core ratios that were deposited upon compression of the trough area. The top row shows the measured microstructures of $C_{125}S_{2.0}$ at positions of 1, 3, 6, 10 and 16 mm. The bottom row depicts the microstructures of $C_{351}S_{1.5}$ at positions of 1, 4, 7, 10 and 13 mm. The mentioned positions were located along the long axis of the wafer substrate from left to right, respectively. The scale bars are $2 \mu\text{m}$.

shell thickness. The deformation of the hydrogel at the interface is, as previously discussed, more pronounced for thicker shells. Very recently, Buchcic *et al.* stated similar observations for polystyrene-PNIPAM CS particles. They found that the adsorption rates at the air-water interface were distinctly slower for CS particles with small shell-to-core ratios. They suggested that this is related to high energy barriers that the particles need to overcome in order to adsorb at the interface.^[92] To conclude, the C-D experiments of particles with small shell-to-core ratios highlight the importance of the hydrogel shell thickness during adsorption.

7.6 Stability in Bulk and at Liquid Interfaces

In this section, the structural behavior of CS particles in bulk and at the interface is compared. For this purpose, the $C_{351}S_{2.9}$ particles served as specific model system. The behavior of these particles at the oil-water interface was already discussed in Sections 7.2 to 7.4. The stability of the $C_{351}S_{2.9}$ particles in the bulk phase is studied in the next sections using CDDM. In similarity to light scattering, this method allows to obtain structural and dynamic information on the particles phase behavior. Investigations up to high volume fractions are realizable. Significant differences regarding the behavior in bulk and at the oil-water interface are revealed with increasing particle number densities. These observations call for the development of particles which have the same degree of stability at the interface as in bulk.

7.6.1 Structural and Dynamic Properties in Bulk

In order to study the structural and dynamic properties in bulk, aqueous dispersions of the $C_{351}S_{2.9}$ particles at different volume fractions were prepared. The range of volume fractions was chosen, so that the dilute as well as concentrated regime were covered. In particular, the stability of these particles in bulk was investigated. Time-lapse sequences of the differently concentrated dispersions were recorded by CLSM and analyzed by CDDM analysis. CDDM provides insights in the q -resolved structural and dynamic properties of dispersions from $C_{351}S_{2.9}$ particles. The volume fractions of these dispersions were determined using two independent methods. On the one hand, the masses of particles and water were used to determine the volume fraction ϕ^* . On the other hand, the effective hard sphere volume fraction, $\phi_{eff,HS}$, was derived directly from experimental results by hard sphere mapping. Both methods are further explained in the Appendix in Sections A.13 and A.14. The results of both methods are summarized in Table A.8 in the Appendix. In the first method, the hydrodynamic radius R_h at 20°C is used to calculate the volume, since R_h can be accessed very reliably by DLS. However, R_h overestimates the total volume of the dispersion, since the considered content of water in the swollen shells is overestimated. As a result, the calculated value of ϕ^* is slightly underestimated. This circumstance is known for soft particles. Thus, $\phi_{eff,HS}$, that was estimated by hard sphere mapping, is used to distinguish the dispersions at different volume fractions throughout this section. The neat aspect of hard sphere mapping is that it allows to derive $\phi_{eff,HS}$ directly from experimental data collected by CLSM. Certainly, it is not fully correct to treat the soft CS particles like hard spheres. However, all investigated dispersions should have volume fractions below the hard-sphere limit for FCC packing of 0.74. This implies that interpenetration of the particles can be excluded. As a result, their behavior in bulk is assumed to be similar to hard spheres. Although, one should note that this assumption

is only used for a rough estimation of the range of volume fractions.

In Figure 7.13 representative CLSM images at different volume fractions that were extracted from the measured time-dependent image sequences are shown.

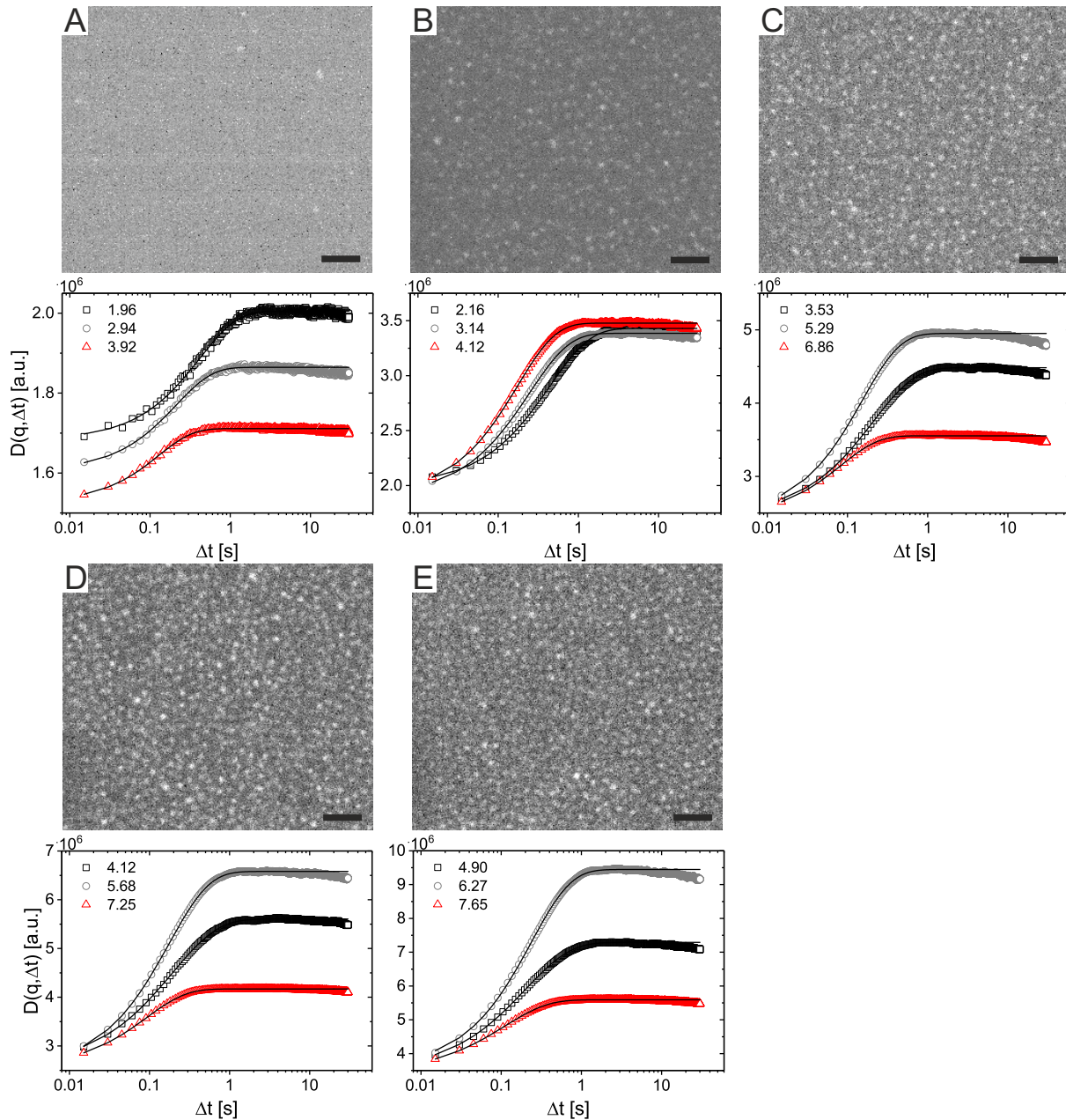


Figure 7.13: CLSM images of dispersions from $C_{351}S_{2.9}$ particles at different volume fractions. From A to E the volume fraction increases including the following values $\phi_{eff,HS} = 0.02, 0.06, 0.27, 0.35$ and 0.47 . The scale bars are $4 \mu\text{m}$. Below the CLSM images, the respective dynamic image structure functions $D(q, \Delta t)$ at three selected values of q versus the lag time Δt are depicted. The solid black line is a fit to the experimental data (empty symbols) using eq. 7.1.

As usual in a CDDM analysis, the CLSM images were used to calculate the dynamic image structure functions DISFs, $D(q, \Delta t)$, in bulk. $D(q, \Delta t)$ describes the intensity

fluctuations of the images which are correlated to the density fluctuations in dependence on the magnitude of the wave vector \vec{q} . The density fluctuations are based on the diffusion of the particles. q describes the length scale and the time scale (lag-time Δt between the images) of these density fluctuations. Below the confocal images in Figure 7.13, DISFs derived from CLSM images of the dispersions at the respective $\phi_{eff,HS}$ for representative q -values are depicted. The intensity fluctuations of all measured DISFs relax within a single relaxation time, so that they could be successfully fitted using the following single expression:

$$D(q, \Delta t) = H(q)[1 - \exp(-\Delta t/\tau(q)^{\beta_s(q)})] + B(q) \quad (7.1)$$

Here, $H(q)$ gives a qualitative dimension of the long-time and short-time limit of the density fluctuations. It depends on the form factor $P(q)$, the static structure factor $S(q)$ and the microscope transfer function $MTF(q)$. The characteristic relaxation time for a respective q is described by τ . τ is the inverse of the relaxation rate Γ which was previously introduced for the analysis of DLS data. $B(q)$ is a measure for the background noise in the images. β_s indicates the stretching exponent which is as well dependent on q . If β_s equals unity, the expression in eq. 7.1 simplifies to the form expected for dilute dispersions and a simple diffusive behavior is described.^[194,195] Equation 7.1 that considers a single relaxation time is suitable to fit the data at all $\phi_{eff,HS}$. Thus, it can be concluded that aggregates were not present in the investigated systems. If the contrary would be the case, usually a broad distribution of relaxation times is obtained for any given q .^[196,197] These results are basically the direct consequence of the observations during the CLSM measurements in which aggregates were not observed. As expected, the most dilute system ($\phi_{eff,HS} = 0.02$) shows a decrease of the characteristic time scale as well as the amplitude of the density fluctuations with reducing length scale, i.e., with increasing q -values. This is shown in Figure 7.13 A by the drop of the long-time values of $D(q, \Delta t)$ and the relaxation time $\tau(q)$ with increasing values of q . At higher volume fractions, both described tendencies are no longer observed. Here, the spatial distribution of the particles has to be considered. Particularly, larger deviations from the described tendencies are noted with increasing volume fractions of the investigated dispersions. In Figure 7.13 B to E this is shown for representative DISFs. Both, $\tau(q)$ as well as the long-time values of $D(q, \Delta t)$, reveal a non-monotonic behavior with q which is a strong evidence for structure-dependent dynamics in the more concentrated dispersions.

In Figure 7.14 A the q -dependent evolution of $H(q)$ at the different volume fractions is depicted which supports these results further. As previously mentioned, $H(q)$ gives a qualitative measure of the difference in the short- and long-time limits of $D(q, \Delta t)$. A non-monotonic evolution of $H(q)$ is found except for the most dilute dispersion at $\phi_{eff,HS} = 0.02$. Volume fractions above 0.02 reveal a maximum in $H(q)$ at a certain q -

position which indicates the appearance of a structural length scale. Increasing values of $\phi_{eff,HS}$ result in a more pronounced maximum that shifts towards larger q -values. This implies the decrease of this structural length scale. If the particles are assumed to not change their size and shape and thus display a constant form factor $P(q)$ with increasing volume fraction, the following relationship can be used to estimate the structure factor $S(q)$:^[198]

$$S(q) = \frac{H(q)\phi_{dil}}{H(q)_{dilute}\phi_{eff,HS}} \quad (7.2)$$

In Figure 7.14 B $H(q)$ is normalized using $H(q)_{dilute}$, i.e., $H(q)$ at $\phi_{eff,HS} = 0.02$. This quotient gives a qualitative estimation of the structure factor $S(q)$, i.e., the q -position of the maximum q_{max} coincides for $S(q)$ and the quotient $H(q)/H(q)_{dilute}$. The fact that a single peak is obtained for $H(q)/H(q)_{dilute}$ versus q highlights again the stability of the $C_{351}S_{2.9}$ particles in bulk over the whole range of volume fractions.

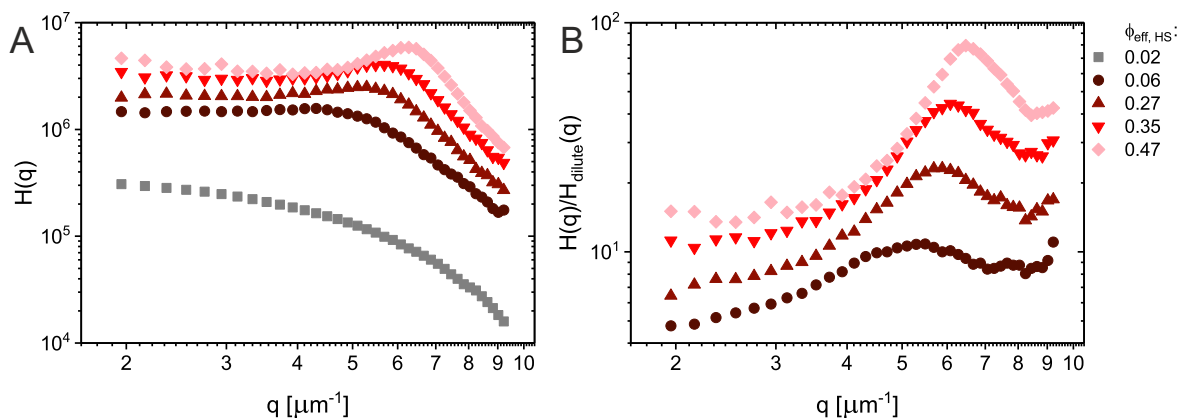


Figure 7.14: A. $H(q)$ as a function of q for dispersions of $C_{351}S_{2.9}$ particles at different volume fractions. B. Approximation of $S(q)$ given by the ratio of $H(q)/H(q)_{dilute}$ versus q .

The CDDM data provides also insights in the dynamics of the dispersions which is typically given by the stretching exponent β_s and the relaxation time τ . Both parameters are q -dependent and allow to draw conclusions on the motion of the particles. The q -dependent developments of β_s for the dispersions at different $\phi_{eff,HS}$ are depicted in Figure 7.15 A.

The data of the samples at $\phi_{eff,HS} = 0.02$ and 0.06 is almost constant over the investigated q -range. In contrast to these observations, β_s distinctly decreases towards larger length scales for denser dispersions. In the dilute regime ($\phi_{eff,HS} = 0.02$), the exponent β_s is assumed to be unity within the error owed to the fitting of the DISFs. In this specific case, the expression introduced in eq. 7.1 reduces to a term describing solely diffusive dynamics.^[194,195,198] Denser dispersions exhibit values of β_s smaller than unity indicating a deceleration of the dynamics or in other words a subdiffusive behavior. For samples with

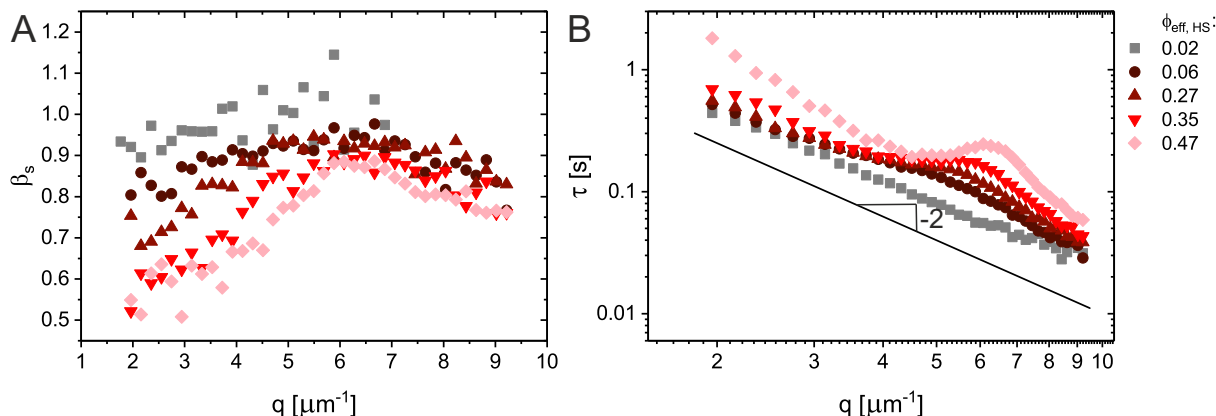


Figure 7.15: Stretching exponent β_s (A) and relaxation time τ (B) as a function of q for dispersions of $\text{C}_{351}\text{S}_{2.9}$ particles at different volume fractions.

$\phi_{\text{eff},HS}$ between 0.27 and 0.47 the described subdiffusive motion was assigned particularly to the low q -range. It is found that the deceleration increases with $\phi_{\text{eff},HS}$. Further, the emergence of subdiffusive behavior covers a broader range of q -values with increasing volume fraction which is related to crowding. These results are confirmed by investigating the evolution of τ as a function of q at the different volume fractions. In accordance to the data discussed above, simple diffusive dynamics are found in the dilute state ($\phi_{\text{eff},HS} = 0.02$), since $\tau(q) \propto 1/q^2$ over the whole accessible q -range. As opposed to this, τ displays an additional increase at q -values in the range of q_{max} (see Figure 7.15 B). This growth of τ is a structure-induced effect termed as de Gennes narrowing in the literature.^[199–202] Apart from that, increasing volume fractions lead to larger discrepancies to the slope of -2 for $q < 4 \mu\text{m}^{-1}$ which is another evidence for subdiffusive relaxation in this range of length scales. The results depicted in Figure 7.15 show that the particles remain mobile and that aggregation is not taking place. Even when crowding influences the samples at high volume fractions, subdiffusive motion and no aggregation was found. This highlights the stability of the samples at different volume fractions.

7.6.2 Comparison of the Structural Behavior

In the following section, the structural behavior of the $\text{C}_{351}\text{S}_{2.9}$ particles in bulk (Section 7.6.1) is compared with the structural behavior of the particles at the oil-water interface (Sections 7.2 to 7.4). Figure 7.16 combines the results from the interfacial and bulk behavior of the particles by showing the evolution of the structure factor $S(q)$ at different particle densities.

Regarding the data collected at the oil-water interface, $S(q)$ (solid lines in Figure 7.16) was calculated using SEM images recorded along different positions of the compression curve, i.e., different surface coverages. Extracts of these SEM images as well as the

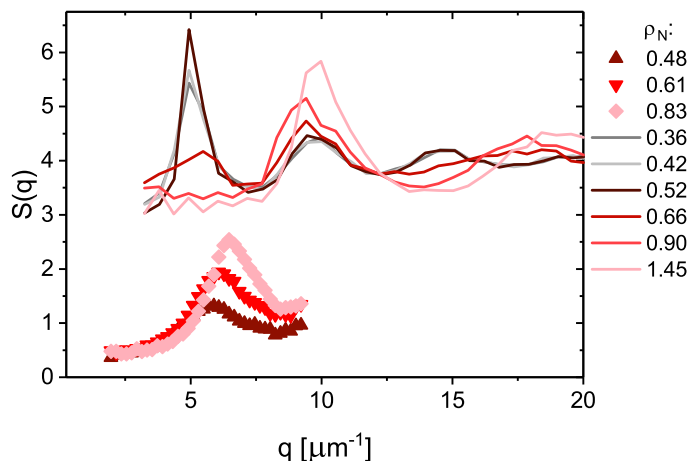


Figure 7.16: Structure factors $S(q)$ of the $C_{351}S_{2.9}$ particles at the interface (solid lines) and in bulk (symbols) versus q at different number densities ρ_N . The number density in bulk is given per volume (particles/ μm^3) and at the interface it is given per area (particles/ μm^2).

derivation of $S(q)$ are depicted in the Appendix in Section A.16. $S(q)$ in bulk (symbols in Figure 7.16) was determined according to eq. 7.2. To allow a direct comparison of the $S(q)$ data collected in bulk and at the interface, the area per particle A_p and the volume fraction ϕ were converted to the particle number density ρ_N per unit area or unit volume, respectively. The SEM images of the interfacial monolayers provide data that covers a larger q -range than the bulk data. Hence, it describes also higher order oscillations. These $S(q)$ profiles of the interface data show two distinct maxima in $S(q)$. The peak at lower q -values refers to the non-close-packed phase in which the shells of the particles are in contact (shell-shell contact). This peak is only present at low number densities. Further, it remains at its position upon increasing particle density. This highlights again that the particles are driven together in clusters at defined distances below full surface coverage. The maximum at higher q -values corresponds to the close-packed phase of the particles. This maximum increases in its peak height due to the growing number of particles that join the close-packed phase with increasing number density. The peak at low q -values appears at smaller q , i.e., larger length scales, as the maximum in $S(q)$ obtained for the bulk data. This demonstrates again that the effective diameter of the CS particles at the interface is increased as compared to their dimension in bulk. Such large effective dimensions at the interface are typical for deformable, surface-active microgels.^[83] The diameter accessible from the bulk data is between the dimensions of the particles in the non-close-packed and the close-packed phase.

Chapter 8

Conclusions and Future Perspectives

8.1 Conclusions

This thesis deals with the phase behavior of hard-core/soft-shell particles in the bulk phase and at the oil-water interface. The following key results were achieved:

1. High yield syntheses of monodisperse single-core core-shell (CS) particles with different overall dimensions, shell-to-core ratios and softnesses.
2. Demonstration of correlations between structural aspects of the particles, crystal structure and optical properties in self-assembled superstructures in bulk.
3. Investigation of electric field-induced transitions and thus the preparation of phases beyond the equilibrium state.
4. Revealing the differences in the self-assembly of different CS particles among themselves and to pure microgels at the interface and comparing these results to the phase behavior in bulk.

1. A high yield of monodisperse single-core CS particle types with different shell-to-core ratio and softnesses was successfully synthesized. To accomplish this task, a detailed analysis of the synthesis of CS particles was performed. As representative CS system gold(Au)-PNIPAM particles were used. Their gold nanoparticle cores were used as a convenient sensor to detect refractive index changes in their environment. Prior to encapsulation of the Au nanoparticles in a cross-linked, soft poly-*N*-isopropylacrylamide (PNIPAM) shell, their surface was functionalized. Here, different functionalizing agents including citrate, amine derivatives with and without vinyl groups and a thiol derivative were tested. The differently functionalized gold nanoparticles were subsequently used for the synthesis of Au-PNIPAM particles. It was revealed that the hydrophobicity at the surface of the modified gold nanoparticles after the functionalization is crucial for a successful encapsulation. Additionally, it was shown that polymerizable groups, like

vinyl groups, are not required. These findings allow to draw conclusions on the reaction mechanism which were further manifested by *in situ* monitoring of a polymerization using UV-vis absorbance spectroscopy and light scattering. The mechanism was found to follow a free radical seeded precipitation polymerization. This implies that oligomer/polymer radicals precipitate onto the gold nanoparticle surface if their surface is appropriately functionalized. As double bonds were not required on the surface of the gold nanoparticles, a grafting-from mechanism could be excluded. The *in situ* studies allowed to divide the reaction into three phases. In the first phase, which endures about 10 minutes, the initiator decomposes and attacks the monomers *N*-isopropylacrylamide and *N,N'*-methylenebisacrylamide. In the second phase, which takes about 22 minutes, oligomer and polymer radicals grow and precipitate onto the gold nanoparticles. After about 35 minutes the third phase is reached, when no significant growth is observed anymore. Knowing how the reaction proceeds, the structure of the final material can be controlled on a high level. This allowed, e.g., the development of a semi-batch protocol, in which the precipitation polymerization was conducted in several steps, to obtain CS particles with large dimensions. Another decisive parameter is the concentration of the functionalized gold nanoparticles in the reaction batch. Here, a suitable range of seed concentrations could be identified. In this range, solely monodisperse, single-core CS particles were obtained. Below these concentrations, a mixture of CS particles and purely organic hydrogels without core was formed. Exceeding this concentration range led to polydisperse CS particles. Within the range where only CS particles were formed, the seed concentration allowed to tune the shell-to-core ratio, i.e., the thickness of the polymer shell. In order to increase the range of accessible shell-to-core ratios further, different monomer feeds were used. This way Au-PNIPAM CS particles with diameters ranging from 168 to 472 nm were synthesized. The softness of the particles was adjusted by variation of the cross-linker content. Another possibility to tune the shell-to-core ratio is to overgrow the gold core within the polymer network. Typically gold cores around 15 nm were encapsulated. The overgrowth of the gold cores resulted in core diameters of 71 nm. Further, silica (SiO₂) nanoparticles with diameters between 125 and 486 nm were encapsulated in cross-linked PNIPAM microgel shells achieving overall diameters between 281 and 1028 nm. The described changes in the particle structure were performed at large scales and resulted in highly monodisperse particles. These were important prerequisites for the self-assembly studies of those particles.

2. Self-assembled structures of hard-core/soft-shell particles in the bulk phase

showed extraordinary order and thus diffraction properties. Different particle structures including CS particles with different sizes, softness, shell-to-core ratio and core size were investigated. It is highlighted that self-assembled structures of all prepared particles resulted in well ordered superstructures displaying sharp Bragg diffraction modes. This underlines the high degree of monodispersity of the synthesized CS particles. Significant correlations between particle structure, optical and diffraction properties of the superstructures upon variation of the volume fraction were revealed. Different dimensions and a sufficient softness of CS particles allowed to tune the diffraction modes over a remarkable range of wavelengths covering the ultraviolet, the visible as well as the near-infrared region. The Bragg modes could be tuned from 381 nm to 1406 nm. This implies lattice constants between 245 nm and 905 nm of the face-centered cubic (FCC) lattices. Firstly, the overall particle size is a crucial parameter regarding the range of accessible inter-particle distances in the superstructures. It offers an easy opportunity to manipulate the diffraction behavior. Secondly, their softness is decisive with respect to the range of accessible diffraction modes. To adjust the softness, particles with cross-linker densities between 10 to 25 mol% referred to the monomer *N*-isopropylacrylamide were synthesized. Softer particles crystallized over a broader range of volume fractions, i.e., inter-particle distances. They were able to achieve considerably high volume fractions of 1.5 that are far beyond the hard-sphere limit for FCC packing of 0.74. In addition, they revealed a certain tolerance regarding defects in the superstructures as their soft polymer shells compensated slight imperfections in the crystal lattice. This supported the overall crystal fraction.

In addition, the influence of the 15 nm gold cores in the superlattices was analyzed by investigating two CS systems of different softness and their respective pitted counterparts. The pitted particles were prepared under harsh dissolution conditions for the gold cores. The success of the dissolution process of the core was confirmed by electron-microscopic and spectroscopic analysis. It was necessary to verify that the size, swelling behavior and internal network structure of the pitted particles is similar to their CS analogues. This was proved by temperature-dependent dynamic light scattering (DLS) and small angle neutron scattering (SANS) measurements. The diffraction behavior of the crystalline superstructures of CS and pitted particles agreed well. SANS measurements of the respective superstructures showed Bragg peaks of several orders which were assigned to FCC lattices. The lattice constants determined by SANS and UV-vis absorbance spectroscopy coincided well. In the superstructures of the CS particles the plasmonic character was significantly enhanced as compared to absorbance spectra of these particles in the dilute regime. This was related to a distinct reduction of single-particle scattering in the crystals as compared to the dilute regime. As the scattering cross-section of the gold cores was too

small, coupling between the Bragg mode and the plasmon resonance was not observed. Particle structures with smaller shell-to-core ratios crystallized as well over a broad range of volume fractions. For this study CS particles with a total dimension of 472 nm and 71 nm Au cores were used. The crystal lattice was determined by three complementary methods which were confocal laser scanning microscopy (CLSM), small angle X-ray scattering (SAXS) and UV-vis absorbance spectroscopy. Again, a six-fold symmetry was assigned to the crystalline superstructures. Lattice constants and volume fraction determined by all three independent methods coincided well. Due to the large size of these particles crystal lattices with lattice constants of 905 nm were obtained.

The diffraction and plasmonic mode overlapped in the absorbance spectra of some samples. Since the scattering cross-section of these gold cores was larger as compared to the results of gold cores with 15 nm, the samples were investigated with respect to coupling. However, coupling could not be unambiguously revealed, so that further investigations are required. To conclude, the range of accessible inter-particle distances in the superlattices and thus the diffraction behavior could be manipulated using a specific particle structure.

3. The application of an external electric field on CS particles in bulk allowed to induce structural transitions. Directing the self-assembly of colloidal dispersions using electric fields is a very elegant method, as it provides the opportunity to achieve non-equilibrium phases beyond hexagonally ordered structures. The electric field-induced transitions of dispersions consisting of SiO₂-PNIPAM particles between volume fractions of 0.16 and 0.40 were successfully studied. Aiming for strong dipolar interactions of the particles, SiO₂-PNIPAM particles with a large hydrodynamic diameter of 810 nm at 25°C were prepared. A sinusoidal electric field at a constant frequency of 100 kHz was applied to the particle dispersions. The field direction (z -direction) was perpendicular to the image plane (xy -plane). The following transitions were observed with increasing field strengths using CLSM: At low volume fractions of 0.16, a fluid to string transition was observed. Increasing the field strength further, the strings approached each other and formed sheets, which were visible as chains in the xy -plane. At a volume fraction of 0.23, a direct transition from a fluid state to a sheet phase was observed upon increasing the electric field strength. The latter one showed a labyrinthine network of chains in the xy -plane. Upon further enhancement of the electric field these sheets approach each other leading to domains of square lattices in the xy -plane. At volume fractions of 0.32 and 0.40, the obtained results were similar. Here, a mixture between fluid and hexagonally ordered domains was found at zero-field condition and low field strengths. Increasing the electric field allowed to obtain square lattices separated by voids in the field of view. These results coincide well with literature on electric field-induced transition of silica particles^[63] and also partly agree with results from studies dealing with charged microgels.^[65] However,

the CS particles respond on a much faster time scale (seconds to minutes) to the electric field as compared to hard silica colloids (hours to days). Summarizing, the electric field influence allowed to leave the equilibrium fluid/hexagonally ordered phase and to achieve non-equilibrium phases like the string, sheet and square-lattice phase.

4. Self-assembled structures of hard-core/soft-shell particles at liquid-liquid interfaces allowed to find correlations between the particle structure and the interfacial microstructures upon compression. A systematic study using CS particles with two different core sizes and different shell thicknesses, i.e., shell-to-core ratios, was performed. Comparisons between these different CS particle structures themselves and to purely organic microgels were drawn. All CS particles revealed a similar temperature-dependent swelling behavior in the bulk phase independent of the shell thickness. This indicates the presence of a comparable distribution of cross-linker density and softness. This was an important prerequisite for the comparison of the particles at the interface. Next, it was focused on their behavior at the oil-water interface. Initially, their particle morphology at the interface was analyzed by freeze-fracture shadow-casting cryogenic scanning electron microscopy (FreSCa cryo-SEM). The surface-active hydrogel shells aim for maximal hydration of their polymer chains leading to a strong deformation at the interface that is balanced by internal elastic deformation of the microgel network. Simultaneously, the covalent link between core and shell prevents the shells to rearrange at the interface. As a result, an upward deformation of the interfacial area around the particles was observed which is related to a complex interplay of interfacial forces as well as shell hydration, adsorption and internal elasticity. The resulting upward deformation of the interface leads to attractive capillary forces at low surface coverage that drive the particles together to areas separated by voids. In these areas the particles are located at defined inter-particle distances. This was further verified by an *in situ* experiment using CLSM which illustrated the particle adsorption at the interface at low surface coverage. Hence, a new mechanism for the formation of attractive capillary interactions was successfully revealed. This is at odds with purely organic microgels without hard cores which are homogeneously distributed at low surface coverage. In addition, it was demonstrated that particles with larger shell-to-core ratios deform to a larger extent at the interface. However, relative to their bulk size all particles showed a similar size increase. This relative size increase was between 1.5 and 1.8 for particles with small silica cores and between 1.2 to 1.4 for particles with large silica cores. The decreased interfacial deformation for particles with large cores might be related to their more hydrophobic character which was found by analyzing the position of these colloids at the interface using freeze-fracture. Further investigations focused on the development of the interfacial microstructures upon compression in a Langmuir-Blodgett trough. Due to the described attractive forces at low surface coverage,

the inter-particle distance in these areas is independent of the state of compression until full surface coverage is achieved. After a uniform monolayer is formed upon compression, a steep increase of the surface pressure is measured while the shells start to be compressed. Hereby, the shell-to-core ratio controls the slope of this steep increase in the compression curve. Smaller shell-to-core ratios with a decreasing compressibility result in a steeper slope. Hence, the shell thickness significantly influences the range of areas over which deformation occurs. Upon compression the non-close-packed lattice is not continuously deformed. Instead, a rapid transition to close-packed clusters with particles in core-core contact is observed which is due to sudden localized collapses of the shells as opposed to a continuous deformation of the shell. These clusters are separated by voids. The clusters appear at much lower surface pressures as compared to purely organic microgels. Furthermore, particles with larger core sizes but similar shell-to-core ratios showed this transition at lower surface pressures. As evident in the SEM and atomic force microscopy (AFM) images of the CS particles with small cores, the silica cores are not in contact in the clusters. In contrary, purely organic microgels can fully rearrange their shape as they are not limited by a covalent link to a hard core. Even higher surface coverages result in monolayer buckling before the voids can close in the case of CS particles. Again, this is different for purely organic microgels which show a complete phase transition to the clustered phase. The described transitions for CS particles upon compression have just recently been confirmed using a theoretical coarse-grained model.^[203] Studying the hexagonal order parameter upon compression provides correlations between the order in the monolayers and the particle structure. The general evolution of this parameter is as follows: First, it increases until full surface coverage is achieved. When clustering starts, the order parameter reduces until it rises again due to hexagonal packing in the growing clusters. Thicker shells seem to enable an effective defect compensation as they are more compliant resulting in larger values for the hexagonal order parameter. Although CS particles with large cores showed a similar qualitative behavior at the interface as their analogues with small cores, the results show that their inter-particle forces and thus their mechanical response is different. This is related to non-trivial effects between the core size and the compressibility of the particles which deserve further work in the future. Additionally, it was demonstrated that particles with very small shell-to-core ratios were not stable at the interface. Their shell deformation was not sufficient to stabilize them at the interface. Consequently, they submerged into the water subphase. Summarizing the results of the phase behavior at the interface, a specific interfacial microstructure can be achieved by manipulating the inter-particle interactions using a particular structure of hard-core/soft-shell particles. These results are an important basis for future work on tailored interfacial microstructures from CS particles with functional cores like gold or silver particles.

Finally, a comparison of the structural evolution in bulk phase and at oil-water interfaces upon increasing particle density revealed significant differences. A representative hard-core/soft-shell model system of silica-PNIPAM particles was used for this study. Confocal differential dynamic microscopy represents an easily accessible method to characterize colloidal dispersions up to high volume fractions. Thus, it was used to characterize the structural and dynamic behavior in particle dispersions, i.e., in the bulk phase, at volume fractions between 0.02 and 0.47. All derived dynamic image structure functions could be described with a single relaxation time that manifested the absence of any aggregation. Examinations on the particle dynamics revealed that the particles remained mobile over the whole range of investigated volume fractions. At a volume fraction of 0.47, when crowding already influenced the dispersion, a subdiffusive behavior was found. This verified again the stability of the dispersions and the absence of aggregates. As outlined above, the same hydrogel shells, that stabilize the particles in bulk, induce capillary attractions at the oil-water interface that lead to aggregation already at low surface coverage. In addition, a highly non-linear reaction of the microgel shells is observed resulting in close-packed particle clusters upon further compression. In conclusion, the identical particle structure, which ensures stability in the bulk phase upon increasing particle densities, is not necessarily providing the same stability at the interface. This is very important for the fabrication of 2D nanostructured material and demands the development of new systems that achieve the same stability at the interface as in the bulk phase.

8.2 Future Perspectives

This thesis answered several key questions regarding the self-assembly of hard-core/soft-shell particles. On top of this, the performed studies generated several ideas for future studies.

In terms of the self-assembly studies in bulk, it would be of significant interest to investigate the self-assembly of Au-PNIPAM particles with respect to plasmonic/diffractive coupling. Self-assembled monolayers of similar particles already revealed coupling between those modes resulting in surface lattice resonances (SLRs).^[61] In this thesis, the absorbance spectra of crystalline samples (3D) from CS particles with a 71 nm gold nanoparticle core were promising regarding SLRs. For future studies even larger gold cores are of interest. Larger gold cores exhibit increased extinction cross-sections and should thus promote coupling.^[204] To realize coupling in three dimensions, particles with higher cross-linker contents should additionally be used. Highly cross-linked shells are able to position the core more in the center of the particle leading to defined inter-particle distances between the gold cores. Moreover, simulations are required to understand the complex optics further.

To extend the performed self-assembly studies in bulk and at the interface, it would be interesting to replace the hard nanoparticle cores by different geometrical shapes. In the case of anisotropic shapes, their alignment in an electric field with increasing volume fraction is of significant interest. Here, for instance, rods that are encapsulated in thin PNIPAM shells would be suitable. Furthermore, in the case of plasmonic nanoparticles hot spots are created at the edges of these particles which can be useful to support coupling effects in crystalline superstructures of these particles.^[205]

In addition, it can be promising to substitute the cross-linked PNIPAM shell by linear PNIPAM ligands. This way, the particle structure is closer to a step-like pair interaction potential. The two length scales that are given by the core and the non-cross-linked shell are defined more precisely as compared to CS particles with a gradually cross-linked shell. The hard component in CS particles with non-cross-linked shells can be estimated, as it approximately corresponds to the inorganic core. In the case of CS particles with gradually cross-linked PNIPAM shells, the hard component of the particle is strictly speaking the addition of the inorganic core and the inner, highly cross-linked part of the polymer shell. As this compressed part is hard to determine, the hard component in CS particles is not clearly defined. Since the interaction potential of Au particles stabilized with linear PNIPAM ligands is close to a step-like pair interaction potential, it might be

easier to support the formation of different crystal phases including quasicrystals.^[15,16] Furthermore, it has already been shown that Au nanoparticles decorated with PNIPAM ligands can be prepared using different gold nanoparticle shapes and sizes and with ligands of varying lengths.^[206,207]

To promote crystal phases beyond equilibrium, external stimuli can be useful, as shown in this thesis. In the bulk phase, the application of shear forces^[208] or electric fields^[63,65–67] are conceivable. For future experiments, it would be additionally interesting to investigate different types of CS particles. Here, different shell-to-core ratios would be of interest in order to systematically investigate the influence of the shell thickness. For studies in the presence of an electric field, the total dimension and charge density of the particles should be increased. Both changes would enhance the polarizability of the particles. In this way, lower field strengths can be used for the experiments and heating of the sample is prevented. At the interface, experiments using external triggers such as ultrasound or electric fields are promising regarding the formation of non-equilibrium phases. Up to now, it has been shown that both external stimuli have improved the quality of self-assembled monolayers.^[209,210] The overall crystalline fraction of silica particles at the air-water interface was enhanced about 20 to 60 times by ultrasonic annealing and barrier-sway.^[209] Electric fields enabled the formation of defect-free monolayers of glass particles with tunable inter-particle spacings controlled by the field strengths at the oil-air interface.^[210] However, so far, a detailed study investigating the influence of these triggers on the self-assembly of different particle structures at the interface is not existing.

The ideas for future studies show that there is still a number of challenges to tackle that will provide access to promising future applications.

A Appendix

A.1 Setup of the Langmuir-Blodgett Trough

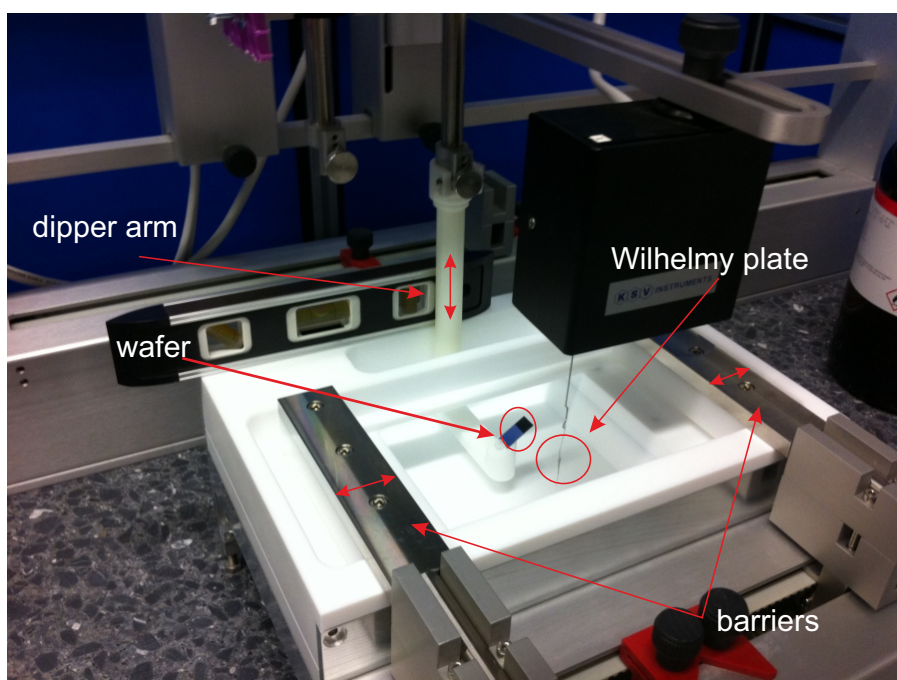


Figure A.1: Photograph showing the experimental setup for compression-deposition experiments in the Langmuir Blodgett trough. Adapted with permission from "Isostructural Solid-Solid Phase Transition in Monolayers of Soft Core-Shell Particles at Fluid Interfaces: Structure and Mechanics", by Rey, M.; Fernández-Rodríguez, M. Á.; Steinacher, M.; Scheidegger, L.; Geisel, K.; Richtering, W.; Squires, T. M.; Isa, L. *Soft Matter* **2016**, *12*, 3545-3557. Copyright 2016 by The Royal Society of Chemistry.

A.2 Setup of the D11 SANS Instrument

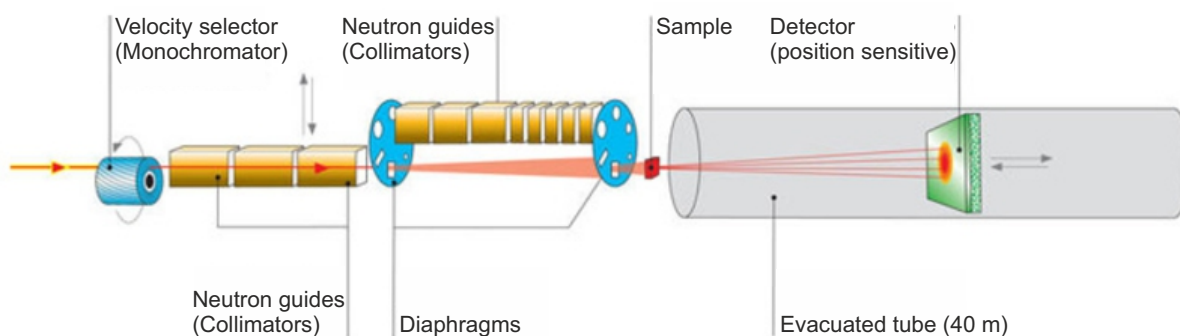


Figure A.2: Schematic setup of the used SANS instrument (D11) at the ILL. Adapted from reference^[211].

A.3 Swelling Curves of Microgel Systems Prepared with Different Gold Seed Concentrations

The hydrodynamic radius of the particles synthesized using different seed concentrations was measured in dependence on the temperature by DLS. The results are shown in Figure A.3.

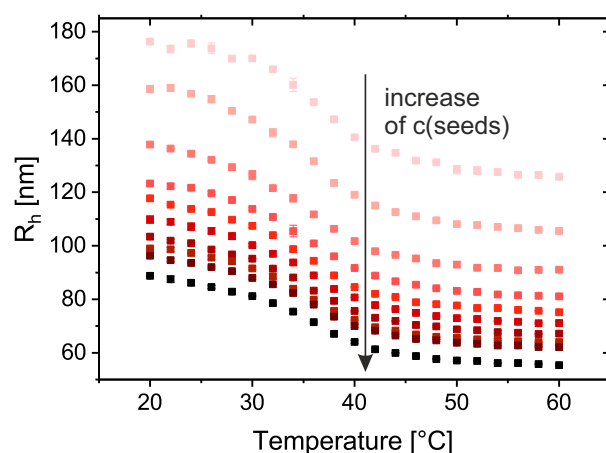


Figure A.3: Temperature-dependent evolution of the hydrodynamic radius for samples prepared with varying gold seed concentration between 0.4 - 8 nmol/L. The error bars are mostly in the order of the symbol size and thus not always visible.

The expected volume phase transition behavior for PNIPAM in water is observed for all samples: R_h decreases at temperatures around the VPTT (here at around 35°C) with

increasing temperature. At temperatures below the VPTT the samples are highly swollen with water. Above the VPTT, i.e., under poor solvent conditions, the particles release water and collapse.

A.4 Diffraction Properties Analyzed Using UV-Vis Absorbance Spectroscopy

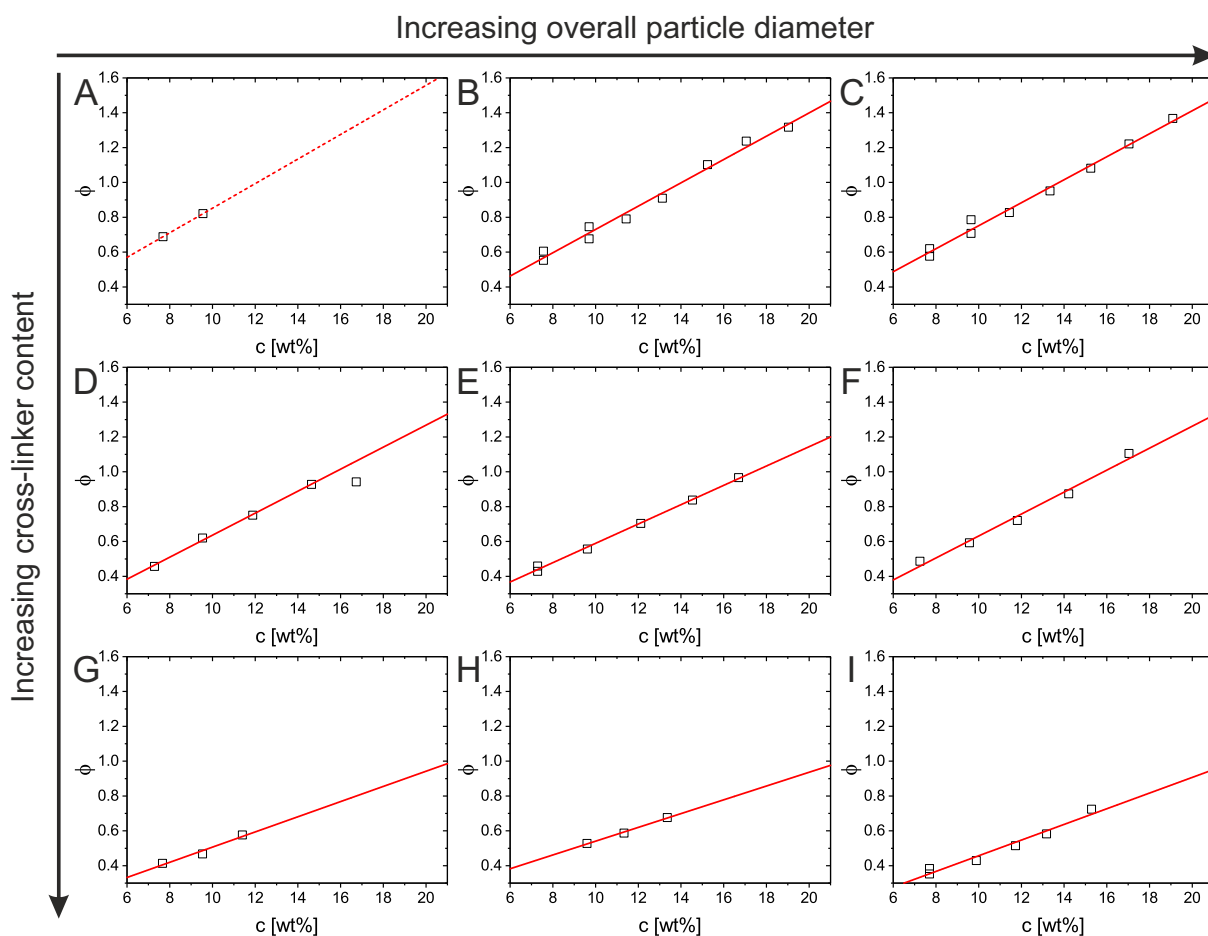


Figure A.4: Volume fraction ϕ determined from UV-vis absorbance spectra analysis versus the weight concentration c of the crystalline samples. The solid red line is a linear fit allowing the calculation of the volume fraction for samples which display no diffraction peak. A. $C_{15}S_{12.0}(10\%)$, B. $C_{15}S_{15.7}(10\%)$, C. $C_{15}S_{16.5}(10\%)$, D. $C_{15}S_{12.5}(15\%)$, E. $C_{15}S_{14.2}(15\%)$, F. $C_{15}S_{17.9}(15\%)$, G. $C_{15}S_{11.2}(25\%)$, H. $C_{15}S_{14.7}(25\%)$, I. $C_{15}S_{16.0}(25\%)$. The regression curve in A might be defective as it is only based on two data points. To emphasize this uncertainty, it is described by a dashed line. In D the data point at 16.7 wt% was not considered for the regression curve as the position of the Bragg peak and thus ϕ could not be determined unambiguously.

Table A.1: Results from UV-vis absorbance spectroscopy of concentrated dispersions consisting of CS particles with 10 mol% cross-linker content: Weight concentration c , wavelength position of the Bragg peak λ_{diff} , full width at half maximum (FWHM) of the diffraction modes, lattice plane distance d_{111} , lattice constant a , the volume fraction as obtained from absorbance spectra ϕ_{UV-vis} , the volume fraction as determined by linear extrapolation ϕ_{fit} and the average inter-particle distance in the crystal lattice d_{cc} .

c [wt%]	λ_{diff} [nm]	FWHM [nm]	d_{111} [nm]	a [nm]	ϕ_{UV-vis}^a	ϕ_{fit}	d_{cc} [nm]
C ₁₅ S _{12.0} (10%)							
7.7	405	29	151 ± 2	261 ± 3	0.69 ± 0.2	0.69 ± n.a. ^c	184 ± 2
9.6	382	6	142 ± 2	246 ± 3	0.82 ± 0.3	0.82 ± n.a. ^c	174 ± 2
11.5	-	-	-	-	-	0.96 ± n.a. ^c	-
13.3	-	-	-	-	-	1.08 ± n.a. ^c	-
15.2	-	-	-	-	-	1.22 ± n.a. ^c	-
C ₁₅ S _{15.7} (10%)							
7.6	552/569	n.a. ^b	205 ± 2/ 212 ± 2	355 ± 4/ 366 ± 4	0.61 ± 0.02/ 0.55 ± 0.02	0.57 ± 0.06	251 ± 3/ 259 ± 3
9.7	532/515	n.a. ^b	198 ± 2/ 191 ± 2	343 ± 4/ 332 ± 4	0.68 ± 0.02/ 0.75 ± 0.02	0.71 ± 0.07	242 ± 3/ 234 ± 3
11.4	505	7	188 ± 2	325 ± 4	0.79 ± 0.03	0.83 ± 0.07	230 ± 3
13.1	482	7	179 ± 2	310 ± 3	0.91 ± 0.03	0.94 ± 0.08	219 ± 2
15.2	452	10	168 ± 2	291 ± 3	1.10 ± 0.04	1.08 ± 0.08	206 ± 2
17.1	435	19	162 ± 2	280 ± 3	1.24 ± 0.04	1.20 ± 0.09	198 ± 2
19.0	426	10	158 ± 2	274 ± 3	1.32 ± 0.04	1.33 ± 0.09	194 ± 2
C ₁₅ S _{16.5} (10%)							
7.7	578/592	n.a. ^b	215 ± 2/ 220 ± 2	372 ± 4/ 381 ± 4	0.62 ± 0.02/ 0.58 ± 0.02	0.60 ± 0.05	263 ± 3/ 270 ± 3
9.6	534/553	n.a. ^b	199 ± 2/ 206 ± 2	344 ± 4/ 356 ± 4	0.79 ± 0.03/ 0.71 ± 0.02	0.73 ± 0.06	243 ± 3/ 252 ± 3
11.4	525	10	195 ± 2	338 ± 4	0.83 ± 0.03	0.85 ± 0.06	239 ± 3
13.3	501	10	186 ± 2	323 ± 4	0.95 ± 0.03	0.97 ± 0.07	228 ± 3
15.2	480	17	178 ± 2	309 ± 3	1.08 ± 0.04	1.10 ± 0.07	219 ± 2
17.0	461	17	171 ± 2	297 ± 3	1.22 ± 0.04	1.22 ± 0.08	210 ± 2
19.1	444	12	165 ± 2	286 ± 3	1.37 ± 0.05	1.35 ± 0.08	202 ± 2

^a The volume fractions ϕ_{UV-vis} were calculated assuming FCC lattices (number of particles per unit cell is 4 and the unit cell volume is given by a^3) using the lattice constant a and R_h at 25°C.

^b The FWHM of the Bragg peak could not be reliably determined.

^c As the linear regression curve in Figure A.4 A was only based on two data points, an error could not be reliably determined. Note that these volume fractions are only rough estimations.

Table A.2: Results from UV-vis absorbance spectroscopy of concentrated dispersions consisting of CS particles with 15 mol% cross-linker content: Weight concentration c , wavelength position of the Bragg peak λ_{diff} , full width at half maximum (FWHM) of the diffraction modes, lattice plane distance d_{111} , lattice constant a , the volume fraction as obtained from absorbance spectra ϕ_{UV-vis} , the volume fraction as determined by linear extrapolation ϕ_{fit} and the average inter-particle distance in the crystal lattice d_{cc} .

c [wt%]	λ_{diff} [nm]	FWHM [nm]	d_{111} [nm]	a [nm]	ϕ_{UV-vis}^a	ϕ_{fit}	d_{cc} [nm]
C ₁₅ S _{12.5} (15%)							
7.3	485	11	180 ± 2	312 ± 3	0.46 ± 0.02	0.46 ± 0.04	221 ± 2
9.5	438	13	163 ± 2	282 ± 3	0.62 ± 0.02	0.61 ± 0.04	199 ± 2
11.9	411	11	153 ± 2	265 ± 3	0.75 ± 0.03	0.76 ± 0.05	187 ± 2
14.6	383	n.a. ^b	142 ± 2	247 ± 3	0.93 ± 0.03	0.93 ± 0.05	174 ± 2
16.7	381	n.a. ^b	142 ± 2	245 ± 3	0.94 ± 0.03	1.06 ± 0.06	173 ± 2
C ₁₅ S _{14.2} (15%)							
7.3	551/564	n.a. ^b	205 ± 2/ 210 ± 2	355 ± 4/ 363 ± 4	0.46 ± 0.02/ 0.43 ± 0.01	0.44 ± 0.03	251 ± 3/ 257 ± 3
9.6	517	13	192 ± 2	333 ± 4	0.56 ± 0.02	0.57 ± 0.03	235 ± 3
12.1	478	16	178 ± 2	308 ± 3	0.70 ± 0.02	0.71 ± 0.04	218 ± 2
14.5	451	9	168 ± 2	290 ± 3	0.84 ± 0.03	0.84 ± 0.04	205 ± 2
16.7	430	9	160 ± 2	277 ± 3	0.97 ± 0.03	0.96 ± 0.04	196 ± 2
C ₁₅ S _{17.9} (15%)							
7.2	677 ^c	15	252 ± 3	436 ± 5	0.49 ± 0.02	0.46 ± 0.08	308 ± 3
9.6	634	11	236 ± 3	408 ± 5	0.59 ± 0.02	0.60 ± 0.09	289 ± 3
11.8	594	20	221 ± 2	382 ± 4	0.72 ± 0.02	0.75 ± 0.10	270 ± 3
14.2	557	14	207 ± 2	359 ± 4	0.87 ± 0.03	0.90 ± 0.11	254 ± 3
17.0	515	15	191 ± 2	332 ± 4	1.11 ± 0.04	1.07 ± 0.12	234 ± 3

^a The volume fractions ϕ_{UV-vis} were calculated assuming FCC lattices (number of particles per unit cell is 4 and the unit cell volume is given by a^3) using the lattice constant a and R_h at 25°C.

^b The FWHM of the Bragg peak could not be reliably determined.

^c This UV-vis absorbance spectra was recorded at 15°C instead of 25°C.

Table A.3: Results from UV-vis absorbance spectroscopy of concentrated dispersions consisting of CS particles with 25 mol% cross-linker content: Weight concentration c , wavelength position of the Bragg peak λ_{diff} , full width at half maximum (FWHM) of the diffraction modes, lattice plane distance d_{111} , lattice constant a , the volume fraction as obtained from absorbance spectra ϕ_{UV-vis} , the volume fraction as determined by linear extrapolation ϕ_{fit} and the average inter-particle distance in the crystal lattice d_{cc} .

c [wt%]	λ_{diff} [nm]	FWHM [nm]	d_{111} [nm]	a [nm]	ϕ_{UV-vis}^a	ϕ_{fit}	d_{cc} [nm]
C ₁₅ S _{11.2} (25%)							
7.7	448	11	167 ± 2	288 ± 3	0.41 ± 0.01	0.40 ± 0.15	204 ± 2
9.5	430	22	160 ± 2	277 ± 3	0.47 ± 0.02	0.49 ± 0.17	196 ± 2
11.4	401	n.a. ^b	149 ± 2	258 ± 3	0.58 ± 0.02	0.57 ± 0.18	183 ± 2
13.1	-	-	-	-	-	0.64 ± 0.20	-
15.3	-	-	-	-	-	0.74 ± 0.21	-
17.2	-	-	-	-	-	0.82 ± 0.23	-
20.0	-	-	-	-	-	0.94 ± 0.25	-
C ₁₅ S _{14.7} (25%)							
7.9	-	-	-	-	-	0.46 ± 0.05	-
9.6	543	9	202 ± 2	350 ± 4	0.52 ± 0.02	0.52 ± 0.06	247 ± 3
11.3	522	n.a. ^b	194 ± 2	336 ± 4	0.59 ± 0.02	0.59 ± 0.06	238 ± 3
13.4	498	n.a. ^b	185 ± 2	321 ± 4	0.68 ± 0.02	0.67 ± 0.07	227 ± 3
15.5	-	-	-	-	-	0.76 ± 0.08	-
16.9	-	-	-	-	-	0.81 ± 0.08	-
18.5	-	-	-	-	-	0.88 ± 0.09	-
C ₁₅ S _{16.0} (25%)							
7.7	656/675	n.a. ^b	244 ± 3/ 251 ± 3	422 ± 5/ 435 ± 5	0.38 ± 0.01/ 0.35 ± 0.01	0.35 ± 0.08	299 ± 3/ 307 ± 3
9.9	632	16	235 ± 3	407 ± 5	0.43 ± 0.01	0.45 ± 0.09	288 ± 3
11.7	595	19	221 ± 2	383 ± 4	0.51 ± 0.02	0.53 ± 0.09	271 ± 3
13.2	571	15	212 ± 2	368 ± 4	0.58 ± 0.02	0.60 ± 0.10	260 ± 3
15.3	531	n.a. ^b	197 ± 2	342 ± 4	0.72 ± 0.02	0.69 ± 0.11	242 ± 3
17.0	-	-	-	-	-	0.77 ± 0.11	-

^a The volume fractions ϕ_{UV-vis} were calculated assuming FCC lattices (number of particles per unit cell is 4 and the unit cell volume is given by a^3) using the lattice constant a and R_h at 25°C.

^b The FWHM of the Bragg peak could not be reliably determined.

A.5 SANS Profiles of Dilute Samples

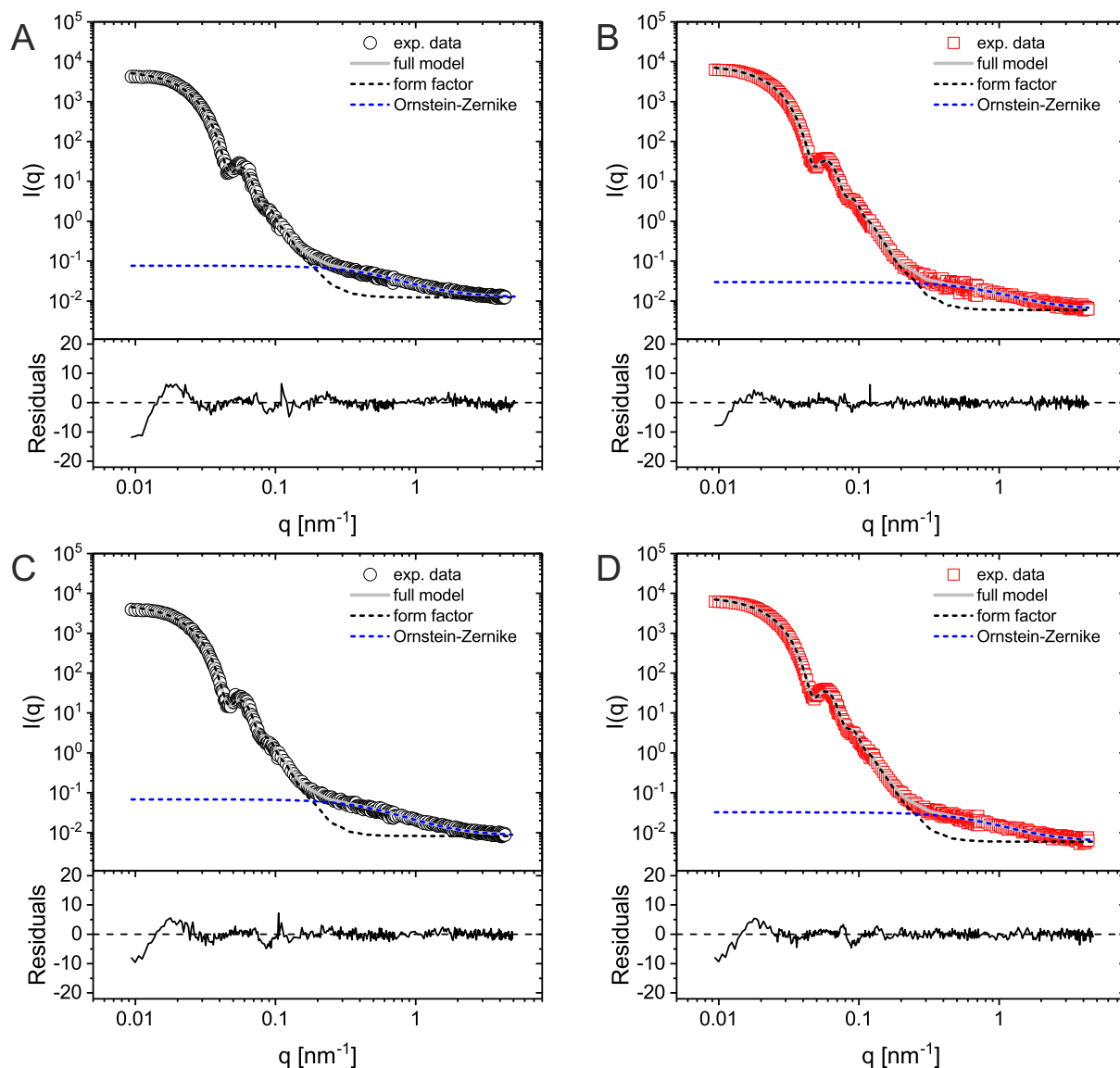


Figure A.5: Radially averaged scattering profiles (empty symbols) measured for dilute dispersions of CS particles and their pitted counterparts: A. $C_{15}S_{16.2}$ (10%), B. $C_{15}S_{14.6}$ (25%), C. $C_4S_{16.2}$ (10%), D. $C_4S_{14.6}$ (25%). The dashed lines represent the form factor contribution (black) or the OZ contribution (blue). Both contributions together result in the full model which is depicted by a solid gray line. The error bars of the data are in the range of the symbol size. Below the scattering profiles, the residuals between the data and the respective fit using the full model are shown.

Table A.4: Overview of the simulation parameters used to fit the scattering profiles of the dilute particle dispersions: The number density ρ_N , I_{offset} which describes incoherent and additional background contributions, the correlation length ξ , the amplitude of the OZ contribution $I_L(0)$, the amplitude of the OZ contribution normalized by the number density $I_L(0)/\rho_N$, the radius of the inner homogeneous volume segment R_{hom} , the thickness ΔR of the outer volume element with an exponentially decaying density, α_{SASfit} describing the density decay, the standard deviation s_{SASfit} , the scattering length density of the solvent $\eta_{solvent}$, the scattering length density η_{shell} of the pure shell material (cross-linked PNIPAM), the scattering length density η_{hom} up to the radius R_{hom} , the volume fraction of solvent ϕ_{in} at R_{hom} and the volume fraction of the solvent ϕ_{out} at $R_{hom} + \Delta R$.

Parameter	C ₁₅ S _{16.2} (10%)	C _d S _{16.2} (10%)	C ₁₅ S _{14.6} (25%)	C _d S _{14.6} (25%)
ρ_N [cm ⁻³]	0.063	0.059	0.117	0.107
I_{offset} [cm ⁻¹]	0.012	0.008	0.006	0.006
ξ [nm]	1.9	1.9	1.2	1.4
$I_L(0)$ [cm ⁻¹]	0.064	0.060	0.024	0.026
$I_L(0)/\rho_N$ [cm ²]	1.0	1.0	0.2	0.3
R_{hom} [nm]	39	38	47	51
ΔR [nm]	64	66	52	49
α_{SASfit}	-2.2	-3.4	-2.7	-2.6
s_{SASfit} [nm]	11	11	10	10
$\eta_{solvent}$ [nm ⁻²]	0.00064	0.00064	0.00064	0.00064
η_{shell} [nm ⁻²]	0.00014	0.00014	0.00014	0.00014
η_{hom} [nm ⁻²]	0.00055	0.00056	0.00056	0.00056
ϕ_{out}	0.94	0.96	0.95	0.95
ϕ_{in}	0.83	0.84	0.85	0.85

A.6 Normalized UV-Vis Absorbance Spectra

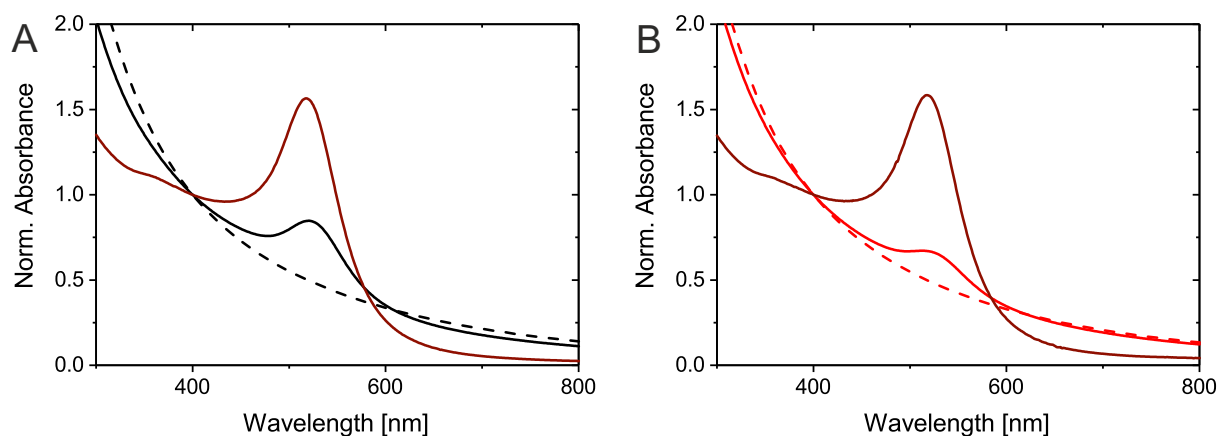


Figure A.6: Absorbance spectra normalized to the absorbance at 400 nm recorded at room temperature. In A the respective spectra of diluted dispersions of $C_{15}S_{16.2}(10\%)$ and $C_dS_{16.2}(10\%)$ and in B of $C_{15}S_{14.6}(25\%)$ and $C_dS_{14.6}(25\%)$ are shown. The solid lines represent the data of the CS particles and the dashed lines show the data of the C_dS particles. The brown solid line indicates the absorbance spectra of the neat gold nanoparticles prior to encapsulation.

A.7 Molar Mass Derived from Absorbance Spectra

A derivation of the molar mass from absorbance spectra is possible if the absorbance spectra are divided in their single components - scattering and absorption - since the gold nanoparticles encapsulated in $C_{15}S_{16.2}(10\%)$ and $C_{15}S_{14.6}(25\%)$ reveal a purely absorptive character. Knowing the spectral component which is solely based on gold core absorption, the extinction cross-section and the radius of the gold cores analyzed by TEM can be used to calculate the number concentration of gold nanoparticles. If it can be assumed that one gold core is encapsulated per CS particle, the number concentration of gold nanoparticles provides the number concentration of CS particles. This quantity in combination with the known weight concentration of the measured dispersions (0.03 wt%) allows to determine the molar mass of the respective CS particles. The procedure is shown in Figure A.7 step-by-step. A short guidance explaining each step is described in the following using the $C_{15}S_{14.6}(25\%)$ particles as representatives:

- i) First of all, the spectra of the CS particles and the respective gold nanoparticle cores prior to encapsulation are normalized to the absorbance at the plasmon resonance. (Figure A.7 A)
- ii) As described in the main manuscript, the absorbance spectrum of the CS particles is a superposition of RDG scattering of the CS particles and absorption stemming

from the gold cores. As a result, the RDG scattering can be derived by subtracting the pure gold nanocrystal core spectrum, that is scaled by a factor f , from the CS spectrum. The RDG scattering is given by the following power law:

$$Abs. = H_{RDG} \cdot \lambda^{-j} \quad (\text{A.1})$$

In this power law $Abs.$ indicates the absorbance at a certain wavelength, H_{RDG} represents the scattering amplitude, λ the wavelength and j is an exponent. A double-logarithmic representation in which $\log(Abs.)$ is plotted versus $\log(\lambda)$ thus leads to a linear relationship. For the described subtraction linearization of the data is used. As the resulting spectrum gives mostly RDG scattering, the linear regression curve used to fit the data gives the parameters H_{RDG} and j of the power law. The obtained spectrum and the fit are shown in Figure A.7 B. The respective parameters used for the fit are listed in Table A.5. The scaling factor f was chosen to obtain minimal residuals between calculated spectrum and fit.

- iii) Figure A.7 C depicts the spectrum of the CS particles as well as the calculated scattering (solid blue line) and absorption contribution (dashed brown line). The latter one is calculated by subtraction of the calculated scattering contribution from the spectrum of the CS particles.
- iv) The spectrum that indicates the gold core contribution (dashed brown line) is normalized to its absorbance at the plasmon resonance. Comparing this spectrum to the normalized spectrum of the gold nanoparticle cores prior to encapsulation a good match is obtained (Figure A.7 D). The resonance peak shape and the width agree well, only slight deviations in the maximum of the plasmon resonance are observed. These deviations are related to the different refractive index of the surrounding medium of the gold nanoparticles in both spectra.^[57] In case of the experimentally measured spectrum water surrounds the gold cores. In contrast, water swollen PNI-PAM shells are in vicinity of the gold cores in case of the calculated contribution.
- v) Using the calculated spectrum of the gold nanoparticles the number concentration c_{cores} of the gold nanoparticles can be calculated. First, the Beer-Lambert law is used to calculate $c_{Au(0)}$. For this purpose, the calculated absorbance at 400 nm, the extinction coefficient of colloidal gold from literature^[179] and a pathlength of 1 cm are inserted in eq. 5.4. $c_{Au(0)}$ allows access to the number concentration c_{cores} of the gold nanoparticles using:

$$c_{cores} = \frac{c_{Au(0)} \cdot M_{Au}}{\frac{4}{3}\pi R^3 \cdot \rho_{Au}} \quad (\text{A.2})$$

In this equation M_{Au} (196.97 g/mol) denotes the molar mass of gold, R is the radius of the gold nanoparticles determined by TEM image analysis and ρ_{Au} (19300 g/L) is the density of gold.

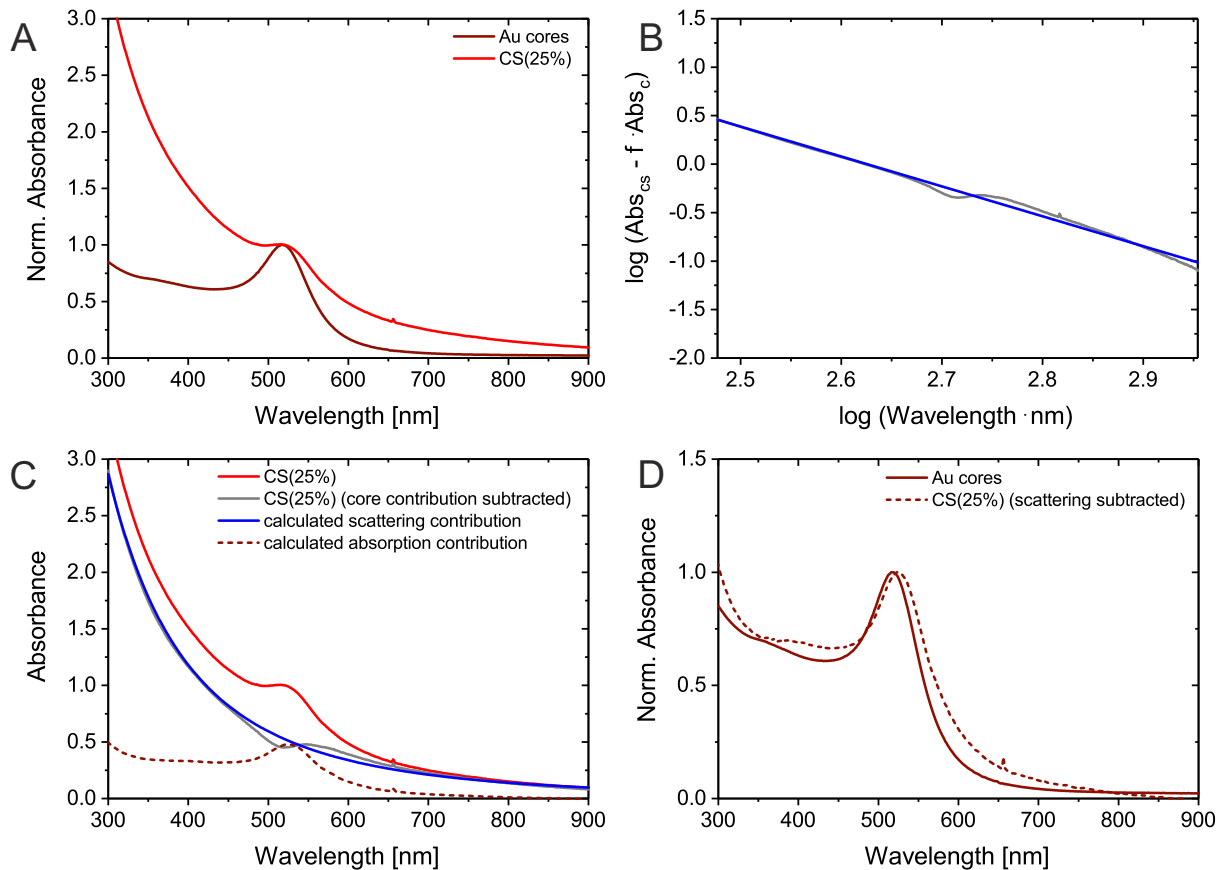


Figure A.7: A. Absorbance spectra of the neat gold nanoparticles prior to encapsulation and of the CS(25%) particles (0.03 wt%) measured at room temperature. Both spectra were normalized to the absorbance at the plasmon resonance. B. Resulting spectrum (gray solid line) after subtraction of the gold nanoparticle contribution from the spectrum of CS(25%) presented in a double-logarithmic plot. The blue solid line is a linear fit to the data. C. Representation of the single contributions of the absorbance spectrum of CS(25%) particles (solid red line): (1) the scattering contribution determined by subtraction of experimentally obtained data in linear representation (CS(25%) minus the core contribution represented by a solid gray line) and its respective fit (solid blue line), i.e., the scattering contribution calculated using the power law. (2) the calculated absorption contribution (dashed brown line) obtained by subtracting the calculated scattering contribution from the spectrum of the CS(25%) particles. D. The calculated absorption contribution (dashed brown line) as compared to the spectrum of the gold nanoparticles prior to encapsulation (solid brown line). Both spectra are normalized to the absorbance at the plasmon resonance.

- vi) Assuming that each CS particle encapsulates one gold particle, c_{cores} of the gold nanoparticles corresponds to the particle concentration of the CS particles. Next, c_{cores} and the weight concentration of the investigated dispersion, which was corrected by a residual water content from TGA, allow access the molar mass M .

The molar masses of the CS particles calculated according to this method are listed in Table A.5. The results are in good accordance with molar masses of similar Au-PNIPAM particles.^[55,154] The molar masses of the respective C_dS particles are also listed in Table A.5. These values were calculated by subtraction of the molar mass of the gold nanoparticle cores from the molar mass of the respective CS particles.

Table A.5: Scattering amplitude H_{RDG} and exponent j of the power law describing the RDG scattering for C₁₅S_{16.2}(10%) and C₁₅S_{14.6}(25%) as well as the molecular weight M for these two CS systems and their pitted analogues.

Particle system	H_{RDG}	j	M [g/mol]
C ₁₅ S _{16.2} (10%)	$5.4 \cdot 10^8$	-3.4	$1.59 \cdot 10^8$
C _d S _{16.2} (10%)	-	-	$1.37 \cdot 10^8$
C ₁₅ S _{14.6} (25%)	$1.2 \cdot 10^8$	-3.1	$2.06 \cdot 10^8$
C _d S _{14.6} (25%)	-	-	$1.86 \cdot 10^8$

A.8 Residual Water Contents of Core-Shell Particles

Figure A.8 shows data of the thermogravimetric analysis (TGA) of freeze-dried material of $C_{15}S_{16.2}$ (10%) (A), $C_{15}S_{14.6}$ (25%) (B) and $C_{351}S_{2.9}$ (5%) (C) particles. The relative mass is depicted as a function of temperature. The first decline in the relative mass between 30 and 225°C can be assigned to the evaporation of residual water. A magnification of the data in this range and a corresponding sigmoidal fit which was used for analysis of the water content is shown in the inset diagrams. The $C_{15}S_{16.2}$ (10%) particles reveal a residual water content δ_{TGA} of 5.7%, the $C_{15}S_{14.6}$ (25%) include 5.3% and the $C_{351}S_{2.9}$ particles 4% of residual water. Further, a second drop between 225 and 550°C in relative mass is observed for the particles which is related to the thermal degradation of the polymer. At temperatures larger than 550°C the relative mass achieves constant values of 10% for $C_{15}S_{16.2}$ (10%), 14% for $C_{15}S_{14.6}$ (25%) and 42% for $C_{351}S_{2.9}$ (5%) particles. These values can be attributed to the gold or silica cores, respectively.

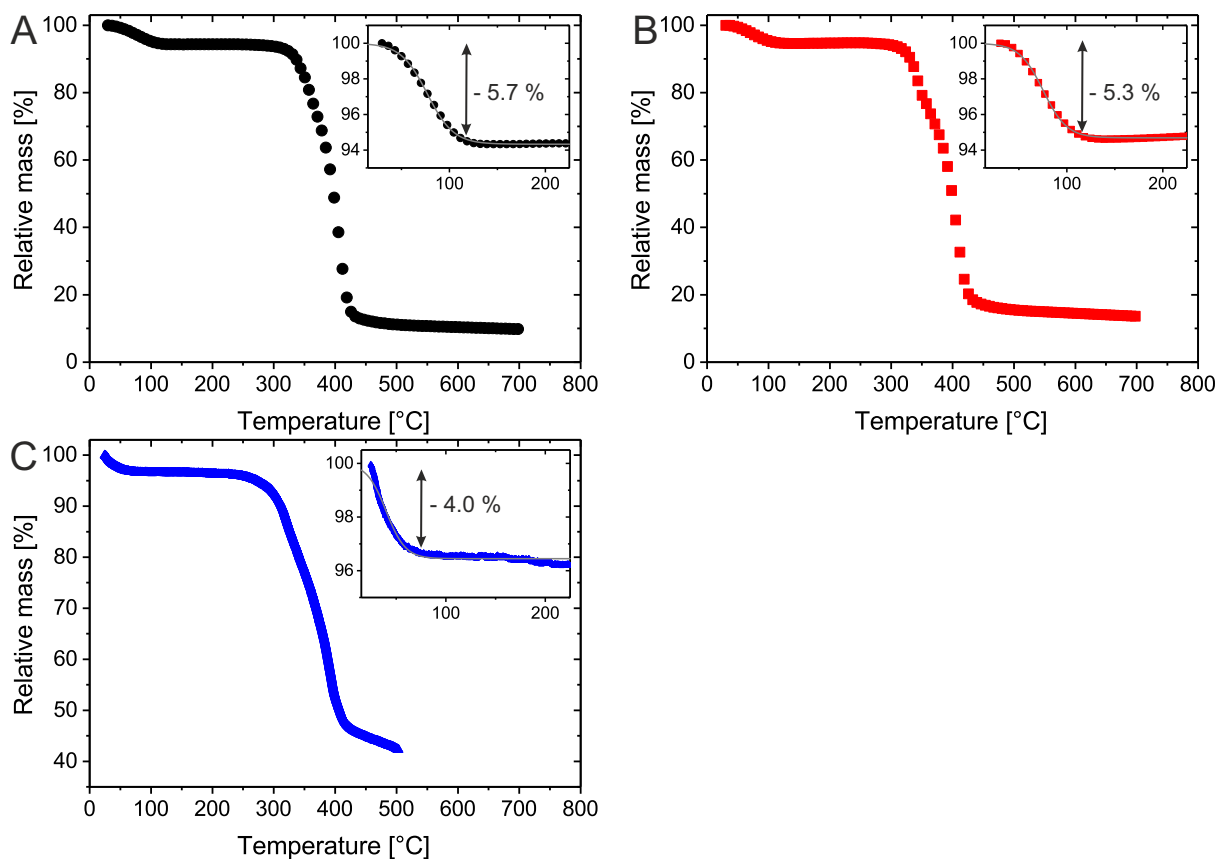


Figure A.8: Relative mass as function of the temperature measured using TGA. Freeze-dried material of CS particles was investigated: A. $C_{15}S_{16.2}$ (10%), B. $C_{15}S_{14.6}$ (25%), C. $C_{351}S_{2.9}$ (5%). The inset diagrams depict a magnification of the data between 15 and 225°C. The data in this temperature range was used to calculate the residual water content δ_{TGA} of the samples. A sigmoidal fit to the data is indicated by a gray solid line.

A.9 Refractive Index of Au-PNIPAM Particles

Figure A.9 represents the measured refractive indices from dispersions at different weight concentrations c of $C_{15}S_{16.2}$ (10%) and $C_{15}S_{14.6}$ (25%) Au-PNIPAM particles. The weight concentrations plotted here were corrected accounting for their residual water content δ_{TGA} which was determined by TGA. The data could be fitted using a linear regression curve. Extrapolation of the regression curves to a weight concentration of 100 wt% provided an average refractive index of 1.53 for both particle types. The measurements were performed at a wavelength of 633.2 nm. As absorption of the gold nanoparticles at this wavelength is nearly absent (see, e.g., Figure A.6), the derived refractive indices can be assigned to the cross-linked PNIPAM.

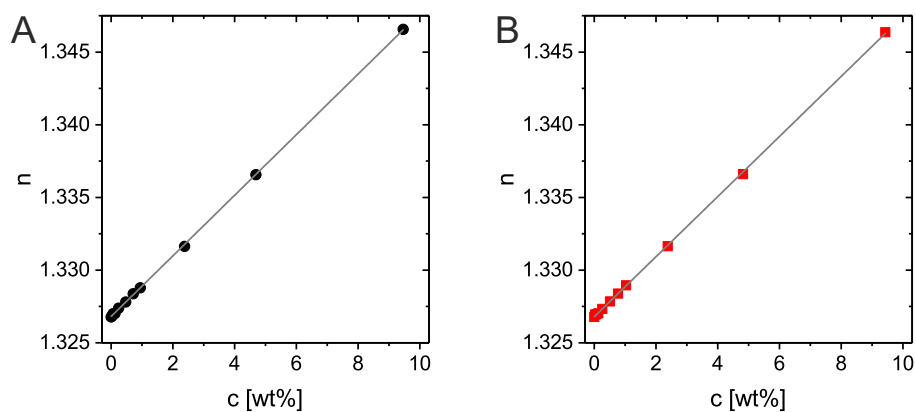


Figure A.9: Refractive index as a function of the concentration of dispersions in D_2O : A. $C_{15}S_{16.2}$ (10%), B. $C_{15}S_{14.6}$ (25%). The solid gray lines are linear fits to the data.

A.10 SANS Data of Crystalline Samples

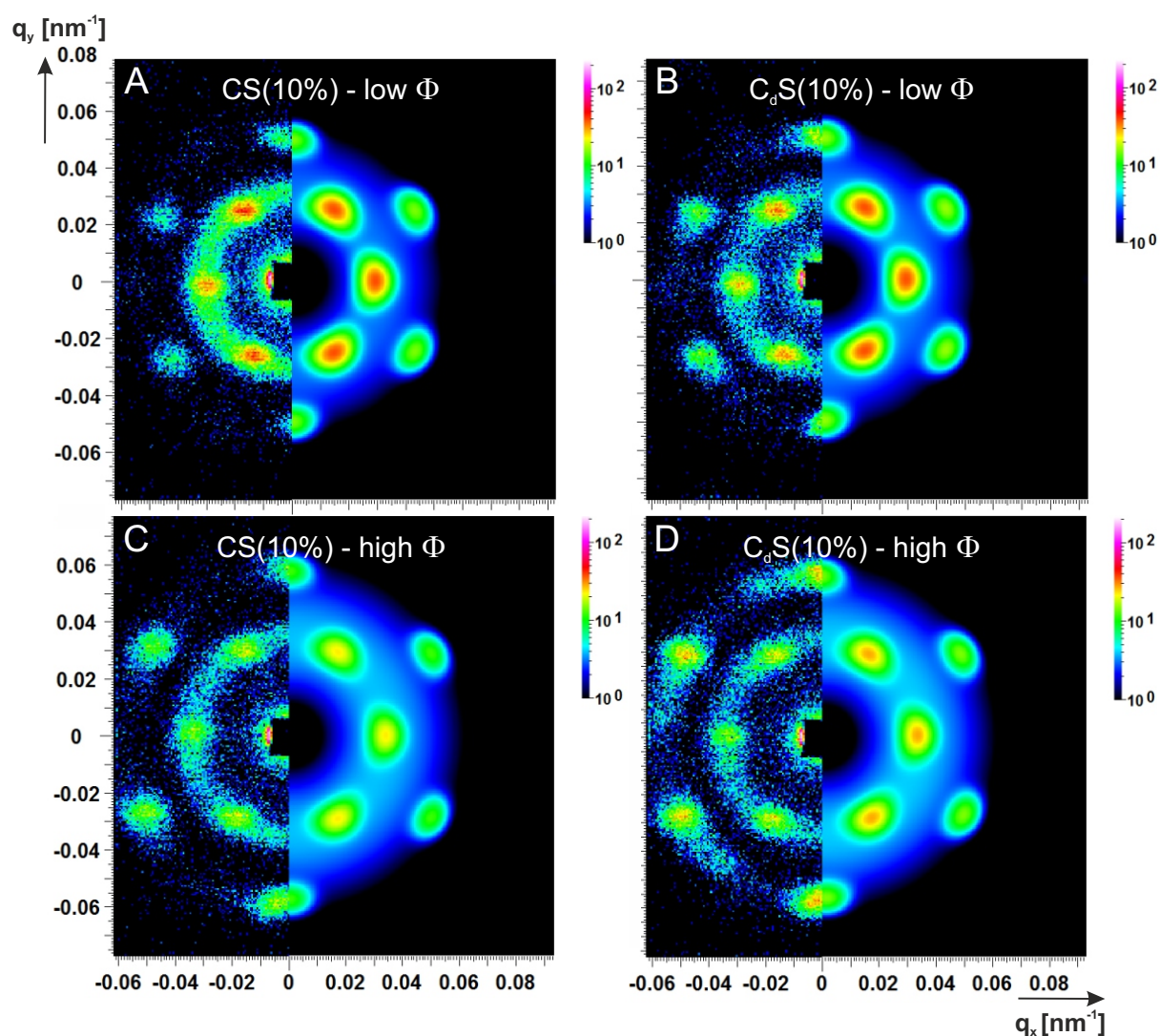


Figure A.10: Experimentally obtained 2D SANS patterns (left half) and calculated SANS patterns (right half) in the radial beam direction [111] of the samples CS(10%) and CdS(10%) at low (A, B) and high (C, D) volume fraction measured at a SD distance of 39 m. Adapted with permission from "Role of Absorbing Nanocrystal Cores in Soft Photonic Crystals: A Spectroscopy and SANS Study.", by Rauh, A.; Carl, N.; Schweins, R.; Karg, M. *Langmuir* **2017**, DOI: 10.1021/acs.langmuir.7b01595. Copyright 2017 by American Chemical Society.

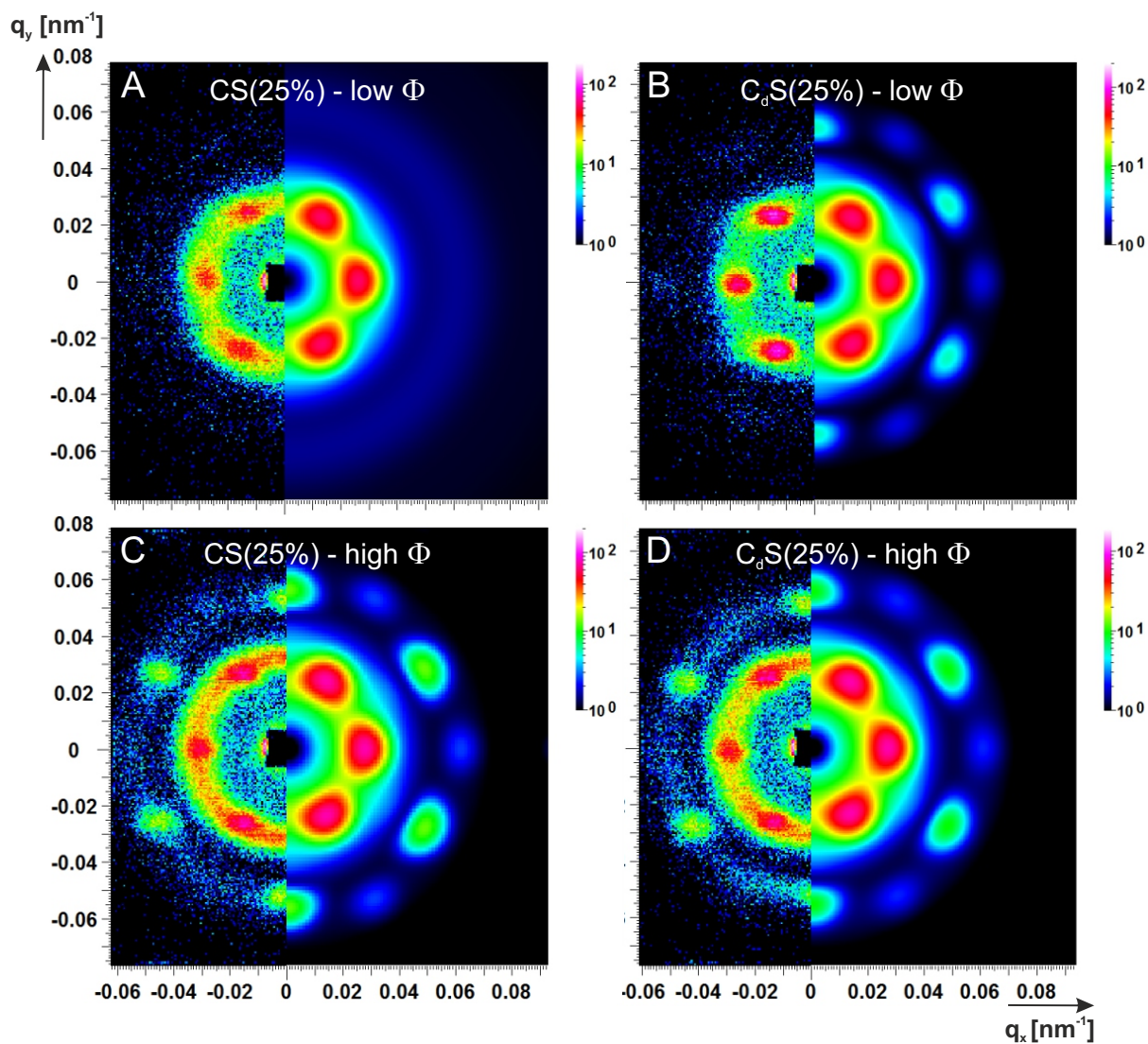


Figure A.11: Experimentally obtained 2D SANS patterns (left half) and calculated SANS patterns (right half) in the radial beam direction [111] of the samples CS(25%) and C_dS (25%) at low (A, B) and high (C, D) volume fraction measured at a SD distance of 39 m. Adapted with permission from "Role of Absorbing Nanocrystal Cores in Soft Photonic Crystals: A Spectroscopy and SANS Study.", by Rauh, A.; Carl, N.; Schweins, R.; Karg, M. *Langmuir* **2017**, DOI: 10.1021/acs.langmuir.7b01595. Copyright 2017 by American Chemical Society.

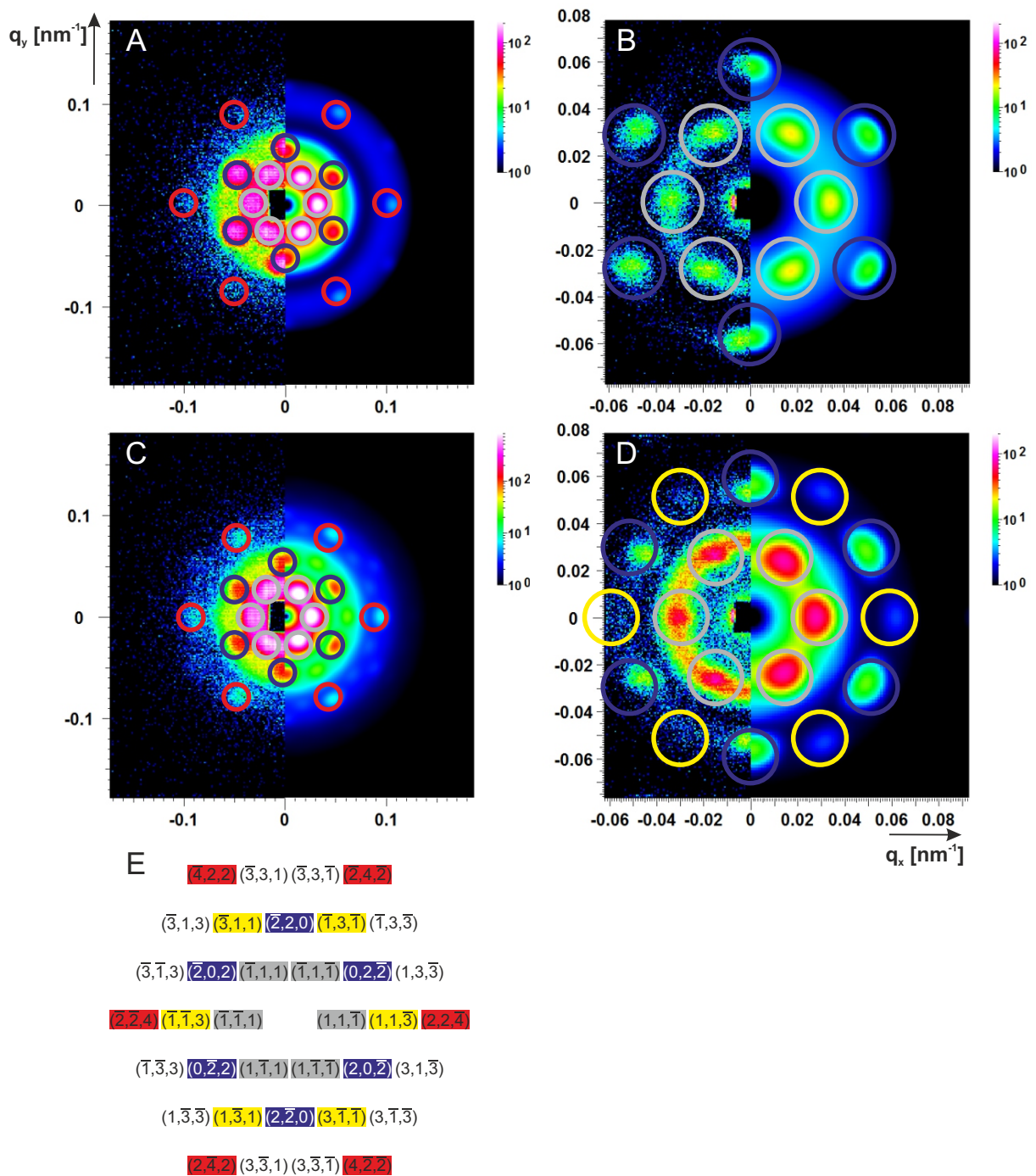


Figure A.12: Indexing of the 2D SANS patterns. A and B illustrate the data of CS(10%) ($\phi_{UV-vis} = 1.04$) and C as well as D of CS(25%) ($\phi_{UV-vis} = 0.56$). In the scattering patterns, the left half corresponds to the experimentally obtained data and the right half to the respective simulation. A and C were recorded at a SD distance of 28 m and B as well as D at 39 m. In E the Miller indices of all theoretically available primary and secondary Bragg reflections of a FCC lattice are shown. The color code in this scheme is the same as for the circles that were used to depict the indexing procedure of the Bragg reflections in A to D. Perfect hexagons were used to arrange the circles.

Table A.6: Results from the simulation of the experimentally obtained 2D SANS patterns at a SD distance of 39 m for the crystalline samples at different volume fractions: Lattice constant a , the longitudinal (D_l) and azimuthal (D_Ψ) domain size, the overall radius (R_{total}), the radius of the core R_{hom} , $\alpha_{Scatter}$ indicating the algebraic density decay in the shell, the contrast ratio of the core and corona at the core-corona interface $\eta_{core-corona}$ as well as the displacement $s_{Scatter}$ from the ideal lattice points.

ϕ	Sample	ϕ_{UV-vis}	a [nm]	D_l [nm]	D_Ψ [nm]	R_{total} [nm]	R_{hom} [nm]	$\alpha_{Scatter}$	$\eta_{core-corona}$	$s_{Scatter}$ [nm]
low	CS(10%)	0.70 ± 0.02	335	700	550	95	30	1.2	0.95	5
	$C_dS(10\%)$	0.72 ± 0.02	335	700	550	95	30	1.25	0.95	5
	CS(25%)	0.43 ± 0.01	340	500	550	99	-	-	-	25
	$C_dS(25\%)$	0.49 ± 0.02	340	500	550	100	-	-	-	25
high	CS(10%)	1.04 ± 0.03	290	700	450	85	30	1.25	0.95	5
	$C_dS(10\%)$	1.02 ± 0.03	295	700	450	85	30	1.2	0.95	5
	CS(25%)	0.56 ± 0.02	320	500	450	99	-	-	-	20
	$C_dS(25\%)$	0.59 ± 0.02	325	500	450	100	-	-	-	20

A.11 Analysis of the Microradian SAXS Measurements

Table A.7: Results from analysis of the scattering profiles in Figure 5.26 measured at different rotational angles ω : Miller indices hkl and q -position q_{max} of the diffraction peak, lattice plane distance d_{hkl} , lattice constant a , inter-particle distance d_{cc} and volume fraction ϕ_{SAXS} .

ω	hkl	q_{max} [nm ⁻¹]	d_{hkl} [nm]	a [nm]	d_{cc} [nm]	ϕ_{SAXS}
0°	2-20	0.02176	288.7	816.7	577.5	0.40
0°	4-40	0.04367	287.8	813.9	575.5	0.41
-55°	200	0.01512	415.6	831.1	587.7	0.39
-55°	400	0.03084	203.7	814.9	576.2	0.41
-55°	600	0.04550	138.1	828.6	585.9	0.39
-55°	2-20	0.02184	287.7	813.7	575.4	0.41
-55°	4-40	0.04365	143.9	814.3	575.8	0.41
+35°	1-1-1	0.01332	471.7	817.0	577.7	0.40
+35°	2-2-2	0.02633	238.6	826.6	584.5	0.39
+35°	3-3-3	0.03966	158.4	823.2	582.1	0.39
+35°	-113	0.02295	251.8	835.2	590.6	0.38
+35°	2-20	0.02178	288.5	816.0	577.0	0.41
+35°	4-40	0.04357	144.2	815.8	576.8	0.41

A.12 Radial Distribution Functions of Superstructures from $C_{71}S_{6.6}$ (15%) Particles

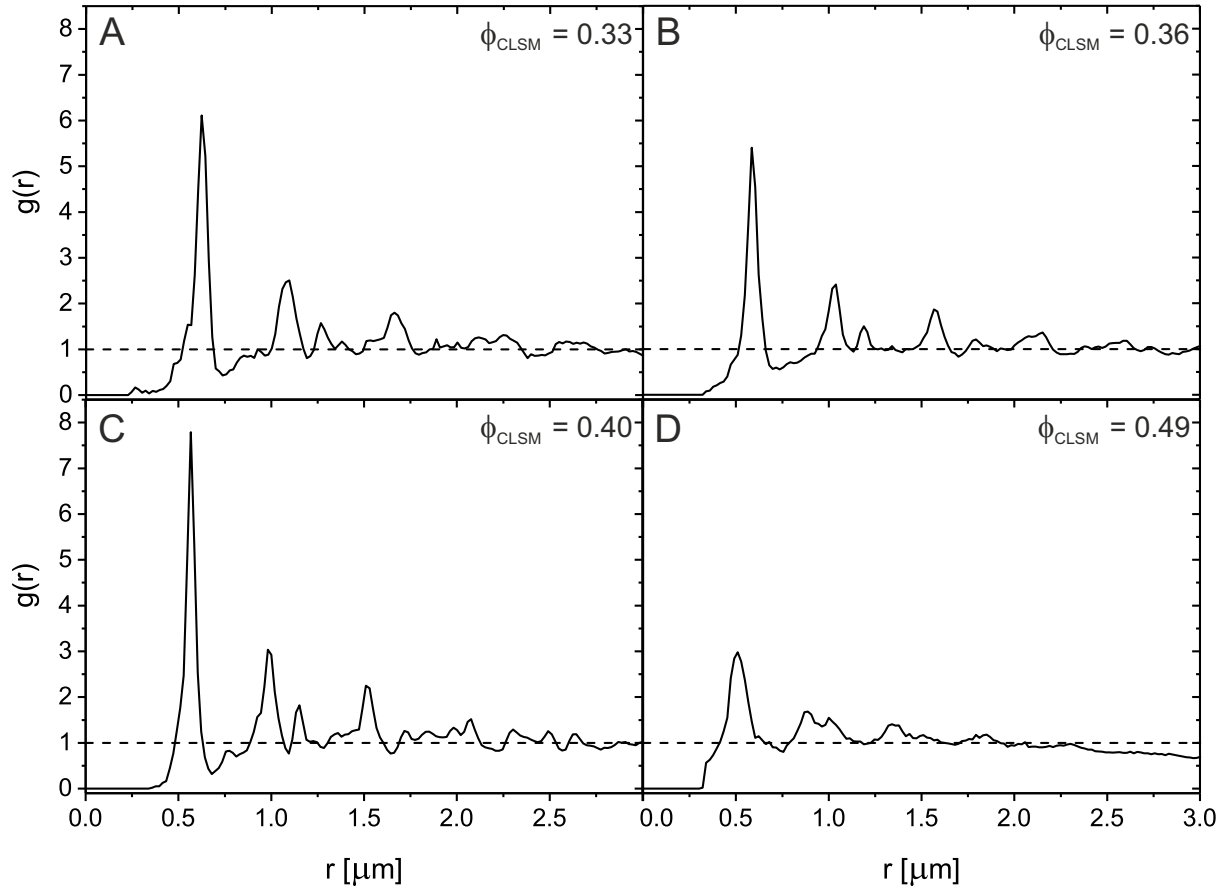


Figure A.13: 3D average radial distribution functions calculated from image sequences describing a volume element in the samples consisting of $C_{71}S_{6.6}$ (15%) particles at different volume fractions ϕ_{CLSM} : A. $\phi_{CLSM}=0.33$, B. $\phi_{CLSM}=0.36$, C. $\phi_{CLSM}=0.40$, D. $\phi_{CLSM}=0.49$.

A.13 Volume Fraction of Dispersions of $C_{351}S_{2.9}$ Particles

The respective dispersions were prepared by redispersion of freeze-dried material in water. As the present study was performed at 20°C the hydrodynamic radius at this temperature was used to calculate the particle volume (see Figure 7.2). The volume fraction ϕ^* is defined as follows:

$$\phi^* = \frac{\left(\frac{4 \cdot \pi}{3} \cdot R_{h,20^\circ\text{C}}^3\right) \cdot N}{\left(\frac{4 \cdot \pi}{3} \cdot R_{h,20^\circ\text{C}}^3\right) \cdot N + V_{H_2O}} \quad (\text{A.3})$$

Here, N is the number of CS particles in the dispersion and V_{H_2O} the total volume of water in the dispersion. N is determined by:

$$N = \frac{m_{particles}(1 - \delta_{TGA})}{m_{CS-particle}} \quad (\text{A.4})$$

In eq. A.4 $m_{particles}$ is the mass of the freeze-dried CS particles and δ_{TGA} is the residual water content (4%) of the freeze-dried CS particles which was determined using TGA (see Figure A.8 C). $m_{CS-particle}$ is the mass of a single CS particle.

The mass of a single CS particle can be estimated using the sum of the mass of the core m_{core} and the mass of the shell m_{shell} .

$$m_{CS-particle} = m_{core} + m_{shell} \quad (\text{A.5})$$

m_{core} and m_{shell} are calculated as follows:

$$m_{core} = \rho_{core} \cdot \left(\frac{4 \cdot \pi}{3} \cdot R_{core}^3\right) \quad (\text{A.6})$$

$$m_{shell} = m_{core} \cdot \kappa \quad (\text{A.7})$$

Here, ρ_{core} is the density of the silica core (1.8 g cm⁻³),^[166] R_{core} is the radius of the silica core and κ is the mass of the PNIPAM shell per unit mass of the core. κ is determined from the results of the TGA (Figure A.8 C) as follows: $\kappa = (m\%_{100^\circ\text{C}} - m\%_{503^\circ\text{C}})/m\%_{503^\circ\text{C}}$. For the used particles the value of κ was 1.285.

In addition, the total volume of water V_{H_2O} is required to calculate ϕ^* :

$$V_{H_2O} = \frac{m_{H_2O} + m_{particles} \cdot \delta_{TGA}}{\rho_{H_2O}} \quad (\text{A.8})$$

Here, m_{H_2O} is the mass of added water in order to prepare the dispersion. ρ_{H_2O} gives the density of water which is 1 g cm⁻³ at ambient temperature.

Table A.8: Mass of CS particles $m_{particles}$ which was dispersed in a respective mass of water m_{H_2O} to prepare the dispersions of different volume fractions. The volume fraction ϕ^* calculated using eq. A.3 and the volume fraction $\phi_{HS,eff}$ determined using hard sphere mapping as shown in Section A.14 are summarized.

$m_{particles}$ [mg]	m_{H_2O} [mg]	ϕ^*	$\phi_{eff,HS}$
3.3	907.0	0.02	0.02
4.7	200.0	0.09	0.06
9.0	199.7	0.16	0.27
13.6	199.7	0.22	0.35
19.2	199.2	0.28	0.47

In Table A.8 the volume fraction ϕ^* calculated according to equation A.3 as well as the effective hard sphere volume fraction $\phi_{eff,HS}$ which could be determined from experimental data using hard sphere mapping (Section A.14) are summarized.

A.14 Hard Sphere Mapping

In this section the hard sphere mapping for the determination of the effective hard sphere volume fraction $\phi_{HS,eff}$ is explained step-by-step:

- i) First, the q -position q_{max} of the first maximum of $S(q)$ of the dispersions at different volume fractions is extracted. $S(q)$ is defined by eq. 7.2. As $\phi_{eff,HS}$ is not yet available, $S(q)$ cannot be calculated. However, the ratio $A(q)/A(q)_{dilute}$ can be determined from the experimental data as shown in Figure 7.14 B. This ratio gives the structure factor qualitatively and most importantly, q_{max} coincides with the values of q_{max} in $S(q)$. The values of q_{max} which were experimentally determined are shown as horizontal, solid gray lines with a slope of zero in Figure A.14.
- ii) Second, the Percus-Yevick prediction is used to calculate theoretical evolutions of $S(q)$ for a large number of hard sphere radii and volume fractions ranging from 0.001 to 0.494 in intervals of 0.001. One should note that 0.494 is already the upper limit of suitable volume fractions as it represents the volume fraction at which the hard spheres start to freeze.^[103] The equations used for these calculations are summarized in the Section A.15. The q -position of the first maximum in these calculated $S(q)$ functions, which is termed as $q_{max,PY}$ in the following, is extracted. Finally, several evolutions of q_{max} with ϕ as the ones shown in red, black and blue in Figure A.14 are obtained.

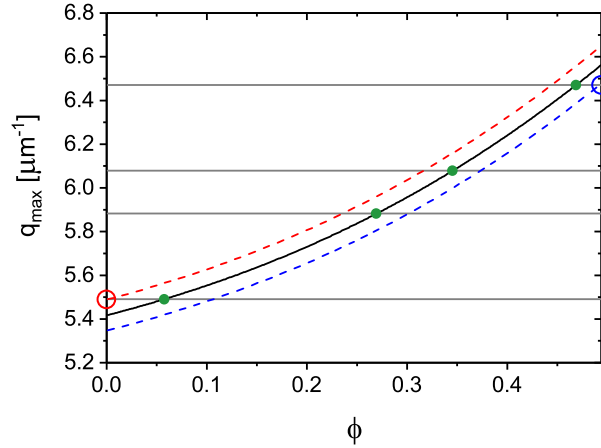


Figure A.14: Determination of the effective hard sphere radius using hard sphere mapping. The solid gray lines correspond to the experimentally determined values of q_{max} . These values were mapped by theoretical values $q_{max,PY}$ calculated using the Percus-Yevick prediction. The blue and red dashed line represent the lower and upper limit of radii/volume fractions used for the calculation of the PY hard sphere behavior for which all experimentally determined q_{max} show an intersection point with the theoretical prediction. The intersection points highlighting the lower and upper limit are labeled with blue and red circles, respectively. As the solid black line corresponds to the average value between the lower and upper boundary, it was used to determine the hard sphere radius and the volume fractions indicated by filled, green circles.

- iii) Next, it is focused on the evolutions of q_{max} versus ϕ in Figure A.14. The dashed lines represent the evolutions of q_{max} versus ϕ which just intersect all experimentally obtained values of q_{max} (gray lines). These intersection points define the lower and upper limit of possible radii/volume fractions. The lower limit is defined by the intersection (blue circle) of the dashed blue line and the solid gray line at $q_{max} = 6.5 \mu\text{m}^{-1}$. The upper limit is given by the intersection (red circle) of the dashed red line and the solid gray line at $q_{max} = 5.5 \mu\text{m}^{-1}$. Finally, this procedure provides the range of possible hard sphere volume fractions and radii that are included in the area between the two dashed lines in Figure A.14.
- iv) As the mentioned area is very narrow, the average value in this range can be used as effective hard sphere radius which is $532.5 \pm 7.5 \text{ nm}$. Using this radius the intersection points (filled green circles) with the experimental data can be used as volume fractions (see Table A.8). Further, this radius is in accordance with the hydrodynamic radius of 514 nm measured at 20°C . The black solid line shows the theoretical data obtained from the Percus-Yevick prediction calculated using this radius.

A.15 Static Structure Factor in Bulk Using the Percus-Yevick Approximation

In the following, the used equations for the calculation of the effective hard sphere structure factor according to the Percus-Yevick approximation are outlined.^[212] The structure factors $S(q)$ were derived using this expression:

$$S(q) = \frac{1}{\nu_1^2 + \nu_2^2} \quad (\text{A.9})$$

Here, ν_1 and ν_2 are defined as follows:

$$\nu_1 = 1 - [12\phi(af_1 + bf_2)] \quad (\text{A.10})$$

$$\nu_2 = -12\phi(af_3 + bf_4) \quad (\text{A.11})$$

The variables a , b as well as f_1 , f_2 , f_3 and f_4 are given by eq. A.12 to A.17. Here, σ is the particle diameter given by $2R$, ϕ is the effective hard sphere volume fraction and y is a rescaled version of the wave vector q defined by $q\sigma$.

$$a = \frac{1 + 2\phi}{(1 - \phi)^2} \quad (\text{A.12})$$

$$b = \frac{1 + 0.5\phi}{(1 - \phi)^2} \quad (\text{A.13})$$

$$f_1 = \frac{y - \sin(y)}{y^3} \quad (\text{A.14})$$

$$f_2 = \frac{\cos(y) - 1}{y^2} \quad (\text{A.15})$$

$$f_3 = \frac{f_2}{y} + \frac{1}{2y} \quad (\text{A.16})$$

$$f_4 = -yf_1 \quad (\text{A.17})$$

A.16 Static Structure Factor at the Interface

To allow a reasonable comparison of the data collected in bulk and at the interface the structure factor of the $C_{351}S_{2.9}$ particles at the interface was determined. Therefore, the respective radial distribution functions $g(r)$ are calculated for different number densities. 2D SEM images recorded at different positions along the compression curve were analyzed using a custom written MATLAB[®] procedure. This procedure considered edge effects by neglecting particles at the edges of the images. Extracts of the corresponding images are shown in Figure A.15. The $g(r)$ functions which were calculated from these images are illustrated in Figure A.16. Below number densities of 0.66 the first maximum of the $g(r)$ function is found at a position of $1.4 \mu\text{m}$. This value corresponds to the inter-particle distance at which extended shells are in contact (shell-shell contacts). Increasing the number density above 0.66 causes the appearance of a second peak at $0.7 \mu\text{m}$. This peak corresponds to the inter-particle distance when the CS particles are in their collapsed state (core-core contacts).

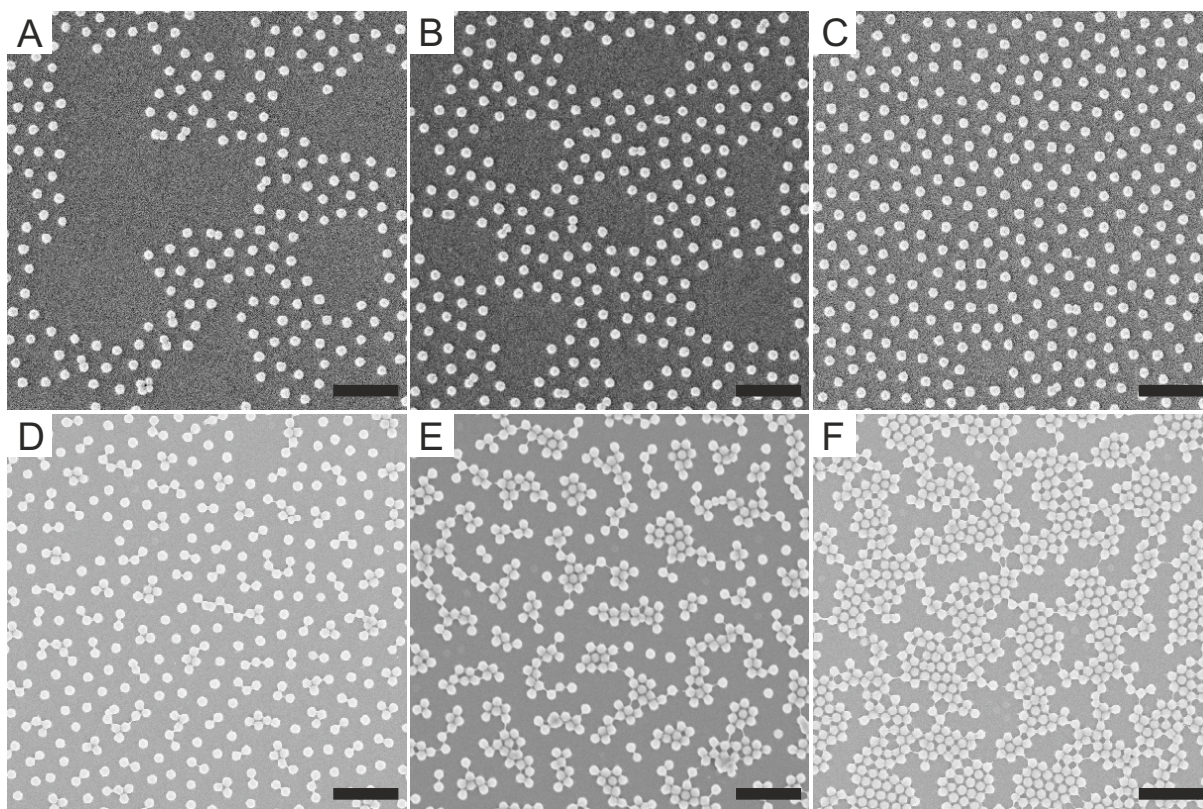


Figure A.15: Representative SEM images of the $C_{351}S_{2.9}$ particles. The images were used for the calculation of the radial distribution functions shown in Figure A.16. The surface pressure Π increases from A to F: A. 0.932 mN/m , B. 1.198 mN/m , C. 1.731 mN/m , D. 7.846 mN/m , E. 17.332 mN/m , F. 22.066 mN/m . The scale bar in these images is $4 \mu\text{m}$.

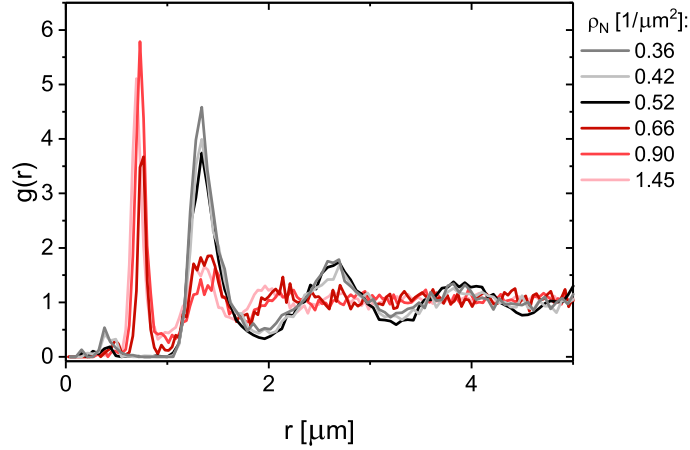


Figure A.16: Radial distribution functions $g(r)$ corresponding to the SEM images depicted in Figure A.15.

The $g(r)$ functions are now used to derive the structure factor $S(q)$ of an isotropic system at different number densities using the following relationship:

$$S(q) = 1 + \rho_N \int e^{-i\vec{q}\vec{r}} [g(r) - 1] d\vec{r} \quad (\text{A.18})$$

The radial distribution function is calculated from an effective 2D system as shown above. Hence, instead of volume integrals area integrals and 2D Fourier transforms are performed. The discrete form of the solution for a $g(r)$ with N data points and for a radial distance $r \leq R$ that is provided in the reference^[213] was used.

$$S(q_i) = 1 + 2\pi\rho_N \sum_{j=1}^N r_j [g(r_j) - 1] J_0(q_i r_j) dr_j \quad (\text{A.19})$$

Here, $J_0(qr)$ is the zeroth-order Bessel function, r_j is given by the quotient $\mu_i R / \mu_N$ with μ_i denoting the roots of the Bessel function and q_i defined by the quotient of μ_i / R . The number density ρ_N for the 2D case is given by the number of particles (N_p) in an image per area (A_{image}) of the image.

References

- [1] Poon, W. C.; Pusey, P. N.; Lekkerkerker, H. N. Colloids in Suspense. *Phys. World* **1996**, *9*, 27–32.
- [2] Pusey, P. N.; Poon, W. C. K.; Ilett, S. M.; Bartlett, P. Phase Behaviour and Structure of Colloidal Suspensions. *J. Phys.: Condens. Matter* **1994**, *6*, A29–A36.
- [3] Xia, Y.; Gates, B.; Yin, Y.; Lu, Y. Monodispersed Colloidal Spheres: Old Materials with New Applications. *Adv. Mater.* **2000**, *12*, 693–713.
- [4] Poon, W. C. Colloids as Big Atoms. *Science* **2004**, *304*, 830–831.
- [5] Poon, W. C. Colloidal Suspensions. *Clarendon Press Oxford* **2012**, 1–52.
- [6] Yunker, P. J.; Chen, K.; Gratale, M. D.; Lohr, M. A.; Still, T.; Yodh, A. G. Physics in Ordered and Disordered Colloidal Matter Composed of Poly(N-isopropylacrylamide) Microgel Particles. *Rep. Prog. Phys.* **2014**, *77*, 056601.
- [7] Li, F.; Josephson, D. P.; Stein, A. Colloidal Assembly: The Road from Particles to Colloidal Molecules and Crystals. *Angew. Chem. Int. Ed.* **2011**, *50*, 360–388.
- [8] Boles, M. A.; Engel, M.; Talapin, D. V. Self-Assembly of Colloidal Nanocrystals: From Intricate Structures to Functional Materials. *Chem. Rev.* **2016**, *116*, 11220–11289.
- [9] Isa, L.; Buttinoni, I.; Fernandez-Rodriguez, M. A.; Vasudevan, S. A. Two-Dimensional Assemblies of Soft Repulsive Colloids Confined at Fluid Interfaces. *EPL* **2017**, *119*, 26001.
- [10] Pelton, R. H.; Chibante, P. Preparation of Aqueous Lattices with N-isopropylacrylamide. *Colloids Surf.* **1986**, *20*, 247–256.
- [11] Mohanty, P. S.; Paloli, D.; Crassous, J. J.; Zaccarelli, E.; Schurtenberger, P. Effective Interactions between Soft-Repulsive Colloids: Experiments, Theory, and Simulations. *J. Chem. Phys.* **2014**, *140*, 094901.
- [12] Paloli, D.; Mohanty, P. S.; Crassous, J. J.; Zaccarelli, E.; Schurtenberger, P. Fluid–Solid Transitions in Soft-Repulsive Colloids. *Soft Matter* **2013**, *9*, 3000–3004.
- [13] Mohanty, P. S.; Nöjd, S.; van Gruijthuijsen, K.; Crassous, J. J.; Obiols-Rabasa, M.; Schweins, R.; Stradner, A.; Schurtenberger, P. Interpenetration of Polymeric Microgels at Ultrahigh Densities. *Sci. Rep.* **2017**, *7*, 1487.

- [14] Stieger, M.; Richtering, W.; Pedersen, J. S.; Lindner, P. Small-Angle Neutron Scattering Study of Structural Changes in Temperature Sensitive Microgel Colloids. *J. Chem. Phys.* **2004**, *120*, 6197–6206.
- [15] Dotera, T.; Oshiro, T.; Zihler, P. Mosaic Two-Lengthscale Quasicrystals. *Nature* **2014**, *506*, 208–211.
- [16] Schoberth, H. G.; Emmerich, H.; Holzinger, M.; Dulle, M.; Förster, S.; Gruhn, T. Molecular Dynamics Study of Colloidal Quasicrystals. *Soft Matter* **2016**, *12*, 7644–7654.
- [17] Atwater, H. A.; Polman, A. Plasmonics for Improved Photovoltaic Devices. *Nat. Mater.* **2010**, *9*, 205–213.
- [18] Karg, M.; König, T. A. F.; Retsch, M.; Stelling, C.; Reichstein, P. M.; Honold, T.; Thelakkat, M.; Fery, A. Colloidal Self-Assembly Concepts for Light Management in Photovoltaics. *Mater. Today* **2015**, *18*, 185–205.
- [19] Noginov, M. A.; Zhu, G.; Belgrave, A. M.; Bakker, R.; Shalae, V. M.; Narimanov, E. E.; Stout, S.; Herz, E.; Suteewong, T.; Wiesner, U. Demonstration of a Spaser-Based Nanolaser. *Nature* **2009**, *460*, 1110–1113.
- [20] Zhou, W.; Dridi, M.; Suh, J. Y.; Kim, C. H.; Co, D. T.; Wasielewski, M.; Schatz, G. C.; Odom, T. W. Lasing Action in Strongly Coupled Plasmonic Nanocavity Arrays. *Nat. Nanotechnol.* **2013**, *8*, 506–511.
- [21] Willets, K. A.; Van Duyne, R. P. Localized Surface Plasmon Resonance Spectroscopy and Sensing. *Annu. Rev. Phys. Chem.* **2007**, *58*, 267–297.
- [22] Karg, M.; Hellweg, T. New “Smart” Poly(NIPAM) Microgels and Nanoparticle Microgel Hybrids: Properties and Advances in Characterisation. *Curr. Opin. Colloid Interface Sci.* **2009**, *14*, 438–450.
- [23] Karg, M. Functional Materials Design through Hydrogel Encapsulation of Inorganic Nanoparticles: Recent Developments and Challenges. *Macromol. Chem. Phys.* **2016**, *217*, 242–255.
- [24] Bresme, F.; Oettel, M. Nanoparticles at Fluid Interfaces. *J. Phys.: Condens. Matter* **2007**, *19*, 413101.
- [25] Garbin, V.; Crocker, J. C.; Stebe, K. J. Nanoparticles at Fluid Interfaces: Exploiting Capping Ligands to Control Adsorption, Stability and Dynamics. *J. Colloid Interface Sci.* **2012**, *387*, 1–11.
- [26] McGorty, R.; Fung, J.; Kaz, D.; Manoharan, V. N. Colloidal Self-Assembly at an Interface. *Mater. Today* **2010**, *13*, 34–42.
- [27] Kralchevsky, P. A.; Nagayama, K. Capillary Interactions between Particles Bound to Interfaces, Liquid Films and Biomembranes. *Adv. Colloid Interface Sci.* **2000**, *85*, 145–192.

-
- [28] Williams, D. F.; Berg, J. C. The Aggregation of Colloidal Particles at the Air-Water Interface. *J. Colloid Interface Sci.* **1992**, *152*, 218–229.
- [29] Hurd, A. J. The Electrostatic Interaction between Interfacial Colloidal Particles. *J. Phys. A: Math. Gen.* **1985**, *18*, L1055–L1060.
- [30] Ge, J.; Yin, Y. Responsive Photonic Crystals. *Angew. Chem. Int. Ed.* **2011**, *50*, 1492–1522.
- [31] López, C.; Blanco, A.; Míguez, H.; Meseguer, F. Photonic Crystals for Laser Action. *Opt. Mater.* **1999**, *13*, 187–192.
- [32] Furumi, S. Recent Advances in Polymer Colloidal Crystal Lasers. *Nanoscale* **2012**, *4*, 5564–5571.
- [33] Shkunov, M. N.; Vardeny, Z. V.; DeLong, M. C.; Polson, R. C.; Zakhidov, A. A.; Baughman, R. H. Tunable, Gap-State Lasing in Switchable Directions for Opal Photonic Crystals. *Adv. Funct. Mater.* **2002**, *12*, 21–26.
- [34] Barrow, S. J.; Wei, X.; Baldauf, J. S.; Funston, A. M.; Mulvaney, P. The Surface Plasmon Modes of Self-Assembled Gold Nanocrystals. *Nat. Commun.* **2012**, *3*, 1275.
- [35] Ye, X.; Chen, J.; Diroll, B. T.; Murray, C. B. Tunable Plasmonic Coupling in Self-Assembled Binary Nanocrystal Superlattices Studied by Correlated Optical Microspectrophotometry and Electron Microscopy. *Nano Lett.* **2013**, *13*, 1291–1297.
- [36] Ross, M. B.; Ku, J. C.; Vaccarezza, V. M.; Schatz, G. C.; Mirkin, C. A. Nanoscale Form Dictates Mesoscale Function in Plasmonic DNA-Nanoparticle Superlattices. *Nat. Nanotechnol.* **2015**, *10*, 453–458.
- [37] Velev, O. D.; Kaler, E. W. In Situ Assembly of Colloidal Particles into Miniaturized Biosensors. *Langmuir* **1999**, *15*, 3693–3698.
- [38] Woodcock, L. V. Entropy Difference between the Face-Centered Cubic and Hexagonal Close-Packed Crystal Structures. *Nature* **1997**, *385*, 141–143.
- [39] Mau, S.-C.; Huse, D. A. Stacking Entropy of Hard-Sphere Crystals. *Phys. Rev. E* **1999**, *59*, 4396–4401.
- [40] Monovoukas, Y.; Gast, A. P. The Experimental Phase Diagram of Charged Colloidal Suspensions. *J. Colloid Interface Sci.* **1989**, *128*, 533–548.
- [41] Sirota, E. B.; Ou-Yang, H. D.; Sinha, S. K.; Chaikin, P. M.; Axe, J. D.; Fujii, Y. Complete Phase Diagram of a Charged Colloidal System: A Synchrotron X-Ray Scattering Study. *Phys. Rev. Lett.* **1989**, *62*, 1524–1527.
- [42] Fernández-Nieves, A.; Fernández Barbero, A.; Vincent, B.; De Las Nieves, F. J. Charge Controlled Swelling of Microgel Particles. *Macromolecules* **2000**, *33*, 2114–2118.
- [43] Saunders, B. R.; Laajam, N.; Daly, E.; Teow, S.; Hu, X.; Stepto, R. Microgels: From Responsive Polymer Colloids to Biomaterials. *Adv. Colloid Interface Sci.* **2009**, *147-148*, 251–262.
-

- [44] Pàmies, J. C.; Cacciuto, A.; Frenkel, D. Phase Diagram of Hertzian Spheres. *J. Chem. Phys.* **2009**, *131*, 044514.
- [45] Gottwald, D.; Likos, C. N.; Kahl, G.; Löwen, H. Ionic Microgels as Model Systems for Colloids with an Ultrasoft Electrosteric Repulsion: Structure and Thermodynamics. *J. Chem. Phys.* **2005**, *122*, 074903.
- [46] Gasser, U.; Hyatt, J. S.; Lietor-Santos, J. J.; Herman, E. S.; Lyon, L. A.; Fernandez-Nieves, A. Form Factor of pNIPAM Microgels in Overpacked States. *J. Chem. Phys.* **2014**, *141*, 034901.
- [47] Hellweg, T.; Dewhurst, C. D.; Brückner, E.; Kratz, K.; Eimer, W. Colloidal Crystals Made of Poly(*N*-isopropylacrylamide) Microgel Particles. *Colloid Polym. Sci.* **2000**, *278*, 972–978.
- [48] Lyon, L. A.; Debord, J. D.; Debord, S. B.; Jones, C. D.; McGrath, J. G.; Serpe, M. J. Microgel Colloidal Crystals. *J. Phys. Chem. B* **2004**, *108*, 19099–19108.
- [49] Gasser, U.; Sierra-Martin, B.; Fernandez-Nieves, A. Crystal Structure of Highly Concentrated, Ionic Microgel Suspensions Studied by Neutron Scattering. *Phys. Rev. E* **2009**, *79*, 051403.
- [50] Gasser, U.; Fernandez-Nieves, A. Crystal Structure of Highly Concentrated, Ionic Microgel Suspensions Studied by Small-Angle X-Ray Scattering. *Phys. Rev. E* **2010**, *81*, 052401.
- [51] Brijitta, J.; Tata, B. V.; Joshi, R. G.; Kaliyappan, T. Random HCP and FCC Structures in Thermoresponsive Microgel Crystals. *J. Chem. Phys.* **2009**, *131*, 074904.
- [52] Gasser, U.; Lietor-Santos, J. J.; Scotti, A.; Bunk, O.; Menzel, A.; Fernandez-Nieves, A. Transient Formation of bcc Crystals in Suspensions of Poly(*N*-isopropylacrylamide)-Based Microgels. *Phys. Rev. E* **2013**, *88*, 052308.
- [53] Mohanty, P. S.; Richtering, W. Structural Ordering and Phase Behavior of Charged Microgels. *J. Phys. Chem. B* **2008**, *112*, 14692–14697.
- [54] Gottwald, D.; Likos, C. N.; Kahl, G.; Löwen, H. Phase Behavior of Ionic Microgels. *Phys. Rev. Lett.* **2004**, *92*, 068301.
- [55] Karg, M.; Jaber, S.; Hellweg, T.; Mulvaney, P. Surface Plasmon Spectroscopy of Gold-poly-*N*-isopropylacrylamide Core-Shell Particles. *Langmuir* **2011**, *27*, 820–827.
- [56] Karg, M.; Hellweg, T.; Mulvaney, P. Self-Assembly of Tunable Nanocrystal Superlattices Using Poly-(NIPAM) Spacers. *Adv. Funct. Mater.* **2011**, *21*, 4668–4676.
- [57] Kelly, L. K.; Coronado, E.; Zhao, L. L.; Schatz, G. C. The Optical Properties of Metal Nanoparticles: The Influence of Size, Shape, and Dielectric Environment. *J. Phys. Chem. B* **2003**, *107*, 668–677.
- [58] Liz-Marzán, L. M. Tailoring Surface Plasmons through the Morphology and Assembly of Metal Nanoparticles. *Langmuir* **2006**, *22*, 32–41.

-
- [59] Auguié, B.; Barnes, W. L. Collective Resonances in Gold Nanoparticle Arrays. *Phys. Rev. Lett.* **2008**, *101*, 143902.
- [60] Yang, A.; Hoang, T. B.; Dridi, M.; Deeb, C.; Mikkelsen, M. H.; Schatz, G. C.; Odom, T. W. Real-Time Tunable Lasing from Plasmonic Nanocavity Arrays. *Nat. Commun.* **2015**, *6*, 6939.
- [61] Volk, K.; Fitzgerald, J. P. S.; Ruckdeschel, P.; Retsch, M.; König, T. A. F.; Karg, M. Reversible Tuning of Visible Wavelength Surface Lattice Resonances in Self-Assembled Hybrid Monolayers. *Adv. Opt. Mater.* **2017**, 1600971.
- [62] Humphrey, A. D.; Barnes, W. L. Plasmonic Surface Lattice Resonances on Arrays of Different Lattice Symmetry. *Phys. Rev. B* **2014**, *90*, 075404.
- [63] Dassanayake, U.; Fraden, S.; van Blaaderen, A. Structure of Electrorheological Fluids. *J. Chem. Phys.* **2000**, *112*, 3851–3858.
- [64] Yethiraj, A.; Van Blaaderen, A. A Colloidal Model System with an Interaction Tuneable from Hard Sphere to Soft and Dipolar. *Nature* **2003**, *421*, 513–517.
- [65] Nöjd, S.; Mohanty, P. S.; Bagheri, P.; Yethiraj, A.; Schurtenberger, P. Electric Field Driven Self-Assembly of Ionic Microgels. *Soft Matter* **2013**, *9*, 9199–9207.
- [66] Mohanty, P. S.; Yethiraj, A.; Schurtenberger, P. Deformable Particles with Anisotropic Interactions: Unusual Field-Induced Structural Transitions in Ultra-soft Ionic Microgel Colloids. *Soft Matter* **2012**, *8*, 10819–10822.
- [67] Mohanty, P. S.; Bagheri, P.; Nöjd, S.; Yethiraj, A.; Schurtenberger, P. Multiple Path-Dependent Routes for Phase-Transition Kinetics in Thermoresponsive and Field-Responsive Ultrasoft Colloids. *Phys. Rev. X* **2015**, *5*, 011030.
- [68] Pickering, S. U. Emulsions. *J. Chem. Soc. Trans.* **1907**, *91*, 2001–2021.
- [69] Schmitt, V.; Ravaine, V. Surface Compaction versus Stretching in Pickering Emulsions Stabilised by Microgels. *Curr. Opin. Colloid Interface Sci.* **2013**, *18*, 532–541.
- [70] Richtering, W. Responsive Emulsions Stabilized by Stimuli-Sensitive Microgels: Emulsions with Special Non-Pickering Properties. *Langmuir* **2012**, *28*, 17218–17229.
- [71] Rey, B. M.; Elnathan, R.; Ditcovski, R.; Geisel, K.; Zanini, M.; Fernandez-Rodriguez, M. A.; Naik, V. V.; Frutiger, A.; Richtering, W.; Ellenbogen, T.; Voelcker, N. H.; Isa, L. Fully Tunable Silicon Nanowire Arrays Fabricated by Soft Nanoparticle Templating. *Nano Lett.* **2016**, *16*, 157–163.
- [72] Verma, A.; Uzun, O.; Hu, Y.; Hu, Y.; Han, H. S.; Watson, N.; Chen, S.; Irvine, D. J.; Stellacci, F. Surface-Structure-Regulated Cell-Membrane Penetration by Monolayer-Protected Nanoparticles. *Nat. Mater.* **2008**, *7*, 588–595.
- [73] Aveyard, R.; Clint, J. H.; Nees, D.; Paunov, V. N. Compression and Structure of Monolayers of Charged Latex Particles at Air/Water and Octane/Water Interfaces. *Langmuir* **2000**, *16*, 1969–1979.
-

- [74] Deshmukh, O. S.; van den Ende, D.; Stuart, M. C.; Mugele, F.; Duits, M. H. Hard and Soft Colloids at Fluid Interfaces: Adsorption, Interactions, Assembly & Rheology. *Adv. Colloid Interface Sci.* **2015**, *222*, 215–227.
- [75] Binks, B. P. Particles as Surfactants - Similarities and Differences. *Curr. Opin. Colloid Interface Sci.* **2002**, *7*, 21–41.
- [76] Aveyard, R.; Binks, B. P.; Clint, J. H. Emulsions Stabilised Solely by Colloidal Particles. *Adv. Colloid Interface Sci.* **2003**, *100-102*, 503–546.
- [77] Arditty, S.; Schmitt, V.; Giermanska-Kahn, J.; Leal-Calderon, F. Materials Based on Solid-Stabilized Emulsions. *J. Colloid Interface Sci.* **2004**, *275*, 659–664.
- [78] Brugger, B.; Rosen, B. A.; Richtering, W. Microgels as Stimuli-Responsive Stabilizers for Emulsions. *Langmuir* **2008**, *24*, 12202–12208.
- [79] Li, Z.; Richtering, W.; Ngai, T. Poly(N-isopropylacrylamide) Microgels at the Oil-Water Interface: Temperature Effect. *Soft Matter* **2014**, *10*, 6182–6191.
- [80] Monteux, C.; Marlière, C.; Paris, P.; Pantoustier, N.; Sanson, N.; Perrin, P. Poly (N-isopropylacrylamide) Microgels at the Oil-Water Interface: Interfacial Properties as a Function of Temperature. *Langmuir* **2010**, *26*, 13839–13846.
- [81] Geisel, K.; Isa, L.; Richtering, W. The Compressibility of pH-Sensitive Microgels at the Oil-Water Interface: Higher Charge Leads to Less Repulsion. *Angew. Chem. Int. Ed.* **2014**, *53*, 4905–4909.
- [82] Style, R. W.; Isa, L.; Dufresne, E. R. Adsorption of Soft Particles at Fluid Interfaces. *Soft Matter* **2015**, *11*, 7412–7419.
- [83] Geisel, K.; Isa, L.; Richtering, W. Unraveling the 3D Localization and Deformation of Responsive Microgels at Oil/Water Interfaces: A Step Forward in Understanding Soft Emulsion Stabilizers. *Langmuir* **2012**, *28*, 15770–15776.
- [84] Destribats, M.; Lapeyre, V.; Wolfs, M.; Sellier, E.; Leal-Calderon, F.; Ravaine, V.; Schmitt, V. Soft Microgels as Pickering Emulsion Stabilisers: Role of Particle Deformability. *Soft Matter* **2011**, *7*, 7689–7698.
- [85] Destribats, M.; Lapeyre, V.; Sellier, E.; Leal-Calderon, F.; Ravaine, V.; Schmitt, V. Origin and Control of Adhesion between Emulsion Drops Stabilized by Thermally Sensitive Soft Colloidal Particles. *Langmuir* **2012**, *28*, 3744–3755.
- [86] Li, Z.; Geisel, K.; Richtering, W.; Ngai, T. Poly(N-isopropylacrylamide) Microgels at the Oil-Water Interface: Adsorption Kinetics. *Soft Matter* **2013**, *9*, 9939–9946.
- [87] Geisel, K.; Richtering, W.; Isa, L. Highly Ordered 2D Microgel Arrays: Compression versus Self-Assembly. *Soft Matter* **2014**, *10*, 7968–7976.
- [88] Pinaud, F.; Geisel, K.; Massé, P.; Catargi, B.; Isa, L.; Richtering, W.; Ravaine, V.; Schmitt, V. Adsorption of Microgels at an Oil-Water Interface: Correlation between Packing and 2D Elasticity. *Soft Matter* **2014**, *10*, 6963–6974.

-
- [89] Rey, M.; Fernández-Rodríguez, M. A.; Steinacher, M.; Scheidegger, L.; Geisel, K.; Richtering, W.; Squires, T. M.; Isa, L. Isostructural Solid-Solid Phase Transition in Monolayers of Soft Core-Shell Particles at Fluid Interfaces: Structure and Mechanics. *Soft Matter* **2016**, *12*, 3545–3557.
- [90] Tsuji, S.; Kawaguchi, H. Colored Thin Films Prepared from Hydrogel Microspheres. *Langmuir* **2005**, *21*, 8439–8442.
- [91] Kim, J.-H.; Lee, T. R. Thermo- and pH-Responsive Hydrogel-Coated Gold Nanoparticles. *Chem. Mater.* **2004**, *16*, 3647–3651.
- [92] Buchcic, C.; Tromp, R. H.; Meinders, M. B.; Cohen Stuart, M. A. Harnessing the Advantages of Hard and Soft Colloids by the Use of Core-Shell Particles as Interfacial Stabilizers. *Soft Matter* **2017**, *13*, 1326–1334.
- [93] Ding, T.; Valev, V. K.; Salmon, A. R.; Forman, C. J.; Smoukov, S. K.; Scherman, O. A.; Frenkel, D.; Baumberg, J. J. Light-Induced Actuating Nanotransducers. *Proc. Natl. Acad. Sci. U.S.A.* **2016**, *113*, 5503–5507.
- [94] Honold, T.; Volk, K.; Retsch, M.; Karg, M. Binary Plasmonic Honeycomb Structures: High-Resolution EDX Mapping and Optical Properties. *Colloids Surf. A* **2016**, *510*, 198–204.
- [95] Brugger, B.; Richtering, W. Magnetic, Thermosensitive Microgels as Stimuli-Responsive Emulsifiers Allowing for Remote Control of Separability and Stability of Oil in Water-Emulsions. *Adv. Mater.* **2007**, *19*, 2973–2978.
- [96] Honold, T.; Volk, K.; Rauh, A.; Fitzgerald, J. P.; Karg, M. Tuneable Plasmonic Surfaces via Colloid Assembly. *J. Mater. Chem. C* **2015**, *3*, 11449–11457.
- [97] Geisel, K.; Rudov, A. A.; Potemkin, I.; Richtering, W. Hollow and Core-Shell Microgels at Oil-Water Interfaces: Spreading of Soft Particles Reduces the Compressibility of the Monolayer. *Langmuir* **2015**, *31*, 13145–13154.
- [98] Nazli, K. O.; Pester, C. W.; Konradi, A.; Böker, A.; van Rijn, P. Cross-linking Density and Temperature Effects on the Self-Assembly of SiO₂-PNIPAAm Core-Shell Particles at Interfaces. *Chem. Eur. J.* **2013**, *19*, 5586–55894.
- [99] Vogel, N.; Fernández-López, C.; Pérez-Juste, J.; Liz-Marzán, L. M.; Landfester, K.; Weiss, C. K. Ordered Arrays of Gold Nanostructures from Interfacially Assembled Au@PNIPAM Hybrid Nanoparticles. *Langmuir* **2012**, *28*, 8985–8993.
- [100] Volk, K.; Fitzgerald, J. P.; Retsch, M.; Karg, M. Time-Controlled Colloidal Superstructures: Long-Range Plasmon Resonance Coupling in Particle Monolayers. *Adv. Mater.* **2015**, *27*, 7332–7337.
- [101] Atkins, P. W.; De Paula, J. *Kurzlehrbuch Physikalische Chemie*. WILEY-VCH Verlag GmbH & Co. KGaA, Weinheim **2008**, *4. Auflage*, 1064.
- [102] Hoover, W. G.; Ree, F. H. Melting Transition and Communal Entropy for Hard Spheres. *J. Chem. Phys.* **1968**, *49*, 3609–3617.
-

- [103] Pusey, P. N.; Van Megen, W. Phase Behaviour of Concentrated Suspensions of Nearly Hard Colloidal Spheres. *Nature* **1986**, *320*, 340–342.
- [104] Royall, C. P.; Poon, W. C. K.; Weeks, E. R. In Search of Colloidal Hard Spheres. *Soft Matter* **2013**, *9*, 17–27.
- [105] Bernal, J. D. A Geometrical Approach to the Structure of Liquids. *Nature* **1959**, *4655*, 141–147.
- [106] Bernal, J. D. Geometry of the Structure of Monatomic Liquids. *Nature* **1960**, *165*, 68–70.
- [107] Frenkel, D. Order through Disorder: Entropy Driven Phase Transitions. *Complex Fluids. Lecture Notes in Physics* **1993**, vol. 415, Springer Berlin Heidelberg, 137–148.
- [108] Pusey, P. N.; Van Megen, W.; Underwood, S. M.; Bartlett, P.; Ottewill, R. H. Colloidal Fluids, Crystals and Glasses. *Physica A* **1991**, *176*, 16–27.
- [109] Pusey, P. N.; Zaccarelli, E.; Valeriani, C.; Sanz, E.; Poon, W. C.; Cates, M. E. Hard Spheres: Crystallization and Glass Formation. *Philos. Trans. A Math. Phys. Eng. Sci.* **2009**, *367*, 4993–5011.
- [110] Wu, X.; Pelton, R. H.; Hamielec, A. E.; Woods, D. R.; McPhee, W. The Kinetics of Poly(*N*-isopropylacrylamide) Microgel Latex Formation. *Colloid Polym. Sci.* **1994**, *272*, 467–477.
- [111] Fernández-Barbero, A.; Fernández-Nieves, A.; Grillo, I.; López-Cabarcos, E. Structural Modifications in the Swelling of Inhomogeneous Microgels by Light and Neutron Scattering. *Phys. Rev. E* **2002**, *66*, 051803.
- [112] Boon, N.; Schurtenberger, P. Swelling of Micro-Hydrogels with a Crosslinker Gradient. *Phys. Chem. Chem. Phys.* **2017**, *19*, 23740–23746.
- [113] Varga, I.; Gilányi, G.; Mészáros, R.; Filipcsei, G.; Zrínyi, M. Effect of Cross-Link Density on the Internal Structure of Poly(*N*-isopropylacrylamide) Microgels. *J. Phys. Chem. B* **2001**, *105*, 9071–9076.
- [114] Still, T.; Chen, K.; Alsayed, A. M.; Aptowicz, K. B.; Yodh, A. G. Synthesis of Micrometer-Size Poly(*N*-isopropylacrylamide) Microgel Particles with Homogeneous Crosslinker Density and Diameter Control. *J. Colloid Interface Sci.* **2013**, *405*, 96–102.
- [115] Pelton, R. Temperature-Sensitive Aqueous Microgels. *Adv. Colloid Interface Sci.* **2000**, *85*, 1–33.
- [116] Sierra-Martin, B.; Rubio Retama, J.; Laurenti, M.; Fernández Barbero, A.; López Cabarcos, E. Structure and Polymer Dynamics within PNIPAM-Based Microgel Particles. *Adv. Colloid Interface Sci.* **2014**, *205*, 113–123.
- [117] Wu, J.; Huang, G.; Hu, Z. Interparticle Potential and the Phase Behavior of Temperature-Sensitive Microgel Dispersions. *Macromolecules* **2003**, *36*, 440–448.

-
- [118] Stieger, M.; Pedersen, J. S.; Lindner, P.; Richtering, W. Are Thermoresponsive Microgels Model Systems for Concentrated Colloidal Suspensions? A Rheology and Small-Angle Neutron Scattering Study. *Langmuir* **2004**, *20*, 7283–7292.
- [119] Riest, J.; Mohanty, P.; Schurtenberger, P.; Likos, C. N. Coarse-Graining of Ionic Microgels: Theory and Experiment. *Z. Phys. Chem.* **2012**, *226*, 711–735.
- [120] Muluneh, M.; Weitz, D. A. Direct Visualization of Three-Dimensional Crystallization Behavior in Microgels. *Phys. Rev. E* **2012**, *85*, 021405.
- [121] Sierra-Martin, B.; Fernandez-Nieves, A. Phase and Non-Equilibrium Behaviour of Microgel Suspensions as a Function of Particle Stiffness. *Soft Matter* **2012**, *8*, 4141–4150.
- [122] Yethiraj, A.; Van Blaaderen, A. Monodisperse Colloidal Suspensions of Silica and PMMA Spheres as Model Electrorheological Fluids: A Real-Space Study of Structure Formation. *Int. J. Mod. Phys. B* **2002**, *16*, 2328–2333.
- [123] Hynninen, A.-P.; Dijkstra, M. Phase Diagram of Dipolar Hard and Soft Spheres: Manipulation of Colloidal Crystal Structures by an External Field. *Phys. Rev. Lett.* **2005**, *94*, 138303.
- [124] Yethiraj, A.; Wouterse, A.; Groh, B.; van Blaaderen, A. Nature of an Electric-Field-Induced Colloidal Martensitic Transition. *Phys. Rev. Lett.* **2004**, *92*, 058301.
- [125] Yethiraj, A.; Thijssen, J. H. J.; Wouterse, A.; van Blaaderen, A. Large-Area Electric-Field-Induced Colloidal Single Crystals for Photonic Applications. *Adv. Mater.* **2004**, *16*, 596–600.
- [126] Tao, R.; Sun, J. M. Ground State of Electrorheological Fluids from Monte Carlo Simulations. *Phys. Rev. A* **1991**, *44*, R6181–R6184.
- [127] Tao, R.; Sun, J. M. Three-Dimensional Structure of Induced Electrorheological Solid. *Phys. Rev. Lett.* **1991**, *67*, 398–401.
- [128] Halsey, T. C.; Toor, W. Structure of Electrorheological Fluids. *Phys. Rev. Lett.* **1990**, *65*, 2820–2823.
- [129] Hynninen, A.-P.; Dijkstra, M. Phase Behavior of Dipolar Hard and Soft Spheres. *Phys. Rev. E* **2005**, *72*, 051402.
- [130] McMullan, J. M.; Wagner, N. J. Directed Self-Assembly of Colloidal Crystals by Dielectrophoretic Ordering Observed with Small Angle Neutron Scattering (SANS). *Soft Matter* **2010**, *6*, 5443–5450.
- [131] Mittal, M.; Lele, P. P.; Kaler, E. W.; Furst, E. M. Polarization and Interactions of Colloidal Particles in AC Electric Fields. *J. Chem. Phys.* **2008**, *129*, 064513.
- [132] Leunissen, M. E.; Vutukuri, H. R.; van Blaaderen, A. Directing Colloidal Self-Assembly with Biaxial Electric Fields. *Adv. Mater.* **2009**, *21*, 3116–3120.
- [133] Pieranski, P. Two-Dimensional Interfacial Colloidal Crystals. *Phys. Rev. Lett.* **1980**, *45*, 569–572.
-

- [134] Vogel, N.; Weiss, C. K.; Landfester, K. From Soft to Hard: the Generation of Functional and Complex Colloidal Monolayers for Nanolithography. *Soft Matter* **2012**, *8*, 4044–4061.
- [135] Isa, L.; Kumar, K.; Müller, M.; Grolig, J.; Textor, M.; Reimhult, E. Particulate Lithography from Colloidal Self-Assembly at Liquid-Liquid Interfaces. *ACS Nano* **2010**, *4*, 5665–5670.
- [136] Butt, H.-J.; Graf, K.; Kappl, M. Physics and Chemistry of Interfaces. *WILEY-VCH Verlag GmbH & Co. KGaA, Weinheim* **2003**, 90.
- [137] Horozov, T. S.; Aveyard, R.; Clint, J. H.; Binks, B. P. Order-Disorder Transition in Monolayers of Modified Monodisperse Silica Particles at the Octane-Water Interface. *Langmuir* **2003**, *19*, 2822–2829.
- [138] Horozov, T. S.; Aveyard, R.; Binks, B. P.; Clint, J. H. Structure and Stability of Silica Particle Monolayers at Horizontal and Vertical Octane-Water Interfaces. *Langmuir* **2005**, *21*, 7405–7412.
- [139] Isa, L.; Lucas, F.; Wepf, R.; Reimhult, E. Measuring Single-Nanoparticle Wetting Properties by Freeze-Fracture Shadow-Casting Cryo-Scanning Electron Microscopy. *Nat. Commun.* **2011**, *2*, 438.
- [140] Scheidegger, L.; Fernández-Rodríguez, M. A.; Geisel, K.; Zanini, M.; Elnathan, R.; Richtering, W.; Isa, L. Compression and Deposition of Microgel Monolayers from Fluid Interfaces: Particle Size Effects on Interface Microstructure and Nanolithography. *Phys. Chem. Chem. Phys.* **2017**, *19*, 8671–8680.
- [141] Yarnell, J. L.; Katz, M. J.; Wenzel, R. G.; Koenig, S. H. Structure Factor and Radial Distribution Function for Liquid Argon at 85°K. *Phys. Rev. A* **1973**, *7*, 2130–2144.
- [142] Crocker, J. C.; Grier, D. G. Methods of Digital Video Microscopy for Colloidal Studies. *J. Colloid Interface Sci.* **1996**, *179*, 298–310.
- [143] Weeks, E. R. [http : //www.physics.emory.edu/faculty/weeks/idl/gofr.html](http://www.physics.emory.edu/faculty/weeks/idl/gofr.html). 08/2017.
- [144] Scheeler, S. P.; Mühlig, S.; Rockstuhl, C.; Hasan, S. B.; Ullrich, S.; Neubrech, F.; Kudera, S.; Pacholski, C. Plasmon Coupling in Self-Assembled Gold Nanoparticle-Based Honeycomb Islands. *J. Phys. Chem. C* **2013**, *117*, 18634–18641.
- [145] Hansen, J.-P.; McDonald, I. R. Theory of Simple Liquids with Applications to Soft Matter. *Academic Press* **2013**, Edition 4.
- [146] Steinhardt, P. J.; Nelson, D. R.; Ronchetti, M. Bond-Orientational Order in Liquids and Glasses. *Phys. Rev. B* **1983**, *28*, 784–805.
- [147] Schmidt, M.; Löwen, H. Phase Diagram of Hard Spheres Confined between Two Parallel Plates. *Phys. Rev. E* **1997**, *55*, 7228–7241.
- [148] Ayappa, K. G.; Mishra, R. K. Freezing of Fluids Confined between Mica Surfaces. *J. Phys. Chem. B* **2007**, *111*, 14299–14310.

-
- [149] Borsali, R.; Pecora, R. Soft-Matter Characterization. *Springer* **2008**, Volume 1.
- [150] Schnablegger, H.; Singh, Y. The SAXS Guide. *Anton Paar GmbH* **2013**, 3rd Edition.
- [151] Frisken, B. J. Revisiting the Method of Cumulants for the Analysis of Dynamic Light-Scattering Data. *Appl. Opt.* **2001**, *40*, 4087–4091.
- [152] Provencher, S. W. A Constrained Regularization Method for Inverting Data Represented by Linear Algebraic or Integral Equations. *Comput. Phys. Commun.* **1982**, *27*, 213–227.
- [153] Provencher, S. W. CONTIN: A General Purpose Constrained Regularization Program for Inverting Noisy Linear Algebraic and Integral Equations. *Comput. Phys. Commun.* **1982**, *27*, 229–242.
- [154] Dulle, M.; Jaber, S.; Rosenfeldt, S.; Radulescu, A.; Förster, S.; Mulvaney, P.; Karg, M. Plasmonic Gold-Poly(*N*-isopropylacrylamide) Core-Shell Colloids with Homogeneous Density Profiles: a Small Angle Scattering Study. *Phys. Chem. Chem. Phys.* **2015**, *17*, 1354–1367.
- [155] Exner, A.; Rosenfeldt, S.; Fischer, S.; Lindner, P.; Förster, S. Defect Accommodation in Nanostructured Soft Crystals. *Nanoscale* **2014**, *6*, 1635–16345.
- [156] Hecht, A.-M.; Duplessix, C.; Picot, C.; de Gennes, P. Structural Inhomogeneities in the Range 2.5–2500 Å in Polyacrylamide Gels. *Macromolecules* **1985**, *18*, 2167–2173.
- [157] Kohlbrecher, J. SASfit: A Program for Fitting Simple Structural Models to Small Angle Scattering Data. *Paul Scherrer Institut, Laboratory for Neutron Scattering, CH-5232, Villigen, Switzerland* **2007**, Version 3.
- [158] Shibayama, M.; Tanaka, T.; Han, C. C. Small Angle Neutron Scattering Study on Poly(*N*-isopropyl acrylamide) Gels Near Their Volume-Phase Transition Temperature. *J. Chem. Phys.* **1992**, *97*, 6829–6841.
- [159] Förster, S.; Fischer, S.; Zielske, K.; Schellbach, C.; Sztucki, M.; Lindner, P.; Perlich, J. Calculation of Scattering-Patterns of Ordered Nano- and Mesoscale Materials. *Adv. Colloid Interface Sci.* **2011**, *163*, 53–83.
- [160] Förster, S.; Apostol, L. *Scatter* **2014**, Version 2.5.
- [161] Förster, S.; Timmann, A.; Konrad, M.; Schellbach, C.; Meyer, A.; Funari, S. S.; Mulvaney, P.; Knott, R. Scattering Curves of Ordered Mesoscopic Materials. *J. Phys. Chem. B* **2005**, *109*, 1347–1360.
- [162] Förster, S.; Burger, C. Scattering Functions of Polymeric Core-Shell Structures and Excluded Volume Chains. *Macromolecules* **1998**, *31*, 879–891.
- [163] Turkevich, J.; Stevenson, P. C.; Hillier, J. A Study of the Nucleation and Growth Processes in the Synthesis of Colloidal Gold. *Discuss. Faraday Soc.* **1951**, *11*, 55–75.
-

- [164] Verhaegh, N. A. M.; van Blaaderen, A. Dispersions of Rhodamine-Labeled Silica Spheres: Synthesis, Characterization, and Fluorescent Confocal Scanning Laser Microscopy. *Langmuir* **1994**, *10*, 1427–1438.
- [165] Stöber, W.; Fink, A.; Bohn, E. Controlled Growth of Monodisperse Silica Spheres in the Micron Size Range. *J. Colloid Interface Sci.* **1968**, *26*, 62–69.
- [166] Bogush, G. H.; Tracy, M. A.; Zukoski IV, C. F. Preparation of Monodisperse Silica Particles: Control of Size and Mass Fraction. *J. Non-Cryst. Solids* **1988**, *104*, 95–106.
- [167] <https://profilab24.com/Hellma-demontierbare-Kuevette-106-QS-01-mm-Schichtdicke>. 10/2017.
- [168] Nöjd, S. Structure, Dynamics and Phase Behaviour of Charged Soft Colloidal Dispersions. *Lund University* **2016**, *Dissertation*.
- [169] Meijer, J. M.; Pal, A.; Ouhajji, S.; Lekkerkerker, H. N.; Philipse, A. P.; Petukhov, A. V. Observation of Solid-Solid Transitions in 3D Crystals of Colloidal Superballs. *Nat. Commun.* **2017**, *8*, 14352.
- [170] Contreras-Cáceres, R.; Pastoriza-Santos, I.; Alvarez-Puebla, R. A.; Pérez-Juste, J.; Fernández-Barbero, A.; Liz-Marzán, L. M. Growing Au/Ag Nanoparticles within Microgel Colloids for Improved Surface-Enhanced Raman Scattering Detection. *Chem. Eur. J.* **2010**, *16*, 9462–9467.
- [171] Contreras-Cáceres, R.; Sánchez-Iglesias, A.; Karg, M.; Pastoriza-Santos, I.; Pérez-Juste, J.; Pacifico, J.; Hellweg, T.; Fernández-Barbero, A.; Liz-Marzán, L. M. Encapsulation and Growth of Gold Nanoparticles in Thermoresponsive Microgels. *Adv. Mater.* **2008**, *20*, 1666–1670.
- [172] Contreras-Cáceres, R.; Pacifico, J.; Pastoriza-Santos, I.; Pérez-Juste, J.; Fernández-Barbero, A.; Liz-Marzán, L. M. Au@pNIPAM Thermosensitive Nanostructures: Control Over Shell Cross-linking, Overall Dimensions, and Core Growth. *Adv. Funct. Mater.* **2009**, *19*, 3070–3076.
- [173] Fernández-López, C.; Pérez-Balado, C.; Pérez-Juste, J.; Pastoriza-Santos, I.; de Lera, A. R.; Liz-Marzán, L. M. A General LbL Strategy for the Growth of pNIPAM Microgels on Au Nanoparticles with Arbitrary Shapes. *Soft Matter* **2012**, *8*, 4165–4170.
- [174] Singh, N.; Lyon, L. A. Au Nanoparticle Templated Synthesis of pNIPAm Nanogels. *Chem. Mater.* **2007**, *19*, 719–726.
- [175] Karg, M.; Schelero, N.; Oppel, C.; Gradzielski, M.; Hellweg, T.; von Klitzing, R. Versatile Phase Transfer of Gold Nanoparticles from Aqueous Media to Different Organic Media. *Chem. Eur. J.* **2011**, *17*, 4648–4654.

-
- [176] Virtanen, O. L. J.; Richtering, W. Kinetics and Particle Size Control in Non-Stirred Precipitation Polymerization of *N*-Isopropylacrylamide. *Colloid Polym. Sci.* **2014**, *292*, 1743–1756.
- [177] Virtanen, O. L. J.; Ala-Mutka, H. M.; Richtering, W. Can the Reaction Mechanism of Radical Solution Polymerization Explain the Microgel Final Particle Volume in Precipitation Polymerization of *N*-Isopropylacrylamide? *Macromol. Chem. Phys.* **2015**, *216*, 1431–1440.
- [178] von Nessen, K.; Karg, M.; Hellweg, T. Thermoresponsive Poly-(*N*-isopropylmethacrylamide) Microgels: Tailoring Particle Size by Interfacial Tension Control. *Polymer* **2013**, *54*, 5499–5510.
- [179] Hendel, T.; Wuithschick, M.; Kettemann, F.; Birnbaum, A.; Rademann, K.; Polte, J. In Situ Determination of Colloidal Gold Concentrations with UV-vis Spectroscopy: Limitations and Perspectives. *Anal. Chem.* **2014**, *86*, 11115–11124.
- [180] Müller, M. B.; Kuttner, C.; König, T. A. F.; Tsukruk, V. V.; Förster, S.; Karg, M.; Fery, A. Plasmonic Library Based on Substrate-Supported Gradiant Plasmonic Arrays. *ACS Nano* **2014**, *8*, 9410–9421.
- [181] Lohse, S. E.; Burrows, N. D.; Scarabelli, L.; Liz-Marzán, L. M.; Murphy, C. J. Anisotropic Noble Metal Nanocrystal Growth: The Role of Halides. *Chem. Mater.* **2014**, *26*, 34–43.
- [182] Langille, M. R.; Personick, M. L.; Zhang, J.; Mirkin, C. A. Defining Rules for the Shape Evolution of Gold Nanoparticles. *J. Am. Chem. Soc.* **2012**, *134*, 14542–14554.
- [183] Rodríguez-Fernández, J.; Pérez-Juste, J.; Mulvaney, P.; Liz-Marzán, L. M. Spatially-Directed Oxidation of Gold Nanoparticles by Au(III)-CTAB Complexes. *J. Phys. Chem. B* **2005**, *109*, 14257–14261.
- [184] Jain, P. K.; Lee, K. S.; El-Sayed, I. H.; El-Sayed, M. A. Calculated Absorption and Scattering Properties of Gold Nanoparticles of Different Size, Shape, and Composition: Applications in Biological Imaging and Biomedicine. *J. Phys. Chem. B* **2006**, *110*, 7238–7248.
- [185] Huang, G.; Hu, Z. Phase Behavior and Stabilization of Microgel Arrays. *Macromolecules* **2007**, *40*, 3749–3756.
- [186] Zyuzin, M. V.; Honold, T.; Carregal-Romero, S.; Kantner, K.; Karg, M.; Parak, W. J. Influence of Temperature on the Colloidal Stability of Polymer-Coated Gold Nanoparticles in Cell Culture Media. *Small* **2016**, *12*, 1723–1731.
- [187] Karg, M.; Prévost, S.; Brandt, A.; Wallacher, D.; von Klitzing, R.; Hellweg, T. Poly-NIPAM Microgels with Different Cross-Linker Densities. *Prog. Colloid Polym. Sci.* **2013**, *140*, 63–76.
-

- [188] Mehdizadeh Taheri, S.; Rosenfeldt, S.; Fischer, S.; Bösecke, P.; Narayanan, T.; Lindner, P.; Förster, S. Shear-Induced Macroscopic “Siamese” Twins in Soft Colloidal Crystals. *Soft Matter* **2013**, *9*, 8464–8475.
- [189] Förster, S. Scatter - User guide. **2013**, *Version 3.0 for Windows 7*.
- [190] Förster, S.; Timmann, A.; Schellbach, C.; Frömsdorf, A.; Kornowski, A.; Weller, H.; Roth, S. V.; Lindner, P. Order Causes Secondary Bragg Peaks in Soft Materials. *Nat. Mater.* **2007**, *6*, 888–893.
- [191] Karg, M.; Wellert, S.; Prevost, S.; Schweins, R.; Dewhurst, C.; Liz-Marzán, L. M.; Hellweg, T. Well Defined Hybrid PNIPAM Core-Shell Microgels: Size Variation of the Silica Nanoparticle Core. *Colloid Polym. Sci.* **2011**, *289*, 699–709.
- [192] Smallenburg, F.; Vutukuri, H. R.; Imhof, A.; van Blaaderen, A.; Dijkstra, M. Self-Assembly of Colloidal Particles into Strings in a Homogeneous External Electric or Magnetic Field. *J. Phys.: Condens. Matter* **2012**, *24*, 464113.
- [193] Danov, K. D.; Kralchevsky, P. A. Capillary Forces between Particles at a Liquid Interface: General Theoretical Approach and Interactions between Capillary Multipoles. *Adv. Colloid Interface Sci.* **2010**, *154*, 91–103.
- [194] Cerbino, R.; Trappe, V. Differential Dynamic Microscopy: Probing Wave Vector Dependent Dynamics with a Microscope. *Phys. Rev. Lett.* **2008**, *100*, 188102.
- [195] Bayles, A. V.; Squires, T. M.; Helgeson, M. E. Dark-Field Differential Dynamic Microscopy. *Soft Matter* **2016**, *12*, 2440–2452.
- [196] Kratz, K.; Hellweg, T.; Eimer, W. Influence of Charge Density on the Swelling of Colloidal Poly(*N*-isopropylacrylamide-co-acrylic acid) Microgels. *Colloids Surf. A* **2000**, *170*, 137–149.
- [197] Safari, M. S.; Vorontsova, M. A.; Poling-Skutvik, R.; Vekilov, P. G.; Conrad, J. C. Differential Dynamic Microscopy of Weakly Scattering and Polydisperse Protein-Rich Clusters. *Phys. Rev. E* **2015**, *92*, 042712.
- [198] Lu, P. J.; Giavazzi, F.; Angelini, T. E.; Zaccarelli, E.; Jargstorff, F.; Schofield, A. B.; Wilking, J. N.; Romanowsky, M. B.; Weitz, D. A.; Cerbino, R. Characterizing Concentrated, Multiply Scattering, and Actively Driven Fluorescent Systems with Confocal Differential Dynamic Microscopy. *Phys. Rev. Lett.* **2012**, *108*, 218103.
- [199] Petekidis, G.; Gapinski, J.; Seymour, P.; van Duijneveldt, J. S.; Vlassopoulos, D.; Fytas, G. Dynamics of Core-Shell Particles in Concentrated Suspensions. *Phys. Rev. E* **2004**, *69*, 042401.
- [200] Pusey, P. N. Intensity Fluctuation Spectroscopy of Charged Brownian Particles: the Coherent Scattering Function. *J. Phys. A: Math. Gen.* **1978**, *11*, 119–135.
- [201] Nägele, G.; Kellerbauer, O.; Krause, R.; Klein, R. Hydrodynamic Effects in Polydisperse Charged Colloidal Suspensions at Short Times. *Phys. Rev. E* **1993**, *47*, 2562–2574.

-
- [202] Phalakornkul, J. K.; Gast, A. P.; Pecora, R.; Nägele, G.; Ferrante, A.; Mandl-Steininger, B.; Klein, R. Structure and Short-Time Dynamics of Polydisperse Charge-Stabilized Suspensions. *Phys. Rev. E* **1996**, *54*, 661–675.
- [203] Ciach, A.; Pekalski, J. Exactly Solvable Model for Self-Assembly of Hard Core-Soft Shell Particles at Interfaces. *Soft Matter* **2017**, *13*, 2603–2608.
- [204] Liu, X.; Atwater, M.; Wang, J.; Huo, Q. Extinction Coefficient of Gold Nanoparticles with Different Sizes and Different Capping Ligands. *Colloids Surf. B* **2007**, *58*, 3–7.
- [205] Alvarez-Puebla, R.; Liz-Marzán, L. M.; García de Abajo, F. J. Light Concentration at the Nanometer Scale. *J. Phys. Chem. Lett.* **2010**, *1*, 2428–2434.
- [206] Honold, T.; Skrybeck, D.; Wagner, K. G.; Karg, M. Fully Reversible Quantitative Phase Transfer of Gold Nanoparticles Using Bifunctional PNIPAM Ligands. *Langmuir* **2017**, *33*, 253–261.
- [207] Ebeling, B.; Vana, P. RAFT-Polymers with Single and Multiple Trithiocarbonate Groups as Uniform Gold-Nanoparticle Coatings. *Macromolecules* **2013**, *46*, 4862–4871.
- [208] Chu, F.; Heptner, N.; Lu, Y.; Siebenburger, M.; Lindner, P.; Dzubiella, J.; Ballauff, M. Colloidal Plastic Crystals in a Shear Field. *Langmuir* **2015**, *31*, 5992–6000.
- [209] Shinotsuka, K.; Kajita, Y.; Hongo, K.; Hatta, Y. Crystal Perfection of Particle Monolayer at the Air-Water Interface. *Langmuir* **2015**, *31*, 11452–11457.
- [210] Aubry, N.; Singh, P.; Janjua, M.; Nudurupati, S. Micro- and Nanoparticles Self-Assembly for Virtually Defect-Free, Adjustable Monolayers. *Proc. Natl. Acad. Sci. U.S.A.* **2008**, *105*, 3711–3714.
- [211] <https://www.ill.eu/instruments-support/instruments-groups/instruments/d11/description/instrument-layout/>. 06/2017.
- [212] Nägele, G. *Lecture Manuscripts of the Spring School of the Institute of Solid State Research* **2008**, *39*, B2.
- [213] Srinivasa Rao, K.; Rajogopalan, R. Interaction Forces in Quasi-Two-Dimensional Charged Dispersions. *Phys. Rev. E* **1998**, *57*, 3227–3233.

Danksagung

An dieser Stelle möchte ich allen danken, die mich während der letzten Jahre unterstützt haben und damit zum Gelingen dieser Arbeit beigetragen haben. Als erstes möchte ich mich bei meinem Doktorvater Prof. Dr. Matthias Karg für die sehr gute wissenschaftliche Betreuung bedanken: Matthias, ich danke dir besonders für die vielen hilfreichen Diskussionen, die Motivation sowie das Ermöglichen von Auslandsaufenthalten und Konferenzbesuchen. Auch nach deinem Umzug an die HHU Düsseldorf konnte ich mich auf deine Unterstützung verlassen. Fachlich sowie persönlich habe ich sehr viel in dieser Zeit gelernt.

Prof. Dr. Lucio Isa, Siddarth Vasudevan, Marcel Rey, Michele Zanini und Lorenzo Barbera danke ich für die Umsetzung spannender Kooperationsprojekte, die produktive Zeit an der ETH Zürich und die gute Zusammenarbeit!

Prof. Dr. Peter Schurtenberger danke ich, dass ich einen Sommer in Schweden mit einem interessanten Forschungsprojekt verbringen durfte. Ich danke der gesamten Physikalischen Chemie in Lund für die freundliche Aufnahme, die Hilfsbereitschaft und die schöne Zeit! Besonderer Dank gilt Janne-Mieke, Sofi, Maxime, Linda, Jérôme, Jasper and Priti. Außerdem möchte ich Janne-Mieke für zahlreiche gute Diskussionen, Ratschläge und für unsere Kooperation, die auch über meinen Auslandsaufenthalt hinaus ging, danken. Dem Elitenetzwerk Bayern sowie der Graduate School an der Universität Bayreuth danke ich für die finanzielle Unterstützung, welche diesen Auslandsaufenthalt erst ermöglichte.

Besonderer Dank gilt Bernd Kopera für die python Skripte und die hilfreichen Diskussionen - ohne dich würde ich wahrscheinlich immer noch Konfokalbilder auswerten! Auch Martin Dulle danke ich für viele interessante Diskussionen.

Desweiteren danke ich Nico Carl und Ralph Schweins für die Unterstützung bei der Durchführung der SANS Messungen am ILL in Grenoble. Bei Andrei Petukhov, Antara Pal und Anastasia Venediktova bedanke ich mich für die Durchführung der SAXS Messungen am ESRF in Grenoble.

Ich danke den technischen Angestellten, Karl-Heinz Lauterbach und Julia Moßner, für Ihre unermüdliche Hilfsbereitschaft sowie all meinen Praktikanten und HiWis für die tolle Zusammenarbeit.

Großer Dank gilt dem gesamten Kolloidale Systeme - Team. Danke Kristina, Arne, Tobi, Kirsten, Julian und Joe für die gute und produktive Arbeitsatmosphäre in unserer Gruppe sowie das Korrekturlesen dieser Arbeit. Vor allem danke ich den weltbesten "Läbbi"-Kollegen, Arne und Kristina. Danke für die super Zusammenarbeit, die vielen guten Diskussionen, die Ratschläge und die gemeinsamen Späße - ihr seid klasse!

Außerdem danke ich der gesamten Physikalischen Chemie I in Bayreuth: Danke euch allen für die schöne Zeit, das supergute Arbeitsklima, die vielen klasse Abende im Kaffeezimmer und auf unserer Terrasse, die Kickerpausen und die legendären Salsaabende. Ihr seid alle super Kollegen! Vor allem danke ich Kristina, Pia, Arne, Fabi, Miri, Patrick, Alex und Christian.

Danke auch an all meine Freunde außerhalb der Uni für den Ausgleich und die nötige und gute Ablenkung. Ich bin sehr froh, dass es euch gibt!

Außerdem möchte ich noch den wichtigsten Menschen in meinem Leben danken:

Ein großes Danke an meine Familie: Mama, Papa, Tini und Jogi, es ist so gut zu wissen, dass ihr immer für mich da seid, an mich glaubt und mich in allem unterstützt.

Basti - ich danke dir für deine unglaubliche Geduld, den Rückhalt und die Unterstützung sowie die Kraft, die du mir gibst! DANKE.

Eidesstattliche Versicherungen und Erklärungen

§8 Satz 2 Nr. 3 PromO Fakultät

Hiermit versichere ich eidesstattlich, dass ich die Arbeit selbstständig verfasst und keine anderen als die von mir angegebenen Quellen und Hilfsmittel benutzt habe (vgl. Art. 64 Abs 1 Satz 6 BayHSchG).

§8 Satz 2 Nr. 3 PromO Fakultät

Hiermit erkläre ich, dass ich die Dissertation nicht bereits zur Erlangung eines akademischen Grades eingereicht habe und dass ich nicht bereits diese oder eine gleichartige Doktorprüfung endgültig nicht bestanden habe.

§8 Satz 2 Nr. 4 PromO Fakultät

Hiermit erkläre ich, dass ich Hilfe von gewerblichen Promotionsberatern bzw. -vermittlern oder ähnlichen Dienstleistern weder bisher in Anspruch genommen habe noch künftig in Anspruch nehmen werde.

§8 Satz 2 Nr. 7 PromO Fakultät

Hiermit erkläre ich mein Einverständnis, dass die elektronische Fassung der Dissertation unter Wahrung meiner Urheberrechte und des Datenschutzes einer gesonderten Überprüfung unterzogen werden kann.

§8 Satz 2 Nr. 8 PromO Fakultät

Hiermit erkläre ich mein Einverständnis, dass bei Verdacht wissenschaftlichen Fehlverhaltens Ermittlungen durch universitätsinterne Organe der wissenschaftlichen Selbstkontrolle stattfinden können.

Bayreuth, den 6. Februar 2018

Astrid Rauh

